HAWAI'I SPACE GRANT CONSORTIUM

UNDERGRADUATE FELLOWSHIP REPORTS

Summer 2008 – Spring 2009

NATIONAL SPACE GRANT COLLEGE AND FELLOWSHIP PROGRAM

NASA

HSGC Report Number 09-18

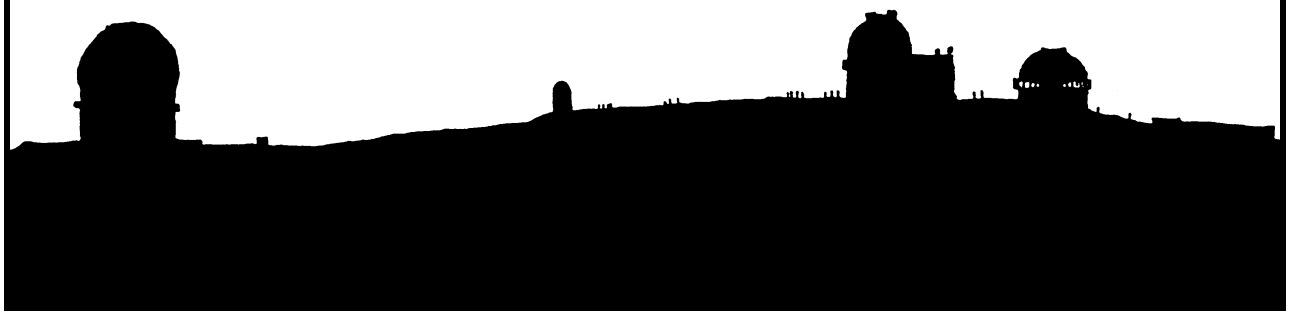

Compiled in 2009 by
HAWAIʻI SPACE GRANT CONSORTIUM

The Hawaiʻi Space Grant Consortium is one of the fifty-two National Space Grant Colleges supported by the National Aeronautics and Space Administration (NASA).

This report may be cited as

Hawaiʻi Space Grant Consortium (2009) *Undergraduate Fellowship Reports*. HSGC Report No. 09-18. Hawaiʻi Space Grant Consortium, Honolulu.

Individual articles may be cited as

Author, A.B. (2009) Title of article. *Undergraduate Fellowship Reports*, pp. xx-xx. Hawaiʻi Space Grant Consortium, Honolulu.

This report is distributed by:

Hawaiʻi Space Grant Consortium
Hawaiʻi Institute of Geophysics and Planetology
University of Hawaiʻi at Mānoa
1680 East West Road, POST 501
Honolulu, HI 96822

TABLE OF CONTENTS

KUMU A‘O CUBESAT TEAM REPORTS

JET PROPULSION LABORATORY (JPL) SUMMER 2008 PROGRAM

NASA AMES ROBOTICS ACADEMY SUMMER 2008 PROGRAM

Foreword

This volume contains sixteen reports from Hawai‘i Space Grant Undergraduate Fellows at the University of Hawai‘i at Mānoa and the University of Hawai‘i at Hilo. The students worked on their projects in the Summer/Fall 2008 and Spring 2009 semesters under the guidance of their faculty mentors and supervisors. We congratulate all of the students for their outstanding reports and warmly thank their faculty mentors and supervisors for generously supporting the Hawai‘i Space Grant Consortium Undergraduate Fellowship Programs.

The Hawai‘i Space Grant Consortium is supported by NASA through its National Space Grant College and Fellowship Program with matching funds from the University of Hawai‘i. The goal of the program is to strengthen the national capabilities in space-related science, technology, engineering, and mathematics (STEM) and to prepare the next generation of space scientists. All of the students' projects are related to the goals of NASA's Strategic Plan.

For more information about the Fellowship Program, please visit our website: http://www.spacegrant.hawaii.edu/fellowships.html

Edward R.D. Scott
Associate Director, Fellowships

IDENTIFICATION AND MAPPING OF HAWAIIAN CORAL REEFS USING HYPERSPECTRAL REMOTE SENSING

Jessica Frances N. Ayau
College of Education
University of Hawai‘i at Mānoa
Honolulu, HI 96822

ABSTRACT

Coral reefs are an important resource to earth's ecosystem, which is why they need to be protected. A global monitoring system would be an important component in protecting the reefs by locating them and tracking their health. Hyperspectral remote sensing has been used to distinguish the spectrum of different coastal ocean bottom types. This project uses two digital processing techniques and the unique spectrums of coral, algae, sand, water at 1m – 2m depth, and water at 3m depth or greater to identify and map these bottom types. The project's methodology utilizes a supervised classification approach and a linear spectral unmixing approach. In the supervised classification approach, I made field observations of selected training sites and identified the bottom types within those sites. I then ran the 1m HICO data image through the classification program and generated a classified map of the five bottom types. I resize the HICO 1m image to 25m and ran it through the classification program. The 25m map's results indicted that there was a pronounced mixed pixel effect. The linear spectral unmixing technique was used as a way to minimize the mixed pixel problem. The approach for this technique involved collecting bottom type spectra with an ocean spectrometer then applying those spectra to a spectral library. Another spectral library was generated from selected training sites from the image. I applied both spectral libraries to the program and generated abundance maps for each of my bottom types. The results of the supervised technique indicated that there was too much of a mixed pixel problem for the technique to be used to monitor coral reefs. The linear spectral unmixing technique was effective for solving the mixed pixel problem but issues with the required spectral library for the technique need to be addressed.

INTRODUCTION

Coral reefs play an important role in the earth's ecosystem in several ways. Their symbiotic relationship with algae is important in producing energy for many marine organisms. Corals also provide shelter for other marine organisms such as fish, worms, eels, and crabs. They also act as natural buffers against hurricanes and tsunamis because they absorb some of the storms energy. Coral reefs provide a steady fishery because they are the residence to many fishes. They are also used by divers and snorkelers for recreation.

There are two major factors that limit the occurrence of coral reefs globally, light and temperature. Corals need sunlight to photosynthesize which is why they are located near the surface in shallow and clear waters instead of the sea floor. Coral reefs are found in tropical and warm areas such as the Indo-Pacific, the Western Atlantic, and the Red Sea because they cannot survive in cold water. Coral reefs are delicate systems that are subject to negative effects of human impact such as pollution, increase in global warming, and the input of land sediment into

the ocean. These effects could cause massive coral bleaching which would eventually cause death (International Year of the Reef, 2007).

Since coral reefs are an important and sensitive resource, a system to identify and assess the health of the reef globally is needed. My project involves using satellite imaging to map and identify coral reefs, which could eventually be used globally. Using satellites to monitor coral reefs will allow for regular monitoring without the significant cost of field work, especially considering the widespread global distribution of coral reefs.

The purpose of my project was to map and identify coral reefs using hyperspectral remote sensing and digital image processing techniques. The digital image processing techniques I used in order to discriminate coral from other ocean bottom types (Hochberg and Atkinson, 2003). I used two hyperspectral remote sensing datasetss from an aircraft at two different spatial resolutions: 1 meter and 25 meters. I examined hyperspectral data of five bottom types: coral, algae, sand, and two water classes. After reading Goodman and Ustin (2002), I found that each of the bottom types in my project has a characteristic spectrum. Figure 1 shows an example of three bottom types and their respective characteristic spectra. Figure 2 shows a plot of two water spectrums, one at 1m – 2m depth and the other at 3m depth or greater.

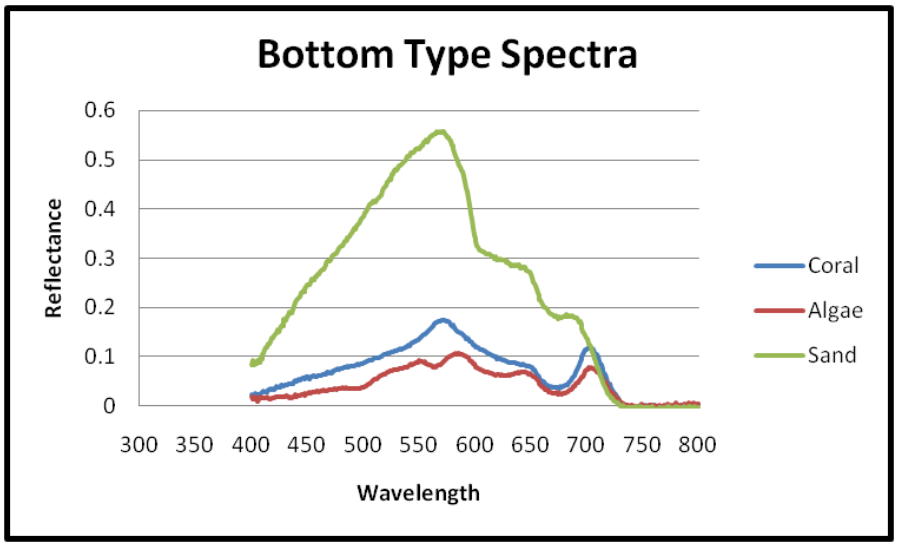

Figure 1: This figure shows a comparison of the spectra of three bottom types: coral, algae and sand. Sand can be easily distinguished from coral or algae by its much higher reflectance. Also, unlike the coral and algae spectra, the sand spectrum does not show a drop in reflectance at 675nm due to chlorophyll absorption. Coral and algae have similar reflectance values so distinguishing the two requires a closer comparison of their spectra. In this plot, coral has a slightly higher reflectance than algae and the peak between 550nm and 600nm are slightly different. Coral's peak goes straight up and then down, while algae's peak goes up then down twice.

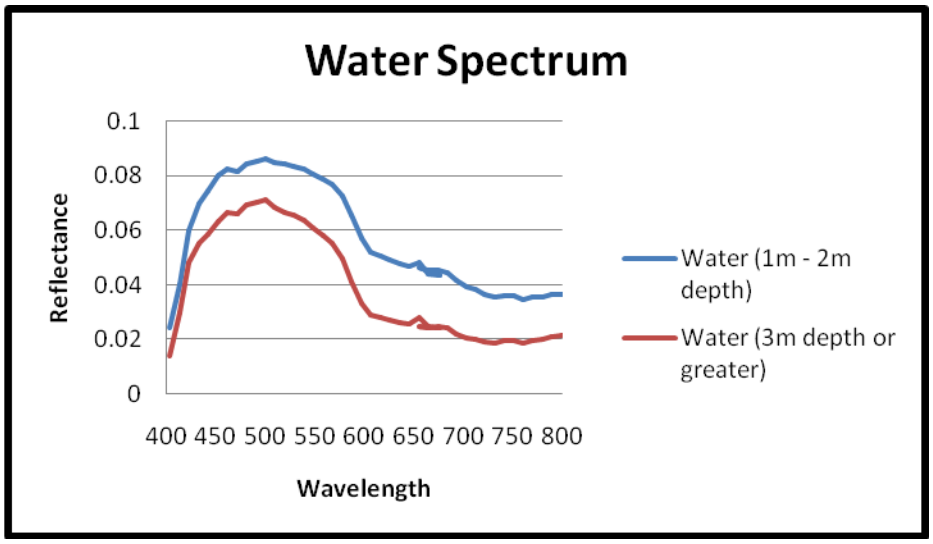

Figure 2: This water spectrum shows that water at different depths have different spectral characteristics. The top curve represents water at 1m – 2m depth which has a higher reflectance then the bottom curve which is 3m depth. Water at different depths has different characteristics because deeper water absorbs more light than reflects light.

METHODS

The goal of this project was to identify and map coral reefs using hyperspectral remote sensing data. I worked both with high-resolution (1m/ pixel) data as well as coarser resolution (25m/ pixel) data, both having been obtained from an aircraft. I used two techniques to identify coral reefs for this project: supervised classification and linear spectral unmixing. The supervised classification technique involved first selecting training sites that defined "end-member" bottom types. This semi-automated technique then compared pixels of unknown bottom types ("unknown pixels") in the image with the selected bottom type classes and decided which class the unknown pixel most closely resembled. The linear spectral unmixing technique required spectra from a spectral library to derive the abundances for each bottom type that comprised a pixel. Unlike the supervised classification technique which assigns the most spectrally similar class to each pixel, the spectral unmixing program determines the fraction of each bottom type to best fit the spectrum for each pixel. This results in an abundance map for each bottom type. I chose Kāneʻohe Bay (Figure 3) for the study area because it was easily accessible and it contained all of the bottom types that I wanted to map. The methods I used to conduct these techniques were divided into three sections which are described below.

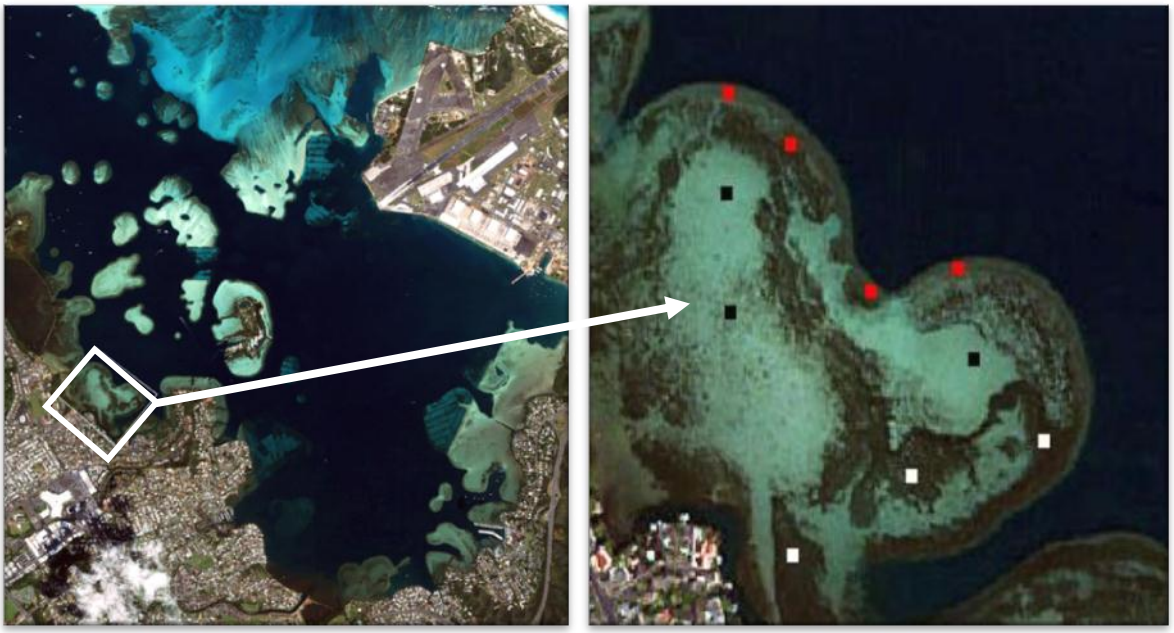

Figure 3: Kāneʻohe Bay was selected as the study area because it contained the desired bottom types and there was easy access to the bay. The white square outlines the area containing the training sites. The arrow points to an enlarged view of the training sites. The red points represent coral, the white represent algae, and the black represent sand.

Supervised Classification of the 1m Dataset

The first part of this project involved using the supervised classification technique on 1m spatial resolution data. These data were obtained from the Hyperspectral Imager for Coastal Ocean (HICO) sensor and were provided by Jeffrey Gillis-Davis, a faculty member of the Hawaiʻi Institute of Geophysics and Planetology (HIGP). These data consisted of three flight lines which covered most of the southern portion of Kāneʻohe Bay. This imagery consists of 60 narrow spectral bands ranging from 380 to 980nm. I also acquired maps and digital aerial photographs of the bay from the Hawaiʻi Coastal Geology Group website (Coastal Geology Group, 2008), which I used to navigate to the training sites. After selecting a study area and training sites, I conducted a kayak-based field reconnaissance to inspect the study area for safety and make observations. In the field, I made visual observations of the bottom types represented in my training sites. Back in the computer lab, I used my training sites to represent my bottom type classes and ran the flight lines through the supervised classification program to generate a set of preliminary maps. A second field visit was conducted to refine my training sites and to check the classification results to see if they were accurate. I did this by selecting certain areas within my training area in which I logged down information about the bottom type present in that area. When I returned to the computer lab I compared what I saw in the field with the preliminary classified map. Based on my observations and understanding the spectra of the five bottom types, I chose refined training sites from the image. I then applied these training sites to the images and reran the supervised classification technique.

Supervised Classification of the Simulated 25m Dataset

The first part of this project involved testing out the technique to see if it would produce accurate results, so for the next part I needed to test the technique to see if it could be used on data collected from satellites. Since some global monitoring satellites will be collecting data at coarser resolutions such as 25m, I decided to resize the HICO 1m dataset to 25m. I mosaicked the 1m and 25m image together and selected training sites from the 1m image because the 25m image was extremely small and blurry which made identifying and selecting training sites difficult. After I selected the training sites, I ran the mosaic image through the supervised classification program. I then compared the results of the 1m spatial resolution dataset to the 25m spatial resolution data in order to evaluate the effectiveness of the technique.

Linear Spectral Unmixing of the AVIRIS Dataset

The third step in this project involved using the linear spectral unmixing technique on a 25m spatial resolution dataset. The 25m spatial resolution was acquired from the Airborne Visible/Infrared Imaging Spectrometer (AVIRIS) and covered the Kāneʻohe Bay area. This data was made available to my mentor after a previous graduate student wrote a proposal requesting the data from NASA's Jet Propulsion Laboratory. I ran a remote sensing atmospheric correction program called FLAASH on these datasets. I then conducted a field reconnaissance of Kāneʻohe Bay in order to collect bottom type spectra with a towed ocean spectrometer system (Provided by the Center for Microbial Oceanography: Research and Education, C-MORE). The ocean spectrometer recorded bottom type spectra, GPS location, temperature, ocean depth, and captured photos. Kahoaliʻi Keahi, a C-MORE Scholar working on developing the spectrometer system, my mentors, and I towed the ocean spectrometer with a kayak over areas that were rich in coral, algae, and sand in order to make sure I collected the desired bottom type spectra. The spectra collected from the ocean spectrometer were used to build my spectral library which then was used for the linear spectral unmixing technique. I also generated a spectral library from training sites on my AVIRIS 25m image to compare the effectiveness of the two spectral libraries. The training sites represented each of my five bottom type classes. The last step involved applying both spectral libraries to the image and running the linear spectral unmixing program.

RESULTS

I ran the 1m HICO dataset through the supervised classification technique after the second field visit and generated a final map (Figure 4). The final map shows a distribution of my five bottom types, coral, algae, sand, water at 1m – 2m depth, and water at 3m depth or greater. Coral is located along the fringe of the coast line in the bay, while algae and sand are both located within the fringe. The water bottom types are specifically located where they are supposed to be. The only down side I found was that there were some misclassifications and overestimating of bottom types. There were areas in the field that were algae but in the classified map were coral and there were areas in the field that were both coral and algae but in the map were coral. I feel that the misclassifications were caused by not selecting training sites that were representative of these spectra. In the case of a mixed pixel, the program will overestimate or underestimate a bottom type because the program will assign a single bottom type class to an area made up of a fraction of that class along with one or more other components. I created a validation chart which consisted of twenty validation pixels, located within all three flight lines,

which are presented in Table 1. Thirteen out of the twenty validation pixels were classified accurately, three were overestimated, and four were misclassified. These results indicate that the methods for generating the training sites need to be close to perfect when using this technique.

Validation Pixel	Supervised Classification	Field Work Observations	Validation
1	Coral	Algae	Misclassification
2	Coral	Algae	Misclassification
3	Algae	Algae	Accurate
4	Sand	Sand	Accurate
5	Coral	Coral	Accurate
6	Sand	Sand and Algae	Overestimating Sand
7	Coral	Coral	Accurate
8	Coral	Coral	Accurate
9	Algae	Algae	Accurate
10	Algae	Algae	Accurate
11	Sand	Sand and Algae	Overestimating Sand
12	Coral	Algae	Misclassification
13	Sand	Sand and Algae	Overestimating Sand
14	Coral	Coral	Accurate
15	Coral	Coral	Accurate
16	Algae	Algae	Accurate
17	Coral	Algae	Misclassification
18	Sand	Sand	Accurate
19	Sand	Sand	Accurate
20	Algae	Algae	Accurate

Table 1: Validation chart for the 1m supervised classification map.

The results from the 25m dataset contained more misclassifications then the 1m dataset. The final map shows my five bottom types classified (Figure 4), but because of the coarser resolution the percentage of coral in the image dropped compared to the 1m image. I expected these results because the coral in my study area were no more than 3m in width and the image covered 25m of ground area, so the coral may have gotten mixed in with other larger bottom types such as the algae, sand, or water at 1m – 2m depth. These results further proved that the supervised classification technique would not accurately classify the coral reefs.

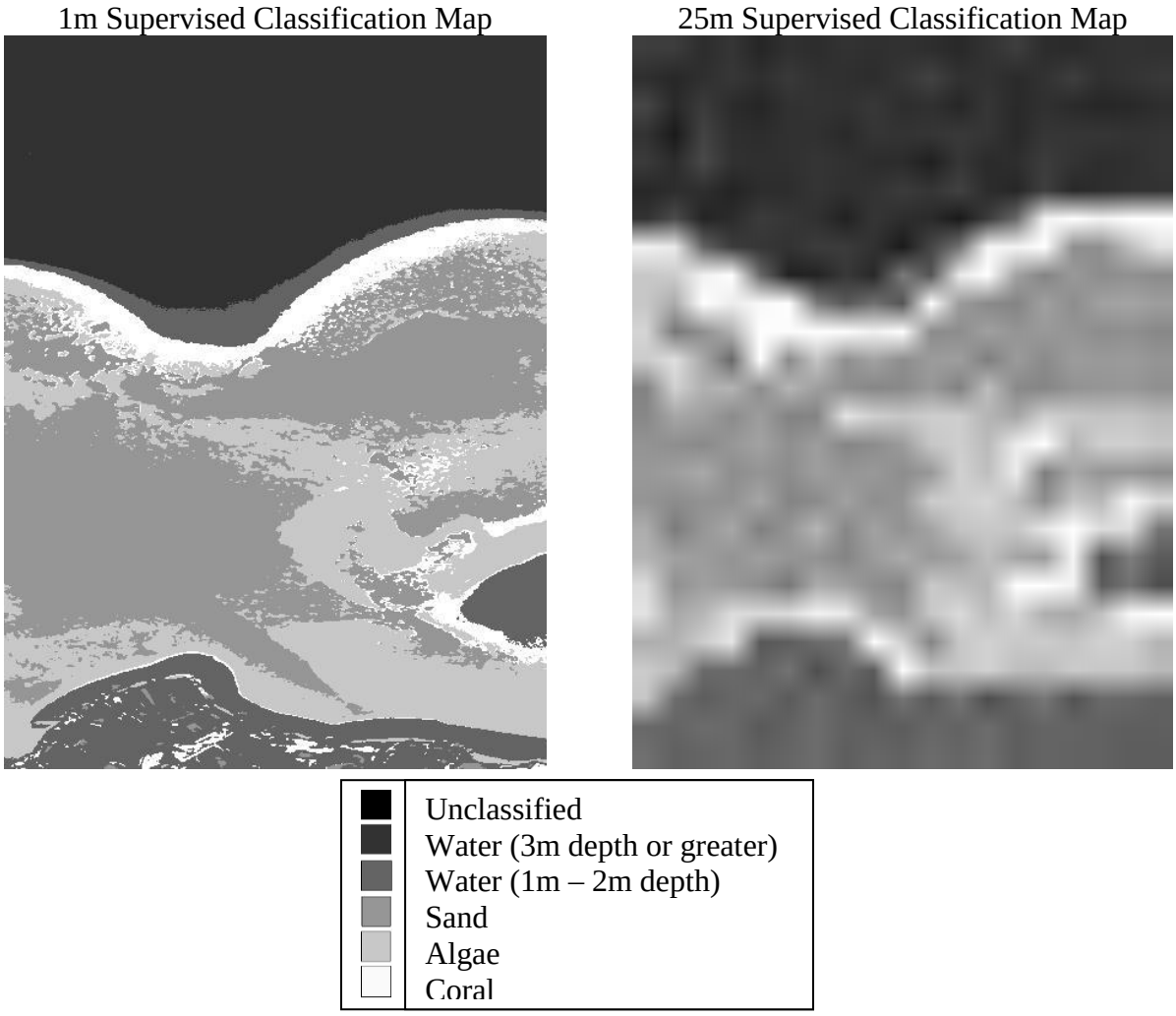

Figure 4: These two maps are the final supervised classification maps from the 1m and 25m HICO dataset. The 1m map shows the bottom types clearly. The 25m was resized because it was extremely small and hard to recognize any of the bottom types. The color key on the bottom shows the different classes I used.

I used the linear spectral unmixing technique to produce an abundance map for each bottom type class present in my spectral library. I had two sets of results by running the unmixing using two separate spectral libraries, one came from the ocean spectrometer and the other came from training sites I selected from the image. The results from the unmixing using the ocean spectrometer spectral library's results were not reasonable. The ocean spectrometer is still being experimented with and needs further testing to establish the correct calibration method. There are also problems regarding the lighting conditions while collecting spectra within the spectrometer which need to be addressed before these data can be used for building a useful spectral library. So I decided to select pixels from the AVIRIS image which I felt were representative of pure bottom types, which are pixels fully made up of a single bottom type. I used the spectra from these pixels to build the image based spectral library.

The abundance maps that I generated from the training sites on the 25m AVIRIS spectral library showed more promising results (Figure 5). The coral abundance map shows that there are low values, 0 to 20 percent, of coral along the fringe reef near the coast. There were also some small areas that showed a large percent of coral but those areas are most likely inaccurate because the fringe reef only covers a small percentage of the pixel. This problem could be the result of not selecting a pure coral pixel, but one which possibly contained a significant portion of algae, when I selected my training sites.

25m Linear Spectral Unmixing Coral Map

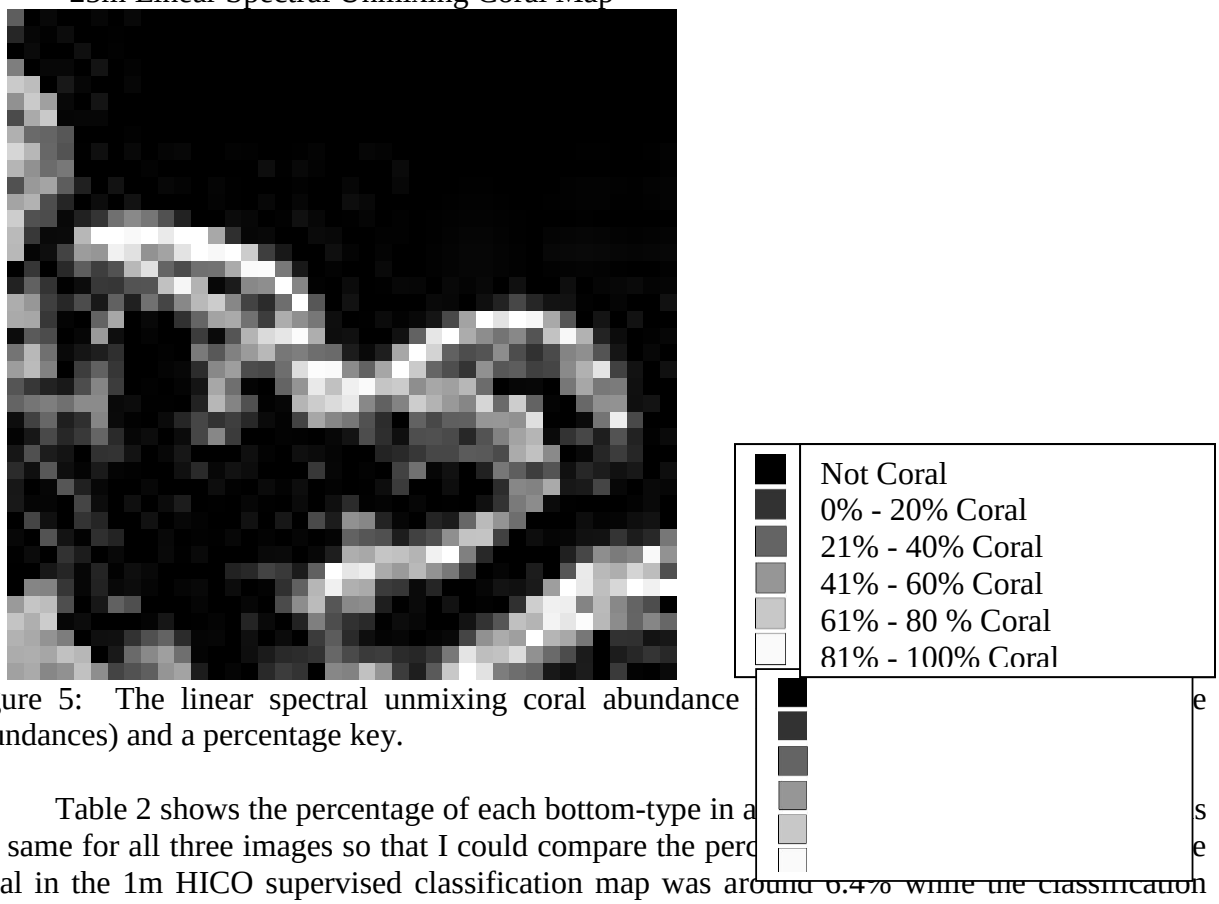

Figure 5: The linear spectral unmixing coral abundance e abundances) and a percentage key.

Table 2 shows the percentage of each bottom-type in a s the same for all three images so that I could compare the perc e coral in the 1m HICO supervised classification map was around 6.4% while the classification map from the resized 25m HICO data showed a decrease to 4.3%. This was caused by the averaging in the resizing process which resulted in more mixed pixels and a lower percentage of coral in the image. It should also be recognized that the classification even at the 1m scale can over or underestimate the area of a single class because it will assign a mixed pixel a single bottom type.

The AVIRIS 25m map was processed through the linear spectral unmixing program. The map has 12.5% of coral in the image almost twice as much as the HICO 1m map. This is possibly due to the coral pixel chosen for the spectral library not being a pure pixel but instead a mixed pixel. This is highly likely considering the distribution of the coral within the reef. It is interesting to note that the coral and algae for all three methods sum to about the same percentage, about 26.5 percent.

	HICO 1m (%)	HICO 25m (%)	AVIRIS 25m (%) Training Sites Spectral Library
Coral	6.4	4.3	12.5
Algae	20.9	22.0	16.2
Sand	31.8	32.6	24.5
Water (1m – 2m depth)	9.7	6.5	33.2
Water (3m depth or greater)	31.2	34.5	13. 7

Table 2: Table of bottom type percentage. The AVIRIS 25m map which was processed through the linear spectral unmixing program showed a high value of coral compared to the HICO 1m and 25m supervised classification maps.

CONCLUSION

The supervised classification technique was an effective tool at classifying pixels that were pure bottom types. However, mixed pixels which contained more than one bottom type proved to be problematic. In these cases, the program tended to overestimate, underestimate or misclassify the mixed pixel. This was a problem in both the 1m and 25m HICO datasets, but particularly in the latter, coarser resolution dataset. Since global monitoring satellites generally acquire data at best 25m spatial resolution, the supervised classification technique as implemented here would not be a wise program to use. Further study could address the use of mixed pixel classes to minimize this effect.

The linear spectral unmixing program appears better suited to mixed pixels because it gives percentage abundances of each bottom type in a pixel, rather than simply classifying the entire pixel as one bottom type. The process is highly sensitive to the quality of the spectral library used as input to the unmixing process. This was highlighted by our difficulty using the ocean spectrometer system to generate a spectral library and using a possibly mixed pixel for our coral end-member in the image based spectral library. Before the linear unmixing technique could be used in a monitoring system, a suitable library needs to be built and validated. The ocean spectrometer is possibly an effective tool for collecting bottom type spectra although questions about calibration and lighting effects remain to be solved.

ACKNOWLEDGEMENTS

I would first like to thank my mentors Harold Garbeil and Dr. Barbara Bruno for all of their knowledge and guidance. You both have taught me so much. Thank you to the Hawaii Space Grant Consortium for giving me the opportunity to complete this project. I like to also recognize Kahoali‘i Keahi (C-MORE Scholar) and C-MORE for providing me with the ocean spectrometer. I would also like to thank Jeff Gillis-Davis for providing me with the HICO flight lines I used for this project.

REFERENCES

Coastal Geology Group. (2008). Imagery currently available for Oahu. (http://www.soest.hawaii.edu/coasts/data/oahu/index.html). (May 10, 2008).

Goodman, J. & Ustin, S. (2001). Hyperspectral Image Analysis of Coral Reefs in the Hawaiian Islands. (2007, Nov. 21).

Hochberg, E. & Atkinson, M. (2000). Spectral Discrimination of Coral Reef Benthic Communities. (http://www.springerlink.com/content/evecep46unmuc1a1/). (2007, Nov. 21).

Hochberg, E. & Atkinson, M. (2003). Capabilities of Remote Sensors to Classify Coral, Algae, and Sand as Pure and Mixed Spectra. (http://cat.inist.fr/?aModele=afficheN&cpsidt=14733438). (2007, Nov.21).

International Year of the Reef. (2007). Benefits of Coral Reefs. (http://www.iyor.org/reefs/benefits.asp). (May 10, 2008)

BIOLOGICAL TREATMENT AND REUSE OF HUMAN SPACE EXPLORATION WASTEWATER

Joshua Lelemia Irvine and P.Y. Yang
Department of Molecular Biosciences and Bioengineering
University of Hawai‘i at Mānoa
Honolulu, HI 96822

ABSTRACT

Extending a human presence in the solar system requires in-situ resource recycling. Entrapped Mixed Microbial Cell (EMMC) process may be considered an alternative to achieving this aim. The intent of this investigation is to develop an operational criteria, process performance and economic evaluation to meet NASA needs. A double-layer EMMC configuration bioreactor of 7L at a packing ratio of 17.1% operated at an HRT of 6 hours, continuous aeration (1-1.2L/L/day), temperature of 25^{o}C ±2 was tested. The organic loading rate fluctuated 1.0-4.5 mg/L/day. The EMMC process performance reached a steady state ~20 days. It demonstrated discharge efficacy of TCOD >94%, SCOD >97% removal, no solids generated, and an average nitrogen removal of 35. 9%. Simultaneous removal organics and nitrogen may be attributed to the long sludge retention times that EMMC achieves because it allows for slow growing bacteria such as nitrifiers to thrive. It would cost $0.08 to treat 10 gallons of wastewater a day (twice as much as water needed to treat). The EMMC reactor design depending on the design can treat 60% to 100% of daily wastewater within one day. It also requires considerably less space compared to physiochemical treatment processes and if integrated with other systems may be capable to renovate water to levels permissible for human consumption.

INTRODUCTION

In situ resource reutilization is necessary for long-term manned mission to be possible. Current physiochemical treatment processes (PTP) of space wastewater rely upon a combination of physical and chemical methods to treat wastewater (Curie and Morcone, 2008). However, disadvantages of incorporating PTPs include large unit-space requirements, significant energy usage, complex operation/maintenance, and the use of chemicals and machinery to achieve treatment/renovation objectives. Biological treatment processes, on the other hand, use microorganisms to metabolize, treat, and even renovate the wastewater to a reusable form.

Entrapped mixed microbial cell (EMMC) may be considered an alternative biological treatment method for in-situ resource reutilization of space wastewater. Extensive research on EMMC in treating domestic and agriculture wastewater have been realized as well as using the system to possibly treat wastewater streams for potable drinking water applications while requiring small spatial area. Consequently, EMMC seems to be a feasible candidate for resource recovery and reutilization for the human space exploration needs (Yang et al., 1988; Yang et al., 1994; Yang et al., 1997; Yang et al., 2002; Yang et al., 2003; Yang et al., 2005; Yang, 2007). The purpose of this investigation is to develop operational conditions and design criteria of the EMMC process to treat the human space exploration wastewater.

METHODS

EMMC Preparation

The EMMC carriers were prepared by modifying the carrier using a plastic bio-barrel as the "frame" (Yang & See, 1991). The carriers house the microorganism which metabolizes the pollutants. The mixed microbial cells used in this study were obtained from dewatered sludge in East Honolulu Wastewater Treatment Plant (EHWTP), Honolulu, Hawai'i.

A mixture of 100 ml of 10% (w/v) cellulose triacetate using methane chloride as a solvent was mixed with dewatered sludge containing about 90% water. After mixing uniformly, the Biobarrel rings were added to be coated with the mixture of gel and microbial cells for carrier shaping. The well-coated bio-carriers were firmed in 100% toluene solution. The hardened carriers were washed with tap-water and then packed in the reactor for further experiments. The organic solvents (methane chloride and toluene) can be recovered by a combination of freezing and distillation methods (Zhang, 1995). Figure 1depicts prepared EMMC carriers.

Design Criteria

The design must be appropriate in size that could be installed into the spacecraft based upon a crew exploration vehicle (CEV) occupying three to six persons within a very confined area. It has been estimated that during long-term human space mission an overall 12.680L of wastewater (hygienic + urine) would need to be treated daily. (Horneck et al, 2003; M. Czuppalla et al, 2004).

System Design and operation

A laboratory scale system of a double-layer configuration was setup as shown in Figure 2. The influent domestic wastewater is pumped from a tank by a peristaltic pump. The influent water pumped is synthetic wastewater (table 1). The water chemical composition mirrors Human Space exploration wastewater which is similar to domestic wastewater of weak strength (table 2). The flow is controlled by digital liquid flow meter. The wastewater enters the bioreactor containing two layers of EMMC—figure 1. Each layer is packed with carriers that have mixtures of activated microorganisms attached to it. A 17.1% carrier packing ratio fills the bioreactor. These microorganisms together degrade the constituents operating under steady-state conditions at a temperature of 25 ± 2°C, and a continuous air flow rate of 1~1.2 L/L void volume/min. The water remains in the bioreactor for a hydraulic retention time (HRT) of 6 hours. After that period of time, the degraded water flows out into the effluent tank. The current design size can meet 60% to 100% of the crew wastewater treatment needs depending on operation.

Feed characteristics

Synthetic wastewater was prepared in stock solution using sucrose as a carbon source. The SCOD and NH_4^+-N concentrations of the synthetic feed incorporated in this study ranged from 100-1,100 mg/L and ##-## mg/L, respectively. The synthetic wastewater composition mirrors domestic wastewater characteristics; table 1 presents the synthetic wastewater composition.

Analytical methods

Influent and effluent samples were collected every 48 hours. The samples were analyzed for total chemical oxygen demand (TCOD), soluble chemical oxygen demand (SCOD), ammonia nitrogen (NH_3-N), nitrite nitrogen (NO_2^--N), nitrate nitrogen (NO_3^-N), total suspended solids (TSS), and pH. All the results present the mean of at least 7 experiment data collected under steady state conditions.

RESULTS

Operation criteria

The process performance of the system was assessed by the hydraulic retention time (HRT) which refers to the amount of time the liquid flows through the bioreactor. Previous studies determined that the optimal HRT to operate the double layer system is at 6 hours. The double-layer design was selected also to be the optimal configuration to yield high carbon and nitrogen removal. The system was operated at an HRT 6 hours under continuous aeration supply at 1-1.2 L/L/day.

Process performance

Nutrients of major concern in wastewater are carbon and nitrogen. Excess levels in waters can lead to environmental hypoxia, odor problems, septic conditions, and if consumed causes poisoning, illness or severe cases, even death (WHO, 2009). pH, Total chemical oxygen demand (TCOD) and soluble chemical oxygen demand (SCOD), ammonia-nitrogen, and Total Suspended Solids (TSS) were monitored; figures 3, 4, 5, and table 2, respectively. The process performance was also evaluated on COD removal efficiency as shown in figure 6.

DISCUSSION

Operation criteria and process performance

Previous studies determined that increased mass transfer efficiencies could be realized utilizing a double-layer EMMC configuration rather than a single-layer. This could be a result of reactors in series contained. A double-layer configuration operating at an HRT of 6 hours and continuous aeration schedule performance was determined as shown in Figures 3, 4, 5, and 6. The system reached a steady state in about twenty days. The total chemical oxygen demand, soluble chemical oxygen demand and ammonia nitrogen removal efficiencies were 94.5%, 97.6%, and 35.9%, respectively, at steady state. A major setback encountered during the study was controlling the influent concentration. The organic loading rate ranged from 1.0-4.5 mg/L/day. Despite the variable organic loading rate, the effluent TCOD and SCOD concentrations were shown to be consistently low.

The EMMC process is capable of effective simultaneous removal of carbon and nitrogen because it is capable of achieving high SRT (Solid Retention Time). This ensures a high biomass concentration is entrapped in the system which allows for slow growing bacteria such as nitrifiers. The systems low nitrogen removal could be attributed that the nitrifiers are still growing, as exhibited in the increased ammonia nitrogen removal over time (Figure 6). It is recommended that more time is required to further evaluate the SRT effects in contributing to effective simultaneous removal of carbon and nitrogen.

Design/Operation criteria and economic evaluation

Based upon the above experimental results, design/operation criteria were developed and are presented in table 4. An economic analysis was calculated from these criteria for the operation of 10 gallons/day. The capital cost was estimated to be $4,046.25 which includes the cost of: EMMC carriers, the bioreactor, air supply and feeding pipes. The annual operation/maintenance cost ($14.60) is principally includes electricity. A useful life of 15 years was assumed (Yang et al, 1997). The Net Present Worth was assessed at $4,171.59. Consequently to treat 10 gallons of 6 man crew exploration per day is $0.08. The above cost analysis is an estimation based for operating the system on earth. The analysis would need to be further revised to include the special space cost considerations neglected in the calculations.

Potential application for long-term manned galactic missions

Short-duration manned or low Earth orbit missions depend on re-supply techniques of water and do not treat any generated wastewater; however, to extend a human presence it is imperative to develop technologies capable of treating and recycling wastewater streams efficiently and quickly. This inquiry is relevant to NASA objectives to identify and test life support systems by 2010 (NASA, pp. 14, 2006, Sub-goal 3.F.2).

Other treatment systems have been considered for this specific application such as wetlands, however, the large space required and complex operation/maintenance required may be infeasible for long-term space applications (Nelson et al, 2001; Nelson et al, 2003). Recently, the agency tested a wastewater recovery using PTP technologies in space. To recover drinkable water, two processes were used to treat (1) urine water and (2) other wastewater streams. The urine water was treated by distillation and the other wastewater streams used a series of chemical treatment and filter processes to produce drinkable water for human consumption (Curie and Morcone, 2008). The concept was successfully tested once after five days of attempt (Schneider, 2008).

EMMC has been demonstrated to remove organics and inorganics under land-limited conditions. It would be best to integrate the EMMC process with other processes, in particular membrane bioreactor (MBR as shown in Figure 8) in order to produce drinkable water for human consumption. The integration of the compact sized MBR proves advantageous because it yields low sludge production, good solid/liquid separation, and eliminates pathogens; though membrane fouling is one area of concern (Nueugjamnong, 2004). Further inquiry on coupling EMMC and MBR is needed to evaluate process performance and operational conditions. This could be explored when I enter at the Biological Engineering graduate degree program at the University of Hawai‘i at Mānoa in the Fall 2009.

CONCLUSION

Entrapped Mixed Microbial Cell (EMMC) was investigated to determine the utility of the biological treatment process to meet the needs of NASA to treat and reuse human space exploration wastewater streams. Currently, NASA depends upon re-supply to replenish water resources on the low Earth orbit and short-term manned missions. A process performance was evaluated for a double-layer EMMC configuration at an HRT of 6 hours, continuous aeration (1-

1.2L/L/day), temperature of 25^{o}C ±2, 17.1 % packing ratio. Efficacies of TCOD >94%, SCOD> 97% removal and no solid discharge of effluent wastewaters were achieved. An economic analysis based on applications on earth determined that it would cost approximately $2.30 USD per month to treat 30 gallons of water. EMMC compared to other biological treatment processes (i.e. activated sludge process etc.) is capable of much longer sludge retention times (SRT) of >100days, useful life of >10years, and suffices land limited conditions. The operation and maintenance of the system is much simpler in contrast to complex physiochemical treatment process. The proposed system design could be integrated with other compact unit processes to provide in-situ water resource reutilization thereby satiating NASA's thirst to achieve their ultimate quest to expand a human presence to the moon, the red planet, and beyond.

ACKNOWLEDGEMENTS

Funding for this research was provided by the Space Grant Hawaii Consortium. The author would like to express gratitude to Dr. P.Y. Yang and members of his lab for their wisdom, advice, and encouragement.

REFERENCES

Curie, Michael and Morcone, Jennifer. "New Water Reclamation System Headed for Duty on Space Station". (2008) NASA press release: 08-199. < http://www.nasa.gov/home/hqnews/2008/may/HQ_08119_ISS_Water_System.html>

M. Czupalla, V. Aponte, S. Chappell, D. Klaus (2004). Analysis of a spacecraft life support system for a Mars Mission. Acta Astronautica 55, 537-547.

G. Horneck, R. Facius, M. Reichert, P. Rettberg, W. Seboldt, D. Manzey, B. Comet, A. Maillet, H. Preiss, L. Schauer, C.G. Dussap, L. Pughon, A. Belyavin, G. Reitz, C. Baumstark-Khan, and R. Gerzer (2003). HUMEX, A Study on the Survivability and Adaptation of Humans to Long-Duration Exploratory Missions, Part 1: Lunar Missions. *Adv. Space Res.* Vol 31, No. 11, pp. 2389-2401.

National Aeronautics and Space Administration (2006). Strategic Plan.<www.**nasa**.gov/pdf/142302main_**2006_NASA_Strategic_Plan**.pdf>

M. Nelson, H.T. Odum, M.T. Borwn, and A. Alling (2001). 'Living off the land': Resource efficiency of Wetland Wastewater Treatment. *Adv. Space Res* Vol. 27, No. 9, 1547-1556, 2001.

M. Nelson, A. Alling, W.F. Dempster, M. van Thillo, and John Allen (2003). Advantages of using subsurface flow constructed wetlands for wastewater treatment in space applications: Ground-Based Mars Base Prototype. *Adv. Space Res.* Vol 31, No. 7, pp. 1799-1804.

Nueugjamong Chackrit (2004). Membrane fouling caused by extracellular polymeric substance during microfilitration process, PhD, Thesis, Asian Institute of Technology, Bangkok, Thailand, 130pp.

Schneider, Mike. "Space Station's Urine Recycling Unit Passes Test" (2008). Associated Press, Discovery News. < http://dsc.discovery.com/news/2008/11/25/astronauts-space-station-02.html>

World Health Organization. "Enfermedades relaccionadas con el agua". (2009). < http://www.who.int/water_sanitation_health/diseases/es/index.html>

Yang, P.Y., Cai, T.D., and Wang, M.L. (1988). Immobilized mixed microbial cells for wastewater treatment. *Biological Wastes. 13,295-312.*

Yang, P.Y., Ma, T., See, T.S. and Nitisoravut, N. (1994). Applying entrapped mixed microbial cell techniques for biological wastewater treatment. *Wat. Sci. Tech., 29, No. 10-11, 487-495.*

Yang, P. Y., Zhang, Z. Q. and Jeong, B.G. (1997). Simultaneous removal of carbon and nitrogen using an entrapped-mixed-microbial-cell process. *Wat. Res., 31:2617-2625*

Yang, P. Y., Shimabukuro, M. and Kimy S. J. (2002). A pilot scale bioreactor using EMMC for carbon and nitrogen removal. Clean Techn Environ Policy, 3, 407-412.

Yang, P.Y., Cao, K. and Kim, S.J. (2002). Entrapped-mixed microbial cell process for combined secondary and tertiary wastewater treatment. *Wat. Envir. Res. 74, 226-234*

Yang, P.Y., Su, R., and Kim, S.J. (2003). EMMC process for combined removal of organics, nitrogen and an odor producing substance. *Journal of Environmental Management 69 (2003) 381-389*

Yang,W. Cicek, N. and Ilg, J. (2005). State-of–the-art of membrane bioreactors: Worldwide research and commercial

APPENDIX

Figure 1. Prepared EMMC carrier

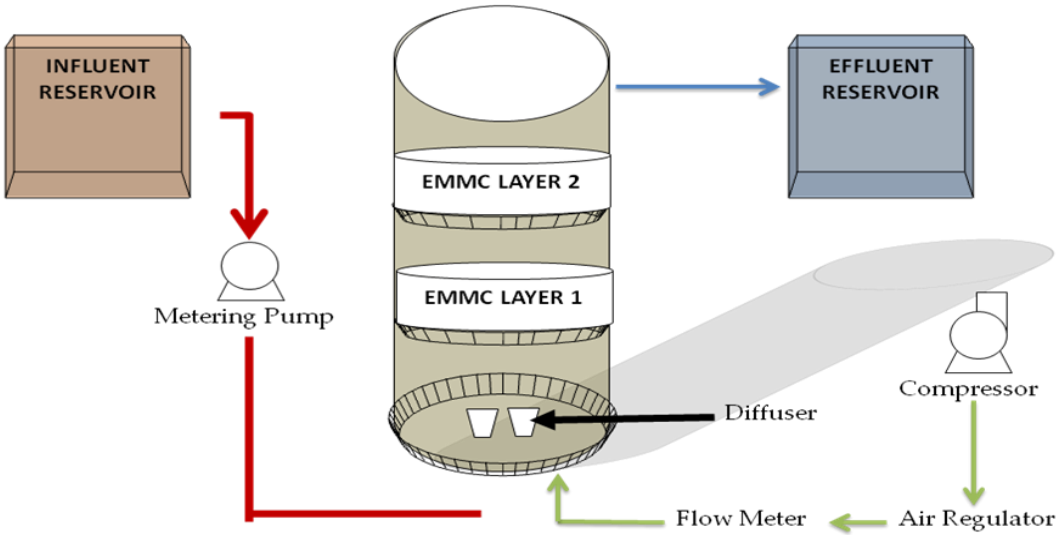

Figure 2. Design 1: Double layer EMMC (reactor volume 7 L, 17.1% packing ratio, HRT 6 hrs)

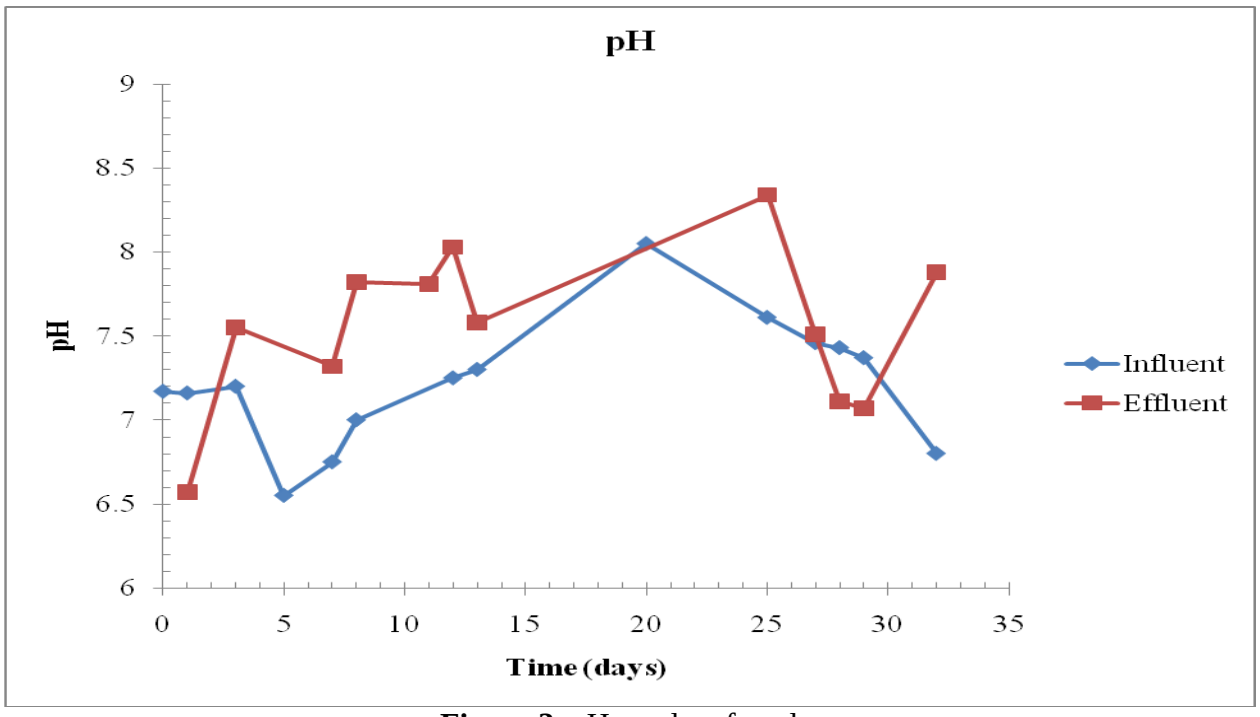

Figure 3. pH results of study

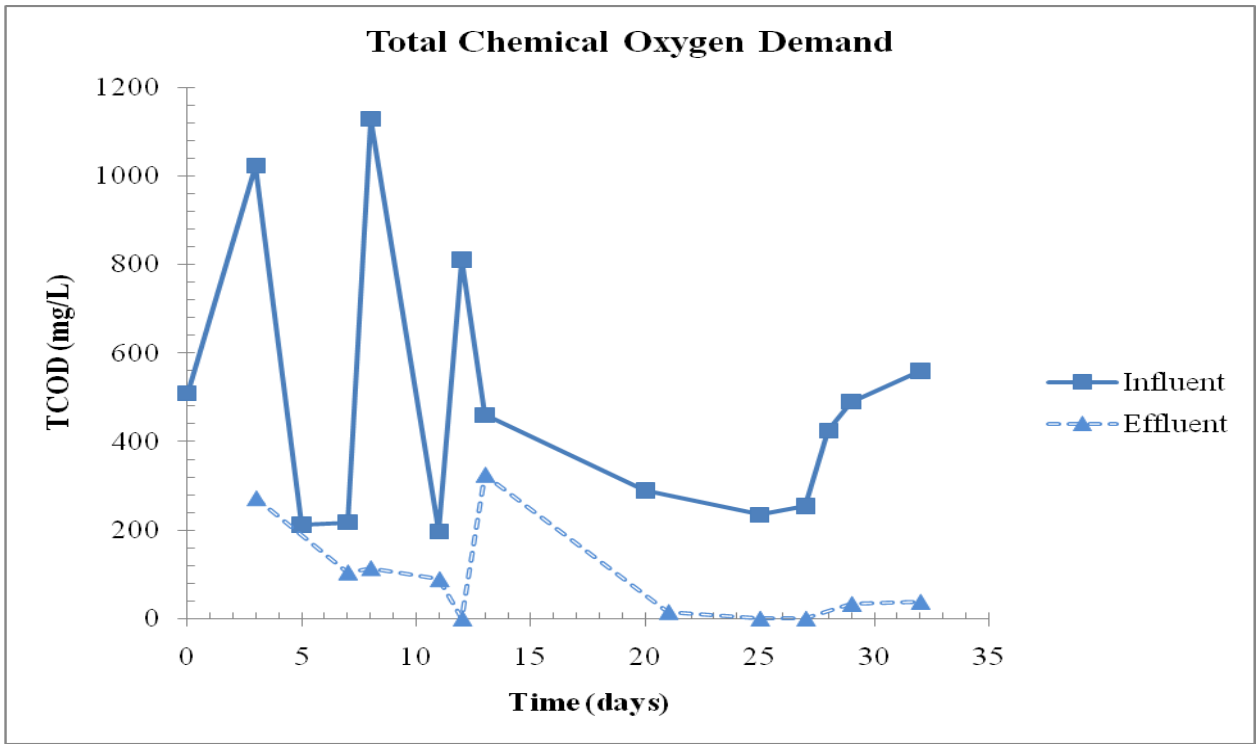

Figure 4. Total Chemical Oxygen Demand

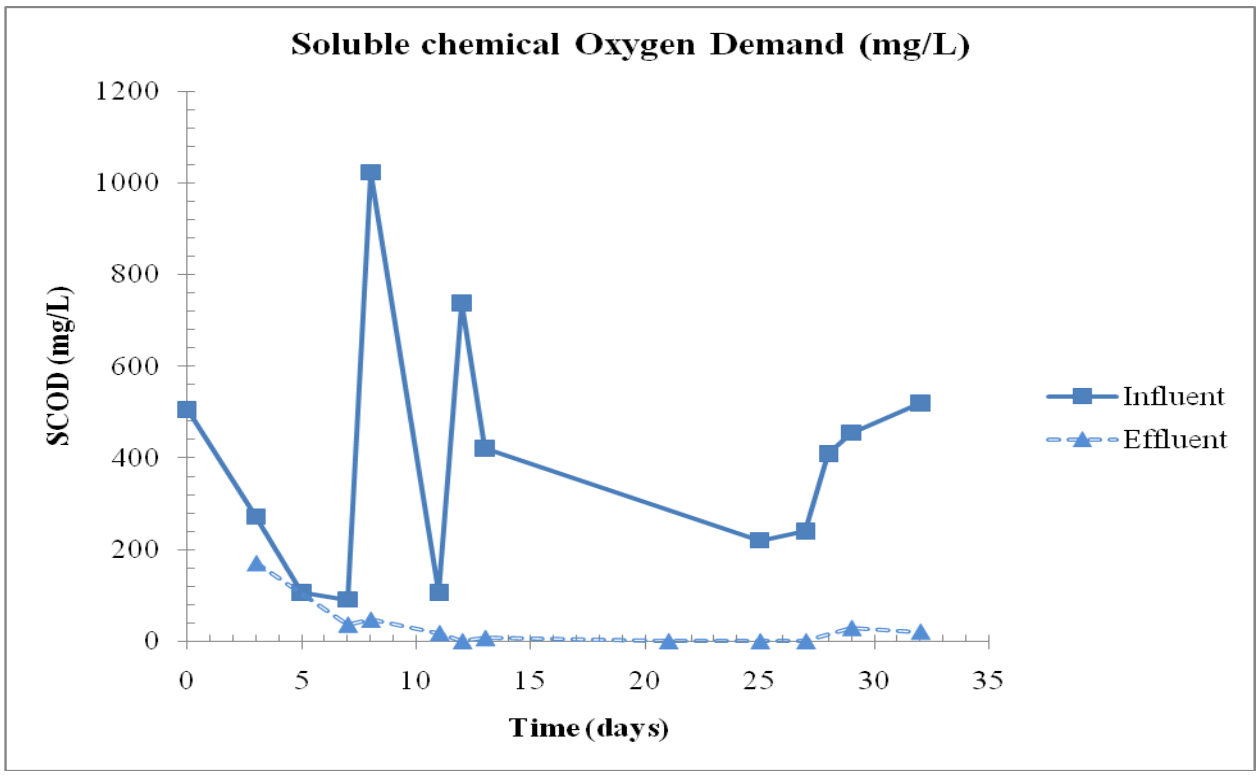

Figure 5. Soluble Chemical Oxygen Demand

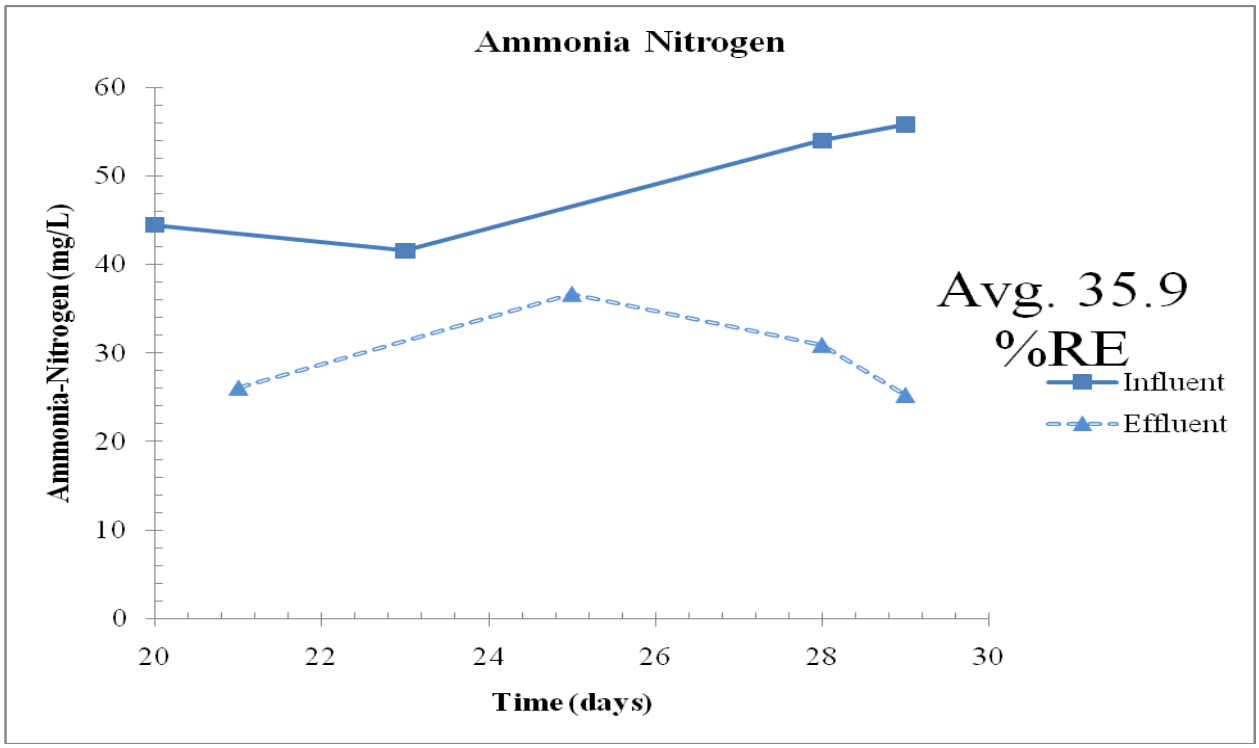

Figure 6. Ammonia Nitrogen, 35.9% average removal efficiency

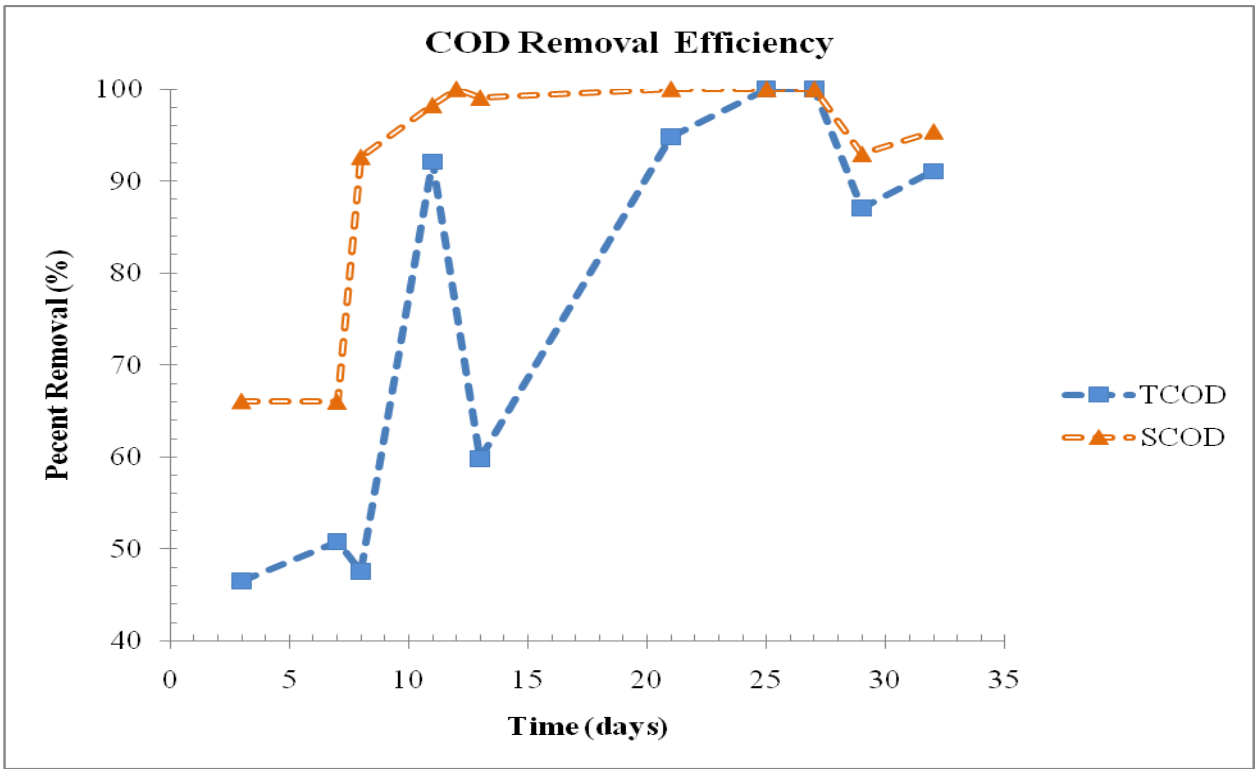

Figure 7. COD removal efficiency

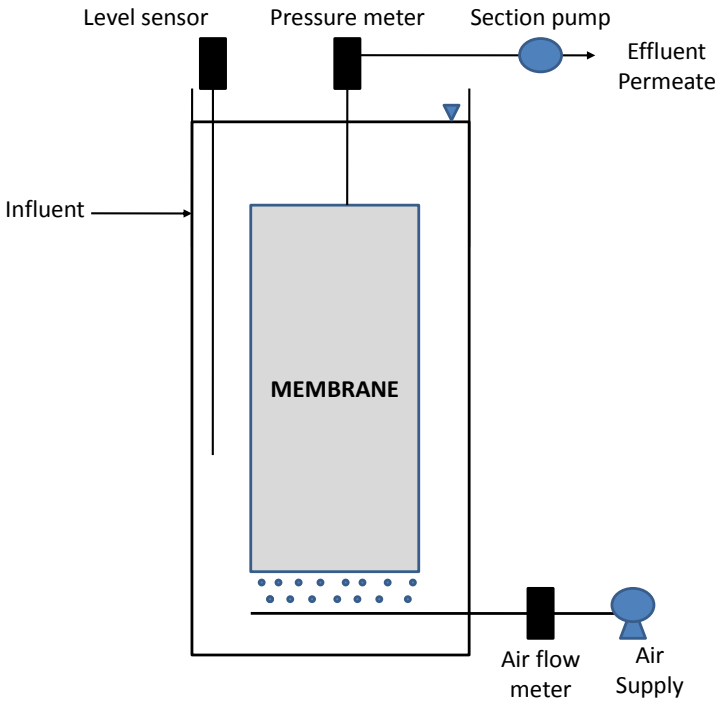

Figure 8. Membrane Bioreactor Configuration (Nuengjamneng, 2004)

Constituent	Concentration (mg/L)
Sucrose, $C_{12}H_{22}O_{11}$	400
Ammonium sulfate, $(NH_4)_2SO_4$	200
Monobasic potassium phosphate, $KH_2PO_4KH_2$	260
Dibasic potassium phosphate, KH_2PO_4	520
Sodium Carbonate,Na_2CO_3	400
Magnesium sulfate, $MgSO_4 \cdot 7H_2O$	100
Manganese sulfate, $MnSO_4 \cdot H_2O$	20
Calcium chloride, $CaCl_2$	20
Ferric chloride, $FeCl_3 \cdot 6H_2O$	20

Table 1. Synthetic wastewater composition.

	Influent	Effluent
SS (µg/L)	66.9± 45	32.7 ± 29
pH	7.22 ± 0.37	7.54 ± 0.53

Table 2. Suspended solids and pH influent and effluent quality

EFFECTS AND APPLICATIONS OF MULTIPLE INTERROGATORS ON RETRODIRECTIVE ARRAYS

Reece T. Iwami
Department of Electrical Engineering
University of Hawai‘i at Mānoa
Honolulu, HI 96822

ABSTRACT

A space-based application utilizing retrodirective array (RDA) technology is presented. The RDA application fulfills several NASA strategic goals regarding space exploration. An overview of aperture antennas and phased arrays is provided as an introduction to RDAs. Two RDA architectures are outlined with emphasis on their methods of achieving retrodirectivity and their behavior in the presence of multiple interrogators. The system design is presented along with an analysis of the proposed space application performance.

INTRODUCTION

In July 2009, the United States celebrated the 40th anniversary of the first lunar landing [1]. In those intervening 40 years, a few nations have sent various missions to Earth's orbit, the moon, and to Mars. Extending human exploration beyond the moon has been somewhat limited due to uncertainties with extraterrestrial environments, the astronomical costs and resources needed for manned missions, and the overall safety of the astronauts. Addressing at least one of these barriers could provide enough incentive for NASA to pursue human space exploration as vigorously as it did 40 years ago.

A space-based application involving a search-and-rescue mission has been envisioned using retrodirective antenna (RDA) technologies developed at the University of Hawaii at Manoa. A search-and-rescue rover equipped with an RDA system would aid in locating and communicating with a lost explorer. Using the unique ability of an RDA to autonomously respond in the direction of an interrogating signal, a rover could pinpoint the location of an emergency beacon transmitted by a stranded explorer.

The operational flow begins with a stranded explorer and a patrolling rover equipped with an RDA but with no knowledge of the missing explorer. The stranded explorer activates an omnidirectional distress beacon that serves as an interrogator to the array. When the RDA receives the beacon, the array retrodirects a highly directive beam in the direction of the explorer. The directive beam focuses most of the RF power towards the interrogator, better utilizing the limited power resources on the rover. Using Direction of Arrival (DoA) information derived by the RDA, the rover will know in what direction to travel to locate the explorer. Communication with the explorer can also be established with the RDA, allowing rescue personnel to reassure the explorer that help is on the way. Fig. 1 illustrates the process flow.

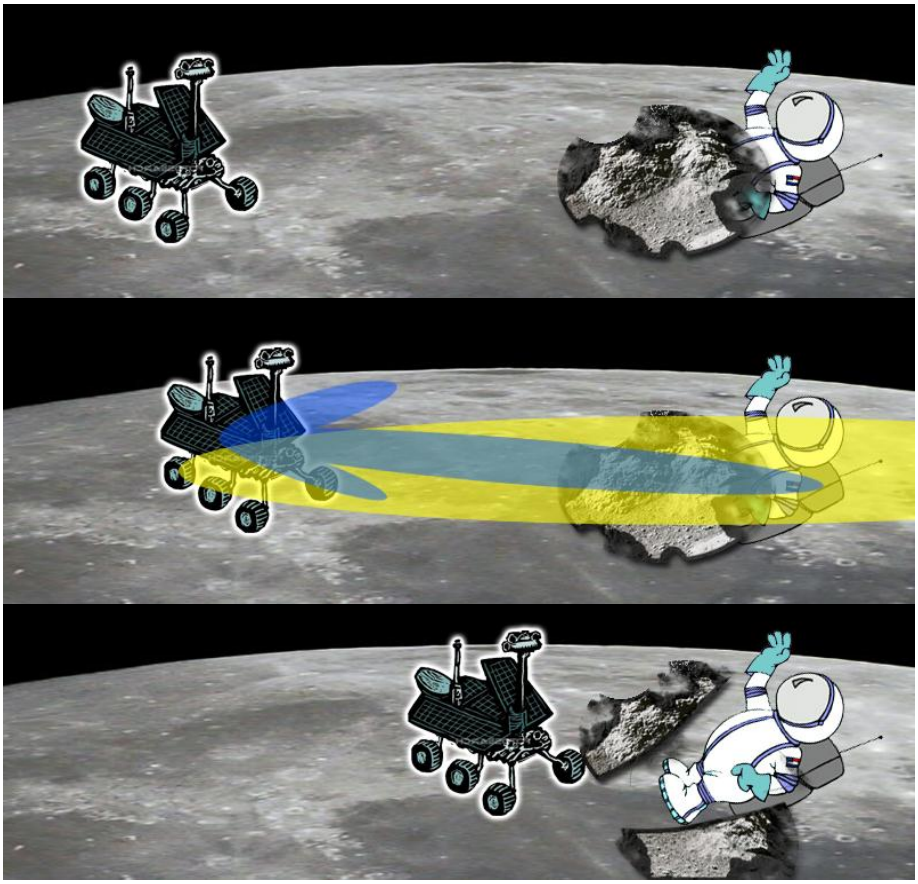

Fig. 1: Process flow of the search-and-rescue application.

This application will serve to fulfill and extend two of NASA's strategic goals regarding a return to human space exploration. By reducing risks involved with space exploration, funding billion-dollar missions become feasible and realistic. Two RDA architectures that meet the design specifications of the application have been researched and outlined in this report. Equipment specifications of the most recent Mars Exploration Rovers are outlined to create a platform for the proposed RDA solution. Finally the design of the application is presented along with a system performance analysis.

RDA BACKGROUND

When illuminated by an interrogator signal, an RDA has the ability to transmit a signal directly back to the source of the initial transmission, without prior knowledge of its location [2]. In contrast to conventional phased-array antennas, RDAs are self-phasing and therefore self-steering, and can be achieved completely autonomously without user control. The additional gain achieved by the RDA can be leveraged to further optimize the communication link based on power, reliability, and data-rate requirements. The higher antenna gain makes more efficient use of limited DC power resources compared to an omnidirectional antenna because radiated power is directed toward the desired target instead of in all directions.

An RDA is a form of aperture antenna. Aperture antennas are a class of antennas known for their high directivity and associated narrow beamwidth. When compared to an isotropic

antenna which radiates in all directions equally, an aperture antenna has much higher directivity, on the order of 10-30 dB depending on the size of the aperture. The increased directivity focuses more signal power in a certain direction, while the narrow beamwidth requires a mechanism for pointing the main beam in the desired direction.

The most common type of aperture antenna is the continuous aperture, usually realized with a parabolic or dish antenna. This type of antenna uses the physical geometry of the reflector to focus the highly directive beam, similar to how a telescope uses a mirror to collect light. Fig. 2 shows the focusing nature of a parabolic reflector antenna. A drawback of the continuous aperture antenna is that it requires mechanical steering to point the antenna's main beam. In high-speed tracking situations, this constraint requires prior knowledge of the location of the target and complex processing to maintain the tracking lock.

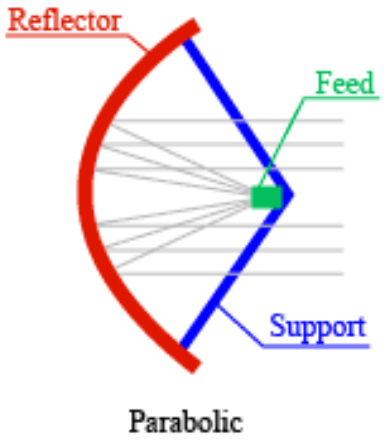

Fig. 2: A parabolic reflector is a type of continuous aperture antenna.

An RDA remedies this problem by utilizing a discrete aperture, otherwise known as a phased array. A phased array is comprised of multiple antenna elements that function together to create an effective aperture. The advantage is that the beam can be electronically steered by varying the phase difference between each element in the array.

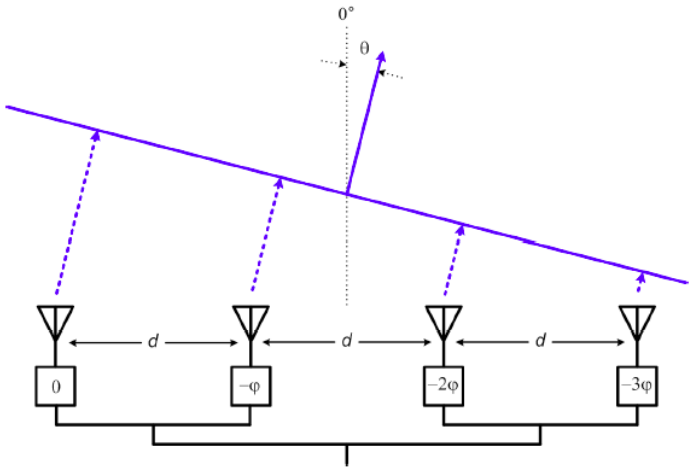

Fig. 3: An electronically steered phased array.

Fig. 3 illustrates the electronically steered beam from a phased array where d represents the separation distance between elements, φ represents the relative phase shift between successive elements, and θ represents the angle of transmission from broadside of the array. The relationship between φ and θ is given by

$$\varphi = k_o d \sin\theta, \tag{1}$$

where

$$k_o = \frac{2\pi}{\lambda}. \tag{2}$$

By applying a constant phase gradient across the array, a plane wave can be steered in a multitude of directions by manipulating the locations where constructive and destructive interference occurs. RDAs have an advantage over ordinary phased arrays in that the electronically steered beam is directed autonomously based on an arriving interrogation signal. The RDA architectures described in this report use this phase progression mechanism in various ways to direct the main beam of the array in the direction of the interrogator.

Characterizing the behavior of RDAs in the presence of multiple interrogators is also important due to the fact that in extraterrestrial environments, instances of more than a single interrogator may exist. Also, when operating in mountainous regions, multipath fading is a big problem due to the numerous reflection paths a signal can take from transmitter to receiver, where those paths act as multiple interrogators. Not all RDA architectures have the ability to function with multiple interrogators because of limitations of their design.

The following sections will discuss two RDA architectures that meet the technical requirements of the proposed space-based application.

Power–Detecting/Phase-Shifting RDA

A power-detecting/phase-shifting RDA architecture measures received RF power to determine the location of the interrogator, and phase shifters to transmit in the appropriate direction [3]. There are two modes of operation for this array: detection mode and transmission mode. In detection mode, the array is swept across the entire 180° range using phase shifters, and power levels are stored in a power-detecting circuit for each respective angle. The RDA then switches to transmit mode and uses the stored data to control phase shifters to position the main beam of the array in the direction of the interrogator (assumed to be the direction of highest power).

The entire detection operation takes less than 18 μs, so near-constant interrogator tracking is possible by switching rapidly between detection and transmission mode. By setting a relative power-level threshold value for the detection mode, the RDA can operate in the presence of multiple interrogators or in multipath environments by transmitting towards the absolute maximum, and several local maxima.

Fig. 4 shows a schematic block diagram of the power-detecting/phase-shifting RDA illustrating the various modules used in both detection and transmit mode.

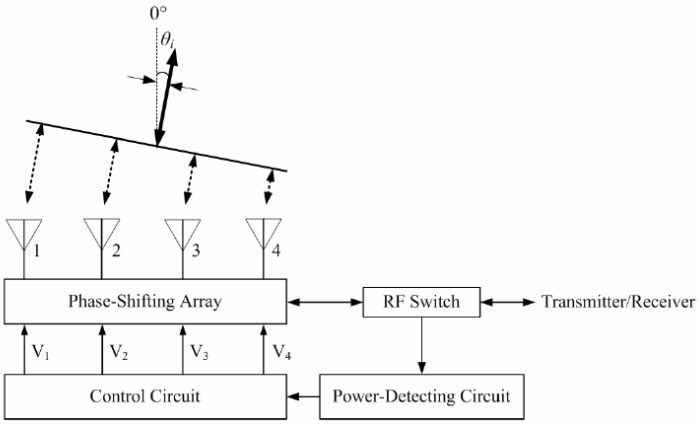

Fig. 4: Schematic diagram of a power-detecting RDA. From [3].

Inter-Element Phase-Detecting RDA

An RDA architecture based on phase detection and phase shifting was recently presented in [4] which used phase-detecting blocks between adjacent element pairs.

Fig. 5 shows a block diagram of the RDA showing phase-detecting blocks, and phase shifters which are manipulated using the control circuit. At the phase-detecting block, the incoming phase difference between the antenna elements is detected and is used as inputs to a control circuit. The control circuit outputs tuning voltages for phase shifters that steer the main beam of the antenna array in the direction of the interrogator, thus achieving retrodirectivity. Direction-of-arrival (DOA) information can also be derived using simple processing techniques on the phase-detection signals in the control circuit.

This design is an improvement on a previous design [5] which featured a single phase detector and a dedicated detector array because it can successfully retrodirect nonuniform wavefronts, which are produced in multipath environments.

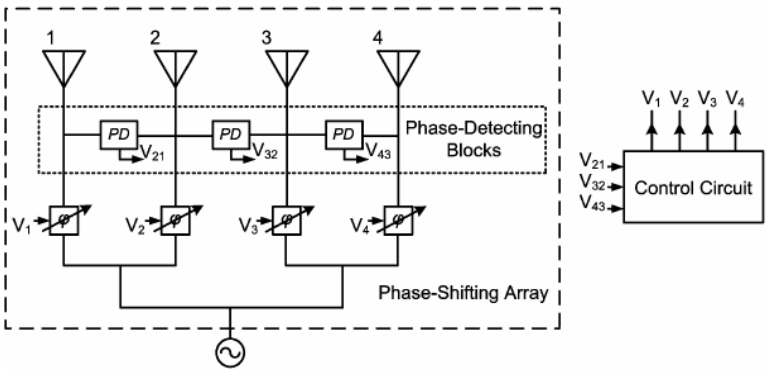

Fig. 5: Schematic block diagram of an inter-element phase-detecting RDA. From [4].

Based on the equipment specifications highlighted in the next section, the architecture that best fits the system requirements will be chosen in the system overview and analysis sections.

EQUIPMENT SPECIFICATIONS

In 2003, NASA launched the Mars Exploration Rovers (MER) as part of its Mars Exploration Program, whose main purpose was a long-term exploration of the red planet [6]. The two rovers were deployed upon landing on Mars in 2004 and successfully collected rock samples, took pictures, and transmitted data back to Earth. These rovers could serve as the platform for the space-based application utilizing RDAs because they represent one of NASA's most recent efforts into space exploration. Fig. 6 shows an illustration of the MER platform.

Adapting the MER platform to aid in search-and-rescue applications for stranded explorers is the main focus of this research. Publicly available documents online were used to determine if the MER platform would be a feasible solution in developing a search-and-rescue vehicle [1], [6, [7]. Most of the information regarding the technical specifications of the rover are proprietary NASA research, and thus not available to the author.

The overall dimensions of the MER platform are 1.5 m high, by 2.3 m wide, by 1.6 m long, and in its current configuration, the rover weighs 174 kg on Earth [7]. The size of the rover is sufficient enough to house the RDA system, and the system will not add an overwhelming amount of mass to the rover. The entire RDA system is has an approximate mass of 2 kg with all included hardware.

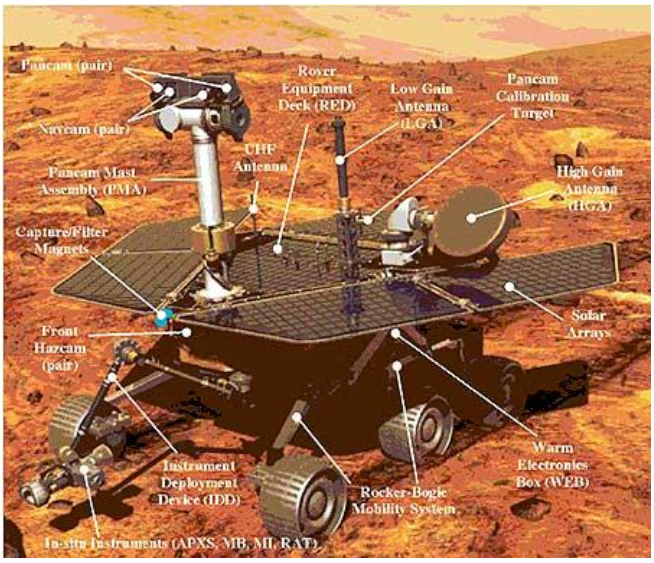

Fig. 6: Illustration of the MER platform rover.

The rover has 1.3 m^2 of high-efficiency solar cells to collect solar energy and convert it to usable power. With clean solar panels and strong sun coverage, the panels produce about 140 watts peak, or about 900 watt-hours total per day. The power from the solar panels goes to the devices that need it and any excess power is stored in two 28-volt, 10-amp-hour, lithium-ion batteries.

There are three radios and accompanying antennas on board the rover. The radios serve to send data back to Earth, either directly with a high gain 1-foot-diameter antenna at 40 watts, indirectly through orbiting satellites at 15 watts, or in worst case scenarios, with an omnidirectional antenna. The proposed system will replace the omnidirectional antenna with an RDA that can be used to communicate and locate a stranded explorer.

The MER platform costs approximately $410M for development, launch, and mission operations. A large part of that sum ($323M) is for the development of the specialized scientific equipment. When replaced on a search-and-rescue rover with the RDA hardware, the overall system cost will be lowered.

SYSTEM OVERVIEW

A space-based application involving the search and rescue of a stranded explorer utilizing RDA technology was developed during this project. The application served to fulfill two of NASA's strategic goals regarding a return to space exploration:

- Strategic Goal 3: Develop a balanced overall program of science, exploration, and aeronautics consistent with the redirection of the human spaceflight program to focus on exploration.
- Strategic Goal 6: Establish a lunar return program having the maximum possible utility for later missions to Mars and other destinations.

The application uses an RDA to locate and communicate with a stranded explorer who is outputting a distress beacon. The RDA architecture used must be able to handle the rugged and mountainous regions associated with extraterrestrial regions, and the two architectures described earlier were compared to assess their ability to meet the mission requirements. The inter-element phase detecting RDA was chosen for its ability to respond to multiple interrogators as well as its ability to obtain phase information needed to perform DOA calculations.

The ability of the RDA to pinpoint the location of the lost explorer is accomplished by using the phase information collected at each element and calculating the direction of arrival of the signal. These calculations are done using a digital microcontroller that processes the outputs of the phase detectors, and translates the data to a certain heading. The microcontroller will then process that heading into rover movement controls to send the rover in the direction of the distress beacon.

Communication channels between rover, base station, and explorer are also being established in parallel. Once the RDA is interrogated with the distress beacon, the rover can forward position data to a base station. Operators at the base station can begin direct communication with the lost explorer, as well as through the rover's communication block. A block diagram showing the functional flow between elements in the system is shown in Fig. 7.

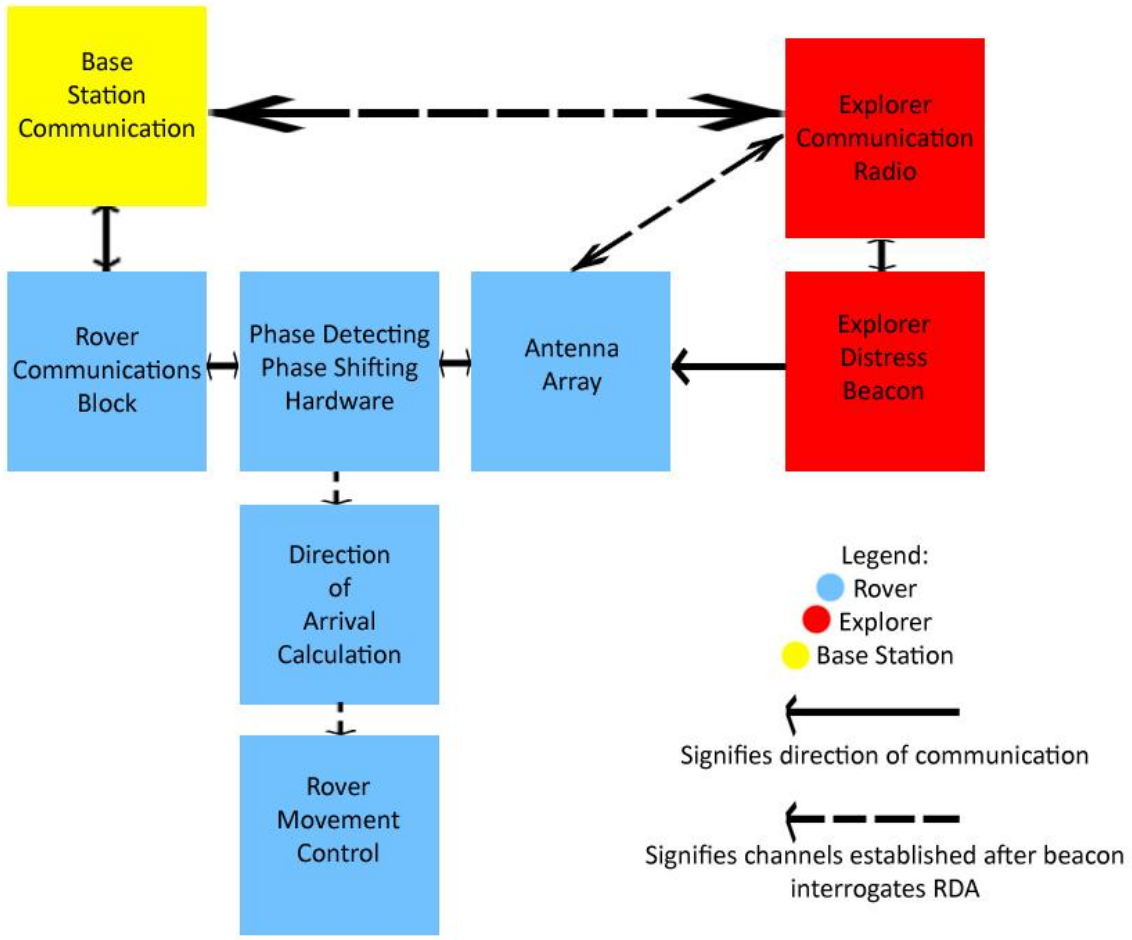

Fig. 7: Block diagram of proposed system.

A hexagonal-shaped system design was chosen with each side containing four λ/2-spaced patch antenna elements. Each side functions as its own subarray, providing an approximate 60° beamwidth per side. This configuration would yield a full 360° field of view in the plane that the rover is traveling on, with a desired gain of about 10 dBi. A 1D layout was chosen for simplicity with the assumption that the explorer and rover were both located on approximately the same plane. The envisioned system is shown in Fig. 8.

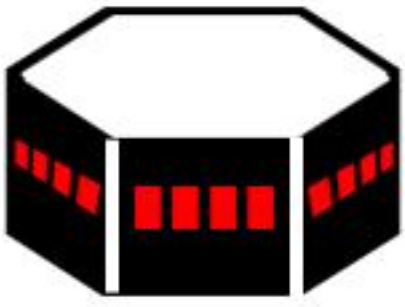

Fig. 8: Conceptual illustration of proposed system.

A radiation pattern was simulated for one side of the RDA system to verify the design of a patch-antenna array. Fig. 9 shows the 3D radiation pattern of an array that is excited in phase at each element, simulating a retrodirected response due to an interrogator signal that impinges the array from broadside.

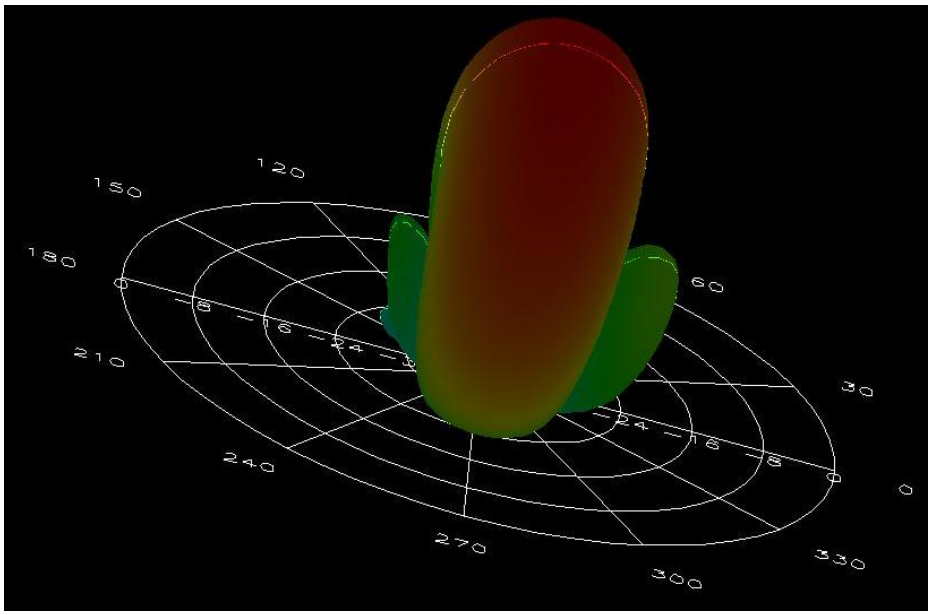

Fig. 9: 3D radiation pattern of antenna array pointing broadside.

The approximate power consumption for the system is about 67.2 W, factoring in the power requirements of the phase shifters, phase detectors, microcontroller, and low noise amplifiers. This power consumption is about half of the peak 140 W available from the solar cells. Any auxiliary power requirements from the rover that exceed the 140 W would need to be satisfied by the onboard batteries.

SYSTEM ANALYSIS

To calculate the path loss between the rover and explorer the following equation known as the Friis transmission equation [8] was used.

$$\frac{P_r}{P_t} = G_t G_r \left(\frac{\lambda}{4\pi R}\right)^2 \tag{3}$$

This measurement, which relates received power (P_r) and transmitted power (P_t) to gain parameters (G_r, G_t) of the antennas, give a baseline measure of how sensitive the rover's receiver would have to be to pick up a lost explorer's distress beacon. The wavelength in free space is given by λ, and R represents the distance between the rover and explorer. Assuming an explorer transmitter power of 1W, an isotropic antenna gain of 1 for the explorer and RDA gain of 10 for the rover, a frequency of 2.4 GHz (λ = 0.125 m), and a distance of 100 m, the received power is calculated to be 98.9 nW. The ratio between received and transmitted power represents the path loss, and this was calculated to be -40 dB. With available receivers with sensitivities greater than

-90 dBm, the system performance is verified for a distance of 100 m. The reader should note that 100 m was chosen for R because that is the per day limit on the rover's movement. This is a limitation of this system that could be remedied with longer onboard battery life.

CONCLUSION

An overview of two RDA architectures that utilized different methods of achieving retrodirectivity was presented to show the various options available when designing a system for a search-and-rescue application. Current Mars rover technology was outlined and proposed as a possible platform for the application. A space based application was presented where a stranded explorer was found using RDA technology. The application was developed to help fulfill two of NASA's strategic goals relating to space exploration. Finally a system analysis was presented as a preliminary verification of the application's effectiveness in an extraterrestrial environment.

ACKNOWLEDGEMENTS

The author would like to acknowledge the valuable assistance and guidance received from his advisor Dr. Wayne Shiroma and graduate research assistant Monte Watanabe. He would also like to thank graduate research assistants Tyler Chun, Alex Zamora, and Justin Akagi for their inputs and suggestions. Finally the author would like to thank the University of Hawaii College of Engineering and the Hawaii Space Grant Consortium for their support of his project.

REFERENCES

[1]"NASA - Apollo 11's 40th Anniversary." NASA - Home. Web. 31 July 2009. <http://www.nasa.gov/multimedia/imagegallery/image_feature_1421.html>.

[2] W. A. Shiroma, R. Y. Miyamoto, G. S. Shiroma, A. T. Ohta, M. A. Tamamoto, and B. T. Murakami, "Retrodirective systems," in *Wiley Encyclopedia of RF and Microwave Engineering*, K. Chang, Ed. New York: Wiley, Feb. 2005, pp. 1681–1684.

[3] J. M. Akagi, A. Zamora, M. K. Watanabe, and W. A. Shiroma, "A self-steering array using power detection and phase shifting," in *IEEE MTT-S Int. Microwave Symp. Dig.*, Atlanta, GA, June 2008, pp. 1325–1328.

[4] A. Zamora, M. K. Watanabe, J. M. Akagi, T. F. Chun, and W. A. Shiroma, "An Inter-Element Phase-Detecting Retrodirective Array for Nonuniform Wavefronts," in *IEEE MTT-S Int. Microwave Symp. Dig.*, Boston, MA, pp. 817-820, June 2009.

[5] G. S. Shiroma, R. Y. Miyamoto, and W. A. Shiroma, "A full-duplex dual frequency self-steering array using phase detection and phase shifting," *IEEE Trans. Microwave Theory Tech.*, vol. 54, no. 1, pp. 128–134, Jan. 2006.

[6]"HowStuffWorks "How the Mars Exploration Rovers Work"" Howstuffworks "Science" Web. 31 July 2009. <http://science.howstuffworks.com/mars-rover3.htm>.

[7]"Mars Exploration Rovers - Mission Overview | Public Outreach |." Mars Institute - To further the scientific study, exploration, and public understanding of Mars. Web. 31 July 2009. <http://www.marsinstitute.info/epo/meroverview.html>.

[8] C. A. Balanis, Antenna Theory Analysis and Design, 3rd Edition. New York: Wiley-Interscience, 2005.

A PLANAR ANTENNA AND MODULAR SUBSYSTEM DESIGN FOR CUBESATS

Reece T. Iwami
Department of Electrical Engineering
University of Hawai‘i at Mānoa
Honolulu, HI 96822

ABSTRACT

Previous University of Hawaii CubeSats constantly used new designs for each succeeding project. Having to redesign the three major subsystems (TTC, PGD, CDH) to accommodate a particular payload resulted in long development times and a steep learning curve for new members. To avoid these problems a modular subsystem design was researched and implemented. The utilization of standard connectors with all subsystem boards, and the independence of payloads in the design of subsystems were adopted to create a modularized CubeSat platform that could be used in future projects without modification. Two different types of planar antennas were also researched and designed to address shortcomings of previous CubeSat antennas.

INTRODUCTION

The University of Hawaii has produced several successful CubeSat designs since 2001, with varying missions spanning retrodirective crosslinks to global imaging. With each new mission the CubeSat group would design each subsystem (Tracking, Telemetry, and Control, Power Generation and Distribution, Command and Data Handling, Payload) using a few components that worked well in the past, but mostly starting from scratch with new components and PCB designs. This mantra catered mostly towards each specific mission and payload, but left future groups having to change designs to fit their own specifications. Therefore, to facilitate future CubeSat designs, a standardized interface approach was adopted. Each subsystem would be designed independently from any particular payload and instead be able to provide all the basic functionality previous subsystems offered, while also being reusable (without redesign) in the future in a “plug- and-play” fashion. The design of a standardized Tracking, Telemetry, and Control (TTC) subsystem is explained in this paper.

Along with the modular subsystem design, several planar antennas were examined for their feasibility in a CubeSat platform. The planar aspect of the antenna would seek to address the need to simplify CubeSats in order to reduce risk related mission failures and to bolster overall system robustness. Two designs were chosen and studied further to the point of design and simulation, with one being fabricated and tested. The methods for the design and testing of the antennas are described in this paper.

TTC SUBSYSTEM REQUIREMENTS

The Tracking, Telemetry, and Control subsystem is in charge of all inter-satellite (satellite-to-satellite) and satellite-to-ground communications. When data needs to be relayed between nodes in a CubeSat network constellation, the TTC subsystem is in charge of establishing communication links between the correct satellites to transfer the data that is needed.

When the ground station wants to retrieve this information, or simply give instructions to the satellite network, a reliable link must be created between satellite and ground station that is sufficient for ranges of about 500 km or low earth orbit (LEO).

Also, a low-power satellite beacon was proposed as a way of identifying the satellite. When satellites pass overhead, they usually broadcast a simple Morse code message that functions as an identifier. Using a separate, low-power beacon would free up the primary transceiver to focus on its data transmission priorities, and allow for constant beacon identification, which was not possible with the relatively high power consumption of the primary transceiver.

With this in mind, communication components were selected with the following requirements:

- The primary transceiver must be capable of communicating through line of sight with another node in the network, as well as a ground station that is around 500 km away.
- The frequency of the transceiver should be in one of the amateur radio bands, allocated for amateur satellite use.
- The antenna for the transceiver should be low profile and non-deployable, resonate at the correct frequency, and must have enough gain with omnidirectionality to communicate with a ground station as well as adjacent satellites in orbit.
- The primary transceiver must be capable of transmitting a complete data stream in an allotted time. This is necessary because satellite passes are very short (5-15 minutes long), and incomplete data transmissions are useless.
- With the goal of CubeSat constellations in mind, the subsystem must be able to configure itself into a complete network capable of file sharing, as well as being able to reconfigure the network in case of node failures.
- The TTC beacon should be a simple Morse code message (duration of less than 30 seconds) that consists of an identifying call sign and some simple satellite health telemetry data. The data must be transmitted with a low-power transmitter that can be on at all times if necessary.

These communication requirements were verified with a link budget analysis using the Jan King excel spreadsheet[1].

COMPONENT RESEARCH AND SELECTION

TTC Inter-Satellite and Satellite-to-Ground Communications

Several Hawaii CubeSats used the MHX 2400 radio for its main satellite communications[2]. While the radio met many of the subsystem requirements mentioned above, it was quite difficult to establish a network configuration in a space based application setting. For this reason, the Xtend radio module was chosen as the new TTC main satellite communications radio. The Xtend radio transmits at 900MHz, for which there is a dedicated band for amateur radio use[3]. The Xtend matches or exceeds the critical features of the MHX 2400, including 1W transmit power, 115kbps throughput, and most importantly, better networking capabilities. While the MHX required a master/slave relationship between nodes in a network (which posed the problem of figuring out which satellite is the master while all others were slaves), the Xtend radio maneuvered around that by implementing peer-to-peer networking which allows radios to communicate with whichever node it can establish a link to. The Xtend radio can easily be configured on a computer using a terminal and AT command line.

Figure 1: Xtend 900MHz RF module.

TTC Beacon

The TTC beacon was designed to be low powered, while still being able to function as a secondary communications system in case the Xtend radio failed. The beacon was implemented with a simple microcontroller and a low-power transmitter. The microcontroller chosen was the PICAXE 28-X1 which was selected because of its ease of use and because it satisfied the requirements of being a low-power controller for the satellite beacon (20mW). The PICAXE also supported I2C which was being implemented as part of the modular subsystem design. The TWS-434 transmitter was chosen because of its frequency of operation (433MHz), low-power design (230mW), and modulation scheme (AM). The microcontroller and transmitter formed the basis of the satellite's beacon system.

DESIGN

Modularity Through the CubeSat Stackable Interface (CSI)

A major facet of designing a modular subsystem is the interface between the different parts of the satellite. A stackable connector that is used for all the boards in a CubeSat bus would provide the necessary data and power connections, and facilitate a standardized design. By stacking the various subsystem boards on top of each other, different modules could be added or subtracted from the system without changing the basic design foundation of the satellite bus. This fit the requirement of developing a baseline CubeSat platform which future projects could base their design off of.

The PC-104 connector fit the requirements of the design and was chosen because of its presence in the technology and small satellite industry. The PC-104 standard is a 120-pin connector that contains a 4x30 pin configuration in a sturdy package[4]. This stackable connector was highly standardized with parameters for PCB placement and mounting hole placements. When stacked with subsystem boards, the PC-104 connector would provide a strong physical connection between all CubeSat systems that would aid in the system integration phase of satellite development.

Along with the standard PC-104 connector, there is also a standard pin assignment that is usually used. Since many of the pins were not necessary in the CubeSat design, a proprietary pin assignment was developed which maximized the pin resources for the different subsystems, and allowed for future payloads to be connected to the bus. Designing for an arbitrary payload involved including an I2C bus, general input and outputs to the microprocessor, as well as standard power lines (5V, 3.3V), solar cell inputs, and raw power lines. The use of the PC-104 connector and the proprietary pin layout is called the CubeSat Stackable Interface (CSI)

Common signals were located near each other and often times included several rows of identical signals. This was implemented for signal integrity as more and more devices are connected to the bus. Also, to shield signals from possible interference, power lines were separated from data carrying lines by ground signals. Digital signals were never placed adjacent to each other (as can be seen by the altering of pin assignment order in the serial port block) to further limit the possibility of signal interference. Four serial ports are available as well as four general purpose inputs and outputs to allow for future payloads to be able to communicate with the CDH microprocessor. Finally, two I2C busses were implemented on the CSI, one for data between master and slave devices, the other for dynamic power management purposes. A pin assignment diagram for the CSI is shown below.

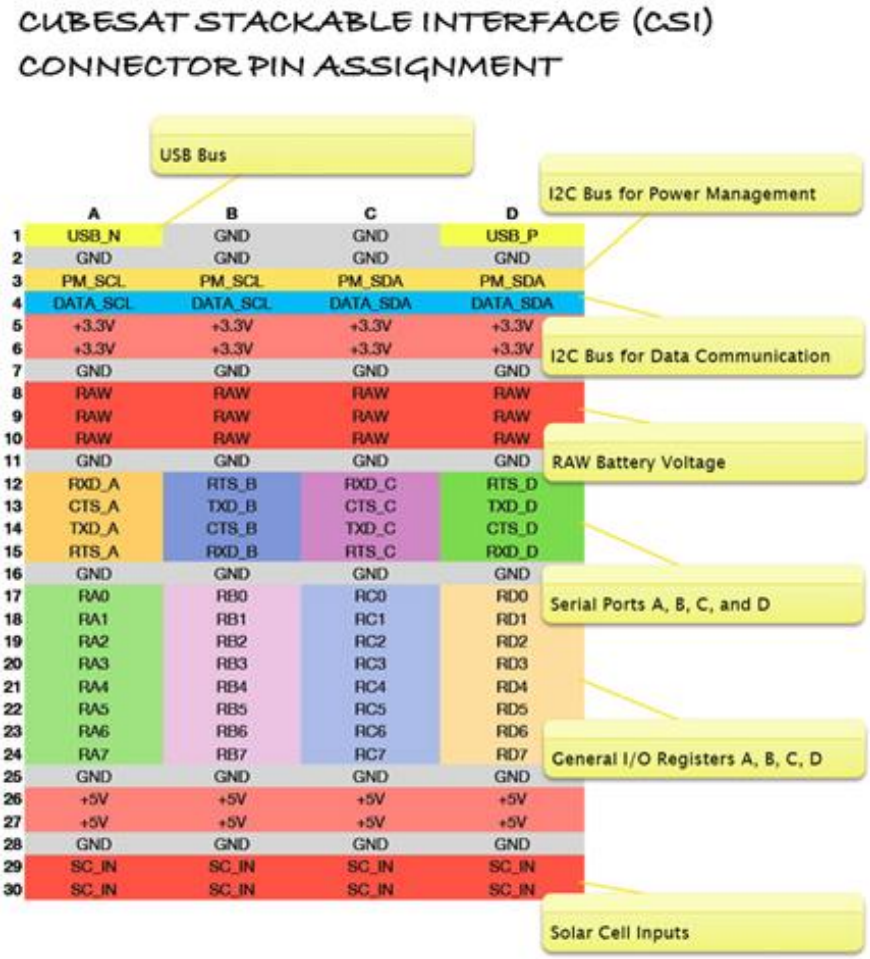

	A	B	C	D
1	USB_N	GND	GND	USB_P
2	GND	GND	GND	GND
3	PM_SCL	PM_SCL	PM_SDA	PM_SDA
4	DATA_SCL	DATA_SCL	DATA_SDA	DATA_SDA
5	+3.3V	+3.3V	+3.3V	+3.3V
6	+3.3V	+3.3V	+3.3V	+3.3V
7	GND	GND	GND	GND
8	RAW	RAW	RAW	RAW
9	RAW	RAW	RAW	RAW
10	RAW	RAW	RAW	RAW
11	GND	GND	GND	GND
12	RXD_A	RTS_B	RXD_C	RTS_D
13	CTS_A	TXD_B	CTS_C	TXD_D
14	TXD_A	CTS_B	TXD_C	CTS_D
15	RTS_A	RXD_B	RTS_C	RXD_D
16	GND	GND	GND	GND
17	RA0	RB0	RC0	RD0
18	RA1	RB1	RC1	RD1
19	RA2	RB2	RC2	RD2
20	RA3	RB3	RC3	RD3
21	RA4	RB4	RC4	RD4
22	RA5	RB5	RC5	RD5
23	RA6	RB6	RC6	RD6
24	RA7	RB7	RC7	RD7
25	GND	GND	GND	GND
26	+5V	+5V	+5V	+5V
27	+5V	+5V	+5V	+5V
28	GND	GND	GND	GND
29	SC_IN	SC_IN	SC_IN	SC_IN
30	SC_IN	SC_IN	SC_IN	SC_IN

Figure 2: CubeSat Stackable Interface (CSI) pin assignments.

PICAXE Beacon

The main goals for the beacon subsystem are to function as an identification beacon for the satellite, as well as a source of simple telemetry data. The identification beacon would function as the satellite's call sign transmitted in Morse code. The beacon also would function as a secondary communication system in case our primary communication system failed. The identification beacon would be transmitted in Morse code, and would be audible to any amateur radio operators outfitted with the necessary equipment. The telemetry data is transmitted serially

using Amplitude Shift Keying (ASK) modulation. This allows for reliable transmission of serial data, which consists of a series of zeroes and ones, with the satellite's low-power transmitter.

The data that will be transmitted is simple telemetry numbers from the satellite. These numbers include: battery voltage and current levels, current being drawn from the solar panels, transmit power, etc. The amount of telemetry data being sent is not large because the entire beacon message, including the identification beacon, should be less than 30 seconds long. This is an important time constraint as LEO orbits have communication windows of about 15 minutes long at best, so to ensure reliable data transmission, the message must be looped several times within the satellite pass window.

The PICAXE microcontroller and the TWS-434 transmitter function together as the satellite's beacon. The PICAXE is hardcoded with the Morse code version of the satellite's call sign, and also handles the data from the CDH subsystem and prepares it for serial data transmission. The PICAXE then outputs the Morse code and telemetry data to the TWS-434 transmitter for transmission down to Earth.

Planar Antenna: PIFA

Previous CubeSats have implemented various types of antennas for their transceivers, ranging from whip antennas to patch antennas. Whip antennas are simple and have an omnidirectional radiation pattern, but they require deployment and that can be complicated in a space environment where there is little physical control of the satellite. Patch antennas are hailed for their low profile (does not require deployment) and beam-like directionality, but on a satellite where little to no attitude control is utilized, this advantage can easily be a strong disadvantage (since the patch antenna could be pointed away from Earth, with nothing going towards the ground station).

PIFAs are used in mobile communications because of their low profile and omnidirectional radiation patterns[5]. One could say the PIFA provides the advantages of the whip (omnidirectionality) and patch antenna (does not require deployment), without the disadvantages. A planar inverted F antenna (PIFA) was researched, designed, fabricated, and tested to see if integration on a CubeSat structure would be possible. The basic physical form of the PIFA is shown below, including the patch, ground plane, substrate, and pin locations.

Graduate student Brandon Takase assisted in the design, fabrication, and testing of a 900MHz PIFA to be used with the Xtend RF module. The PIFA antenna dimensions are scalable, and a report done by Anpeter Nguyen[6] was referenced to find the appropriate dimensions of all components based on the radio's operating frequency. The measurements depend on wavelength, which is related to operating frequency in free space by c, the speed of light. Below are calculated values for 900MHz operation with a physical size of 6.8cm x 14.7cm x 1.47 cm (perfect for the long side of a 1.5U CubeSat which measures 10cm x 10cm x 15cm).

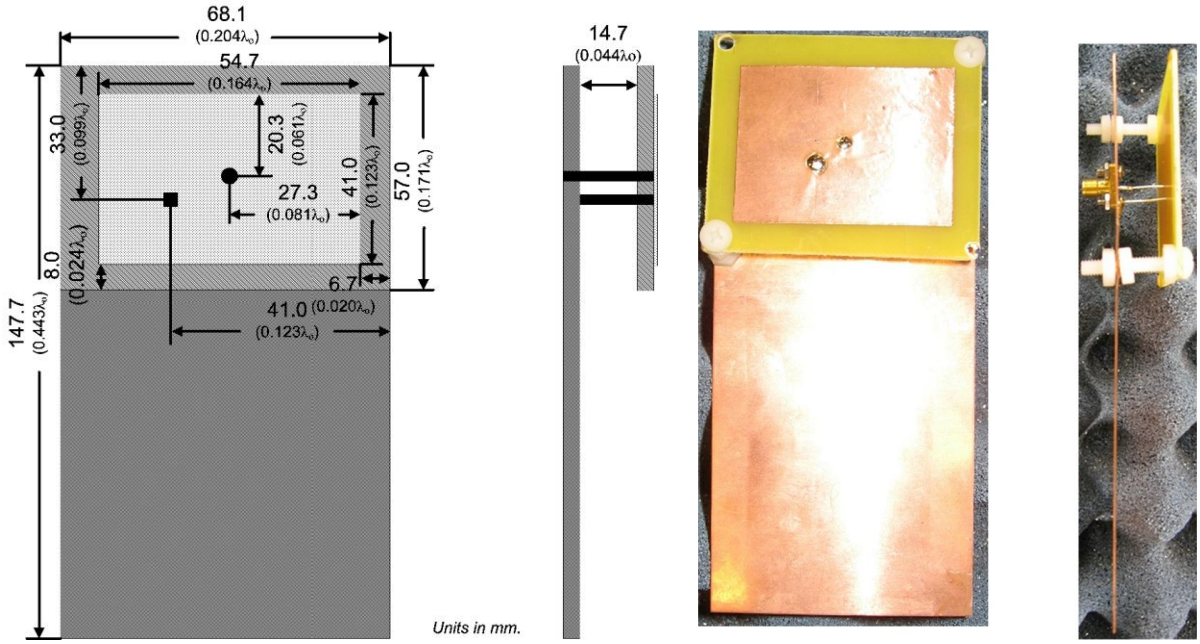

Figure 3: PIFA physical dimensions drawing alongside the fabricated PIFA.

PIFA Testing and Measurement

Following the PIFA fabrication, standard antenna parameters were measured to quantify the antenna's performance and verify the fulfillment of design requirements. The measurements were done with the assistance of Brandon Takase in a microwave engineering lab at the University of Hawaii at Manoa.

The first measurement taken was the return loss of the antenna; this is known as the S11 scattering parameter. By looking at the return loss, one can determine at which frequencies the antenna will resonate and therefore output propagating waves (with an ideal return loss of -∞ dB which indicates zero return loss). When the PIFA was hooked up by itself to port 1 of the network analyzer, the return loss as a function of frequency as seen below was obtained. The highest return loss of -37.2 dB occurs at 937MHz, while a frequency range of 775MHz to 1025MHz satisfies the 2:1 VSWR (at -10 dB) threshold. This wide frequency range is more than enough to encompass the Xtend radio frequency hopping spectrum of 902-928MHz. This measurement verified that the antenna operates at the desired 900MHz frequency.

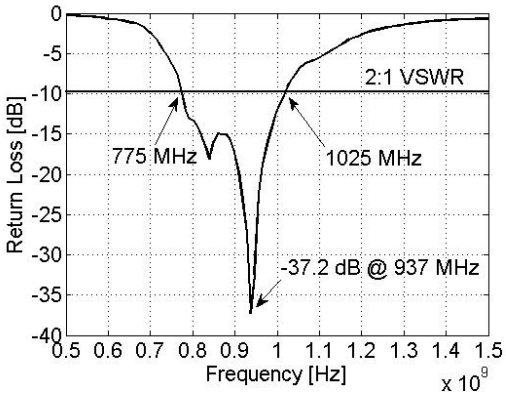

Figure 4: PIFA Return Loss vs. Frequency.

The second measurement taken was the PIFA's radiation pattern. A transmitting horn was fixed at a position and the PIFA was rotated around 360° with the receive power plotted as a function of rotation. Different polarizations of the transmitting horn and orientations of the PIFA were used. The radiation pattern received at the PIFA is shown below. From the results, the PIFA is omnidirectional in the *x-z* plane when the horn in oriented in co-polarization position. This was as expected, and a good sign that this antenna radiates omnidirectionally at the designed frequency of 900MHz.

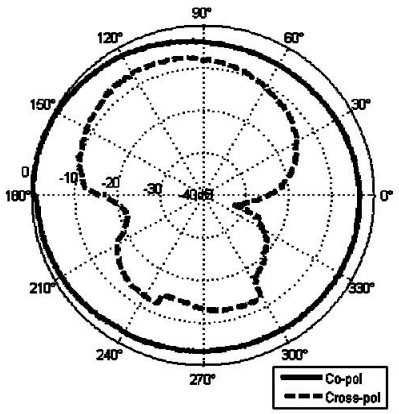

Figure 5: Radiation pattern of PIFA in x-z plane.

The preliminary results obtained for the PIFA were very good. The antenna functioned at the correct frequency and was omnidirectional in the *x-z* plane. Brandon Takase recommended that a more accurate measurement would be to mount the antenna onto a satellite structure. I obtained a sample 1.5U aluminum CubeSat structure and mounted the antenna on, and simulated a complete structure with copper plating on all sides. This measurement yielded poor results compared to the original measurements. This degradation of performance led to an exploration of a new antenna type.

Planar Antenna: Printed Dipole with Integrated Balun

Another approach studied for the satellite's antenna was the printed dipole with integrated balun. A dipole antenna is one of the most basic antenna types, and it exhibits the omnidirectional characteristic of the satellite subsystem requirements. A basic dipole antenna uses two elements which length is a function of operating frequency, and for the resonant type antenna this length is $\lambda/2$. The printed dipole antenna implements a basic dipole on a dielectric substrate, like FR-4 or PCB material. This printed dipole could be mounted flush on the side of a CubeSat and thus reduce the complexities of a deployable antenna. This antenna type was chosen because it fit all of the design specifications set out for the satellite antenna, namely being omnidirectional and planar.

Because the printed dipole was to be fabricated on a substrate using microstrip line and SMA connectors, a balun was needed to convert from an unbalanced feed (microstrip line) to a balanced feed (two feed points of the printed dipole). This was a complex step which was solved by including a top microstrip patch which served to fulfill the balun requirement. The balun requirement involves feeding the two elements of the dipole at a 180^o phase difference of current. By using an integrated balun, the performance of the antenna (radiation pattern, operating frequency) would approach predicted antenna theory.

Advanced Design Systems (ADS) software from Agilent was used to design the antenna and simulate its performance. Referring to the IEEE journal paper by Chuang and Kuo[7] which designed a similar antenna for a different frequency, a prototype antenna was designed which operated at the 900MHz frequency range of the Xtend radio. The antenna layout can be seen in the figure below. At 900MHz, the longest dimension of the antenna is about 12cm, which will fit nicely in a 1.5U CubeSat structure.

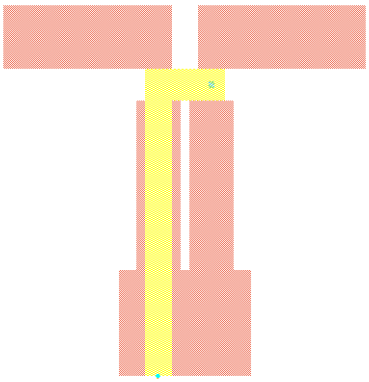

Figure 6: Prototype layout for 900MHz printed dipole antenna.

The simulated return loss shows good performance at our radio's frequency range of 902-928MHz. The plot below shows the S11 or return loss plot, with the red line representing the antenna's usable frequency bandwidth (frequencies below the red line represent the frequency bandwidth). The two markers point out the low and high end of the radio's frequency range, verifying that the antenna matches nicely with the radio.

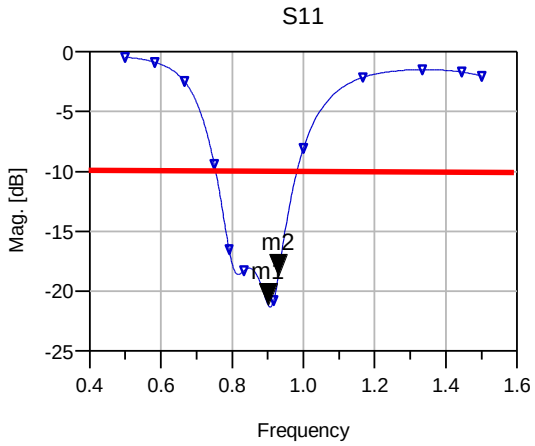

Figure 7: S11 Return Loss plot of 900MHz printed dipole antenna.

The 3D simulated radiation pattern is shown in the figure below. Notice how the pattern is omnidirectional in one plane (plane perpendicular to the plane of the paper). This is very close to the ideal case of a basic dipole antenna, with only slight differences due to the inefficiencies of using a dielectric substrate. The omnidirectional pattern of the antenna fulfills the requirement for omnidirectionality in at least one plane.

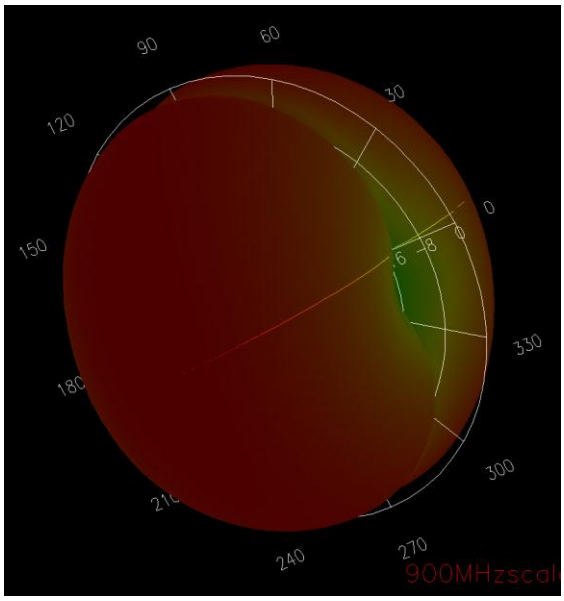

Figure 8: 3D radiation pattern for 900MHz printed dipole antenna.

The successful implementation of the integrated balun is illustrated in the figure below. The arrows in the figure depict the surface current vectors of the antenna at a given instant in time. The arrows represent both phase and magnitude (direction of arrow, size of arrow). As one can see, the current vectors at both feed points show arrows of equal magnitude in 180^{o} phase shift (arrows are pointed in opposite directions). This result verifies that the integrated balun successfully implements the balun requirement.

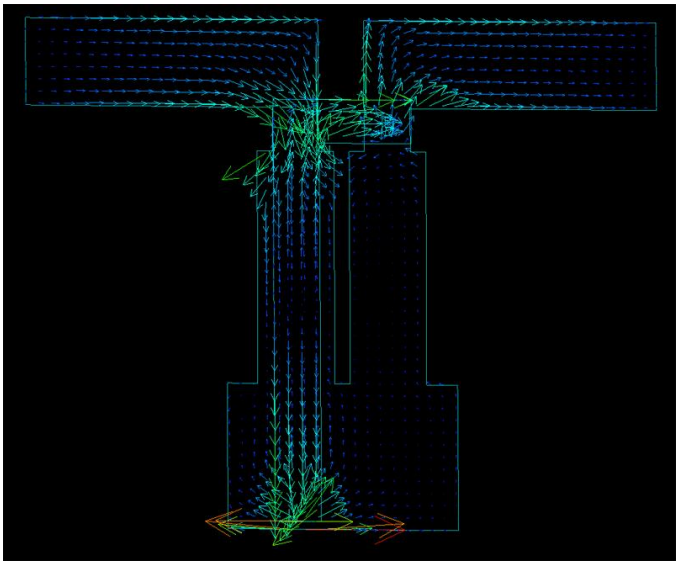

Figure 9: 2D plot of surface current vectors of 900MHz printed dipole antenna.

FUTURE WORK

For future work, the printed dipole design will be exported to be fabricated and tested in the same fashion as the PIFA (radiation pattern, return loss). If the design is verified with measurements to meet the design specifications, a cross dipole configuration based on this antenna will be studied to implement circular polarization. Circular polarization is an additional requirement that will serve to increase the satellite's link margin. Based on these results, the best antenna design (PIFA, printed dipole, cross dipole) will be chosen to be used in the standardized modular subsystem design.

CONCLUSION

A modular subsystem design for the TTC subsystem was described in detail in this paper. The motivation for this standardized design and the methods of implementing such a design, from choosing components to creating an interface for all subsystems to communicate, were discussed. The modular design that was examined will serve as a platform for future CubeSats to use to facilitate more streamlined production and allow for increasingly complex payloads and more sophisticated missions. Two antenna designs were explored and will be further compared to legacy antennas to determine which type will best suit the future of the University of Hawaii's CubeSat platform.

ACKNOWLEDGEMENTS

I am especially grateful to NASA and the Hawaii Space Grant Consortium for supporting student projects like my own. I want to thank my mentor Dr. Wayne Shiroma for providing me guidance and knowledge related to my project. I would also like to acknowledge the entire CubeSat SNC group for their support, as well as Brandon Takase for his help with the PIFA development.

REFERENCES

Chuang, Huey-Ru, and Liang-Chen Kuo. "3-D FDTD design analysis of a 2.4-GHz polarization-diversity printed dipole antenna with integrated balun and polarization-switching circuit for WLAN and wireless communication applications." IEEE Transactions on Microwave Theory and Techniques 51 (2003): 374-81.

Nguyen, Anpeter. Novel UHF Antennas for Small Satellites and Mobile Applications. (2006): 3-23.

Takase, Brandon O. "Novel Antenna Technologies for Small-Satellite and Terrestrial Applications." Thesis. University of Hawaii at Manoa, 2008.

Tamashiro, Tyler. Designing and Implementing a Complete Communication Subsystem for Small Satellites. (2007): 1-6.

"IARU Sat Coordinator." AMSAT-UK. International Amateur Radio Union. 20 Jan. 2009 <http://www.amsat.org.uk/iaru/>.

"PC/104 Consortium Website." PC/104 Consortium. PC/104 Embedded PC Modules. 20 Jan. 2009 <http://www.pc104.org/>.

MECHANICAL PERFORMANCE AND ALIGNMENT OF CARBON NANOTUBES GROWN ON UNIDIRECTIONAL CARBON FIBER TOWS FOR COMPOSITE SPACE APPLICATIONS

Kaveh Khosroshahi
Department of Mechanical Engineering
University of Hawai‘i at Mānoa
Honolulu, HI 96822

ABSTRACT

Polymer/fiber reinforced composites have many desired applications where high strength and low weight are critical factors. However adding Multi-Walled Carbon Nanotubes (MWCNTs) to the base composites could significantly improve not only mechanical, but also thermal and electric properties of the base composite specimens [1]. In this project, emphasis was put on shear mechanical properties since other properties improvements have been demonstrated by Ghasemi-Nejhad and co-workers [1]. An introduction of this project is presented here and is followed by the methods used in this study along with the description of the apparatus, materials, and procedures used to manufacture and test the nanocomposite specimens. Results are discussed in details along with the interpretation of the data. Summary of the results is included in the conclusion section.

INTRODUCTION

Nanocomposites have found an increasingly wide variety of applications in the past decade. Among them are nano-materials specifically designed for thermal management, electromagnetic shielding, radiation shielding, and structural components where improved mechanical properties are desirable. The main objective of this research is to study the mechanical performance of polymer/carbon fiber reinforced nano-composites with carbon nanotubes included on unidirectional carbon fiber tows. Also, an innovative attempt was made to obtain alignment of carbon nanotubes along the direction of the fibers. These composites have very high strength to weight ratio meaning they have low densities (light weight) but very strong and this is precisely what is desired in space applications. Strengths were increased by the insertion of a layer of Multi-Walled Carbon Nanotubes (MWCNTs) interphase in between the layers of unidirectional carbon fiber tows. To demonstrate these improvements, samples with and without MWCNTs were tested and compared for short beam shear strength.

METHODS

The first step was to manufacture the base carbon/epoxy composite specimens for short beam shear tests. Custom molds were designed and made out of Aluminum 6061-T6. These molds were designed in the Inventor 2008 CAD program and manufactured in the machine shop by myself. Molds with a depth of 3 mm were made for short beam shear test samples. Figure 1a and 1b show the fixture design and the fabricated piece, respectively.

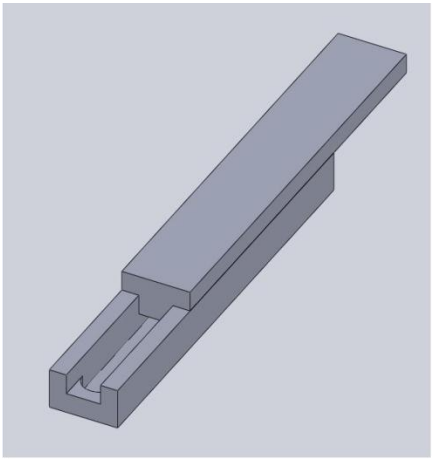

Figure 1a. Mold CAD Drawing

Figure 1b. Fabricated Al 6061 Mold

Next, 8 layers of 15.9 ft/lb Unidirectional Carbon Fiber T700 with the thickness per layer of 0.015 inches obtained from Soller Composites were used to manufacture the carbon/epoxy base composite. SC-15 epoxy resin [2] obtained from Fiberglass Hawaii was used for wetting the fibers. A hand lay-up technique was employed to manufacture the composites in the Aluminum 6061 molds. The samples were then put inside the Compression Molding Machine or the Hot Press [3] under a uniform pressure of 12000 psi and heated from room temperature to 200^{o}C in 1 hour, and held at that temperature for one more hour before cooling it down to the room temperature. The uniform pressure allows to dramatically reduce the amount of voids and air pockets that are present within the layers that were laid-up affecting the strength and performance of the specimen. Figure 2 depicts the cure cycle employed to cure the composite specimen inside the Hot Press.

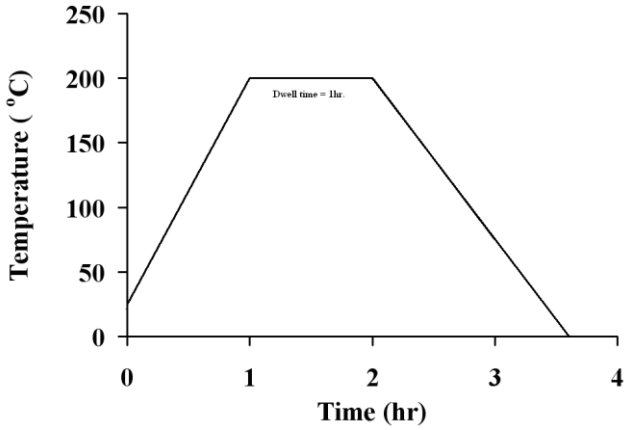

Figure 2. Thermoset cycle employed for the cure of composite.

The second step in this approach involved the growth of MWCNTs on a Silicon (Si) and Silicon Oxide (SiO2) substrate employing chemical vapor deposition (CVD). A gaseous mixture

of ferrocene (0.1g), as a catalyst source, and xylene (10 mL), as a carbon source, was preheated to 185^{o}C and passed over the substrate placed inside the furnace at 800^{o}C for 30 mins with the help of Argon gas. The MWCNTs grew selectively on the substrate with controlled thickness and length [4]. In order to manufacture composites with MWCNTs, the CNTs were sandwiched in between ¼ inch thick tabs and passed through a roller to obtain alignment in the direction of the fibers. Then the aligned MWCNTs were put in between each layer of carbon fiber in the laminating process. The curing was done in the same manner as the base composites inside the Compression Molding Machine.

After the manufacturing process was completed, the parts were machined to develop shear test samples based on ASTM standard D 2344. Next, the Instron Testing Machine [5] was used to test the specimens in Short Beam Shear Test. It should be noted that, for Tension and Compression tests, large areas of MWCNT for so many layers of composites were required and within the time frame left in the project, it was not possible to manufacture this level of MWCNT in the remaining time frame, and hence only Short Beam Shear Tests samples were manufactured and tested according to the ASTM standards [6]. Hence, to characterize the samples, the short beam shear test was performed on the base and CNT composites. The test was performed on 8-ply laminates and the fracture load and mode were used to calculate the shear strength.

RESULTS

Short beam shear test was performed on samples with and without CNT films for mechanical characterization. Figure 1 below shows a typical short beam shear load versus deflection curve for the base sample and sample with CNT films embedded in between the plies. As evident from the figure, the CNT samples carried 2.5 times the load of the base sample. However, the thickness of the CNT samples were thicker and when the short beam shear strength of the composites is calculated using the formula shown below, a 70% improvement in the CNT composite is observed over the base composite. The values for the shear strength for the base and CNT composite are shown in Table 1.

Short beam shear strength = (0.75 * Max load) / (width * thickness)

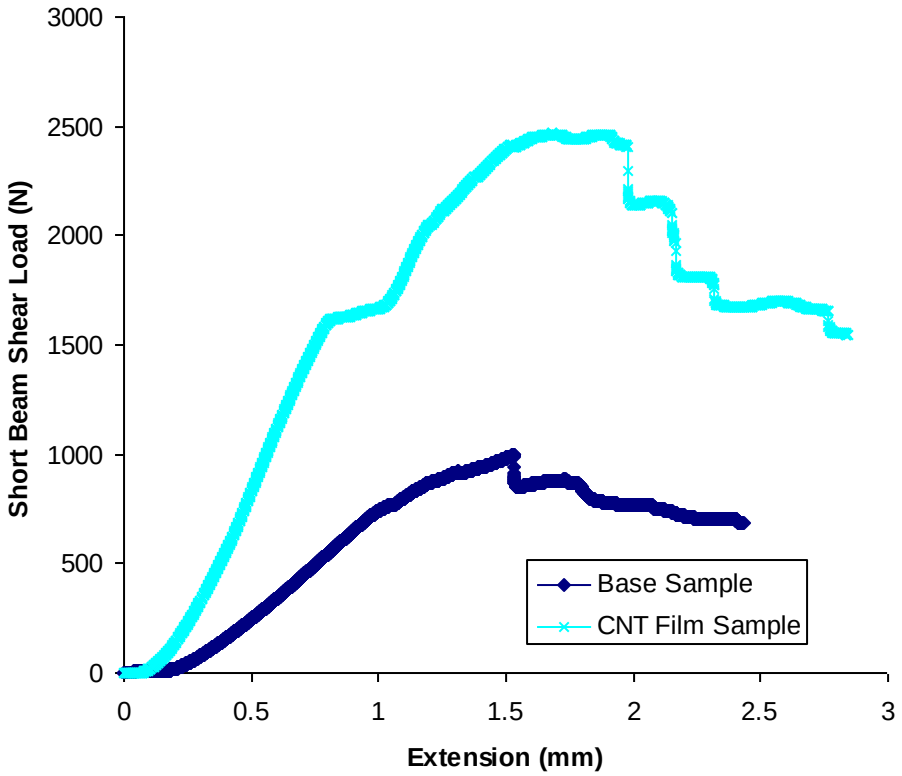

Figure 1. Typical Shear load vs. Deflection curve

Table 1. Short Beam Shear Test Results

	Base Composite	CNT composite
Shear Strength	26.8 MPa	45.44 MPa

CONCLUSION

In this project, I was able to successfully manufacture composites using the molds and manufacturing technique discussed above. To obtain a basic understanding on the effects of the inclusion of CNTs in continuous fiber composites, short beam shear test was performed on samples with and without CNT films. A 70% improvement in the shear strength was obtained,

thereby verifying the effectiveness of the current manufacturing scheme involving CNT films. These results open up a wide range of research opportunities in this field in the future.

REFERENCES

[1] Veedu, V. P., Cao, A., Li, X., Ma, K., Soldano, C., Ajayan, P. M., and Ghasemi-Nejhad, M. N., " Multifunctional composites using reinforced laminae with carbon nanotube forests," ***Nature Materials***, June 2006, Vol. 5, pp. 457-462.

[2] SC-15 epoxy resin and hardner, Part A and B obtained from Fiberglass Hawaii, 3 to 1 mixing ratio by weight. Curing time: 2 hrs at 200^{o}C

[3] Compression Molding Machine (Hot Press) exerts vertical uniform pressure through heating plates, located in UHM ME AMMLlaboratory room in Holmes 140.

[4] Chemical Vapor Deposition (CVD) method of growing MWCNTs.

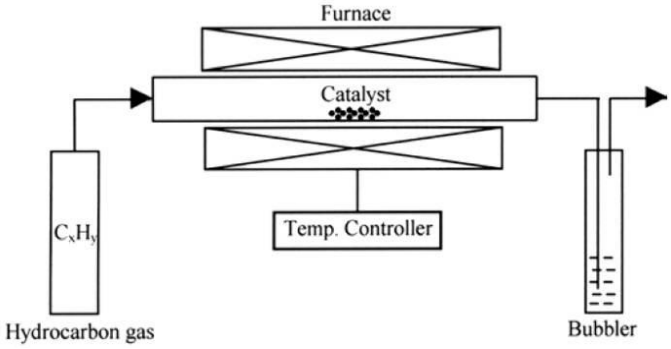

3a. CVD Process

3b. CVD furnace located in UHM ME AMML lab in Holmes 140.

[5] Instron Testing Machine is a world leading manufacturer of test equipment designed to evaluate the mechanical properties of materials and components., located in UHM ME AMML laboratory in Holmes 140.

Instron Testing Machine

[6] ASTM D 2344/ D2344-00, “Standard test method for Short-Beam Strength of Polymer Matrix Composite Materials and Their laminates”, Annual book of ASTM standards 2006.

MAGMATISM AND FAULTING AT KILAUEA VOLCANO: AN ANALOG TO THARSIS VOLCANOES ON MARS

Erin E. Miller
Department of Geology and Geophysics
School of Ocean and Earth Science and Technology
University of Hawai‘i at Mānoa
Honolulu, HI 96822

ABSTRACT

The growth mechanism of the Tharsis Montes on Mars can be better understood through research of an Earth based analog, such as the Hawaiian volcanoes. In June 2007, the southern flank of Kilauea volcano underwent a geodetically identified slow slip event, or "slow earthquake", the study of which may lead to an enhanced understanding of slow earthquakes, volcano spreading, and tsunami-generating slumping. This event coincided with a temporary seismic deployment designed to better resolve the patterns of triggered microseismicity associated with slow earthquakes at Kilauea. Twenty temporary seismometers deployed on the southern flank of Kilauea volcano, Hawaii collected seismic data from before, during, and after the slow earthquake, which was triggered by an east rift zone dike intrusion on June 17-19, 2007. The purpose of this Space Grant project was to use the Antelope software's user interface in order to interactively relocate 1629 microearthquakes that occurred prior to the dike intrusion. Another relocation method will later be applied to the experiment dataset, where researchers will apply waveform cross correlation, high precision relocation, and double difference tomography. The final results of this project will ultimately provide a set of microearthquake locations that are far more precise than human error would allow for. Here, 1629 microearthquakes were successfully located using Antelope, and epicenters appear to cluster between 19.3º and 19.35º latitude, as well as between -155.25º and -155.2º longitude, extending southward from 19.35º to 19.27º latitude. This new set of locations are now ready for the application of waveform cross-correlation and high precision relocation, in order to obtain precise hypocenters to aid in the study of detachment faulting, volcanic spreading, and slow earthquakes.

INTRODUCTION

Mars, which is the fourth planet from the Sun, plays host to Olympus Mons, the largest volcano in the Solar System. Olympus Mons is one of the four major volcanoes in the Tharsis region of Mars [Figure 1]. It boasts a height of 24 km, and has been suggested to be similar to Mauna Loa, which is the largest volcano on Earth. Olympus Mons is about one hundred times larger than Mauna Loa by volume (McBride and Gilmour, 2003), but its ratio of volcanic height to diameter is comparable to that of other Hawaiian volcanoes (McGovern and Solomon, 1993). These shared characteristics are likely due to similarities in the growth of the Tharsis Montes and the Hawaiian Islands. The formation of the Hawaiian Islands is due to a mantle plume located in the middle of the Pacific Ocean (McBride and Gilmour, 2003). This mantle plume generates copious amounts of magma, which erupts onto the sea floor and eventually builds up to form islands. Plate tectonics move the Pacific Plate over the Hawaiian mantle plume, causing the Hawaiian Islands to form and eventually be moved away from their magma source. Conversely,

plate tectonics does not exist on Mars, so although the Tharsis Montes are also a product of mantle upwelling, these volcanoes are able to grow much larger because they never move away from their magma sources (McBride and Gilmour, 2003). As a result, Tharsis region has remained a site of recurring volcanism for most of Martian history (Solomon et al., 2005) and also contains some of the youngest observed surface ages on the planet (< 100 Myr) (Hartmann et al., 1999; Hartmann and Neukum, 2001).

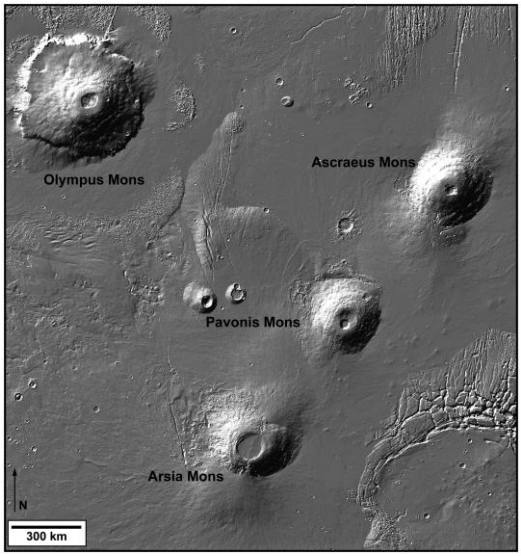

Figure 1. Picture courtesy NASA/JPL-Caltech. The Tharsis Montes.

Given the noted similarities between both the physical characteristics and origin of the Tharsis Montes and the Hawaiian Islands, one may theorize that their growth mechanisms may also be analogous. A study completed by McGovern and Solomon (1993) concluded that the best growth model for the Tharsis Montes would include a basally detached volcano, similar to Hawaiian volcanoes.

A basally detached volcano contains a detachment fault between the growing volcano and the preexisting crust upon which it sits. Detachment faulting may be facilitated when the volcano grows on top of a layer of fluid-filled sediment, which helps to create a lubricated fault zone (Morgan et al., 2000). The presence of sediment in the Tharsis region thus has been inferred to support the existence of basal detachment among the Montes (McGovern and Solomon, 1993; McGovern and Morgan, 2008). The Hawaiian Islands also sit atop a layer of sediment, making these volcanoes basally detached. When magma is injected into a basally detached volcano, the flanks of the volcano may respond by spreading laterally outward [Figure 2] (Morgan et al., 2003).

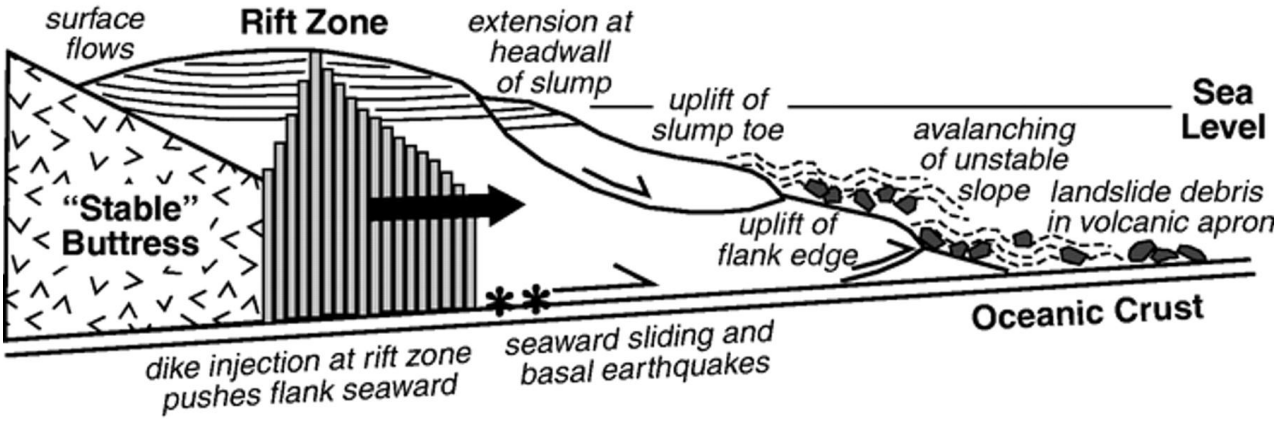

Figure 2. From Morgan et al., 2000. Model for volcano growth and deformation at Kilauea volcano. Magma intrudes at rift zone, feeding surface eruptions and dike intrusion, and flank moves away from rift zone. Seaward displacement of flank causes earthquakes along volcano base, and lateral compression and overthrusting along distal flank. Slumps may form on unstable slopes, causing extension along upper flank and uplift at slump toe. Collapse of unstable flank and uplifted bench leads to debris avalanches, which add material to volcanic apron surrounding volcano.

The process of volcano spreading produces earthquakes on the detachment (Morgan et al., 2000). For example, the volcanic spreading occurring along the southern flank of Kilauea volcano can be detected in the patterns of microseismicity or large earthquakes produced when faulting occurs (Morgan et al., 2000). Some of the slip occurring in this region is also aseismic, including slow earthquakes (Brooks et al., 2006). Unlike regular earthquakes, where rupture occurs over time scales of seconds to minutes, a slow earthquake (SE) releases its energy over a longer period of hours to several months. Though SEs are slow to release their energy, some subduction zone events have been observed to have magnitudes as high as 7.5. In some cases, seismic tremor is observed to be associated with SEs, although the tremor is very low in amplitude, making it difficult to detect (Houston and Vidale, 2007). Seismologists term the seismic tremor associated with SEs as "non-volcanic tremor" to distinguish it mechanistically from the tremor also commonly observed during volcano eruptions or intrusions (Rubinstein et. al. 2007). Swarms of non-volcanic tremors have been observed at subduction zones during slow-slip events, and may be a reflection of the accumulation of stress at a subducting plate (Obara, 2004).

By studying the microearthquakes produced the detachment fault at Kilauea's volcanic flank, we hope to better understand the mechanics of volcanic growth and spreading. In specifically studying this phenomenon on the Hawaiian Islands, it is possible to extend our knowledge from terrestrial sources up to the Tharsis Montes on Mars. This project aims to study the detachment fault beneath Kilauea Volcano in detail by studying the microearthquake swarms that occurred during the slow earthquake triggered by the June 17-19, 2007 "Father's Day" dike intrusion. This study may lead to new knowledge of the growth mechanisms of basally detached volcanoes, which could be useful for future studies of both the Hawaiian Islands and the Tharsis Montes.

METHODS

Seismic data were obtained using a dense cluster of twenty temporary broadband seismometers, deployed specifically to monitor the flank response from a predicted slow earthquake. These data were then analyzed using the Antelope software, developed by Boulder Real Time Technologies. The software collects the data from seismometers after an earthquake event and runs an initial, automated search for all of the microearthquakes that occurred before, during, and after the event. Approximately 1600 microearthquakes occurred in the 29 day period preceding the June 2007 dike intrusion, according to the detection and association algorithms run by the Antelope software. The software locates events and presents them to the end user for inspection and refinement. The user must then make interactive adjustments to the locations and arrival time picks estimated by the software.

Though the software can adequately detect earthquakes within the waveforms recorded by the seismometers, it is fairly inaccurate in determining where exactly the Primary (P) and Secondary (S) waves of an earthquake first arrive within a waveform, and therefore the initial, automated location of the earthquake may be several kilometers from its true location. When the end user reassigns the proper locations for P and S waves within the waveform shown by the program, the physical location of the earthquake is recomputed. The series of steps that must be taken by the end user in order to relocate an earthquake are depicted in Figure 3. For this particular study the procedure is as follows: P-waves should only be picked on the z-axis, not the north or east running axes. This is because P-waves propagate longitudinally, and therefore

show a clean signal on the z-axis. One S-wave should be identified on either the north or east running axis, as S-waves propagate transversely, and therefore the cleanest signal is found on the north or east axes. After the P-waves and S-waves have been picked in the waveform, the Antelope software calculates the new location and its associated root-mean-square residual (between predicted and observed arrival times), which is called sdobs. An acceptable sdobs for these picks is less than 0.100. Qualitatively, this responds to the consistency of the new location with the picked arrival times. Following this procedure the end user may generate a figure depicting the new locations.

Figure 3:

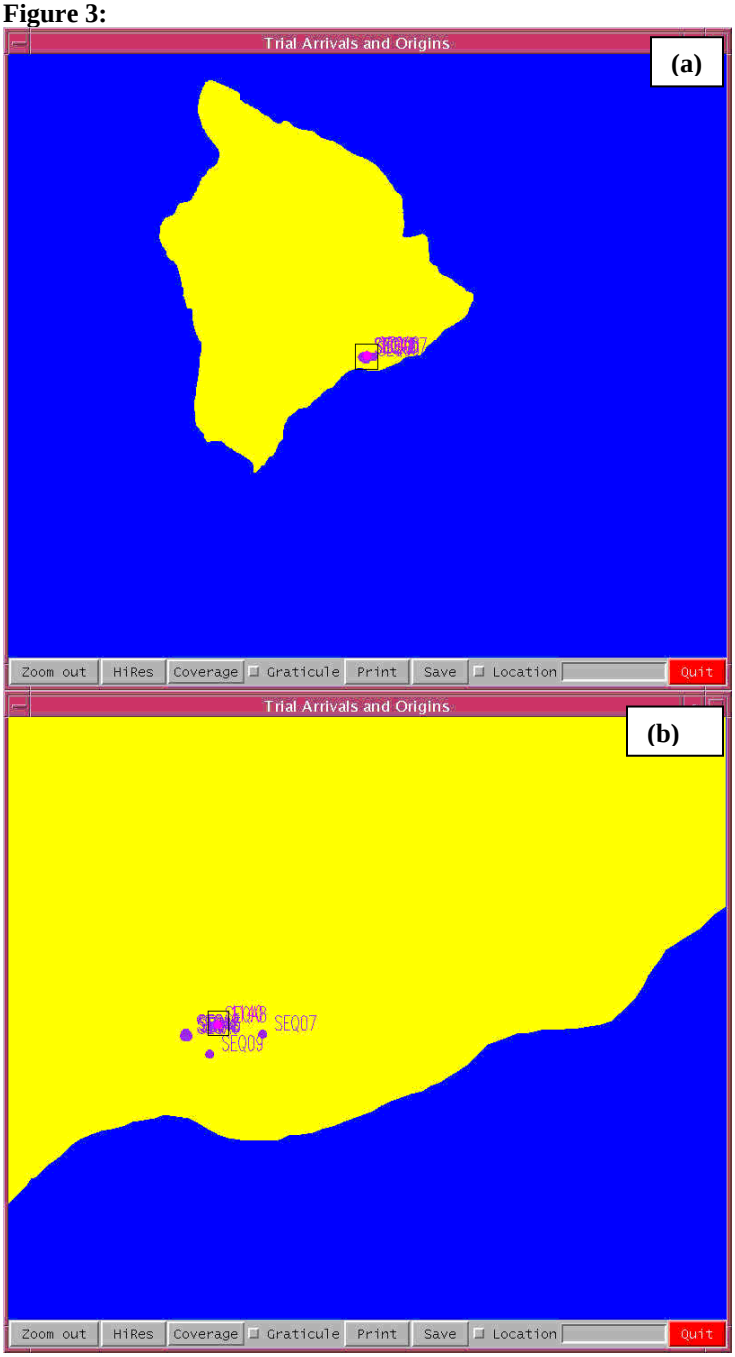

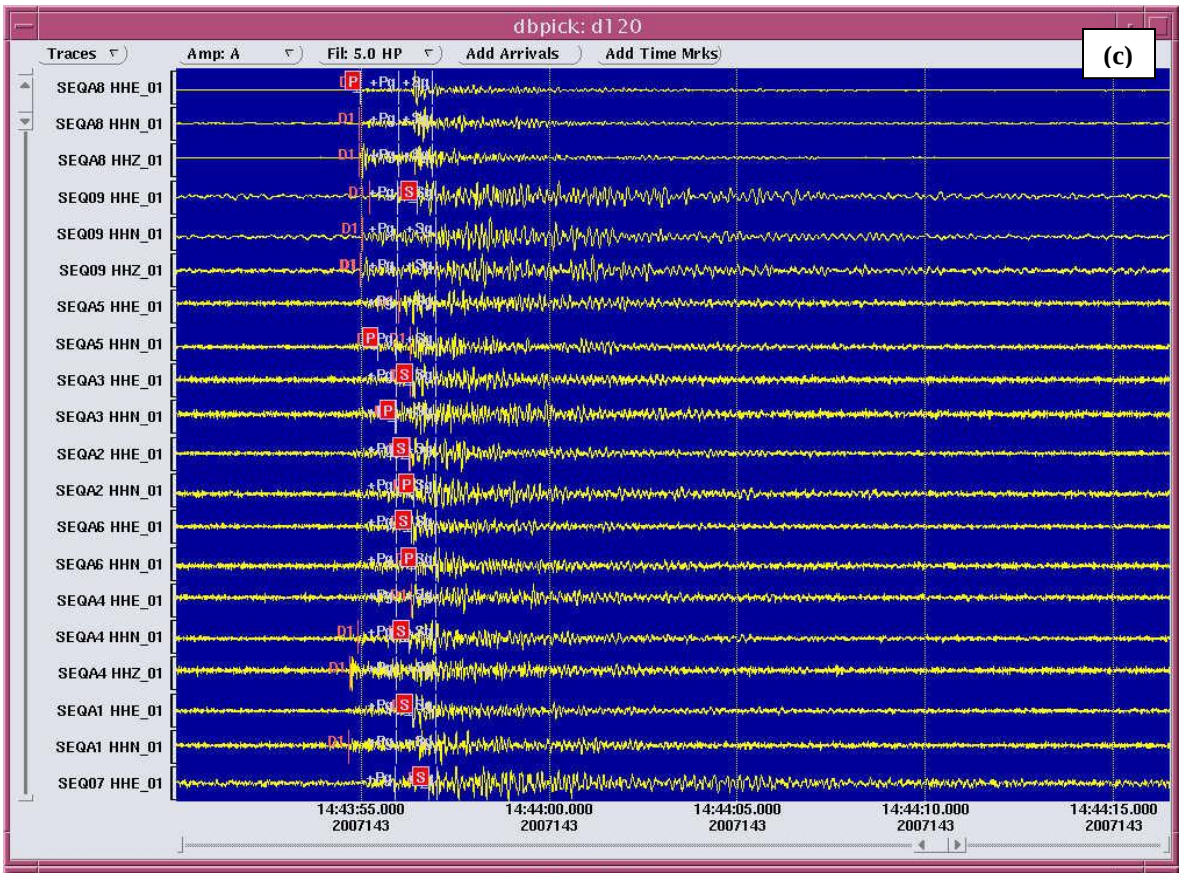
dbpick: d120
Traces
Amp: A
Fil: 5.0 HP
Add Arrivals
Add Time Mrks
(c)
SEQA8 HHE_01
SEQA8 HHN_01
SEQA8 HHZ_01
SEQ09 HHE_01
SEQ09 HHN_01
SEQ09 HHZ_01
SEQA5 HHE_01
SEQA5 HHN_01
SEQA3 HHE_01
SEQA3 HHN_01
SEQA2 HHE_01
SEQA2 HHN_01
SEQA6 HHE_01
SEQA6 HHN_01
SEQA4 HHE_01
SEQA4 HHN_01
SEQA4 HHZ_01
SEQA1 HHE_01
SEQA1 HHN_01
SEQ07 HHE_01
14:43:55.000
2007143
14:44:00.000
2007143
14:44:05.000
2007143
14:44:10.000
2007143
14:44:15.000
2007143

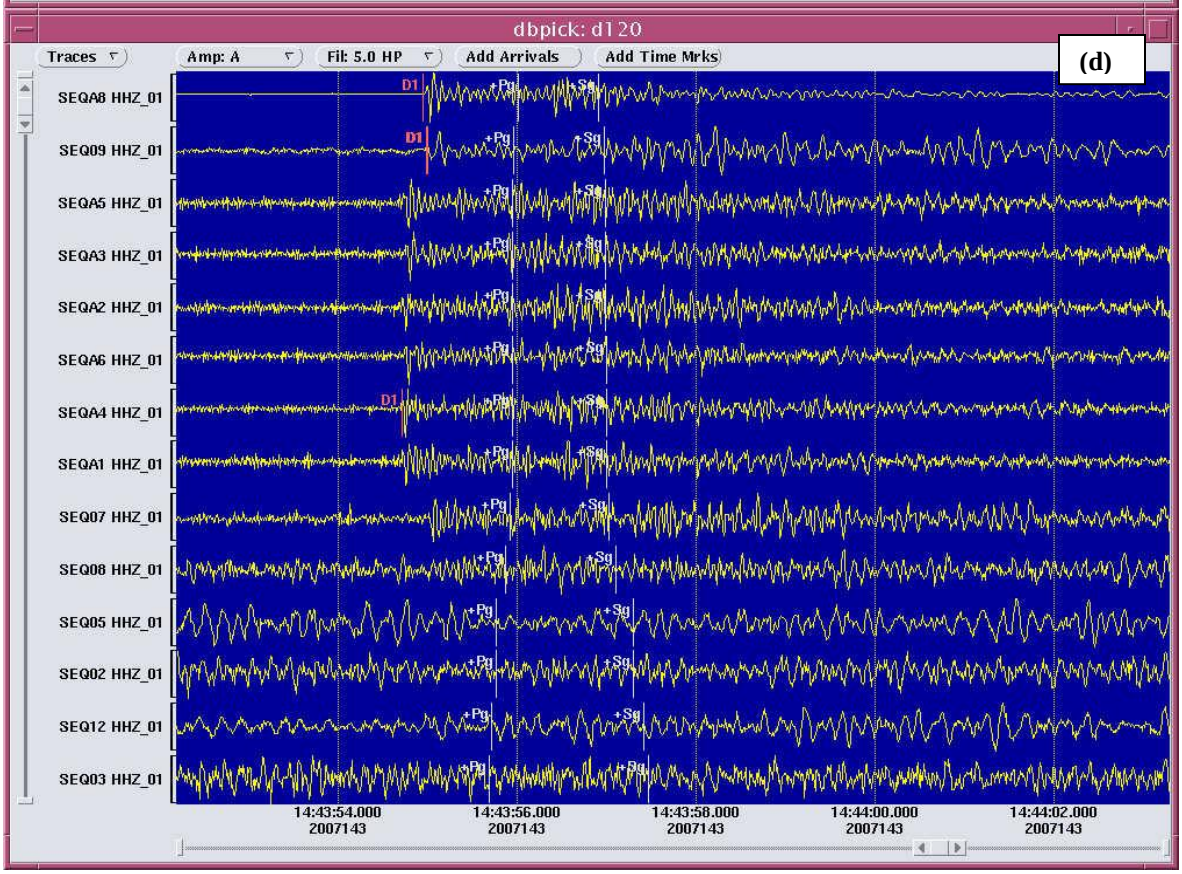
dbpick: d120
Traces
Amp: A
Fil: 5.0 HP
Add Arrivals
Add Time Mrks
(d)
SEQA8 HHZ_01
SEQ09 HHZ_01
SEQA5 HHZ_01
SEQA3 HHZ_01
SEQA2 HHZ_01
SEQA6 HHZ_01
SEQA4 HHZ_01
SEQA1 HHZ_01
SEQ07 HHZ_01
SEQ08 HHZ_01
SEQ05 HHZ_01
SEQ02 HHZ_01
SEQ12 HHZ_01
SEQ03 HHZ_01
14:43:54.000
2007143
14:43:56.000
2007143
14:43:58.000
2007143
14:44:00.000
2007143
14:44:02.000
2007143

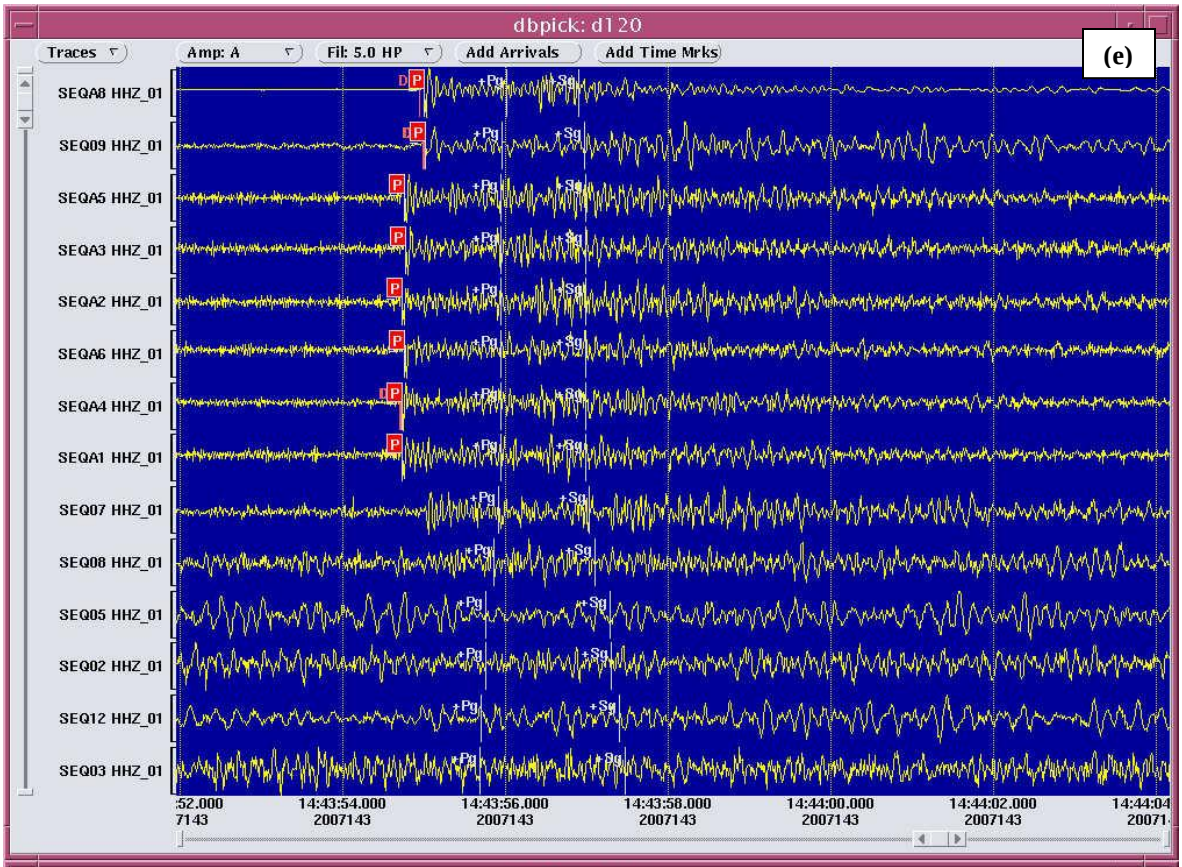
dbpick: d120
Traces
Amp: A
Fil: 5.0 HP
Add Arrivals
Add Time Mrks
(e)
SEQA8 HHZ_01
SEQ09 HHZ_01
SEQA5 HHZ_01
SEQA3 HHZ_01
SEQA2 HHZ_01
SEQA6 HHZ_01
SEQA4 HHZ_01
SEQA1 HHZ_01
SEQ07 HHZ_01
SEQ08 HHZ_01
SEQ05 HHZ_01
SEQ02 HHZ_01
SEQ12 HHZ_01
SEQ03 HHZ_01
14:43:54.000
14:43:56.000
14:43:58.000
14:44:00.000
14:44:02.000

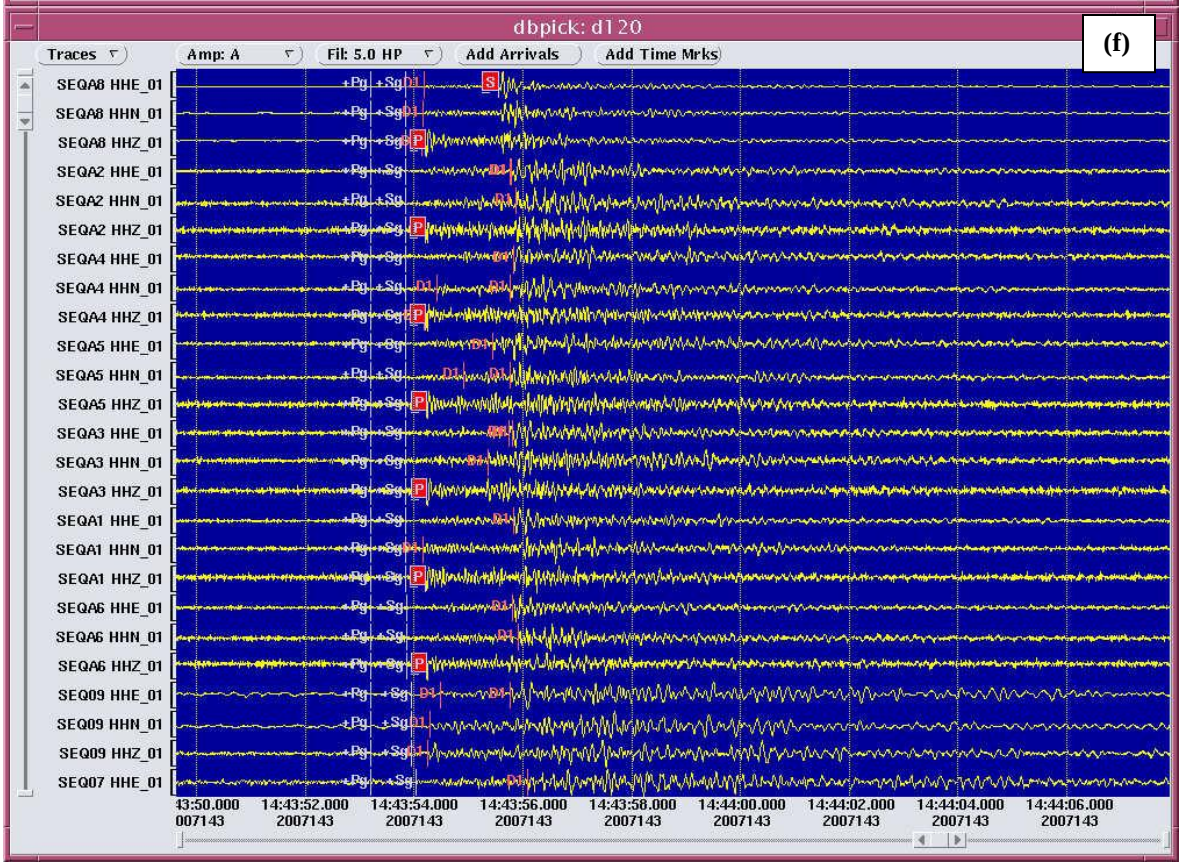
dbpick: d120
Traces
Amp: A
Fil: 5.0 HP
Add Arrivals
Add Time Mrks
(f)
SEQA8 HHE_01
SEQA8 HHN_01
SEQA8 HHZ_01
SEQA2 HHE_01
SEQA2 HHN_01
SEQA2 HHZ_01
SEQA4 HHE_01
SEQA4 HHN_01
SEQA4 HHZ_01
SEQA5 HHE_01
SEQA5 HHN_01
SEQA5 HHZ_01
SEQA3 HHE_01
SEQA3 HHN_01
SEQA3 HHZ_01
SEQA1 HHE_01
SEQA1 HHN_01
SEQA1 HHZ_01
SEQA6 HHE_01
SEQA6 HHN_01
SEQA6 HHZ_01
SEQ09 HHE_01
SEQ09 HHN_01
SEQ09 HHZ_01
SEQ07 HHE_01
14:43:52.000
14:43:54.000
14:43:56.000
14:43:58.000
14:44:00.000
14:44:02.000
14:44:04.000
14:44:06.000

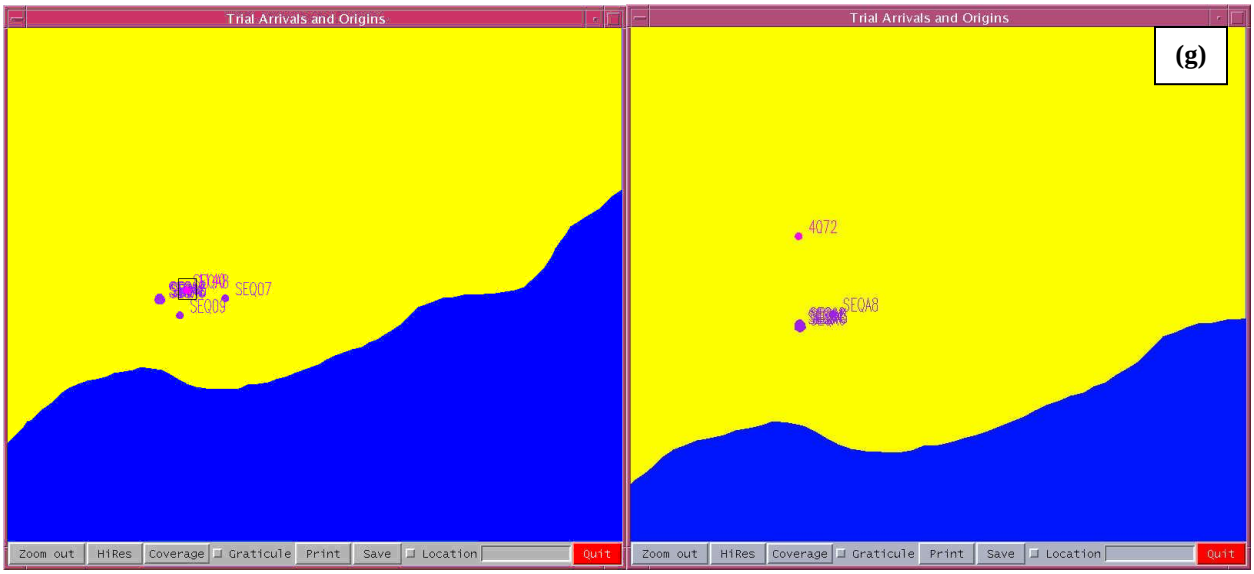

Figure 4: (a) Seismic network (stations labeled SEQ##) and detected earthquake (dot labeled 1140 within box) located on southern flank of Kilauea volcano. (b) close-up of seismic network and earthquake from figure (a). (c) Original waveform showing arrivals and detections located by Antelope Software. (d) Original waveform showing only signals originating on the z-axis. (e) Picks of P-waves on the z-axis waveforms. (f) Waveform showing arrivals as picked by end-user. (g) New, more accurate location of earthquake, renamed as event 4072 (right) and old location of earthquake (left).

RESULTS

Figures 4, 5, and 6 depict various stages of progress in locating microearthquakes. These plots all fall within the range of 19.20º-19.35º latitude and -155.35º – -155.05º longitude. The blue and yellow triangles represent the temporary seismic network set up to collect microearthquake data. Figure 4 depicts all of the earthquakes located into this range after sorting through 500 events. Figure 5 depicts earthquake locations after sorting through 1100 events, and Figure 6 depicts earthquake locations after sorting through all 1629 events in the data set.

Figure 4, which was generated after relocating 500 events, shows a cluster of earthquakes between 19.3º and 19.35º latitude. This cluster becomes more defined in Figures 5 and 6 as more events are located. Also becoming more distinct as more events are located is a cluster of earthquakes between -155.25º and -155.2º longitude, which extends southward from 19.35º to 19.27º latitude

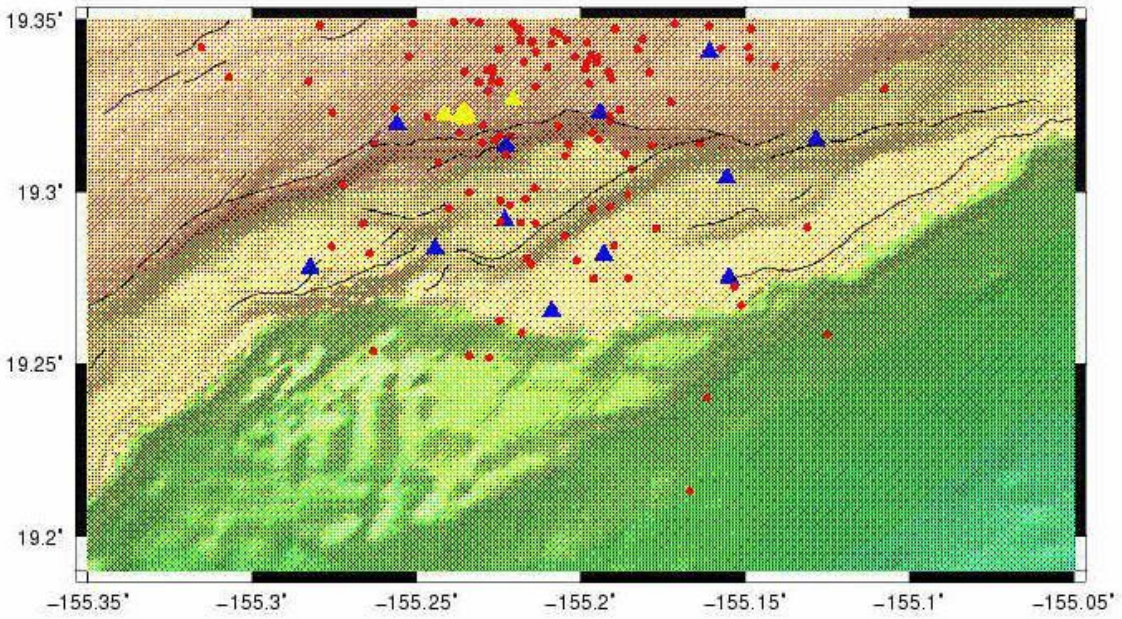

Figure 4: Earthquake epicenters after locating 500 microearthquake events.

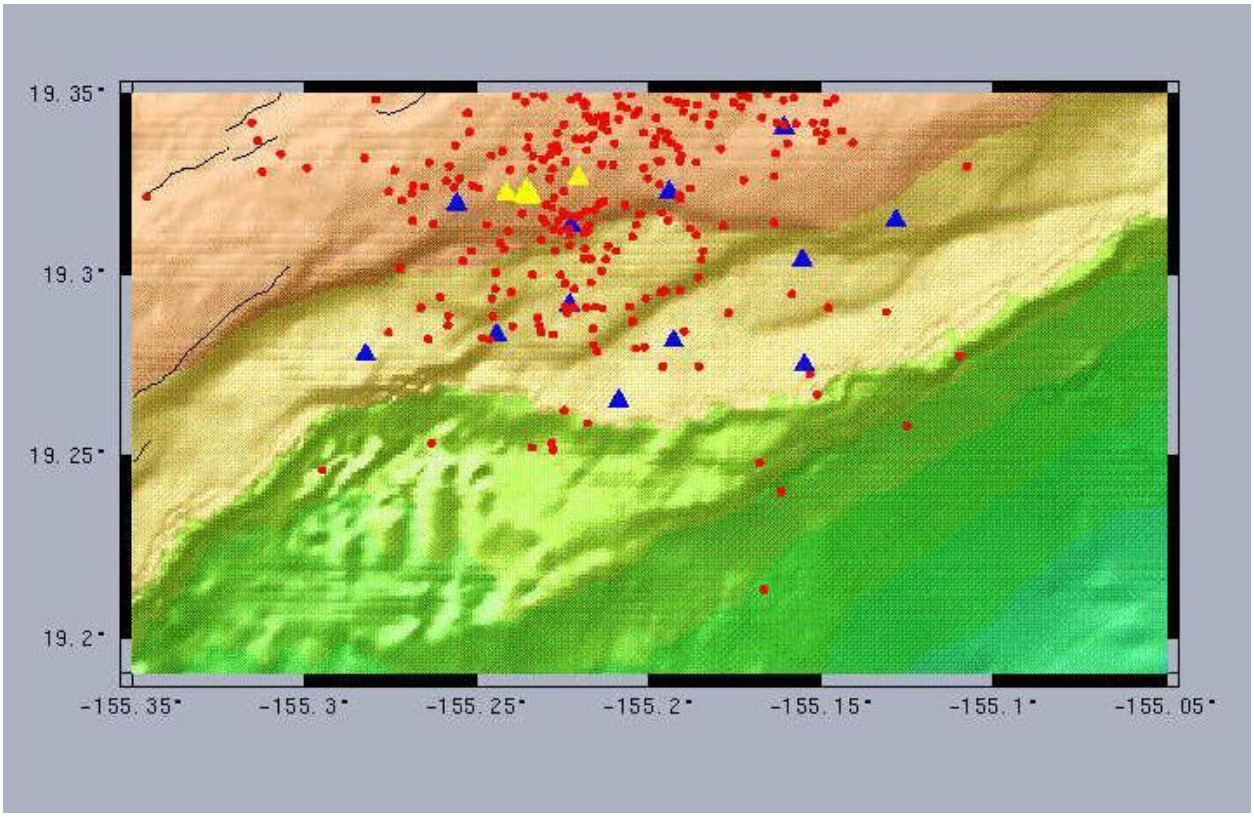

Figure 5: Earthquake epicenters after locating 1100 microearthquake events.

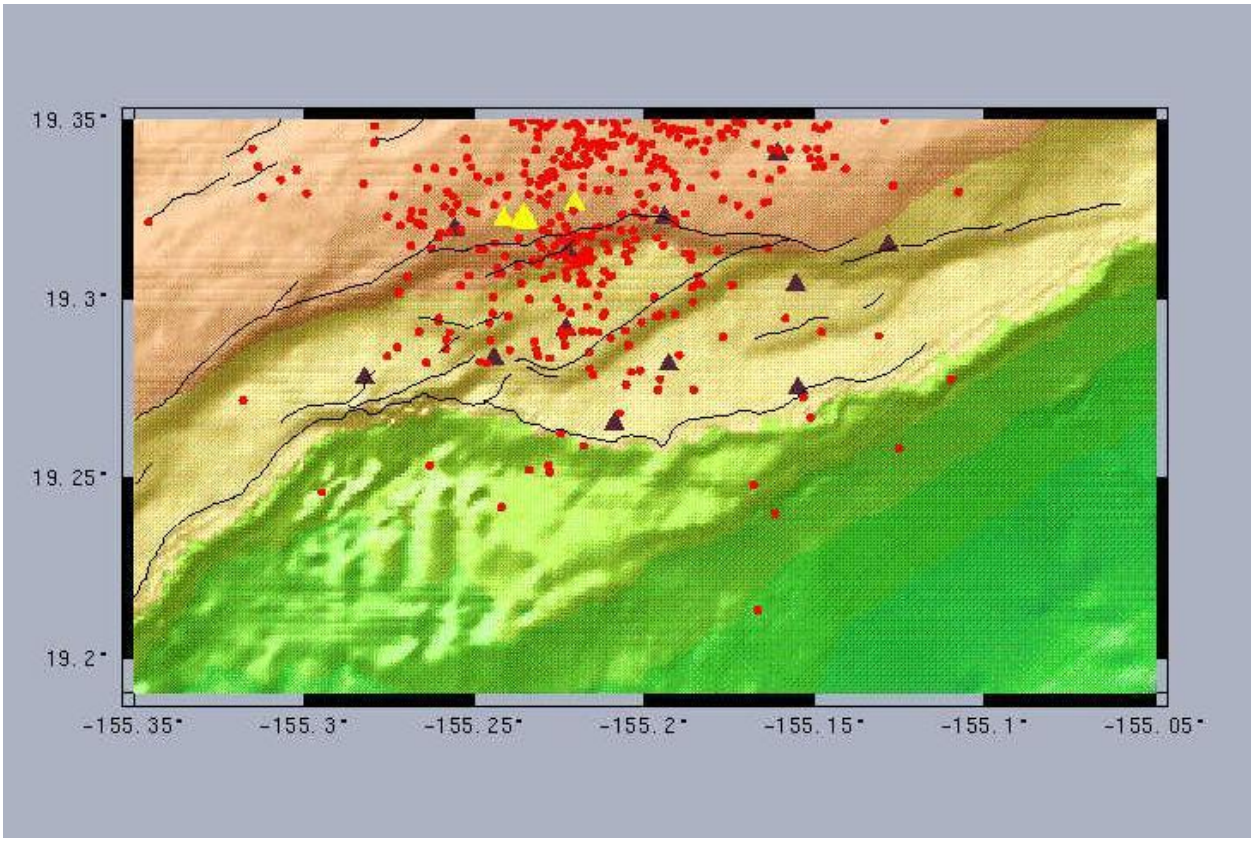

Figure 6: Earthquake epicenters after locating 1629 microearthquake events.

DISCUSSION

The earthquake clusters depicted in figure 6 may represent subsurface faults occurring either within the volcano flank or at the basal detachment. Due to the inherent imprecision of locating microearthquakes by hand, there is still error in the new locations. By relocating the microearthquakes using a cross-correlation relocation method the true depth of the microearthquakes can be determined. The depth at which these earthquakes occur will determine whether they are located within the volcano flank or at the basal detachment.

This data set represents the time period before the June 2007 slow earthquake, and in future studies will be compared to data sets from during and after the slow earthquake. The entire set of data will eventually be studied using waveform cross-correlation based relocation and double difference tomography. This relocation method will further constrain the locations of the earthquakes, and give high precision earthquake location. Such high precision relocation has yielded impressive results in other regions, including the discovery that microearthquakes in creeping faults actually concentrate in narrow streaks aligned with the same direction as fault slip (Rubin et al 1999).

The precise relocation of the microearthquake data obtained from the southern flank of Kilauea volcano should yield results that will improve our understanding of processes such as volcanic spreading and slow earthquakes. This knowledge is crucial to the Hawaiian Islands, off of which major tsunami-generating landslides have occurred (Morgan et al 2000). However, this information may also be extended beyond terrestrial applications to other planetary bodies with

volcanism. It is reasonable to believe that the Tharsis volcanoes on Mars follow similar behavior of volcanic spreading and slope slumping.

CONCLUSIONS

The Tharsis Montes on Mars are similar to the Hawaiian Islands, and therefore conclusions drawn from studying the growth characteristics of Hawaiian volcanoes can be applied to the Tharsis Montes. This Space Grant project lays a foundation for better understanding slow slip as a mechanism for volcanic spreading by analyzing earthquake data. The hand relocating of 1629 events which occurred prior to a magmatically triggered slow slip event on the southern flank of Kilauea volcano, Hawaii plays a crucial role in attempting to understand the complex behaviors of the basal detachment, volcanic spreading, and slow earthquakes. The relocated data which falls within 19.20º-19.35º latitude and -155.35º – -155.05º longitude distinctly shows two sets of clusters, which may indicate fault zones either within the southern flank of the volcano or along the basal detachment. Further analyses of this data set, which include using a waveform cross-correlation relocation method, will better constrain the locations of the micro-earthquakes. After comparing this data set with data from during and after the slow slip event, scientists will be able to visualize the deformation taking place within the flank of the volcano as the slow earthquake occurred. The same deformation process being studied on Kilauea volcano may also have occurred on the Tharsis Montes. However, because there are not presently any seismometers maintained on Mars, studying Kilauea volcano is one of the best ways to better understand the processes which may have helped formed the Tharsis Montes.

ACKNOWLEDGEMENTS

I would like to thank the Hawaii Space Grant Consortium for providing me with funding throughout the past year. I would also like to thank my mentor, Dr. Cecily Wolfe, who has given me support, encouragement, and plenty of research experience which will follow me for a lifetime. Mahalo!

REFERENCES

Brooks, B.A., Foster, J.H., Bevis, M., Frazer, L.N., Wolfe, C.J., and Behn, M. (2006) Periodic slow earthquakes on the flank of Kilauea volcano, Hawaii. *Earth and Planetary Science Letters* ***246***, 207-216.

Hartmann, W. K., M. Malin, A. McEven, M. Carr, L. Soderlom, P. Thomas, E. Danielson, P. James, J. Veverkas, Evidence for recent volcanism on Mars from crater counts, *Nature*, ***397***, 586-589, 1999.

Hartmann, W., G. Neukum, Cratering chronology and the evolution of Mars, *Space Sci. Rev.*, ***96***, 165-*194*, 2001.

Houston, H. and Vidale, J. E. (2007) Earthquakes: Relationships in a slow slip. *Nature* ***447***, 49-50.

McBride, N., and I. Gilmour, An Introduction to the Solar System, Cambridge University Press, Cambridge, UK, 2003.

McGovern, P. J., and J. K. Morgan, Volcano spreading and lateral variations in the structure of Olympus Mons, Mars, *Geology*, in press, 2008.

McGovern, P. J., and S. C. Solomon, State of stress, faulting, and eruption characteristics of large volcanoes on Mars, *J. Geophys. Res.*, ***98***, 23,553-23,579, 1993.

Morgan, J.K., Moore, G.F., Hills, D.J., Leslie, S. (2000) Overthrusting and sediment accretion along Kilauea's mobile south flank, Hawaii: evidence for volcanic spreading from marine seismic reflection data. Geology 28, 667–670

Obara, K., H. Hirose, F. Yamamizu, and K. Kasahara (2004), Episodic slow slip events accompanied by non-volcanic tremors in southwest Japan subduction zone, *Geophys. Res. Lett.*, 31, L23602, doi:10.1029/2004GL020848.

Rubin, A.M., Gillard, D., and Got, JL. (1999) Streaks of microearthquakes along creeping faults. *Nature* ***400***, 635-641.

Rubinstein, J.L., Vidale, J.E., Gomberg, J., Bodin, P., Creager, K.C., and Malone, S.D. (2007) Non-volcanic tremor driven by large transient shear stresses. *Nature* ***448***, 579-582.

Solomon, S. C., *et al*., New perspectives on ancient Mars, *Science*, ***307***, 1214-1220, 2005.

THE MAPPING OF VEGETATION ABUNDANCE, DIVERSITY AND HEALTH IN A HAWAIIAN LOCALE USING REMOTE SENSING

Whitney Renee Reyes
Botany Department
University of Hawai‘i at Mānoa
Honolulu, HI 96822

ABSTRACT

Monitoring vegetation is critical to maintaining the health of native Hawaiian ecosystems. Over two semesters (Fall 2008 and Spring 2009), my research explored ways in which remote sensing can assist in monitoring invasive vegetation in Hawai‘i. The goal during the first semester was to explore remote sensing techniques for mapping invasive vegetation on the island of Oahu. Specifically, I analyzed the techniques of maximum likelihood supervised classification and linear spectral un-mixing using ENVI software. The focus was to create abundance and diversity maps of one site on Oahu and then determine their accuracy. Neither the supervised classification nor linear spectral un-mixing produced results that proved reliable when taken out to the field. For this reason, neither program was used for analyzing health monitoring possibilities.

The goal of the second semester was to explore vegetation health monitoring techniques using remote sensing. The focus was to analyze the spectra of plants under stressful conditions and the possibilities of using remote sensing to monitor the health of an area. The t echnique used for monitoring health consisted of calculating a Normalized Difference Vegetation Index (NDVI). For analyzing the possibilities of monitoring vegetation health, a six-year NDVI time series was compared to precipitation data to analyze the correlation between the two and how it differs at each site. Should any regular monitoring be used with this method a base NDVI would be critical as each site possesses unique characteristics.

INTRODUCTION

In the Hawaiian Islands, $4 million is spent annually on the monitoring and eradication of invasive species (DLNR, 2009). If more efficient methods were developed for monitoring, then more time and money could be spent on the physical (mechanical) eradication process. Remote sensing is a monitoring tool that is potentially very efficient. This is how the original motivation for this project was generated. Large changes in the distribution, abundance or health of vegetation in an area can indicate that there is a disruption or change in that area. Factors that can disrupt vegetation include precipitation changes, the introduction of a new invasive pest or plant along with a variety of other possibilities. In the Hawaiian Islands, native species are especially sensitive to changes in the surrounding environment. Over the course of two semesters this project has analyzed the effectiveness of remote sensing to monitor changes of vegetation on the island of Oahu.

The goal of the first semester of this project was to explore the effectiveness of mapping abundance, diversity and health of vegetation at a single location using hyper-spectral remote sensing. The hypothesis tested was that each plant species at the site would have a unique spectrum that would allow it to be mapped and its growth tracked. The techniques used in

mapping were a maximum likelihood supervised classification and a linear spectral un-mixing program in ENVI. The objectives to be completed were the selection of a study site, generation of a spectral library, spectral un-mixing and then an evaluation of the maps created in the un-mixing process.

In contrast, the goal of the second semester was to explore the ability to monitor vegetation health on the island of Oahu using remote sensing. If the spectrum of a stressed species is known, then by applying this to a remote sensing image it should be possible to map the stressed areas of an island. This technique would require the vegetation on the island to be known in detail, however using a different method could possibly be more effective and not require a detailed knowledge of the vegetation in the area. The techniques used to analyze vegetation health were a Normalized Difference Vegetation Index (NDVI) and stress tests. The objectives to be completed were to analyze the effect stress has on a plant's reflectance and to investigate remote sensing for drought and stress monitoring by calculating and analyzing NDVI.

This project helps to fulfill NASA's goal 3.A.3 which is "Progress in quantifying global land cover change and marine productivity and in improving the carbon cycle and fresh water availability," by analyzing techniques for mapping vegetation changes in the Hawaiian Islands.

METHODS

To address the first objective, a site along the Ka Iwi Coast of Oahu was chosen for study (figure 2, point 9). This site was chosen because of its ease of access, easily classifiable ground cover types, large stands of vegetation, and availability of high spatial and spectral resolution remote sensing data. Vegetation types at the site were determined during field visits and by analyzing high resolution IKONOS data. From IKONOS data it was possible to perform a maximum likelihood supervised classification using ENVI image analysis software.

To use a maximum likelihood supervised classification technique, a region of interest is created that contains a known type of ground cover. When the user has created regions for each type of ground cover in the study area, these can then be made into "rules" which are applied to the remotely sensed image. ENVI then classifies the rest of the pixels based on these "rules". The map produced using this technique may then be analyzed for ground accuracy. In theory, supervised classification is capable of producing an overall vegetation type map of an area. However, in reality pixels may span large areas and are often composed of multiple ground types ("mixed pixels"). This may result in vegetation types being misclassified as the wrong species. Because supervised classification is not able to account for mixed pixels in an image, a different technique may be necessary especially when the ground cover distribution lends itself to a high percentage of mixed pixels.

An initial field visit was conducted to the Ka Iwi Coast on September 28, 2008 to determine if the site was acceptable. Data were collected during field visits on October 16, 2008 and January 20, 2009, and a field spectrometer was used to identify the spectral reflectance of each species at the site. The spectrometer used was an Analytical Spectral Device FieldSpec Pro. Each spectrum was collected using a leaf clip or a raw fiber optic cable for non-vegetation samples. A spectral library was created to maintain reflectance data collected from representative plants within the study area. Once the spectral library was created it was applied to an AVIRIS image generated April 2002. The linear spectral un-mixing program in ENVI applies the reflectance of each species to a hyper-spectral image and attempts to calculate the proportions of each of the ground cover to best fit the spectrum of each unknown pixel. The result of the un-

mixing program is a multi-banded image where each band represents a ground cover or vegetation type. An example of these maps is shown in figure 4. Each band shows the fractional abundances of ground cover in each pixel of the scene. This species representative band can then be analyzed for accuracy.

From multiple field visits it became obvious that reflectance is directly altered by the health or "greenness" of the vegetation. In these field visits there were species that seemed to have a significant amount of reflectance variation each time whereas other species had a consistent reflectance regardless of the changes in weather conditions. To determine precisely how spectral reflectance is altered by changes in precipitation, a stress test was designed using precipitation as the stressor. These tests were performed because moisture is likely to be the most important environmental factor and because this stress factor could be readily mimicked in a laboratory setting. To run this experiment, two species of grasses were chosen and transplanted from the Ka Iwi site into six inch round pots using standard potting soil. The two chosen species were Bermuda grass (*Cyndon dactylon*) and Buffel grass (*Cenchrus ciliaris*). These two grasses were chosen because they seemed highly responsive to changes in precipitation during field visits and they are also found on various locations on the island of Oahu. Two Bermuda grass and four Buffel grass samples were transplanted and when both groups had become well established, one Bermuda grass plant and two Buffel grass plants were taken to a different location and they stopped receiving water. The spectra of both groups were taken weekly over the course of three weeks to monitor any changes in the control group and/or in the experimental plants experiencing the "drought". A plot could then be created to show the spectrum at the different stages in health shown in figures 7 and 8.

A Normalized Difference Vegetation Index (NDVI) is calculated using the reflectance of the red (0.6-0.7 μm) and the near infrared (0.7-1.1 μm) bands. It is calculated by dividing the difference of the red and near infrared responses by the sum of these two bands. This method has been used regularly since 1989 by the United States Forest Service and other organizations to monitor the relative vigor or "greenness" of an area. The United States Geological Survey (USGS, 2005) monitors the continental United States and Alaska, but not Hawaii. This project seeks to analyze its effectiveness specifically for the island of Oahu.

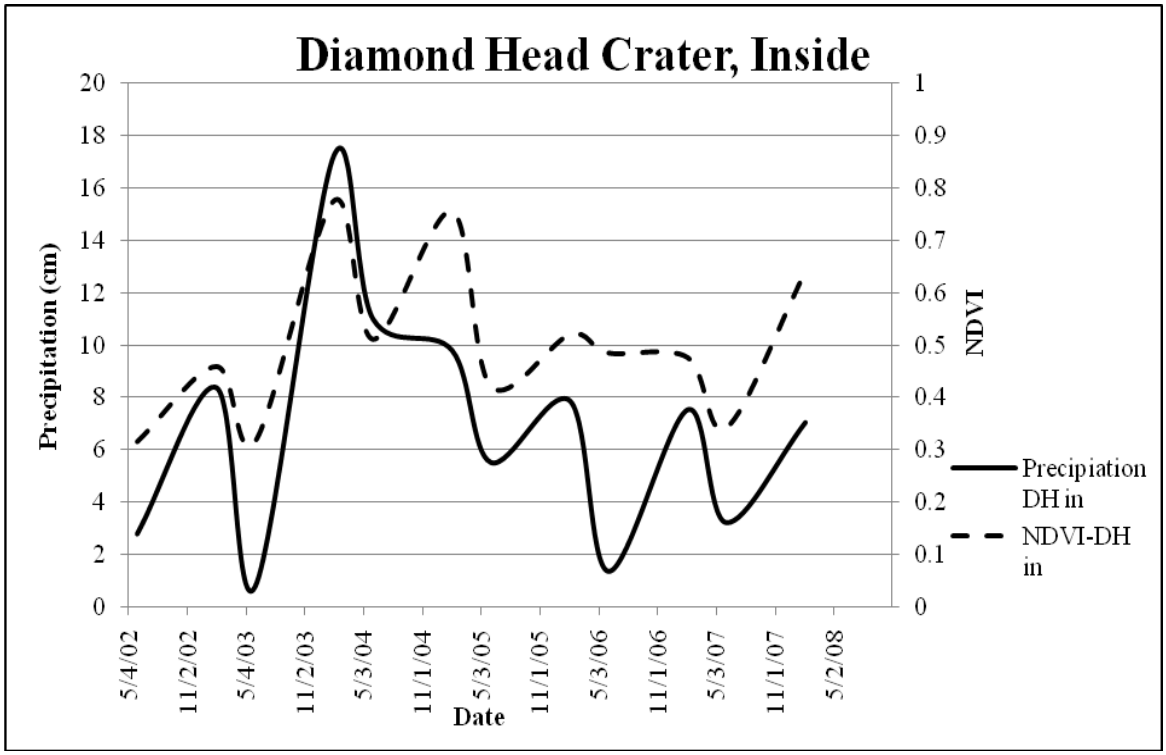

Figure 1: NDVI and precipitation time series at the Diamond Head site.

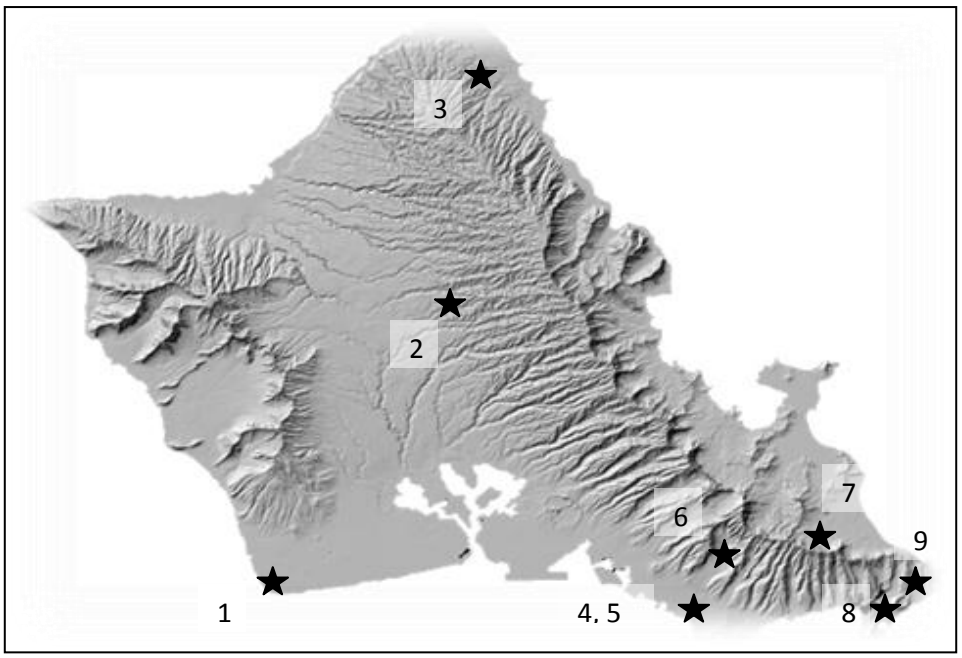

Figure 2: Study sites on Oahu. 1: Barber's Point, 2: Wahiawa, 3: Kawela Bay, 4, 5: Diamond Head Crater (inside and outside), 6: Manoa Valley, 7: Waimanalo, 8: Kokohead Crater, 9: Ka Iwi coast.

The method used for analysis of the effect of precipitation on vegetation was to calculate NDVI for both the wettest and driest seasons of each year from 2002 to 2008 and then compare that to the seasonal precipitation averages for the corresponding time period. For this task, MODIS AQUA data were acquired from NASA (from **www.wist.echo.gov**) for the months of December, January, February, June, July and August from 2002 to 2008. MODIS data are taken every 16 days at 250 meter resolution. Thus, there were, on average, 2 NDVI values per month. Each 16 day scene was layered in ENVI to create a time layer and the calculated NDVI could then show the values for each pixel in scene. Using the region of interest this was applied to nine different sites (figure 2).

The values for each site were averaged to produce a mean NDVI value for each month. These values were then averaged for each season to produce a seasonally averaged NDVI at each location. Average monthly precipitation data were acquired from the National Climate Data Center website (http://www.ncdc.noaa.gov). These average monthly data were again averaged to produce an average precipitation per season. The two seasonal averages were then plotted on an x-y graph with a double y axis. This graph is shown for the Diamond Head Crater site in figure 1.

It was then possible to look at these graphs for each of the nine sites and analyze the trends that occur at each site. This would be necessary if a monitoring system were being considered.

There were nine sites chosen on the island of Oahu (figure 2). The selected sites were chosen because they fit the two criteria of having precipitation data that were consistent over the six year time period and also the variability of the location based on the other sites. Having different representative vegetation types was very important. It was necessary to know how different types of vegetation would respond to changes in the environment, specifically precipitation. Each was graphed on a plot with its NDVI time series versus its precipitation time series.

Table 1. Geographic and Vegetative Information of Study Sites

Site Name	Site # in figure 1	Latitude and Longitude	Approximate Elevation	Dominant Vegetation Type
Barber's Point	1	21 18'50.14'' N. 158 1'59.70'' W.	3 meters	Dry grasses and shrubs
Wahiawa	2	21 29' 38.84'' N. 158 59' 07.05" W.	315 meters	Trees and bushes
Kawela Bay	3	21 42'14.69'' N. 157 58'28.19'' W.	6 meters	Shrubs and dry grasses.
Diamond Head (outside)	4	21 15' 37.04'' N. 157 48' 47.06'' W.	60 meters	Dry grasses and Haole Koa.
Diamond Head (inside)	5	21 15'42.38'' N. 157 48'47.06 W.	60 meters	Trees, bushes, green grasses.
Manoa Valley	6	21 19' 58.65'' N. 157 48' 02.05'' W.	113 meters	Lush, green jungle, tall trees.
Waimanalo	7	21 20' 20.49'' N. 157 45' 38.46'' W.	3 meters	Haole Koa and grasses
Kokohead	8	21 17' 10.89'' N. 157 40' 49.40'' W.	88 meters	Grasses.
Ka Iwi Coast	9	21 18'0.29''N. 157 39'27.55''W.	3 meters	Haole Koa, Grasses.

RESULTS AND DISCUSSION

Maximum Likelihood Supervised Classification

The maximum likelihood supervised classification technique in ENVI created vegetation maps using one meter IKONOS data. The maps were made using the criteria of five major land cover types at the selected site along the Ka Iwi coastline. Although the results were reasonably accurate, the classification of features like roads and the ocean caused mixing of pixel classifications. The results of a supervised classification are shown in figure 3.

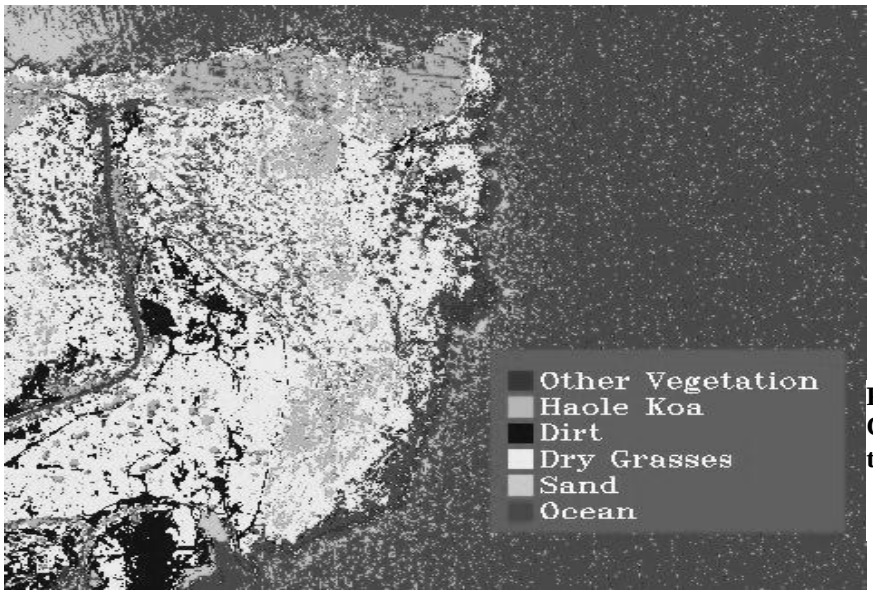

Figure 3: Supervised Classification map of the Ka Iwi site.

Linear Spectral Un-mixing

The spectral library that was created from spectra taken at the Ka Iwi site was applied to an atmospherically corrected 20 meter AVIRIS image. The AVIRIS image acquired was from April 19th of 2002. When a linear spectral un-mixing method was applied to this image in ENVI using the spectral library the results were not as anticipated. Although some species were being correctly identified there were still major discrepancies in both the types of vegetation and their distribution using this method. For example, there were negative abundances being assigned and there was no Haole Koa (*Leucaena leucocephala*) being assigned at the site, where Haole Koa is abundant.

A. 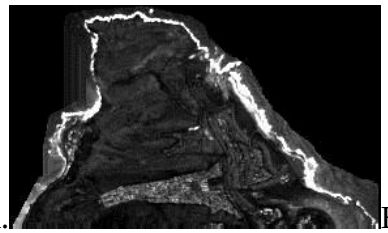 B. 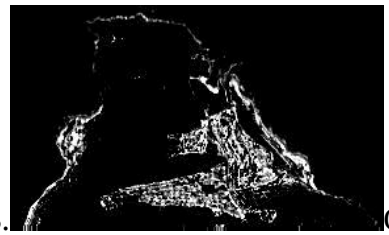 C. 

Figure 4: An example of the abundance maps that are produced in the linear spectral un-mixing program. Each pixel has an assigned value for the fractional abundance of each species found there. A: RMS error, B: Naupaka (*Scaevola taccada*)**, C: Mangrove** (*Rhizophora mangle*)**.**

In figure 4 it can be seen that both the residential and the shoreline break cause some pixel identification confusion. In figure 4A the amount of error per pixel is shown in white. In figure 4B the Naupaka (*Scaevola taccada*) presence is not accurate, the image shows Naupaka along the coastline and in the residential area, but little in the top of image where the site was located. When taken to the site, this map was not an accurate representation of the Naupaka found there. In image 4C there is no Mangrove (*Rhizophora mangle*) shown at the site, but rather in places where it is known from field work not to be found at all. The un-mixing was not able to detect any significant Haole Koa in the study area, which is contrary to the fact that it is a principal component of the vegetation in the area.

These discrepancies were unexpected and created a significant obstacle to mapping the abundance and diversity of vegetation in the area. One of the possible reasons for this discrepancy was that the AVIRIS image had been taken in spring when the area was greener than when the field spectra had been collected in the fall months. After re-collecting field spectra in early February a new spectral library was created and reapplied to the AVIRIS image. However, the results showed little difference from the first dataset analyzed. In the beginning of this project it was proposed that each species would have a unique spectral signal, but this is not true. When the spectral reflectance of Haole Koa (*Leucaena leucocephala*), Mangrove (*Rhizophora mangle*) and Naupaka (*Scaevola taccada*) were analyzed, they were all very similar, so they could not be distinguished from each other by the linear spectral un-mixing program. This led to a result that did not show accurate fractional abundances and occurrences of any of these three species.

Normalized Difference Vegetation Index

Therefore, at the second semester the focus changed to mapping the health changes on the island of Oahu using a different technique. Instead of using a linear spectral un-mixing technique to map changes in health, a normalized difference vegetation index (NDVI) was calculated over a period of six years and then compared with precipitation data over the same

time period to analyze the changes in "greenness". The hypothesis being that plant vigor is directly related to the amount of precipitation that an area receives. The NDVI versus precipitation graphs show a noticeable correlation of the NDVI curves following the rise and fall in precipitation. Different locations showed different levels of NDVI response. The analysis then focused further on what different vegetation and ground types were found at each of the different sites and if or how these would affect NDVI. The sites that appeared to have less trees and more grasses and small bushes seemed to be more responsive to changes in precipitation. Areas that have a heavy cover of vegetation are more likely to show low amounts of NDVI response to changes in the levels of precipitation.

Figure 5 shows that NDVI for Manoa valley is not highly dependent upon precipitation. This is assumed to be because it is such a lush area that the "greenness" does not change noticeably with changes in precipitation. The precipitation levels at the site are relatively high so perhaps if this level is maintained than the NDVI is essentially level. The slight lowering in NDVI in this graph is most likely from another cause. The R^2 value is very low in this analysis, indicating that the correlation of plant vigor and precipitation is low for the site.

Figure 6 shows that NDVI for the Ka Iwi coastline increases as precipitation increases. This is likely due to the fact that the vegetation consists primarily of dry grasses that respond quickly to any change in precipitation. In this graph the R^2 value is much higher indicating that this site's plant vigor is highly related to the level of precipitation that the area receives.

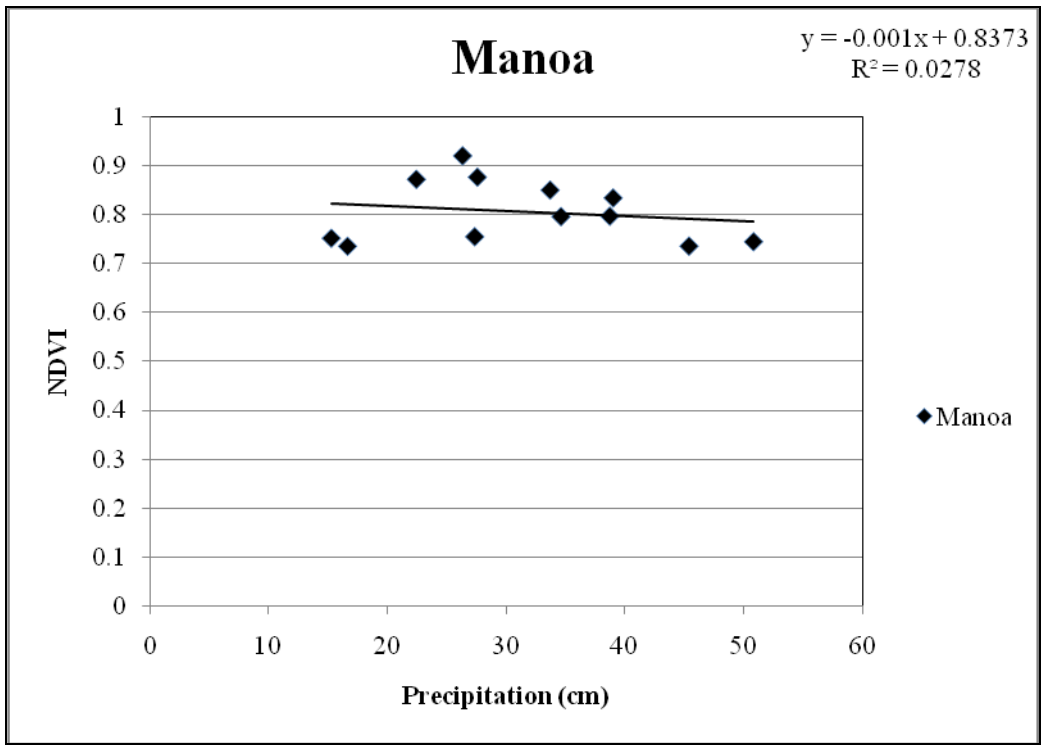

Figure 5: Relationship between Normalized Difference Vegetation Index (NDVI) and monthly precipitation for the Manoa Valley site. Each point represents a bi-yearly average taken over a six period.

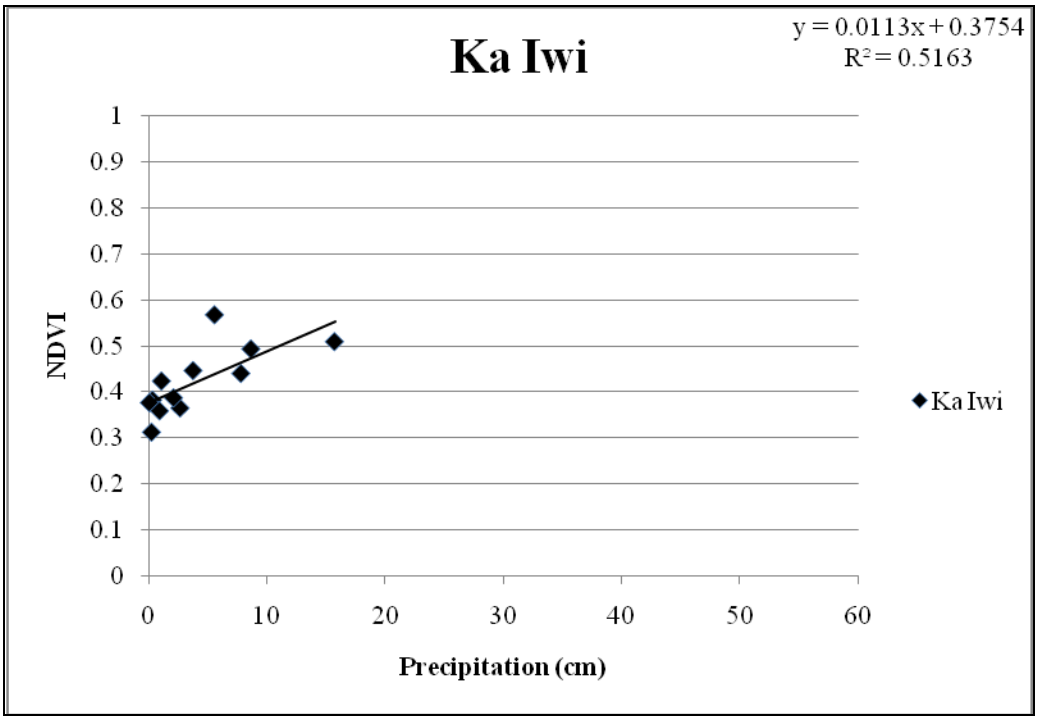

Figure 6: Relationship between Normalized Difference Vegetation Index (NDVI) and monthly precipitation at the Ka Iwi site. Each point represents a bi-yearly average taken over a six period.

Each chosen site has a minimum and maximum monthly precipitation and NDVI values. It is possible that if there is a maximum amount of precipitation than there is also a maximum NDVI value which essentially flat lines after a level of precipitation has been reached.

Stress Tests

In order to better understand the way that a plant's reflectance is altered by changing health, stress tests were designed using precipitation as a stressor. The series of stress tests made it possible to look at how a plant's reflectance spectrum changes as the health of the plant declines. Graphs were made to represent both *Cenchrus ciliaris* and *Cyndon dactylon.* Figure 7 and 8 show the three spectra samples taken during 3 consecutive weeks of water deprivation for the *Cenchrus ciliaris* and the *Cyndon dactylon* samples.

For calculating "greenness" as an indicator of plant health the near infrared (840nm) and red (640nm) wavelengths are used in the NDVI calculation. In this graph there is a drop in reflectance as the weeks progressed and the health declined. At the two wavelengths for the calculation of NDVI there is a trough at 640 nm that flattens over time and at 840 nm the reflectance gradually decreases with health. Using this information it is then possible to examine areas with a high population of *Cenchrus ciliaris* and the reflectance of the area remotely and determine the approximate health of the area. If there were a severe drop in the reflectance of the area it would give a cause for concern.

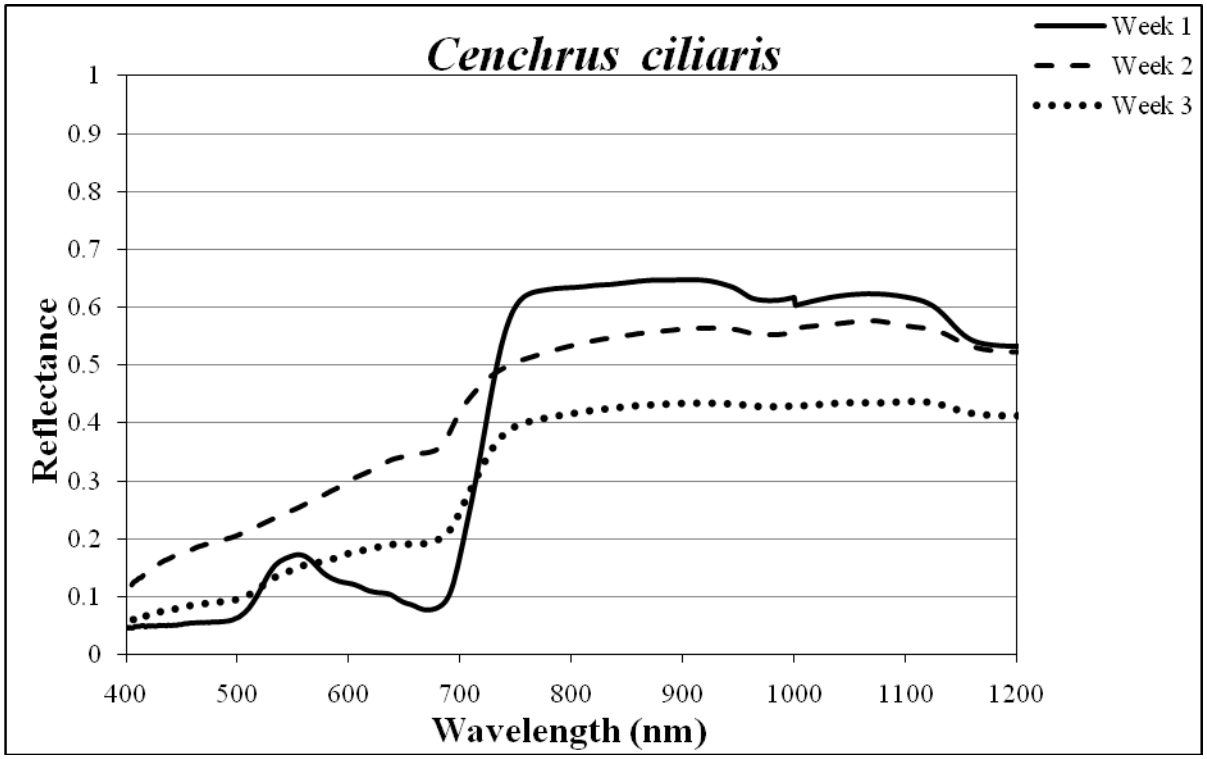

Figure 7: Stress test results for *Cenchrus ciliaris* deprived of water over three weeks. There is a green peak (high at 550, low at 670nm) when healthy, but this flattens out as the sample becomes yellow (week2) and then brown (week 3) as the plant dies.

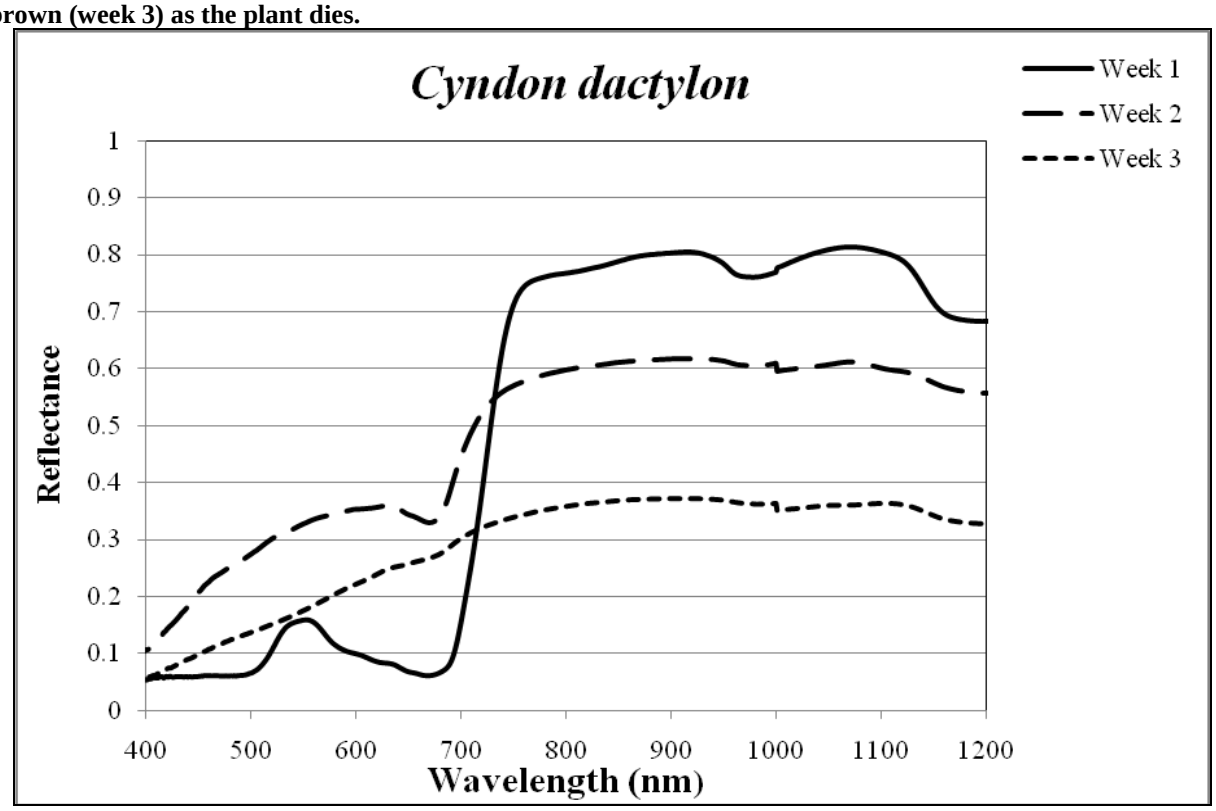

Figure 8: The stress test results from the *Cyndon dactylon* sample deprived of water over three weeks. There is a green peak (high at 550, low at 670nm) when healthy, but this flattens out as the sample becomes yellow (week2) and then brown (week 3) as the plant dies.

Challenges

There were several problems encountered in the course of this project. In the fall portion of the project the maximum likelihood supervised classification and linear spectral un-mixing program in ENVI did not correctly identify the plants at the study site. This created a large issue in making abundance and diversity maps that were accurate to the species present.

In the spring term the problem arose when the linear spectral un-mixing model would not work for a vegetation health monitoring system. There was then a need to find a system that would work at different resolutions.

CONCLUSION

During the fall of 2008 this project analyzed the effectiveness of a maximum likelihood supervised classification and linear spectral un-mixing program to map vegetation at a site on the island of Oahu. In the spring of 2009 this project used a normalized difference vegetation index to map changes in "greenness" of nine different sites on Oahu and analyzed two grass species response to changes in precipitation.

For the purposes of mapping the abundance and diversity of vegetation in an area the linear spectral un-mixing program in ENVI is not the most effective technique for the location. This was due to the similarities in the spectra of some plants. In this situation the supervised classification technique was just as accurate as the linear spectral un-mixing model. The only problem being that to determine which species are being misclassified the area needs to be "ground-truthed".

Therefore in the case of monitoring the health of plants in an area the Normalized Difference Vegetation Index (NDVI) was more accurate than the linear spectral un-mixing technique. Although this hinders the ability to pick out the individual groups or stands of vegetation to monitor one species, it works on the area as a whole. The Normalized Difference Vegetation Index is a wonderful way to look at how different areas respond to changes like precipitation. This is critical information because one value can not be set as being a healthy or not healthy situation for the island as a whole. It is highly dependent upon the location because each area is so unique. Especially on the island of Oahu, areas that are in close in proximity can still respond very differently. In the case of Manoa valley and other areas with very high amounts of precipitation and vegetation NDVI monitoring is less effective due to the amount of change that would have to be present for it to deviate from the average. For the Hawaiian islands a NDVI monitoring method might be well suited for some areas but not for others.

ACKNOWLEDGEMENTS

I would like to thank The Hawaii Space Grant Consortium for the wonderful opportunity and great experiences.

I would like to give special thanks to my mentors Harold Garbeil and Barbara Bruno. Harold's constant assistance and guidance always motivated me when I felt stuck. Barbara always gave motivation, great inspiration and new ideas. I will forever remember the help and advice that I have received from them both.

I would like to thank Barbara Gibson for the use of her spectrometer, without which the project could not have happened. A special thank you to Eric Pilger, who helped with all my technical problems. Thank you to Robert Peck who assisted in the editing process.

REFERENCES

Department of Land and Natural Resources (DLNR) (2009). Notes from meeting of the Board of Natural Resources. (March 13, 2009) http://hawaii.gov/dlnr/chair/meeting/submittals/090313/C-FW-Submittals-C1.pdf

United States Geological Survey (USGS)(2005). Advanced Very High Resolution Radiometer Normalized Difference Vegetation Index Composites. (Fact Sheet 2005-3114, November 2005). http://pubs.er.usgs.gov/djvu/FS/2005_3114.pdf

Used to identify invasive grasses:
Hawaii Ecosystems at Risk Project (HEAR), (2009). Plants of Hawaii, (http://hear.org/starr/plants/)

Remote Sensing and Precipitation Data downloaded from:
NOAA Satellite Archive: http://www.ncdc.noaa.gov
NASA Archives: http://www.wist.echo.gov

KUMU A‘O CUBESAT TELECOMMUNICATION SUBSYSTEM: ANTENNA DESIGN, TESTING, AND MOUNTING

Amy C. Blas
Department of Electrical Engineering
University of Hawai‘i at Mānoa
Honolulu, HI 96822

ABSTRACT

The antenna of the Kumu A‘o satellite is a vital part of the telecommunications design. The correct antenna will make the sending and receiving of signals easy and efficient. Designing, testing, and mounting the antenna is a challenge due to many of restrictions and requirements. The antenna design was implemented using electromagnetic equations to find the wavelength. The testing of the antenna was done in two ways using Electromagnetic CAD software such as HFSS and a network analyzer. The results were to find the SNR and VSWR of the antenna. The mounting system proved to be the most challenging part of the antenna due to the small space allowed within the CubeSat. The monopole antenna combined with a passive attitude control system (PACS) is the most efficient way to communicate with the ground station. The PACS will ensure that the signal propagation of the antenna is strongest when facing the earth.

INTRODUCTION

The Kumu A‘o (source of learning) CubeSat project began in the summer of 2007 and is slated to be completed in the summer of 2009. The Kumu A‘o satellite project has helped over fifteen electrical and mechanical students gain valuable research experience in the aerospace field. A satellite project is significant in giving engineering students at the University of Hawai‘i hands on experience in team work and communication to designing, testing and fabricating a low earth orbit (LEO) satellite. The telecommunications subsystem will provide communications with the CubeSat at the ground station. One of the key components in satellite communications is antenna design.

ANTENNA DESIGN

Antenna Requirements

An antenna is an electrical device that sends and receives radio or television signals. The antenna designed for the Kumu A‘o must meet several requirements. The antenna must be able to propagate a signal within the Ultra High Frequency (UHF) radio bandwidth. The bandwidth that is allocated for satellite use by the Amateur radio satellite frequency organization (AMSAT) is 420 – 450 MHz. The other main requirement for the antenna is that it must fit in a P-POD which is the enclosure that will launch the satellite from the rocket when in space. The amount of extra space inside the P-POD is approximately 6.5 mm and when the antenna is connected to the CubeSat in the P-POD it must be able to fit this small space. Therefore a mounting and deployment system must be created to ensure the antenna fits the requirement. There are several different types of antennas that could be used, but the one chosen is a monopole antenna. This

antenna is one of the simplest antennas that can be created and it will be designed to send and receive signals at 434MHz, which fits the AMSAT frequency range.

Monopole Antenna

The monopole antenna was chosen because the design has been space proven. Several other CubeSat that have had successful launches using the monopole antenna have also been able to communicate with their team ground station. The antenna was designed using simple equations as shown below. Since the operational frequency to transmit the signal is 434 MHz, the wavelength can be found using equation 1. Also, the monopole antenna is a quarter wavelength antenna, meaning that the wavelength is divided by four. The actual antenna will be created using spring steel or measuring tape. This material has also been proven to work in space. In addition, spring steel is a flexible metal that when bent and released the shape of the metal does not change. Therefore, the simplicity and flexibility of a spring steel monopole antenna is a perfect solution to the 6.5 mm requirement in the P-POD. Once the CubeSat is launched into space, a deployment system can be activated which will allow the antenna to take shape and snap into place.

$$\lambda(wavelength) = \frac{c}{f} = \frac{3.00x10^8 m/s}{434MHz} = 0.6912\ m = 69.12\ cm$$

Equation 1 Finding Wavelength

$$monopole\ length\ = \frac{1}{4} * \lambda = \frac{1}{4} * 69.12\ cm = 17.28\ cm$$

Equation 2 Quarter Wavelength

ANTENNA TESTING

High Frequency Structure Simulator (HFSS)

HFSS is a powerful program that can simulate different antenna properties like voltage standing wave ratio (VSWR), signal to noise ratio (SNR), and the radiation. VSWR and SNR are used to find the efficiency of the antenna. Initially, a CAD model of the CubeSat and the monopole antenna was first created on HFSS. Figure 1 illustrates the final design that was used to test the antenna parameters that was previously mentioned. VSWR is a test that checks the maximum standing wave amplitude compared to a standard. Good results from the VSWR will be a range of 1-2; two being the worst of the two. The tests from the simulator proved that the VSWR is approximately 1.72:1. This means that the standing wave that the antenna will be created is 1.72 times greater than what it should be. The results are not ideal, but the antenna is still operable with acceptable results. SNR compares the amount of noise that the antenna is creating. Using simple math equations the SNR will show the amount of the sent

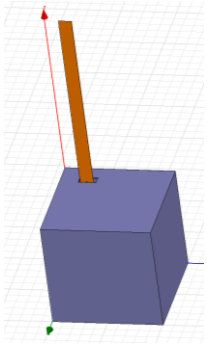

Figure 1 HFSS CubeSat

signal is being sent out of the antenna and the amount being returned to the antenna. An SNR of -10dB or below is ideal, the lower the better. The simulated SNR results are approximately -11.53dB. This means that 93% of the transmitted signal is sent out of the antenna and 7% is reflected back into the antenna.

The last test performed using HFSS was the radiation pattern of the antenna. The radiation pattern shows the strongest location of the transmitted signal. The monopole antenna radiation pattern is similar to a donut as shown in Figure 3 below. The two figures show a cross section cut and a 3D model of the radiation pattern. The donut shape of the radiation pattern can be seen in the cross section cut. The signal is strongest at the outer ends of the donut shape. For example, if the antenna is pointed to the north, the strongest signal will propagate to the east and west of the CubeSat. The 3D radiation pattern is slightly bent to the left and forward. This is due to the position of the monopole antenna which will be located in the top left corner of the CubeSat as shown in Figure 1. The problem with the donut propagation is that when the CubeSat is in space, there is no way to ensure that the satellite's east and west will be always facing the earth. A PACS will be implemented to ensure or give the satellite a higher probability of its strongest signal facing earth or the ground station.

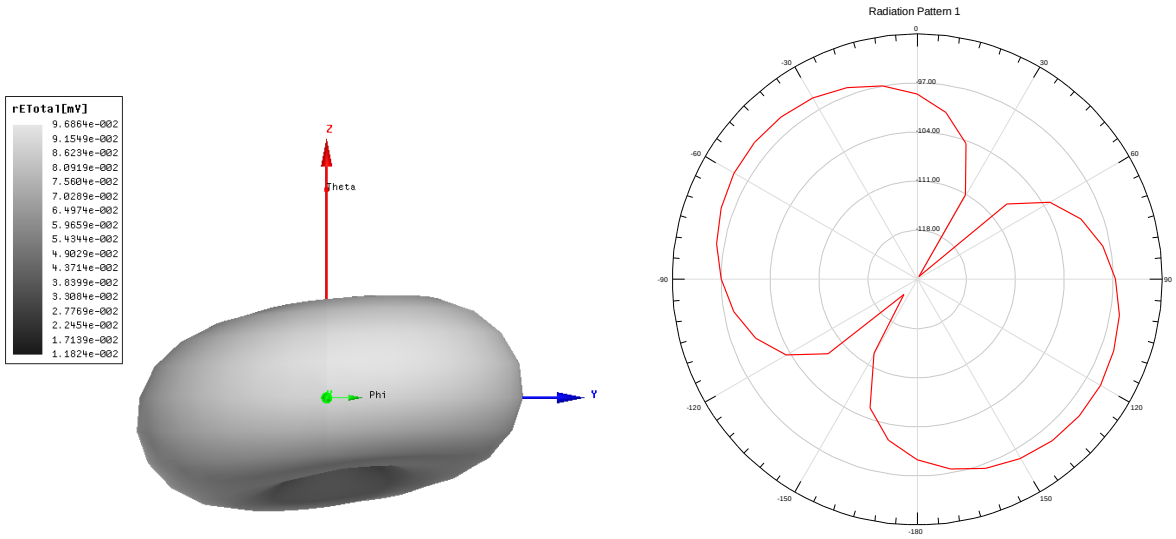

Figure 2 Monopole antenna radiation pattern

Real-World Testing Implementation

To test the antenna in the 'real-world', a network analyzer is needed. The network analyzer tests the SNR, VSWR, and impedance of the antenna and antenna connections. The impedance of the antenna should be as close as possible to the impedance of the ground station. The same impedance means that there will be almost perfect transmission and the VSWR is 1:1. When the impedance of the antenna and the ground station are different the VSWR is not perfect and there will be noise and some transmission lost. The tests were done in the lab and the network analyzer was connected to the antenna using a coaxial cable. The antenna is approximately 17.2811 cm of spring steel. It is also connected to an SMA connector. The SMA connector will be used to connect the spring steel to a coaxial cable. Figure 4 shows one of the first fabricated antennas. The antenna was mounted inside an empty CubeSat engineering

model. Before the antenna could be tested, the SMA connector and the CubeSat had to be grounded. The grounding was implemented with a wire, which added impedance. The connections to the network analyzer are as follows: spring steel to SMA connector to coaxial cable to network analyzer.

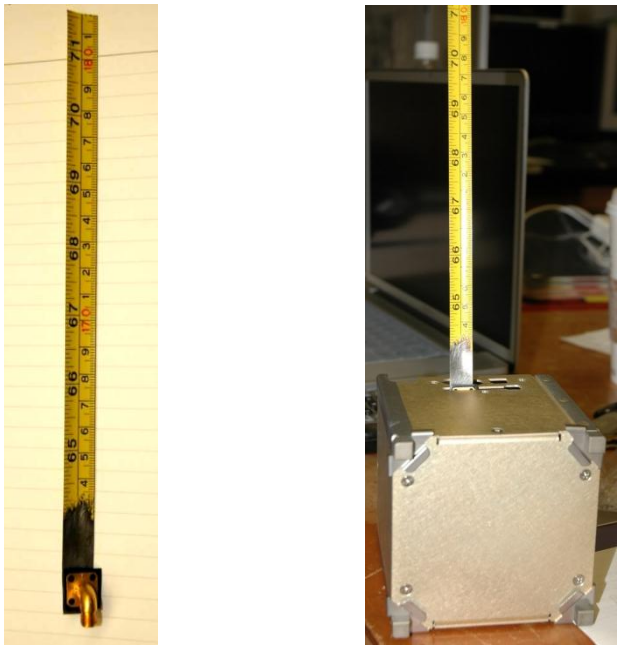

Figure 3 Fabricated Antenna with SMA connector mounted inside the CubeSat

Real- World Testing Results

The results of the lab tests are very good. Figure 4 shown below, is the print screen results of the network analyzer lab tests. The SNR is approximately -14.669 dB meaning that 96.6% of the signal will be transmitted out and that 3.4% will be reflected back into the CubeSat. The VSWR results were also better than the simulated results at 1.45:1. Table 1 compares the HFSS simulation and the network analyzer results. The impedance, as mentioned above, is different. The antenna impedance and coaxial cable connection is supposed to be 50 ohms, but the testing results were at 66.776 ohms. The grounding wire and another wire that connected the spring steel to the coaxial cable added more impedance to the system. When doing more tests, the mounting and connections will be changed to take into account the impedance of the entire system.

Results	HFSS	Network Analyzer
SNR	-11.53 dB	-14.67 dB
VSWR	1.72:1	1.45:1

Table 1 Testing Results

Figure 4 Network Analyzer Results

ANTENNA MOUNTING SYSTEM

Antenna Mounting

The mounting system that will be installed will fix the problem of the added impedance. All the connections in the mounting system are of direct contact. A cage will be created to mount the antenna to the TNC board and the CubeSat. This arrangement will add higher stability and strength to the mounting of the antenna. Figure 5 is the design of the antenna mount. The cage will be connected to the TNC pcb board. The spring steel will be connected to a SMA connector inside the cage and held in place by two plastic pieces. The SMA connector will be attached to a coaxial cable that will connect to the transceiver. The transceiver creates the signal that will be sent out from the antenna. The cage is designed to act similar to a Faraday cage. Faraday cages block out electromagnetic waves from entering and exiting the cage. This will help prevent electromagnetic waves from going inside the CubeSat. The cage that we are designing will not be completely closed; one requirement for a Faraday cage, but the cage will still block electromagnetic waves.

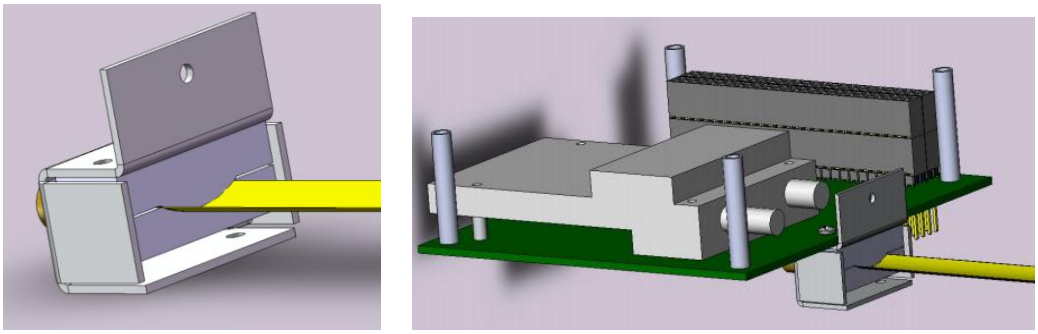

Figure 5 Model of the Antenna Mounting using HFSS

CONCLUSION

The Kumu A‘o telecommunications antenna design has been space proven to work. The simulation results were not ideal, but the antenna will still work well. The real-world tests results were very good, but with the high impedance the mounting system needed to be changed. The new antenna mounting system will fix the impedance problems and allow for better stability for the antenna. More tests will be done to ensure that our new system does fix the impedance problems.

ACKNOWLEDGMENTS

A big thanks to my mentors Lloyd French, Wayne Shiroma, and Byron Wolfe, each of you have helped me grow mentally and intellectually. This research project would have never have finished without the guidance you have given me. Thank you Dr. Luke Flynn, Dr. Ed Scott, and Ms. Marcia Rei Sistoso for all the support you have given me in the last two semesters with HSGC. I would also like to give my gratitude to the Native Hawaii Science and Engineering Program (NHSEMP), Joshua Kaakua, Kelli Ching, and Bubba. Without their help and support the Kumu A’o CubeSat and I would not have gotten this far. The SWE members deserve my gratitude for supporting and helping me with late night papers. Last but not least, I would like to give a big thanks to the past and present Kumu A’o CubeSat team: Zachary Lee-Ho, Matthew Patterson, Dennis Dugay, Jeremy Chan, Isaac Rodriguez, JimyLeah Castro, Reid Yamura, Jordan Torres, Tyson Seto-Mook, Aaron Akashi, Windell Jones, and Sebastian De’Angeles. The time we spent in the lab together has been some of the best times in my college career. We have gone through a lot of good and bad times, but we made it this far. Thanks for all the good times!

REFERENCES

Antenna-theory.com: The online source for learning about and understanding antennas. Available [Online]: http://antenna-theory.com/

Loy, Matthew, and Sylla, Iboun. ISM-Band and Short Range Device Antennas. Texas Instruments Incorporate, 2005. March 2005 < http://focus.ti.com/lit/an/swra046a/swra046a.pdf>

Suite101.com: Understanding the Faraday Cage. Available [Online]: http://electricitymagnetism.suite101.com/article.cfm/understanding_the_faraday_cage

Wikipedia, The Free Encyclopedia Website: Dipole Antenna. Available [Online]: http://en.wikipedia.org/wiki/Dipole_antenna

SYSTEMS ENDINEERING FOR THE KUMU A‘O CUBESAT

Jeremy K. Chan
Department of Electrical Engineering
College of Engineering
University of Hawai‘i at Mānoa
Honolulu, HI 96822

ABSTRACT

The Kumu A‘o CubeSat team is the 5th team from the University of Hawai‘i at Mānoa to carry out a CubeSat mission from start to finish. Systems engineering was used in the capacity of coordinating the expectations between engineering groups within the team over its 2 years of work, as well as turning a potentially complex project into a methodical and parallelized effort. The Kumu A‘o CubeSat system involves four key segments: the launch vehicle, satellite, ground station, and mission operations center. The four segments are equally important to the success of the mission, and each item was planned to the extent of reasonably minimizing the risk to the mission. It is with this relatively large student project that much learning has taken place on how to take space bound ideas into reality.

INTRODUCTION

Whether used for space/planetary exploration, world wide communications, or zero-g research, satellites fulfill specific needs which would otherwise be prohibitively expensive or impossible. Created during the Summer of 2007, the Kumu A‘o CubeSat team is the 5th student driven satellite team under the University of Hawai‘i (UH) small satellite program. The Kumu A‘o CubeSat project aims to produce a working reference of a CubeSat satellite bus which can be re-used for an arbitrary mission. The standardized bus can provide a way of accelerating all small satellite developments done by students and professionals at the University of Hawai‘i.

The Kumu A‘o CubeSat team is participating in a rigorous engineering mission which will take its spacecraft into low earth orbit (LEO). The Hawai‘i Space Flight Laboratory (HSFL) is generously providing a launch vehicle which is tentatively set for launch in the 2011 timeframe. The CubeSat will ride upon the launch vehicle as a space-available, non-interfering secondary payload. With a proven flight heritage, doors are opened to new missions as well as new research opportunities for students.

BACKGROUND

In the realm of satellites, the bus refers to the entire electrical and mechanical systems of a satellite which support a payload. An analogy would be how an airplane is the bus for payloads consisting of passengers, cargo, and armaments. The standardized CubeSat bus will be similarly adaptable to arbitrary payloads which will allow the design to be re-used and improved upon for future missions. The primary benefit of the standardized bus is to allow customers such as scientists to concentrate on creating a payload which will ride upon the CubeSat bus.

A CubeSat is a standardized satellite specification created jointly by CalPoly at San Luis Obispo and Stanford University. The basic unit is a 10x10x10cm cube structure, weighing in at

one kilogram per CubeSat unit. The specification is a vehicle for integration of CubeSats as secondary payloads aboard launch vehicles. Launch vehicles are typically meant for other very important and expensive primary payloads. The key for making the launches possible is risk mitigation to the primary payload. Through the risk mitigation provided by the standard, which includes a very successful flight heritage, the launch provider and primary payload customer have an easier time allowing CubeSats aboard their launch vehicles. As of 2007, a general figure for a CubeSat launch from Russian providers is approximately $50,000 per kilogram. The price makes launching CubeSats accessible for universities. However, the cost is expected to rise as launch vehicles mature in their flight heritage, and thus offer more guarantees.

MISSION

The Kumu A‘o CubeSat team’s mission is to successfully develop, launch, and operate a CubeSat in orbit. In order to make the mission a success, several criteria need to be met:

1. Develop a functional CubeSat bus that can be re-used for future missions
2. Operate the CubeSat in orbit
3. Provide an educational opportunity for primarily Native Hawaiian students, as well as other minorities.
4. (Secondary) Evaluate the 1U CubeSat kit (www.CubeSatkit.com) to see how versatile the kit is as a CubeSat bus and structure.

These primary mission success criteria represent the top-level requirements for the project. Everything designed must go towards fulfilling at least one of the above requirements. The top-level requirements simultaneously drive the project’s system concept and requirements definition.

SYSTEMS ENGINEERING

Systems engineering can be summed up into one sentence, “to guide the engineering of complex systems.” Being a technical subset of project management, systems engineering can be a large effort. One of the primary values of employing good systems engineering practices to this project is to reduce the overall risk to the CubeSat project. All potential risks to the project must be realized and mitigated by systems engineering as much as feasibly possible. Due to the expenses of launching a single CubeSat, and the near irreparability of the CubeSat in space, there are no second chances for the Kumu A‘o CubeSat. To provide the most probable chance for success, systems engineering must be employed to manage all the potentially complex, conflicting, and interdependent information.

Since systems engineering can be applied to small simple projects to extremely large complex projects, the efforts were scaled appropriately. The chosen set of methods include using basic project definition items, such as mission concept analysis, needs analysis, and requirements to communicate the firm project details to the team. The rest of the systems engineering techniques are applied as necessary to manage risks to the project, and to provide good documentation on the engineering decisions.

Part of the systems engineering process is mission analysis. Mission analysis allows you to see whether a mission is feasible within a given amount of constraints. The top level

requirements, along with available program support dictate the details of the possible mission plans. As of today, the mission analysis and any applicable trade studies have already been completed by the former Kumu A‘o CubeSat team’s systems engineer, Zachary Lee-Ho, in a previous space grant fellowship in the Spring of 2008. The discussion in this paper will therefore be limited to what has been decided and what the mission entails.

LAUNCH AND ORBIT PARAMETERS

At the time of writing, the Kumu A‘o Cubesat is tentatively scheduled to be launched aboard a HSFL launch vehicle in the 2011 timeframe. The launch vehicle will insert its primary payload along with the CubeSat as a secondary payload into LEO. At the time of writing, the orbit is planned to be sun synchronous at an altitude of 600km, 98 degree inclination, and with a 9AM local ascent. Figure 1 shows a representative orbit profile as rendered by the AGI Satellite Tool Kit 8 software.

An expanded picture is shown below in Figure 2 to illustrate a day in the sun synchronous orbit. Although the ground track lines will shift as time passes, the basic pattern of line of sight will remain. The dark blue lines (Label 3) represent the satellite in the dark, yellow (Label 2) represents the satellite in the sun, and teal (Label 1) represents line of sight between the satellite and Hawai‘i.

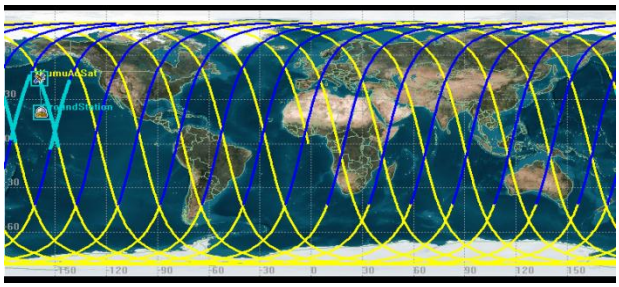

Figure 1: Ground Track of Proposed Satellite Orbit

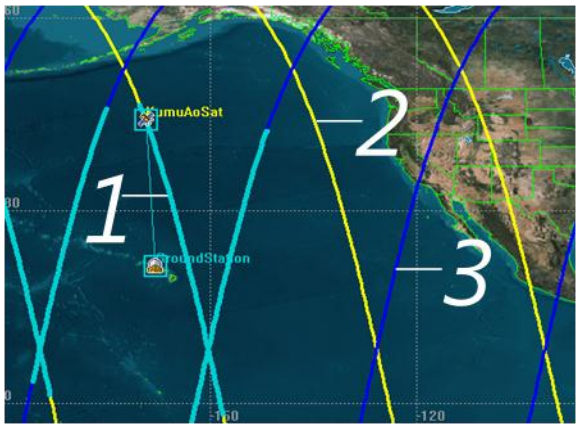

Figure 2: Orbit over Hawaii

In planning, the orbit information is vital for analysis in the areas of power generation, communications, and thermal estimates. When the satellite is launched and orbiting the earth, the actual Keplerian orbit parameters, or TLE’s, will be tracked and published by NORAD. Accurate modeling of ground track orbits can be done thereafter. In mission operations, the orbit parameters will be used in accurate ground track projections which will enable automated field tracking of the satellite for radio communications. That will in turn allow mission operation center volunteers to be scheduled appropriately.

OPERATIONAL DESCRIPTION OF SYSTEM

To fulfill the mission objectives, the system was designed with a few key components that are shown in Figure 3. To have a working satellite operation, four system segments are needed: the satellite itself, a means of launching the satellite into orbit, a way to communicate with the

satellite in space from the ground, and an operations center for managing the satellite's operation and data. The launch vehicle is not shown in the below diagram, but will be discussed in the subsequent subsections.

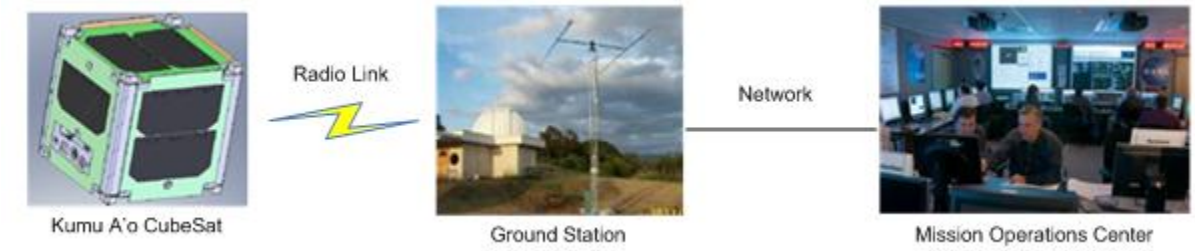

Figure 3: High level system block diagram

The Kumu A'o CubeSat will orbit the earth approximately every ninety minutes. The satellite will collect data on various subsystems and environmental conditions as the device traverses the sunny and dark sides of the earth. The satellite will eventually come across Hawai'i up to three times per day.

When the satellite flies over Hawai'i, a ground station, whether automated or manned, will be used to contact the satellite for a telemetry session. When a successful link is achieved, the ground station can then downlink all the data that the satellite has onboard. The data can then be post-processed for evaluation by an engineering team.

SYSTEM INTERFACES

At the system and subsystem level, the Kumu A'o CubeSat team employs interface control documents (ICD) to cover the agreements between the systems engineer and two segments/subsystems involved in the system. The ICD map shows the relationships between subsystems. An example would be interfacing between the satellite and the ground segments.

All interfacing physical connectors, pin assignments, electrical, protocol, control mechanisms, etc. are documented in each ICD. This allows each discrete engineering team to build their product and be able to perform a simulated test to the interfaced subsystem without necessarily actually having the other subsystem. The ability to perform tests will allow for a smooth integration process. Each line in Figure 4 represents an ICD which has been documented to date.

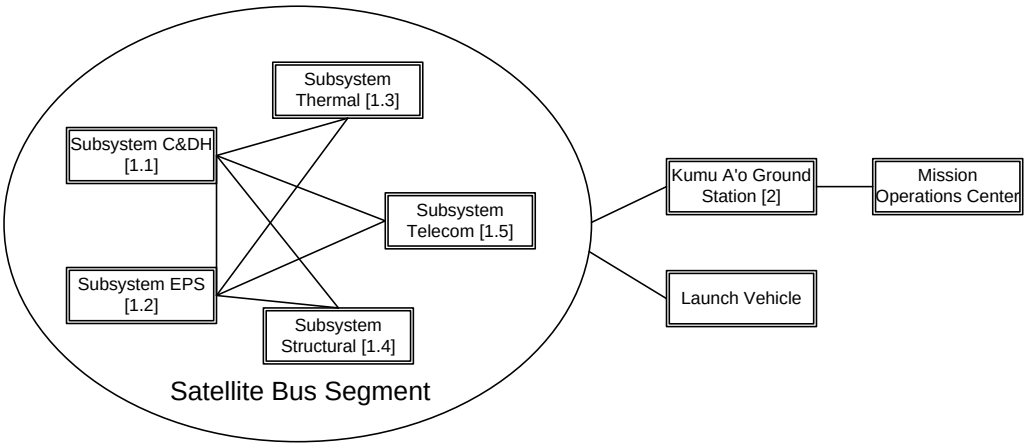

Figure 4: Subsystem level ICD documentation map

CUBESAT

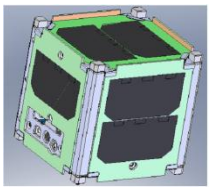

Figure 5: CubeSat

The satellite is the centerpiece of the system. The main goal for the satellite itself is to verify its own performance in space. The results will provide vital data to the design of future satellites as well as to provide proof of success. Any data gathered from successful communication will go toward the flight heritage of the design.

Each subsystem will be monitored for performance data. The data will then be buffered for later transmission to the ground station. When the satellite is within range of a ground station, the satellite will have an opportunity to connect with the ground station for a telemetry session.

To find the ground station, the CubeSat will beacon via radio with Morse code and packet radio on set intervals. Each beacon will be set at an interval which makes sense for the available power budget, and optimizes the chance for a communications window.

CUBESAT: SUBSYSTEMS

The CubeSat consists of five major subsystems. Each subsystem is required for the satellite to function properly, and thus constitute the basic satellite bus. Beginning with the *command and data handling subsystem* (C&DH), the C&DH subsystem manages all system modes and subsystem control. C&DH has the only computer capable of controlling all subsystems to achieve mission goals. All other subsystems are fully controlled by C&DH.

The *electrical power subsystem* (EPS) is important for generating, storing, and distributing power in a controlled manner. Power for the CubeSat is generated using solar cells which must be converted into a usable form. The power is then stored into a lithium ion battery, and then distributed to the rest of the subsystem on both regulated and unregulated power busses.

The *thermal* subsystem is vital to the physical survival of the CubeSat electronics and durability of materials. Keeping in line a goal for low cost development, some selected components are allowed to be industrial or at worst case, operational in commercial temperature ranges. Certain components such as the EPS battery cannot be used at under -20C. The thermal subsystem must ensure that the satellite will not freeze, nor will the environment become too hot

for components to operate. The performance of the thermal calculations will be verified using onboard sensors. The data gathered during the mission will be vital to future payloads.

The *structural* subsystem provides physical safety mechanisms for pre-launch, keeps the CubeSat intact and within physical constraints through launch. The subsystem works in conjunction with the thermal subsystem to stabilize electronics temperatures. The subsystem includes all structural changes such as antenna deployments.

Lastly, the *telecommunications* subsystem provides a radio link through space down to an earth ground station. The subsystem must ensure that enough power is being radiated, and in the right directions. Any protocols that must be used to compensate for unmitigated constraints also fall under this subsystem's domain.

CUBESAT: LAUNCH MODE

It is expected that the satellite may sit 'on the shelf' for approximately a year before launch, so any rechargeable battery inside the system will discharge itself by the time the actual launch date comes around. In addition, certain parts such as its primary and secondary batteries, and solar cells may degrade over time. Thus, the power budgets were calculated based on end-of-life (EOL) expectations. The shelf life of the flight model version of the CubeSat is estimated at one year. If the storage time is actually longer, *the degraded components must be replaced* to ensure the mission's success.

Before integration of the CubeSat into a Poly-Picosat Orbital Deployer (P-POD), the launch vehicle's deployment enclosure for CubeSats, a pre-flight system check will be performed on the satellite with a field ground station. The system check will include a full battery charge. It is entirely possible that after integration into a P-POD that there will be no further access to the CubeSat. Thus, the launch mode at the worst case begins from the time that the CubeSat is integrated into the P-POD.

During launch mode, the satellite will be completely disabled via a deployment switch. The deployment switch prevents the EPS's battery and solar cells from distributing power to the rest of the system. Although possibly inaccessible due to launch vehicle integration procedures, the P-POD has an access panel could allow diagnostic equipment to be connected and charge the satellite before flight. Use of the P-POD access panel may be allowed if the CubeSat is integrated into the P-POD but the P-POD is stored over a prolonged period of time.

CUBESAT: POST-LAUNCH MODES

When the CubeSat is deployed from a P-POD, the CubeSat is energized and goes through a few post-launch procedures. The first thing the satellite does is starts up a timer which makes the satellite sleep for the first fifteen minutes. This initial sleep is called the *standby mode*, and is required of all CubeSats using Cal Poly's CubeSat standard.

If the satellite was actually still on the ground, a deployment switch actuation will look like a P-POD deployment event. However, the fifteen minutes of the CubeSat's standby operating mode provides two key features: time to recover from an accidental activation, or to provide an interface to the ground station for battery charging and pre-flight subsystem diagnostics. These features will be important to the pre-flight preparation for the satellite launch.

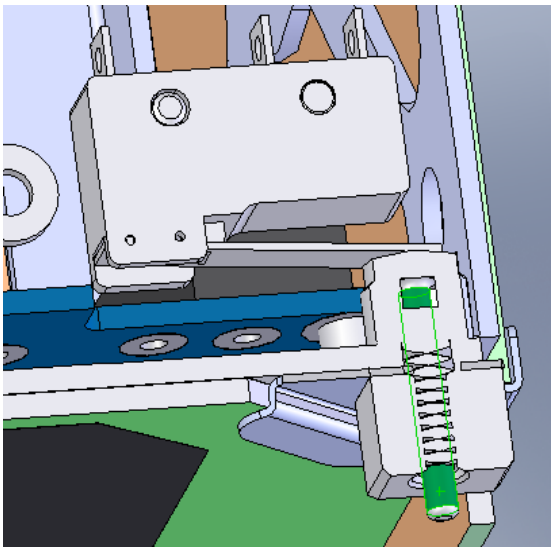

Figure 6: External deployment switch on a Cubesat foot

If the satellite was just deployed from a P-POD, the satellite will count down from its standby mode, starting a chain of important events. After the initial fifteen minute standby mode, the first of its events is to start deploying the satellite's antenna. The satellite's antenna deployment system will be able to attempt deployment multiple times. The deployment system continues to attempt antenna deployment in forty-five minute intervals until a successful communications link has been established. Meanwhile, additional hold-off on orbital modes is set for fifteen minutes.

As soon as the orbital mode delay expires, the time will be at thirty minutes after deployment. Assuming the deployment was successful, the satellite will advance to the next step where the system status will be logged to storage. A post-launch completion flag will be written to non-volatile memory. The post-launch completion flag will disable the post-launch modes, and allow the satellite to reboot quickly. This allows the satellite to be significantly more efficient after rebooting due to a power failure or failsafe triggered reset.

Finally, after the permanent post-launch completion flag is set, the satellite transitions into its orbit modes. Based on the battery condition, comprising energy capacity and light-load battery voltage, the satellite will choose one of its four orbital modes. Going into orbital modes is a critical transition, as the remainder of the satellite's operational lifetime will be spent exclusively in its orbital modes.

CUBESAT: ORBITAL MODES

As a CubeSat, the device does not have a large power generation capability in comparison to the power consumption expected for communications. Thus, to accomplish the satellite's goals, modes must be used to have some degree of power management automation.

The Kumu A'o CubeSat is expected to have an orbit cycle of about ninety-three minutes with full earth coverage occurring approximately every twenty-four hours. The orbits will

involve mostly sunlight where the satellite will obtain both electrical and thermal energy. Electrical energy generated via photovoltaic cells on the outer cube surfaces is stored in a lithium-ion battery. Energy is collected over several orbits to provide enough power to operate the satellite's subsystems for a limited time.

When the orbits take the satellite into the dark side of the earth, thermal energy is lost, and stored electrical energy is expended to keep the satellite operational. The dark/light side cycles will keep the satellite in a near constant struggle to keep its battery full while being operational. The CubeSat must make sure that the satellite subsystems are turned on/off to ensure that there is always enough energy to perform its duties when called upon by operations personnel on the ground. To achieve the above goals, there are four orbital modes for the satellite. Figure 7 on the next page shows the transitions based on noted conditions between the various modes.

Beacon mode is the standard operating mode of the satellite. In intervals of eighty seconds, the satellite will transmit a Morse code beacon, followed by a packet of telemetry data. Every third beacon will be an extended Morse code telemetry beacon followed by a packet of telemetry data. Each beacon will allow fifteen seconds for the ground station to send a response to establish a telemetry session. Meanwhile, beacon mode will monitor the battery, and if the state of charge falls below a threshold, the satellite will transition to recharge mode.

Throughout the mission, we're attempting to keep the depth of discharge (DoD) of the battery down to less than forty-percent to ensure a reasonable life expectation of the battery for up to one year of operation. DoD is defined by the amount of energy removed from a fully charged battery (% Empty).

To enforce DoD minimization, *recharge mode* is the reduced operating mode of the satellite. The radio transceiver onboard the satellite is the single largest power draw on the system which makes it a prime target for cutting power consumption. The difference from the beacon mode is that every eighty seconds, the satellite will only listen for a telemetry session request from the ground station for a length of ten seconds. And just like beacon mode, every four minutes, the satellite will transmit the normal extended Morse code telemetry beacon with its packet of telemetry data. The reduction of transmission time in recharge mode still allows an operations center to wake up the satellite for telemetry while gathering more energy than used.

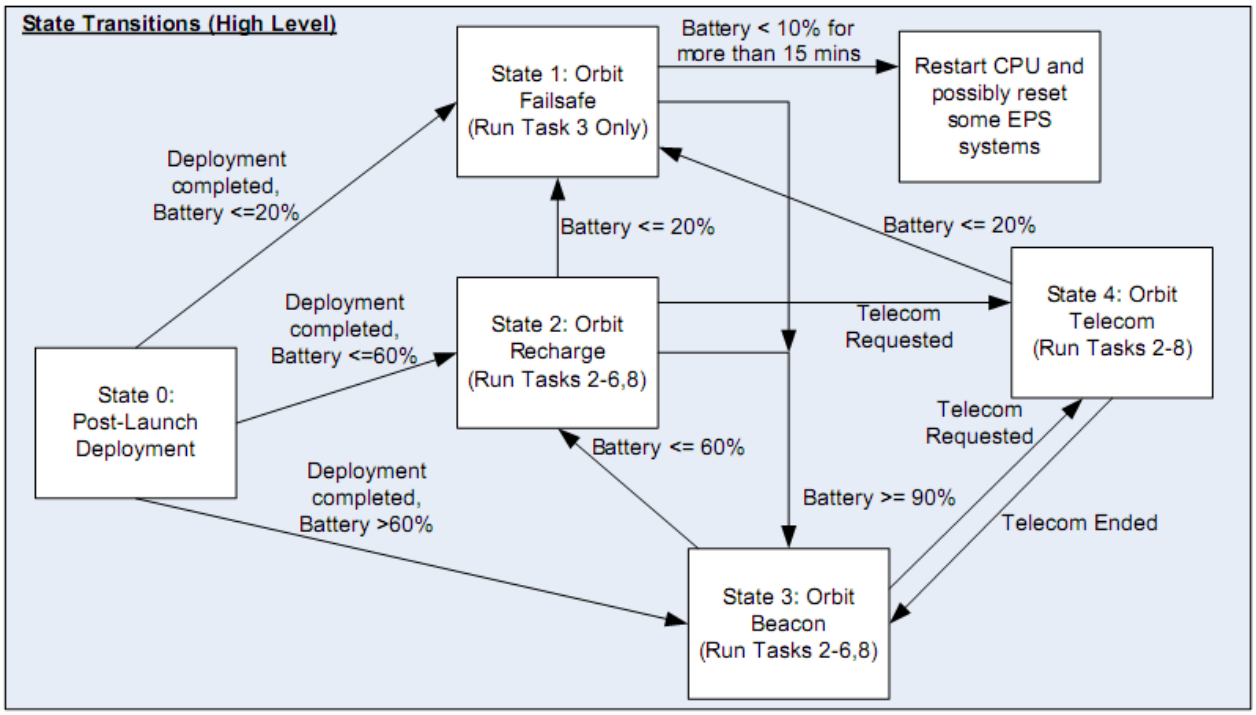

Figure 7: Orbit Mode Transitions: The battery percentages are based off of its state of charge (%Full)

If a request for telemetry is sent during either the Beacon or Recharge modes, the satellite will enter its *telecom mode*. The telecom mode is where telemetry requests will be allowed, and also where the satellite expects to expend much of its stored energy in transmissions. Normal beaconing continues in this mode, but in very short five second intervals to aid in the calibration of active satellite tracking antenna systems. Beaconing will only be held off if a file transfer or other command servicing transmission is in progress. The telecom mode can be ended by either: the ground station sending a disconnect command, the ground station not contacting the satellite within ten minutes, or the battery nearly depletes and forces a transition to failsafe mode.

Failsafe mode is used in the absolute worst case operating situation where energy storage levels are extremely low. A bad situation can result from a brownout if the voltages on the system start to fall below operating levels. The radio transceiver used will also fail to work if the battery voltage is too low. Components like the radio and will still draw energy if connected to a battery. Thus, failsafe mode is thus used to avoid total depletion of the battery and to keep volatile memory systems online. As this is a failsafe mode, a minimal set of components are energized, and even minimal energy collection from solar cells will be acceptable in eventually bringing the system back online. From the modes described above, the satellite can achieve the control it needs to keep itself alive and well maintained.

LAUNCH VEHICLE

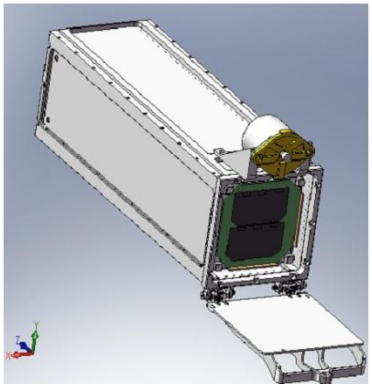

The CubeSat will be designed to be launched on nearly any rocket which can support a P-POD. The P-POD was created by students at the California Polytechnic State University in San Louis Obispo to make it possible to attach CubeSats as secondary payloads on important launches. Figure 8 shows a CubeSat in a P-POD Mk-III container with a CubeSat already inserted into the container.

Figure 8: Cal Poly P-POD Mk-III

The P-POD reduces risk to the primary payload of a launch vehicle by setting requirements for CubeSats, and having all final CubeSat certification testing and P-POD integration done in cooperation with CalPoly. That ensures that all CubeSats being loaded into the P-POD will absolutely conform to Cal Poly's CubeSat specifications. The result is that Cal Poly can certify to the launch provider that the CubeSats will not pose a threat to the primary mission within a Cal Poly specified P-POD lumped specification.

Without the P-POD, certifying that a CubeSat is not a threat to another payload can be prohibitively complicated. This is especially true if a launch provider is being asked to launch multiple CubeSats without a P-POD. It can become nearly impossible to get a cost effective launch if each CubeSat had to be certified individually by the launch provider.

Figure 9 shows the CubeSat launch sequence. In order to launch a CubeSat, the satellite needs to be qualified for flight, integrated into a P-POD, and then have the P-POD launched into orbit. The launch vehicle avionics will then control detachment of the P-POD, and the subsequent release of CubeSats thereafter. The satellite will then likely take a similar LEO orbit of the primary payload.

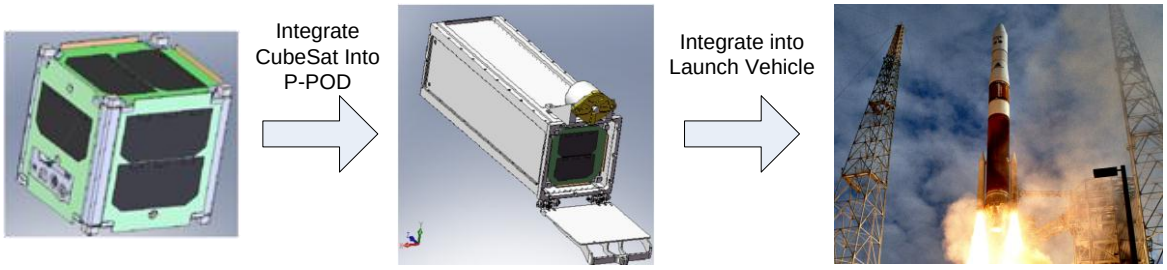

Figure 9: CubeSat launch sequence

GROUND STATION

The ground station is a vital component of the system, providing a link on the ground to the satellite. Figure 10 shows a picture of our Leeward Community College ground station, built and owned by HSFL. The ground station will be available to the Kumu A'o CubeSat team for use on a non-interference basis.

Figure 10: HSFL Ground Station

The ground station is equipped with a high gain directional antenna mounted on a two-axis rotor. The rotors are connected to a satellite tracking computer which has software to control which way the antenna

points, and which frequency the radio is set for communications. The frequency is also Doppler Shift compensated in pre-calculated offsets as the satellite passes overhead.

A second computer, called the MOC interface computer, will be tied into the mission operations center (MOC) network, and the computer will provide automation of telemetry data downloads. The computer will also provide the MOC with a real-time remote interface to the satellite. From the remote MOC, the operations team will be able to control the satellite in orbit.

CONCLUSION

A satellite operation requires multiple segments which are necessary to form a cohesive system. From the satellite itself to the people who will launch and operate the satellite, all the components of the system are equally important for a successful mission. Identifying and planning each detail goes far in a long term mission's risk mitigation. Since this project is relatively small to the potentially large scope of systems engineering, a balanced was achieved between the available resources and the level of risk mitigation we needed for the mission. As the team fabricates the design today, the benefits of the forethought are realized.

ACKNOWLEDGEMENTS

There are many of whom I owe for the opportunity to work this great project. This is by no means an adequate acknowledgement, but with these limited words: First, I would like to thank the Hawai‘i Space Grant Consortium (HSGC), especially to: Dr. Ed Scott, Marcia Rei Sistoso, and Dr. Luke Flynn for all their help with financing the project and providing fellowships for our students. The conferences that we've attended, with your support, have been invaluable in helping us to see new career opportunities and methods of developing CubeSat subsystems. I'd like to thank Lloyd French for being a great mentor on systems engineering. Lloyd's unending support was invaluable to my development as an engineer, and I also know that it was the same case for all of us that Lloyd has helped. I would like to thank the University of Hawai‘i's Small Satellite Program, led by Dr. Wayne Shiroma for the generously provided lab space for our team. To Byron Wolfe and Jason Akagi of the Hawai‘i Space Flight Laboratory, thank you for your mentorship throughout the years. You were valuable in bringing knowledge from previous projects and helping us to learn project management. Your advice also helped to keep our project moving along. To the Native Hawaiian Science and Engineering Mentorship Program (NHSEMP), I would like to thank you for all your support. You also helped to keep our team together through travel, as well as helped to fund our project. Without your help, we would not have been able to afford much of the parts we have fabricated today. Lastly, to the Kumu A‘o CubeSat team, I'd like to thank all of you for your hard work, past and through this summer of 2009. I hope that this experience was as valuable for you as it was for my development as an engineer. I will always remember each one of your individual efforts, sacrifice, and support that you have given us all: Aaron Akashi, Amy Blas, Jimy-Leah Castro, Sebastian De Angelis, Dennis Dugay, Shantel Hunt, Cherie Kinoshita, Zachary Lee-Ho, Isaac Rodrigues, Tyson Seto-Mook, Jordan Torres, Reid Yamura, Windell Jones, David Luis, Michael Menendez, Matthew Patterson, Sae Yoon. Good luck to all of you and your careers!

REFERENCES

The CubeSat Program, California Polytechnic at SLO. (2008, October 2). [Online] CubeSat Design Specification Revision 11 from http://cubesat.atl.calpoly.edu/media/CDS_rev11.pdf

Larson, Wiley J., Wertz, James R. (1999) Space Mission Analysis and Design, Third Edition

THE KUMU A‘O CUBESAT STRUCTURAL AND THERMAL SUBSYSTEM

Windell H. Jones
Department of Mechanical Engineering
University of Hawai‘i at Mānoa
Honolulu, HI 96822

ABSTRACT

The Kumu A‘o cube satellite will need to survive two extreme environments one in which is during launch and the other during its mission life. Prior to launch, the engineering model of the satellite is required to pass a launch loads test simulating the actual loads during launch. In addition, the satellite’s endurance in space temperatures will be tested in a thermal-vac chamber prior to launch. Before these tests are performed, the satellite will need to be designed to handle these two extreme environments. This will be done using FEA software that calculates the effects of random vibration and temperature cycling on the satellite’s PCBs. An initial guess as to the external temperatures expected in orbit is predicted along with the frequency and magnitude of the most violent vibrations during launch. Finally some PCB population recommendations are made according to established ESA (European Space Agency) standards.

INTRODUCTION

Kumu A‘o, a cube satellite developed by the University of Hawai‘i at Mānoa College of Engineering, is scheduled for launch within the next two years. The orbit of Kumu A‘o will be at distance of 600km, circular, retrograde and sun-synchronous with an angle of inclination of 98 degrees. The satellite’s main purpose is to demonstrate the flight worthiness of a cube satellite bus standard developed by UHM CoE. The first main objective of the Structural and Thermal subsystem is to ensure that the satellite will endure the launch loads of launching to orbit. It is during launch that it is the largest loads in the shortest period of time will be acting on the satellite during the satellites entire mission life time. While in orbit, the satellite must survive the temperature cycling experienced. The structural and thermal team will ensure that the satellite’s temperatures will remain within a temperature range that the electronics can tolerate for the entire mission life. Lastly, to ensure that a reliable link is maintained between the satellite and ground-station, an effective yet simple form of attitude control system will need to be implemented on the satellite.

This final report will give an overview of the progress made in the temperature monitoring and vibration analysis areas of the Structural and Thermal Subsystem for the Kumu A‘o satellite. The temperature modeling and attitude control system design are left as later work to accomplish.

TEMPERATURE MONITORING

Over the past three months changes have been made from the original design of the shareboard. Enough changes were made such that the design of the shareboard will be overviewed again here.

The temperature monitoring circuit samples a total of eight thermistors. Six of these thermistors are located on the exterior of the satellite where they will measure the temperature of the body-mounted solar panels. The other two thermistors will be located inside the satellite with one on the battery and the other on the transmitter.

The shareboard is a printed circuit board that holds circuits from the structural, telecom, and CDH subsystems hence its name. These circuits consist of the temperature monitoring circuit, the data/morse multiplexing circuit and transceiver, and the nichrome wire burn circuit for antenna deployment.

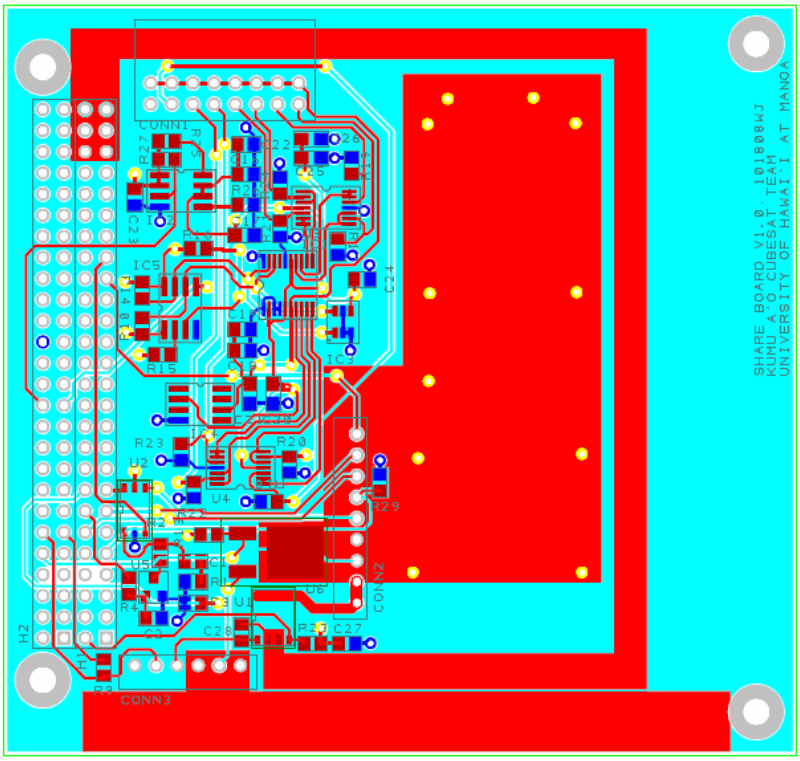

Figure 1. Draft layout of the shareboard PCB

Layer Changes

Previously, to save on cost and complexity, the shareboard was designed with only two layers. Both of these layers contained a mixture of signals and power traces. When the structural and telecom circuits were added to the PCB layout, it was obvious that more layers were needed in order to ensure low resistance pathways for high current traces.

All the signals and power traces were routed on a 4 layer board manually in PCB artist according to the schematic shown below. The middle two layers deliver the 0V and +3.3V traces from the dedicated EPS rails on the PC104 bus to all the ICs on the shareboard. The outer layers are primarily the signal layers for the non-power circuit connections. Since the transceiver draws up to 1.5A of current, an exceptionally large trace is routed to the transceiver connector from the dedicated Vbatt rails on the PC104 bus. In addition, the ground return for the radio is shared with the ground return of the nichrome wire burn circuit. To sink heat from the nichrome burn MOSFET, it is attached to the HIGH_CURR_0V copper pour on the top layer. In addition

another copper pour was made to fill the bottom layer to provide a low-resistance return for the nichrome burn circuit and the transceiver. The copper pours on the top and bottom layers are connected together electrically with vias.

Circuit Changes

Prior to this semester, the design for the temperature monitoring circuit was the only part of the shareboard that was presented. Since then, the nichrome wire burn circuit and the data/Morse multiplexing circuit have been integrated into the schematic and printed circuit board design.

The voltage divider theory was presented for the temperature monitoring circuit in the final report for last year therefore it is only mentioned here that the chosen resistor value for the bottom voltage divider was chosen to be 350kohms for the 100kohm thermistor voltage dividers and 35kohms for the 10kohm thermistor voltage dividers. The reasoning supporting the selection of these values is provided in last year's final report.

The lowpass filter discussed in last year's report was taken out of the design because it was discovered that the TNC already has this filter as part of its circuitry therefore was not needed. Instead, the 1 kHz pulse train from CDH that generates the Morse code tones is fed through a DC blocking capacitor and two series resistor before being passed to the transceiver.

A temperature sensing IC, the TMP100 by Texas Instruments, was placed on the PCB close to the ADC to monitor the temperature of the ADC while it is sampling.

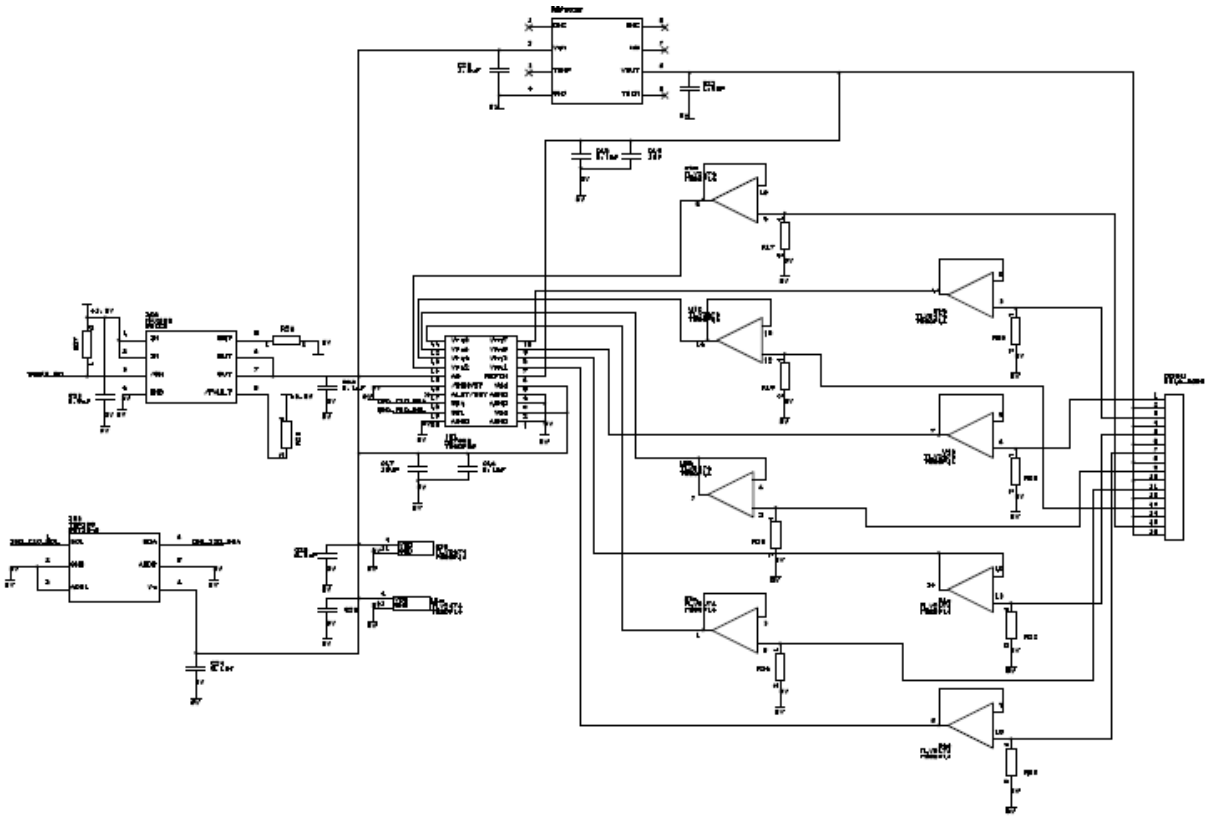

Figure 2. The temperature monitoring circuit consists of six ICs: the ADC, two quad ADCs, voltage reference, a temperature-sensing IC and a power switch.

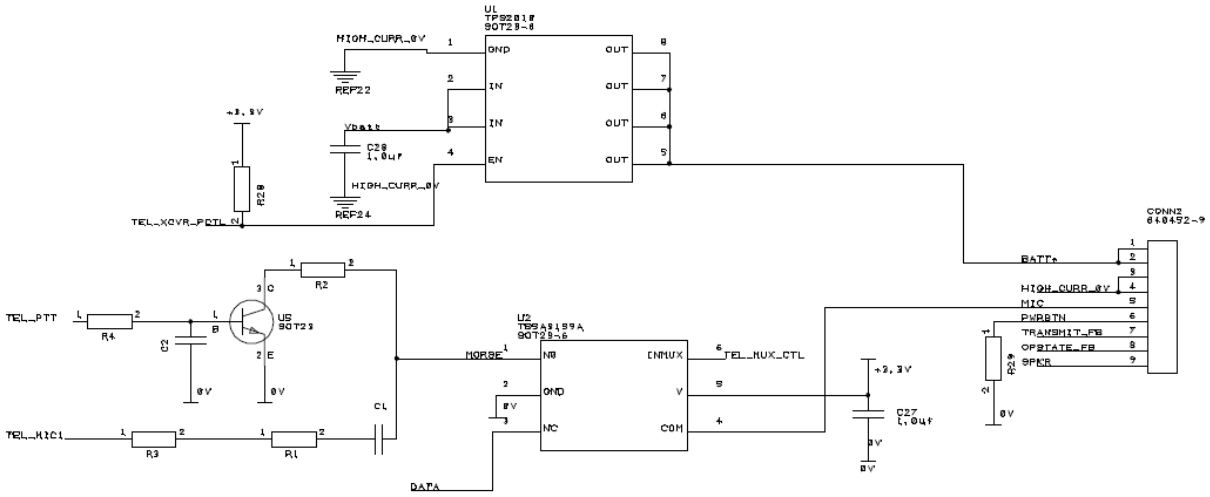

Figure 3. The telecom circuit consists of three main portions aside from the transceiver: the data/Morse multiplexer, PTT circuit, and high current power switching IC.

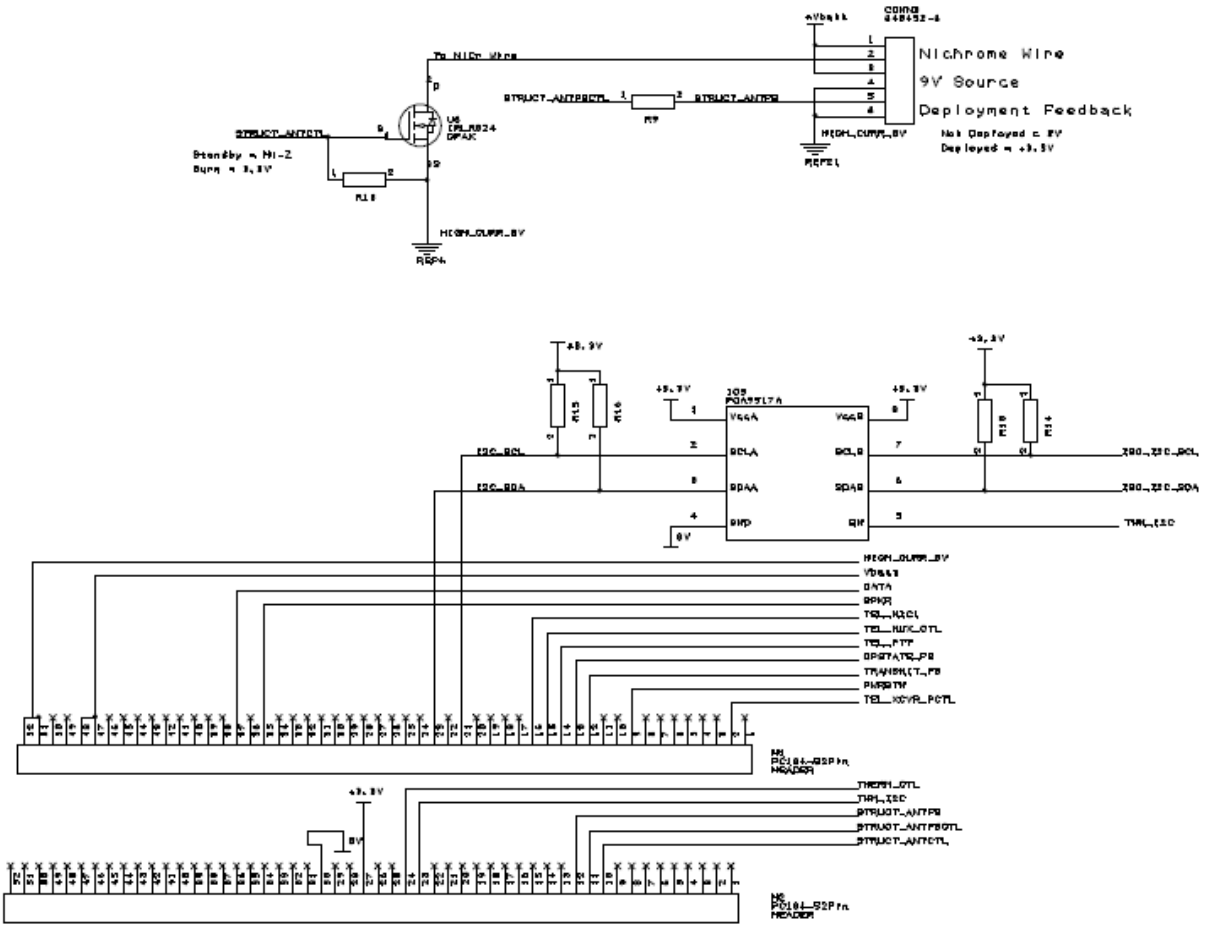

Figure 4. The structure circuit in the upper portion of this figure consists of MOSFET and a feedback switch and the bus interface consists mainly of the 12C isolator other than the PC104 headers.

TEMPERATURE MODELING

The temperature modeling for the satellite is very critical since the satellite is expected to experience a wide temperature range. It is important that this temperature range is within the operating range of the ICs and even more important that the battery's temperature to not fall outside of its range. Otherwise, the battery's capacity will degrade and will no longer receive a charge. The temperature distribution within the satellite is no easy task, and to derive an accurate temperate profile, a finite element modeling program should be used. Although there are many such programs capable of doing this, the program chosen is called CFDesign.

Aside from calculating the steady state temperature of critical components within the satellite, temperature evaluations will be made on specific points over time to determine the time response of the temperature sensitive components within the satellite. By knowing this, the maximum time the satellite can be in the sun or in the dark, based on the operating temperatures of the battery and some of the ICs, can be determined and compared to the operating temperatures of the critical components within the satellite. If it is determined that the components will get too cold or hot, then the heat will need to be distributed so that components remain in their operating temperature range.

Data acquired by CalPoly SLO's CP3 temperature sensors indicate that at an orbit with an apogee of 787.5km and perigee of 659.5km the temperature fluctuations were at most +/-30degC. Since our orbit is circular and at an altitude less than the smallest dimension of the CP3 orbit, it is predicted that our temperature swing will be less than +/-30degC. If this is so, the internal temperature of the satellite will never be lower than -30degC or greater than 30degC therefore thermal insulation or heaters would not be required.

VIBRATION ANALYSIS

The harshest dynamic environments experienced by the satellite will be during launch. Due to the harsh dynamic loads due to vibration experienced during launch, it is most probable that things will fail before the satellite's mission begins! As instructed by the project manager of the LEONIDAS project, the satellite should withstand an axial acceleration of up to 12.5Gs. The maximum lateral acceleration due to the spin of the booster was also calculated to be at most 6Gs. These are the maximum accelerations that any of the SPARK 1 payloads is expected to experience. The axial accelerations are due to forces being transmitted from the launch vehicle to the satellite due to vibrations between stages and shock during stage separations. These maximum accelerations are not expected to occur at all times, but randomly and during the most violet frequencies of the launch. It is important to know at which frequencies these potentially damaging vibrations will occur so that the interface between the satellite's structure and the circuit board stack can be tuned so that the natural frequencies within the stack does not overlap these frequencies.

For launch vehicles with an established heritage, a plot called a Power Spectral Density plot or PSD plot can be obtained from the vehicle's users' guide to identify the most energetic vibrations for the launch. However, since the SPARK 1 payload fairing for the launch vehicle is still under development, these frequencies are not yet known. Instead, we were instructed to use frequencies from the PSD plots that were published in the DNEPR safety compliance requirements document for the DNEPR launch back in 2006 and apply the 12.5Gs to be the maximum axial accelerations at those frequencies.

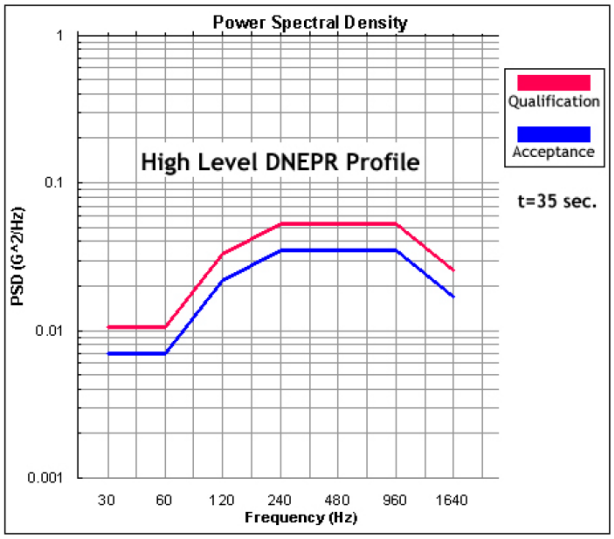

Figure 4. High-intensity random vibration PSD plot for DNEPR launch vehicle.

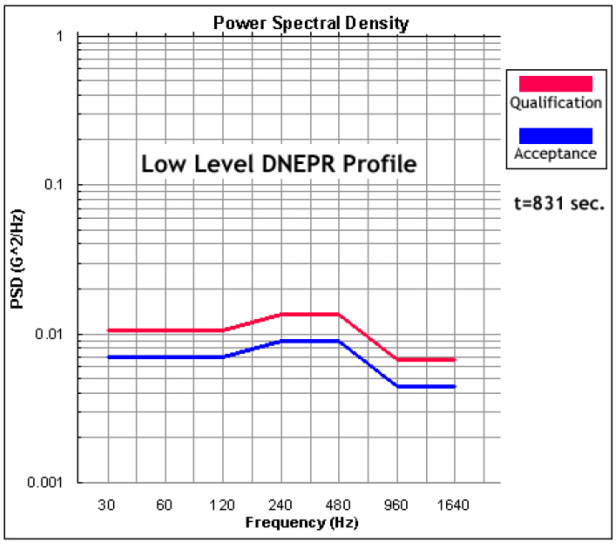

Figure 5. Low intensity random vibration PSD plot for DNEPR launch vehicle.

Since the vibration response through the launch vehicle's structure is random as opposed to periodic, a PSD chart will plot the mean square acceleration at a given frequency. The frequencies in which the vibrations are most intense are indicated by the highest points of a PSD plot. Therefore, the frequencies in which we can expect the most violet vibrations to occur and are between 240Hz and 960Hz and the maximum acceleration expected at these frequencies are expected to be no more than 12.5Gs. Since the payload faring for the SPARK 1 is still in development, the PSD data for our specific launch vehicle is not available. Instead, it was recommended that the team uses the DENPR PSD profiles as a minimum requirement to meet for now.

SOLDERING PREPARATION AND STANDARDS

Since the satellite will be under relatively large accelerations for very short periods of times, it is critical that there be a standard in place for soldering of PCB components onto the PCBs. Although there are many soldering standards already established by well known organizations such as NASA and the ESA, the team does not have all the resources to adhere to all of these standards. Therefore, only ones deemed important to follow by the team will be chosen as standards for our team. It is important to note that the reasoning behind choosing to follow standards is to ensure that that the solder joints mechanical characteristics of the joints are sufficient to survive the vibrations of launch. It is especially important for the team to develop a soldering ethic that prevents cold solder joints as they are brittle and can fail under vibration.

One of the critical parameters in preventing cold solder joints is a high enough solder tip temperature. It is very important that all solder within a joint "flows". This means that the lead/tin alloy must melt and all the flux within the joint must be in its liquid state. In addition to a minimum temperature, it is also important to not have the tip as too high of a temperature. Otherwise excess heating of the component pins can damage the component. In addition, there is a maximum time of contact that is governed by the time required to flow the joint. ESA is currently in the process of renumbering and reissuing their standards. Two of three batches of

standards have already been released with the third and final batch scheduled to be released by the end of February. Unfortunately, the standards for manual soldering are part of the third batch so a reference cannot be made here. So an older set of standards will be referenced.

ESA's space product assurance standards for manual soldering of high reliability electrical connections states that for normal soldering of electronic components, **a soldering-bit temperature of 280 ºC is recommended**. It also states that at **no instance shall the solder-bit temperature exceed 330 ºC**. One exception allows the soldering-bit to be at temperatures up to 360 degC for joints heat sinked or for large PCB ground planes.

In addition to the soldering temperature, it is also important to clean and demoisturize the PCBs prior to soldering. According to the same standards as above, **PCBs should be baked in an oven at 90 ºC to 120 ºC, depending on the laminate materials, for a minimum of 4 hours, or by a vacuum bake at a lower temperature.**

CONCLUSION

This paper revisits the design of the shareboard and outlines the modifications from the design presented in the last final report. A brief discussion of the temperature profile modeling for the satellite was made along with identifying the most violent vibration frequency and acceleration magnitudes for the launch. Then finally a more detailed discussion was made for soldering standards that are being proposed to the team to ensure the prevention of cold-soldered joints that can be a sort for entire satellite failure during launch. The bulk of this report was spent on predicting the launch loads that the satellite will be under and the temperature range while in orbit based on CalPoly data. Since the launch loads include violent vibrations resulting in accelerations up to 12.5Gs, a brief look was made into identifying proper soldering-tip temperatures according to the ESA to prevent cold-soldered joints that can fail during launch.

ACKNOWLEDGEMENTS

Although this report only contains work completed over a single semester since the submission of the previous final report for this subsystem, it should be mentioned that the Hawai‘i Space Grant Consortium has provided the conduct to formalizing the design process of the thermal and mechanical subsystem of the Kumu A‘o cube satellite. Without their aid, the progress of this subsystem would most likely be less direct. Much appreciation goes to Dr. Shiroma and the Hawai‘i Space Flight Laboratory for providing us the facilities to meet and work as a team. I would like to also thank all of the Kumu A‘o cube satellite team for their aloha spirit and teamwork. Specifically, I would like to thank Mr. Jeremy Chan and Mr. Zachery Lee-Ho for their guidance with designing the share board.

REFERENCES

European Cooperation for Space Standardization (1999) ECSS--Q--70--08A Space product assurance: The manual soldering of high-reliability electrical connections. Requirements & Standards Division Noordwijk, The Netherlands

Jones W. (2008) The Kumu A‘o Cube Sat Share Board. *Undergraduate and Graduate Fellowship Reports*, pp.93-107. Hawaii Space Grant Consortium, Honolulu.

KUMU A‘O CUBESAT TELECOMMUNICATION SUBSYSTEM FRABICATION, TESTING AND PROTOCOLS

Isaac C. Rodrigues
Department of Electrical Engineering
University of Hawai‘i at Mānoa
Honolulu, HI 96822

ABSTRACT

After preliminary tests on the Telecommunications subsystem, the entire Telecommunications Subsystem was prototyped to verify a successful communications link. The Telecommunications Subsystem has been fabricated and integrated into the Engineering model. With the near completion of the Telecommunications hardware integration, a telecommunications protocol has been designed to address unavoidable communications issues.

INTRODUCTION

The Kumu A‘o (source of learning) CubeSat project began in the summer of 2007. The project originated from the four founding students from the LEONIDAS project and expanded into a team consisting of eleven electrical and mechanical engineering students. A satellite project is significant in giving engineering students at the University of Hawai‘i hands on experience in space exploration from concept design to operating a low earth orbiting (LEO) satellite. The Concept Design, Preliminary Design Review (PDR), and the Critical Design Review (CDR) were accomplished in the fall of 2007. The telecommunication subsystem has procured components and has moved from the component off the shelf (COTS) integration and testing phase to the Printed Circuit Board design of the modified TinyTrak4 TNC and the Shared Board, which will host the Yeasu VX-3R transceiver as well as power enable and Morse code toggle. The Telecommunications Subsystem will provide software integrated custom telecommunications protocol that has been designed to custom fit the Kumu A‘o CubeSat. The protocol will compensate for the unreliable link generated by spin as well as an unknown antenna orientation due to the lack of a dynamic attitude control system.

INTEGRATION AND TESTING

Prototyping

Prototyping is an integral part in the fabrication of the design. Prototyping involves a physical representation of a PCB schematic design. Prototyping was used to test and confirm the design concept of our space station and obtain actual results. The actual results were used to adjust the original design to compensate for any theoretical losses. Figure 1-1 is the prototyped version of the modified TinyTrak4 and the telecommunications portion of the shared board. The prototyped versions of the components were implemented on perf boards as bread boards are highly unreliable due to the unknown state of the copper plate beneath the leads. The size of the prototyped TNC and Shared board circuits are duplicated exactly to the size of our PCBs. This is not possible in highly congestive circuits as the size of the components used on a PCB is severely reduced. The application of a perf board in prototyping provides a more secure

prototype, less susceptible to connection losses. When the design concept is finalized and proven to work we can move on to designing the PCBs that will be used.

Prototyping the TNC and the PTT/Morse Code Enable were the first steps in prototyping the Telecommunications subsystem. The TinyTrak4 had been verified to work, but changing the design of the TinyTrak4 and linking the modified TNC to The MSP430 was yet unverified. Upon Completing a new schematic and Block diagram representation of the Telecommunications subsystem each component was prototyped to confirm signals and voltage levels. Following successful testing of each main component within the telecommunications subsystem each component was connected for further integration of the subsystem.

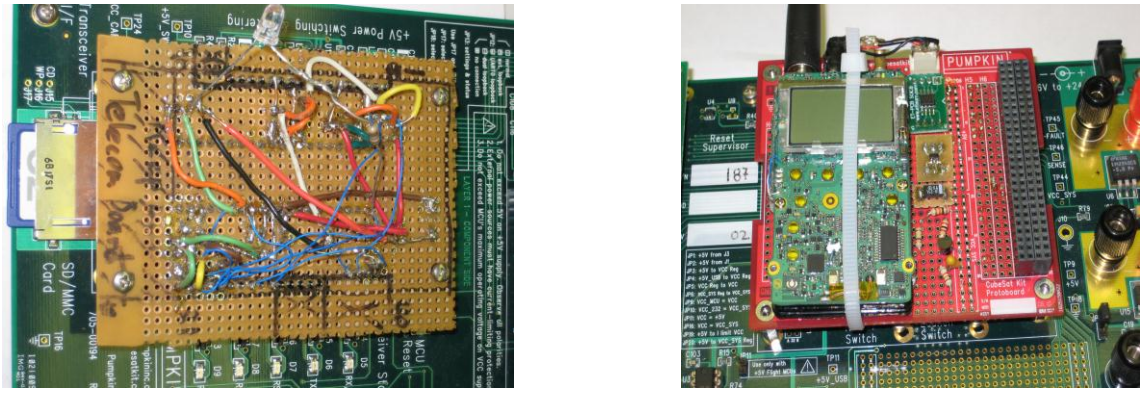

Figure 1-1: Modulated Telecom Subsystem mounted on development board

TNC Testing consisted initially with replacing the TinyTrak4 with the prototyped version and verifying that the modified version could sill carryout the same function as the TinyTrak4. The entire circuit was initially prototyped and with each successful test expendable components were removed. The final test consisted of the modulated TNC being able perform the same operations as the TinyTrak4, except it was modulated to its actual size and able to operate solely with the MSP430.

Prototyping affords the opportunity of being able to confront quickly things that may have been overlooked in the design stage. For example, one such problem was the type of feedback and control signals we would like to send from the Yeasu VX-3R into the microprocessor. After determining which signals would be appropriate the corresponding reference points were accessed to remotely control the transceiver.

The shared board contains 4 circuits primary to the Telecommunications subsystem: Transceiver Power Enable, TNC/ Morse code mode switching, Morse code PTT circuit, and the Transceiver. Prototyping the shared board verified that switching between normal mode and Morse code as well as verifying that the feedback and control signals operate as expected.

Flat Sat

The Kumu A‘o Flat Sat, shown if Figure 1-2, consists of the prototyped versions of each subsystem integrated together. Fabrication of the prototyped Flat Sat gave us insight on how the different subsystems will be connected. As the communications system evolved the Flat Sat was referenced the ensure compatibility with the system before fabrication and integration. The Flat Sat also addressed initial issues of integration between the separate subsystems. For the

telecommunications subsystem the FlatSat was able to simulate a secure data link between the space station and the ground station. The telecommunications testing done with the Flat Sat will be mentioned later, but the prototyped Flat Sat addressed issues and tangible result that helped illustrate how the telecommunications subsystem would integrate with the rest of the CubeSat.

The Kumu A‘o FlatSat was the first stage in prototyping. The FlatSat is used to confirm that the prototyped designs of each subsystem will be able to integrate with one another. The FlatSat hardware components for telecommunications consist of the modulated shared board and the modulated TNC circuits. Both components are connected to the CubeSat Kit Development Board.

The testing of the telecommunications subsystem consisted of verifying switching between Morse code and the TNC communications, verification of the feedback and control signals from the transceiver, and acquiring successful packetization and depacketization of data packets by the TNC. Test software was developed to enable the FlatSat to operate on its own. The FlatSat was tested to see if we were able to access a menu and retrieve data from it while it was remotely operating. Successful transmission and reception of both Morse code and Data packets verified that the design of the telecommunications subsystem was functional.

After the test software was loaded onto the Development Board, ground station simulation was performed by connecting a transceiver to a TinyTrak4 to demodulate the signal. The ground station computer used Tera Term Pro to access the menu of the test software and finally send and receive data.

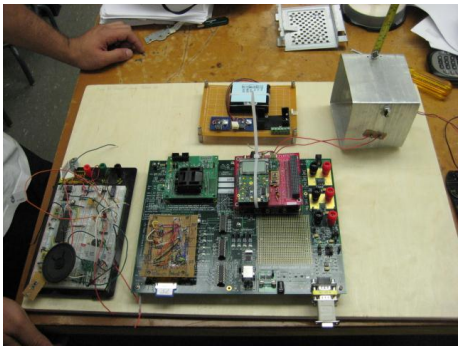

Figure 1-2: FlatSat: C&DH & Telecom (bottom middle, Thermal (Bottom left), Electrical Power systems (Middle Top), Antenna Deployment (Top Right).

Printed Circuit Board (PCB) Design

The PCBs . Using PCB Artist there is a multitude of information needed that would facilitate the fabrication process. Initially we standardized the components on our PCB. Parts must be created for the individual components on the PCB. The parts can be created through various standards already incorporated in the program, for example a Dual Inline Pin chip. The pin allocations can then be specified on the created part to ensure that each lead is connected to the correct pin. After all the parts are created, we were able to generate schematics for our PCBs that will show how the individual components are connected. Once the components are

connected we can generate a model of the actual PCB board where we were able to place the components on the PCB model. The correct orientation of the components on the board can maximize available space. In the PCB model schematic we can also specify the layer on which each lead will be. Once the PCB model is completed and verified at can be sent for fabrication.

PCB Fabrication

In Figure 1-3 we can see the populated two layer PCB board used for both PCBs. The boards were fabricated with the leads specified by the PCB model. With our standardized parts we soldered our parts onto the board. As you can see in Figure 1-3 the TNC PCB has extra room and was a relatively small circuit. On the other hand the shared board needed extra room to fit the transceiver. Initially the transceiver did not fit but after a couple revisions we were able to conserve enough space to fit the transceiver comfortably.

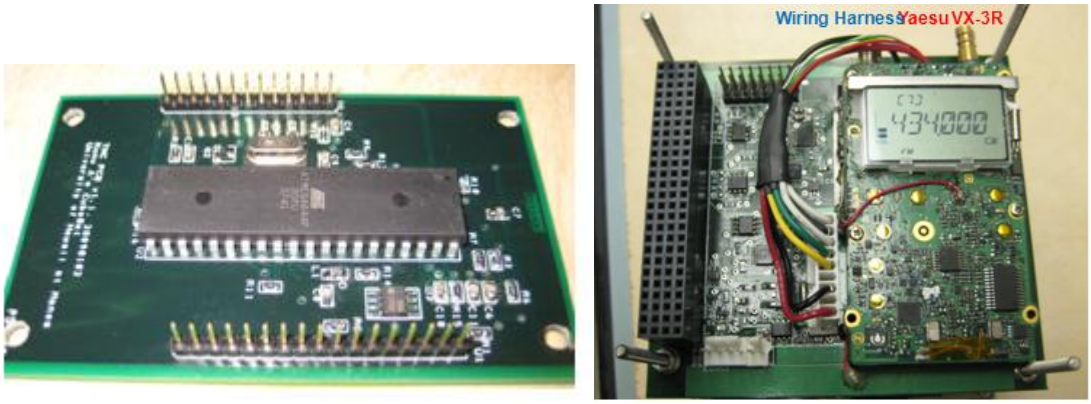

Figure 1-3 (Left) TNC PCB (Right) Shared Board PCB w/ Yeasu VX-3R transceiver

TELEMETRY/TELECOMAND PROTOCOLS

With an unreliable link generated by undetermined antenna positioning due to rotation created at deployment and a non dynamic attitude control system. The telecommunications team developed a communications protocol that would address this unreliable link and provide maximum possible data transfer. Our telecommunications protocol is based off the OSI model shown in Figure 2-2 and will contains layer 2 through 4 implementations. The protocol will be implemented through software in the MSP430 on the space station as well as in the ground station software. The protocols generated on the MSP will be programmed in C and in JAVA at the ground station. Working with the Command and Data Handling subsystem our protocol task force will program the protocols into our software to be implemented. Figure 2-1 is a block diagram showing how an Unreliable Link (UL) data packet will be generated from an initiator and how a UL protocol Packet will be read and assembled at the target to be read into the processor. The source and destination points of a UL packet are referred to as the target and initiator. The flow diagram shows that on inbound packets after passing through the transceiver and the TNC and being depacketized a controller will determine the packet type and further depacketize the data before being stored and processed. The packet types and their purposes will be explained later. On outbound packets it should be noted that the packet type is assigned before modulation and implementation of layer 1 and 2 protocols on the data.

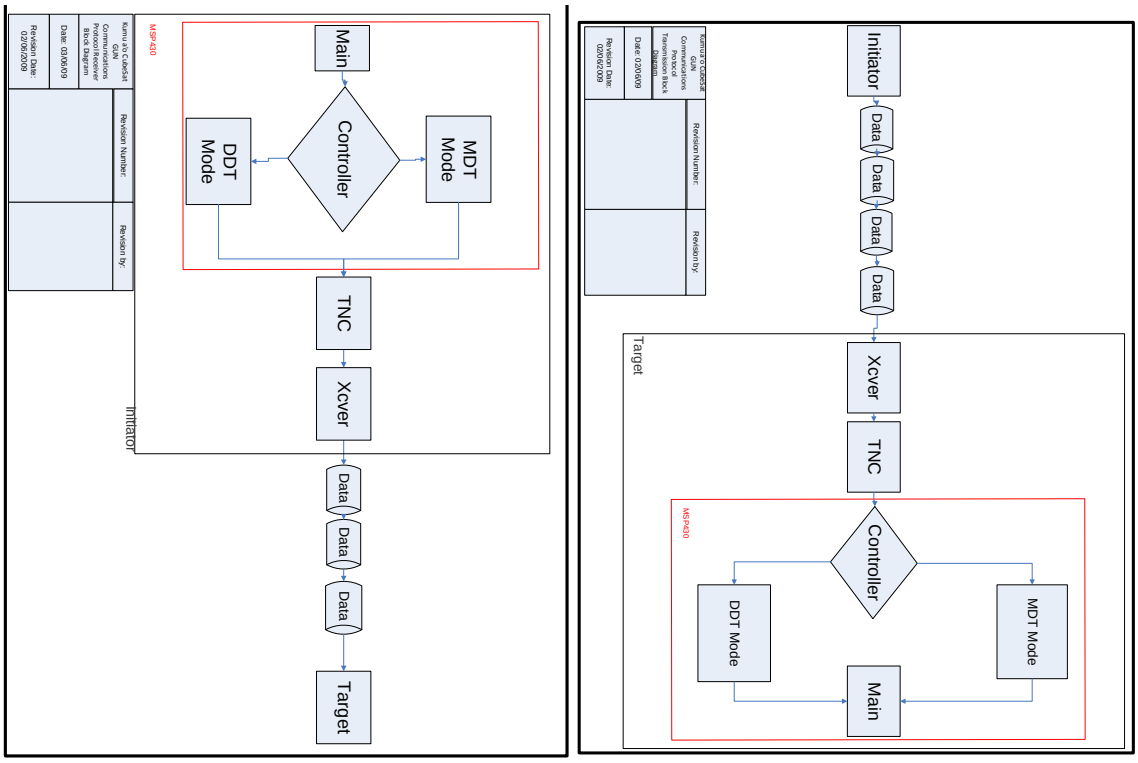

Figure 2-1: Data flow block diagram for Target and Initiator

Determining an effective form of attitude control and an antenna design that works on a CubeSat is an extensive task. The ineffectiveness of these systems leads to an ineffective communications system. The CubeSat generates unreliable links due to its unknown antenna orientation at any given time. An attitude control system, using magnetometers for example, would orient the CubeSat in the direction of the Earth allowing us to orient the propagation of our signal toward the earth. The attitude control system on the Kumua'o CubeSat has yet to be developed; therefore the problem exists of an unknown antenna orientation. An isotropic radiator, which generates a signal in all directions, could be a solution, but isotropic radiators are very hard to develop and CubeSats are limited to only a small amount of power. This type of antenna would transmit EIRP in all directions with a much weaker transmit power than that of a Dipole or Monopole Antenna. The solution relies therefore in the way in which transmissions and receptions are carried out, also referred to as telecommunications protocols. The ensuing portion of this report will give a detailed description into the design of the Kumua'o CubeSat and the solution to this communications problem.

Unreliable Link Communications (ULC) protocol

The Unreliable Link Communications (ULC) Protocol communications protocol consists of a controller and two modes of transmission DDT and MDT. DDT is used for initial communication and will be able to effectively send smaller amounts of information. It will be used for short commands usually associated with transmissions from the ground station. MDT will be used for Bulk data transfer and will be able to continuously transfer data per window of communications. MDT mode will be able to send mass amounts of data and is associated with CubeSat to ground station communication. Involved in the communication will be an Initiator

and a target. The Initiator is sending DDT and MDT data packets and the target will be receiving those respective data packets.

Controller

There are several parameters that the controller will be responsible of controlling. The request and deliver parameter will read in successfully received packets and determine which mode of transmission will be used based on the data requested. The controller will also be responsible for block sizing which will determine the begin block and end block of each data packet. Each block will have a transfer session number to record the last successfully received packet, which will be recorded to be sent at the next available window after a connection has been established. The controller will also be able to send data into the Microprocessor for reprogramming once a large data array has been accumulated. For transmission the controller will be ingrained into the software to make it easily accessible to packet information, this will also omit the need for a separate microcontroller or processor. The receiver controller will read in data packet types and rout the packets to the appropriate mode of verification and reconstruction, which are the MDT and DDT modes.

Direct Data Transfer Mode (DDT)

DDT is responsible for status and short report aspects of operation. When a reliable source is attempting to connect to an unreliable destination DDT mode will repeatedly send a single data packet for specified time intervals until the full packet is received. DDT mode will attach a DDT header on a data packet consisting of an initiator ID and the transfer session number, which will let the ground station know which data packet, was successfully received. When the timer has expired DDT mode will cease and wait for a DDT mode reply. When receiving a DDT mode transmission, incomplete data packets will be discarded, which means there will only be error checking and not error correcting. And the target will be set on a timer to receive the inbound data packet. When the entire packet is received the command will be sent to the processor to be read. In order to determine whether or not a full data packet has been received there be a check sum that will verify the packet in its entirety. DDT mode relies of an interval of stable connection in order to transmit and receive full packets of data.

Mass Data Transfer Mode (MDT)

As stated above MDT mode is responsible for bulk data transfer. The MDT packet is received from the controller and then sent out. Communication is successfully achieved by breaking up large quantities of data into smaller pieces and adding a position number to each block into the header. The data is randomly sequenced and then sent to a target. A timer transmits the signal for a specified unit of time, and then the initiator will await confirmation from the target on which packets were received. A new array is then created of the packets that were not received on both sides, and then retransmitted for confirmation. In each successive transmission the data is continually randomly oriented until confirmation that all data has been successively transmitted and the entire message has been recreated. The receiver will consist of an algorithm to reassemble the bulk data packet. This will consist of taking the spotted data array and continue to reconstruct portions of the packet by reading the position number in the header until the full data packet is constructed. The verification of the data packets integrity will be received by a check sum, and like DDT mode will only be concerned with error checking and not error correction.

Because of the random orientation of our signal propagation we could effectively send signals in all directions as well as be able to communicate with other unreliable targets and initiators. For example, if other CubeSats were in the same vicinity using the ULC communications protocol the two CubeSats would be able to relay information back and forth to one another creating successful communication with unreliable links. Enough CubeSats oriented with this protocol could create a network of CubeSats relaying information based on their position.

Level 1 Protocols

Using the OSI model for networks, as seen in Figure 2-2, layer one is also referred to as the physical layer. The physical layer determines how data is transmitted in its most fundamental state to a medium. It is concerned with the interaction of a single device with a medium and controls access, flow, and modulation in the medium. Layer1 will be a protocol to determine the form of the information whether it be Binary data or a Modulated Audio Frequency Shift Keyed signal used to represent the binary data.

OSI Model			
	Data unit	Layer	Function
Host layers	Data	7. Application	Network process to application
		6. Presentation	Data representation and encryption
		5. Session	Interhost communication
	Segment	4. Transport	End-to-end connections and reliability
Media layers	Packet	3. Network	Path determination and logical addressing
	Frame	2. Data Link	Physical addressing
	Bit	1. Physical	Media, signal and binary transmission

Figure 2-2: OSI Model

RS-232

Recommended Standard-232(RS-232) is used in our system as the Layer 1 protocol between the MSP430 and the TNC. It is a standard for serial binary signals connected to Data Terminating Equipment (DTE). A TNC falls under the category of (DTE) because binary data inputted on the processor end and an audio signal is outputted at the transceiver end. RS-232 determines the standard in which the binary data is transmitted over the channel until it reaches the TNC.

Audio Frequency Shift Keying (AFSK)

AFSK is the layer 1 protocol showing how the data is represented as it is transported from the TNC to the transceiver and transmitted over free space. AFSK is a form of modulation. It is applied by representing digital data as changes in frequency or pitch of an audio tone. The result is an encoded signal that is able to be transmitted through our transceiver. As mentioned above AFSK is far more inefficient when compared to other modulation techniques, but it passes through equipment intended for audio, such as a radio, very easily. In effect The AFSK modulation technique characterizes the data from transceiver to transceiver.

Level 2 Protocols

Layer 2 is referred to as the Data link layer. The Data link Layer provides a procedure for transport between network entities and also error correction. In a layer 2 protocol the bits from level one can be organized onto frames encapsulating the data transferred. It is important to note that the protocols developed for this project will work in unison with the Ax.25 and Kiss protocols. As our layer 2 protocols will designate a frame it will be encapsulated with in either the KISS or Ax.25 protocol depending on whether the information is before the TNC or after the TNC.

KISS

"Keep It Simple, Stupid" (KISS) is a layer 2 protocol used with a TNC that provides direct computer to TNC communication using a simple protocol. The TNC replaces the Ax.25 protocol from the computer with KISS protocols for transmission. Using KISS protocols is a function of the TinyTrak4 and therefore must be incorporated into the design. Even though KISS as an interface directly to the processor is not commonly used the TinyTrak4 provides transitions between KISS and Ax. 25 so that data arriving at the processor is in Ax.25 format and no further conversions are necessary.

Ax.25

Ax.25 is a commonly used protocol for the data link layer for data transmitted out of the processor. It is designed for use by amateur radio operators, which important in trying to qualify for amateur frequencies. Using a common protocol lessens the need to publicize extensive information so that all amateur operators have access to the space state as is a requirement for qualifying for an amateur frequency. The Ax.25 protocol encapsulates data in to Ax.25 frames in a way that can successfully pass over a serial link to a TNC. In effect the Ax.25 protocol determines the frames to work with the RS-232 physical layer protocol.

ULC protocol layer 2

Due to our unreliable link our data must be framed in a separate way prior to the Ax.25 frame. Ax.25 and KISS protocols will still determine the frames so that the data can be successfully transmitted in their respective mediums, but our layer two protocol provides an error check on the physical data to determine if data has been corrupted due to the unreliable link so that the packet in its entirety can be discarded. Based on the information needed to be sent our higher level protocols will determine packet size and numbers which will determine the frame need for transmission.

HIGHER LEVEL

DDT &MDT

DDT & MDT can be considered layer 3 protocols for they determine functional and procedural means of transferring variable length data sequences. Based on the information needed to be sent the controller will determine which mode of transmission is need. Once the packeting and numbering is determined the data is then prioritized for data burst lengths then sent to layer 2 for a check sum that can be used at the receiver for error checking. At the receiver side the packets are individually checked for errors and either passed to layer 3 for processing or discarded. The packets that pass layer 2 are directed by the controller to the appropriate mode for either processing (in DDT) or reassembly and storage (MDT). In the case of a blackout in the

channel a request for retransmission can be sent with assembly state information so the initiator can re prioritize and retransmit.

CONCLUSION

The Telecommunications Subsystem hardware has been tested and proven to work effectively. Further design and implementation is required to ensure functionality in space. Successful communication is largely dependent on the design and effectiveness of the system. The Electrical Power and Command and Data Handling subsystem play a large role in the design of a Communications subsystem. With the ULC protocol developed, the CubeSat will be able to function and transfer data despite an unreliable link. The implementation of the protocol has yet to be completed, but upon completion testing will be done to ensure effective communication.

ACKNOWLEDGEMENTS

CubeSat has taught me many fundamental concepts of being an engineer that are not learned in class. I would like to thank the Hawai‘i Space Grant Consortium and the Native Hawaiian Science and Engineering Mentoring Program for assistance and support for our project as well as my mentors Byron Wolf and Lloyd French for guidance and wisdom.

REFERENCES

Byonics. (2008) TinyTrak4 hardware manual.

Yeasu. (2007) VX-3R operating manual.

Holger Karl. (2005) Protocols and Architecture for Wireless Sensor Networks. Wiley.

http://en.wikipedia.org/wiki/OSI_model. 10 June 10, 2009

Indra Widjaja. (2004) Communication Networks Fundamental Concepts and Key Architectures.

Mcgraw-Hill.

KUMU A‘O CUBESAT: THERMAL SENSORS ON A CUBESAT

Tyson K. Seto-Mook
Department of Electrical Engineering
University of Hawai‘i at Mānoa
Honolulu, HI 96822

INTRODUCTION

A. Abstract

CubeSat is a project that will develop, test, launch, and operate a functional satellite at a fraction of the cost of a commercial satellite. The CubeSat project provides a way for the students to learn the various steps involved with mission design within a reasonable amount of time. Currently at the University of Hawai‘i at Mānoa, UH students are designing CubeSat called the Kumu A‘o CubeSat. The Kumu A‘o’s primary objective is to develop a fully functioning cubesat bus to serve as a prototype for future UH cubesat missions. CubeSat’s, in general, have many different mission. However, the Kumu A‘o’s mission is to observe the thermal environment a CubeSat endures while in space. A temperature gathering routine will be executed to gather thermal data on each side of the CubeSat. The design will be using thermisters as sensors and the MSP340 micro controller to gather the temperature data values. This will give information to the temperature ranges a CubeSat experiences while in space.

B. Background

The CubeSat is a valuable project to the industry and universities across the globe. Since commercial satellites are expensive and take years of planning, CubeSat is a great way for students to understand the basics of developing and operating satellite. The CubeSat will weigh about 1 kilo grams and will have a volume of 10 cm3. This is a much smaller satellite that will have a very reasonable cost, which will be a small fraction of manufacturing and launching large satellites, which is over $300 M. It will also take a more reasonable amount of planning, unlike commercial satellites. CubeSat allows universities to engage in satellite experience and space exploration at low cost. CubeSat, in turn, allows students to gain valuable knowledge and experiences for future careers and aspirations. The CubeSat project is best fit to accommodate the space industry in collaboration with colleges.

The UH CubeSat project mission goals are to present an engineering demonstration performed by UH students. The main objectives are to develop, test, launch, and operate Hawai‘i’s first launched CubeSat. In addition, this project is to also create a reference model for future students pursuing the CubeSat project in the future. We will also try to create a plug and play template that will allow easy exchange between different types of payloads. To achieve this we are first starting out with the CubeSat kit, which is manufactured by Pumpkin Incorporated. This kit provides us with bear minimum hardware such as, a chassis and a flight module, to help jump start our CubeSat design. The kit will also save us time in starting the CubeSat from scratch. Also so that there is more focus towards the analysis of the subsystems and to house the payloads. Our CubeSat goal is to have it survive for a period of three months in space and send us status updates.

The CubeSat student team is currently comprised of nine undergraduate engineering students; two mechanical engineers and seven electrical engineers. A former CubeSat student Byron Wolfe and professor Lloyd French, with JPL experience, will be available as the mentors and advisors to the CubeSat team. They will provide advice to the team of both technical and non-technical issues. However, decisions of project matters will be established solely by team members and the project engineer.

This progress report will take a detailed look at the design phase of the thermal sensor module of the command and data handling subsystem.

HARDWARE DESIGN

This section provides a description of the thermal sensor circuit and each of its components.

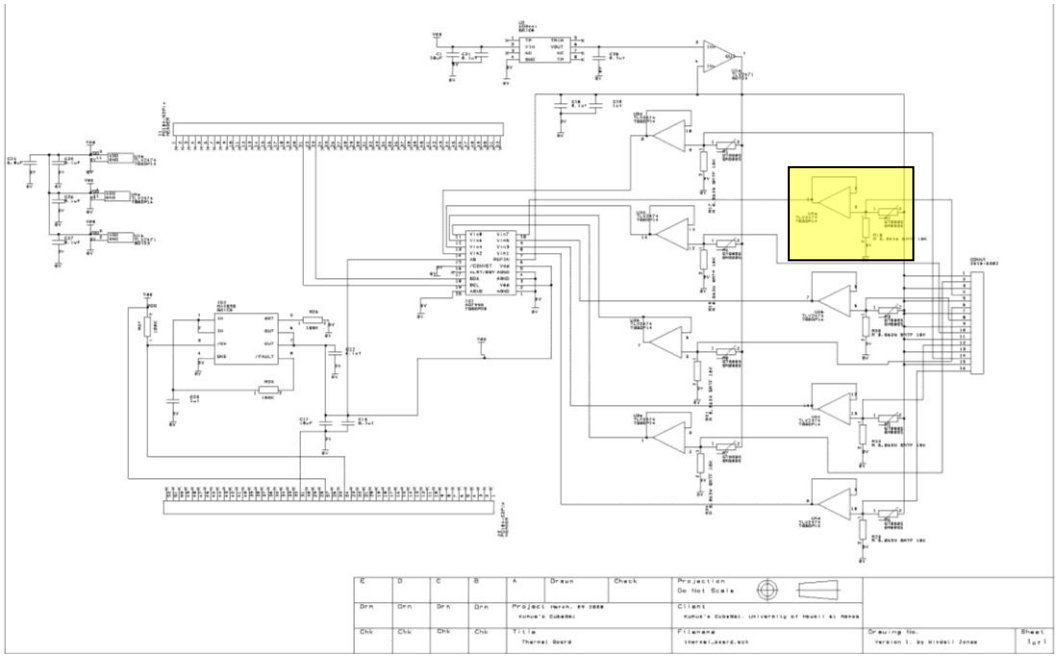

Figure A – Thermal hardware design layout

A. General Overview

Figure A shows our schematic design layout for our thermal sensor circuit. Starting from the top, we have our voltage reference chip which out puts an accurate low noise 2.5 volt signal to our thermiser sensors. It is then fed through a voltage buffer to increase the signals current so that more power may be drawn from that signal. This signal is then connected to our voltage divider circuit which contains the thermister. From there the signal is passed through another voltage buffer, which is placed here to maintain signal accuracy, then to the analog to digital converter. The analog to digital converter then converts the signal and sends the converted data to the MSP430 via the I2C protocol. Which is then stored into memory.

B. Voltage Reference (ADR441)

The ADR441 chip is a voltage reference chip that provides an accurate low noise signal to the thermister voltage divider circuits. This chip is used to maintain data accuracy for our temperature readings.

C. Thermister

Thermisters will be used as our sensors to measure the thermal characteristics of our CubeSat while orbiting. A thermister is a resister which varies its value depending on its temperature. This sensor was chosen because of it temperature sensing range. Although the circuitry involved in implementing these sensors are more complicated than our other leading choices, these thermisters had a range that was more suited for a space environment. We also chose to use these as our sensors because they are low cost and had good accuracy. The highlighted portion of Figure A shows how we will be using thermister in our circuit. Through this set up we can use the voltage divider equation to get the voltage across the thermister to check its voltage value. We then send that signal through a voltage buffer, which will help maintain signal accuracy, and then to the ADC. Once we've gotten the data from the analog to digital converter, we can then figure out the temperature taken by using the voltage divider equation again to get the resistant value of the thermister and comparing it to its resister to temperature chart.

D. Analog to Digital Converter (AD7998)

The analog output from the voltage divider is an input into the analog to digital converter's (ADC) input pins, pins 7 through 14. Pin 6 is used as the ADCs voltage reference and it will be getting 2.5 volts. Pins 18 and 19 are the I2C communication pins, where 18 is the SDA data line and 19 is the SCL data line. The address select pin will use pin 32 of the PC104 bus so we can control the I2C address of the ADC.

To start a conversion we must first set the configuration register. We can do this by sending a write sequence though I2C to the ADC. Then we can set the address pointer to the configuration register and then writing 16 bits of data to it. In the 16 bits the first 4 bits are "don't care bits," which are then followed by the input select bits. These are the bits you set to logic 1 in order to tell the ADC which inputs we want to be converted. The last 4 bits of data are alert bits which we will not be using. To retrieve data, we first have to set the address pointer back to the conversion results register then start a read sequence to the ADC through I2C. During the read sequence, the ADC powers up and automatically starts its conversion which takes about 3 micro seconds. The results are then stored into the ADCs conversion results register. The ADC will send 16 bits of data back to the microcontroller with the most significant bit being an alert bit, if we have set any alters, followed by 3 bits of data stating which input the next 12 bits of data was taken from.

Although The MSP430 microcontroller does have ADC pins, we chose to use an external ADC in order to reduce the cost of pin consumption. We also chose to use and external ADC to have the ability to power down the whole interface to reduce the cost of power consumption.

E. Inter-Integrated Circuit (I2C)

The I2C is a communication protocol with a five step process. The process consists of the start, address, acknowledge, data transfer and stop steps.

The start state is initiated by the bus master, which is typically a microcontroller. To issue a start condition, the bus master pulls the Serial Data line (SDA) line to a low then pulls the Serial CLock line (SCL) line to a low. This sequence of signals on the bus lines indicate to the bus slaves that an address will be broadcasted on the bus lines.

The address state is initiated by the bus master by broadcasting a 7 bit address of the device it wishes to communicate with on the SDA bus line. Along with 7 bits, an 8th bit is also sent to notify the device if it will be read from or written to. If the address matches the device, it will then proceed to the acknowledge state. If the address does not match the device, it ignores the rest of the following data until a stop signal is broadcasted on the bus.

The acknowledge state is a signal sent back from the chosen slave device to the bus master. This tells the master that the slave is ready to communicate. The signal is given by having the device pull the SDA line low until the master generates one clock signal on the SCL line.

The data transfer state is then initiated. This is where the slave device sends or receives 8 bits of data to or from the master. When all the data is finished being sent, a stop signal is broadcasted on the I2C bus lines.

The stop state is initiated by the bus master driving both bus lines back to high; first starting with driving the SCL line to a high signal followed by driving the SDA line to high signal.

F. MSP430 Microcontroller

The MSP430 is an ultra-low-power 16-bit RISC mixed-signal processor which is used for low cost and low power consumption systems. The microcontroller can be programmed in either C++ or C. since I am more familiar with C rather than C++ we will be programming the microcontroller in C. For this particular interface we will be communicating from the microcontroller to the ADC through I2C.

G. Power Switch (MAX890)

The MAX890 is a low voltage p-mos mosfet power switch. It will be used to shut down the whole thermal sensor system. The reason why we have this switch is so that we can save on power consumption. Since we are unsure how much power we may really need for the whole CubeSat, it is safer to be able to shut down the thermal sensors and turn it on only when we need to gather sensor readings.

SOFTWARE DESIGN

This section provides a description of what my software design for the thermal sensor circuit.

A. General Overview

Since there are many programmers working on the CubeSat, each routine may be implemented differently. This creates uncertainties on how my software routine will fit in with the main C&DH program.

The solution to this problem was to create a thermal routine so that it is independent of the main C&DH program. This will allow the routine to work well with other routines without conflicting with other routines. Not only will it be easier for the separate routines, but it will also keep them well organized.

For example, Instead of having one function read a sensor and calculate its value individually, there are two functions. One function that will read all sensors and store them in memory and, another that will read and convert the sensor value from memory when needed.

This also allows us to save power by turning on the system, read all 8 sensors at once, then immediately turning off the thermal system. Then analyze the sensor values at a later time. On the other hand, keeping the whole system on while individually reading and analyzing a sensor value will be inefficient in time and power.

B. C Language Structure Design

The C structure will contain 8 integer fields; sensor1 through sensor8. Each field will hold its respected sensor value taken from the ADC. Along with the field of this structure will contain several member functions. Each member function will have a unique task in manipulation of the structure field's. A member function is a function which is exclusive to the structure it is declared in. This minimizes data corruption from other routines within the system.

C. Data Members

In this C structure, there will be eight data members. The data members are unsigned characters (integers) that will the hold 16 bits of data retrieved though I2C from the ADC. The most significant bit will be an alert bit, followed three bits that tells us which sensor was read, and finally the last twelve bits are the value of the sensor.

D. Member Functions

This object will contain several member functions, which can be placed into three different function types. There is the constructor/destructor, accessor, or mutator function type.

With in the constructor and destructor type functions there will be two functions, an initiation and shutdown function. The initiation function will clear current sensor values, turn on the thermal system, and ready the ADCs registers for conversions. The shutdown function will turn off the thermal system.

With in the accessor function type there will be one main function, the get sensor function. This function will only be allowed to read, from the desired sensor value in memory, and return its value to the main command and data handling program.

With in the mutator function type there will also be one main function, the read sensor function. This is the function that will communicate with the ADC, through I2C, and attain the sensor's value and store them in memory.

E. Integration of thermal C structure

By keeping everything exclusive to the member functions only, it will keep program well organize and easy to use. The main command and data handling program will now only have 3 functions to call instead of having several lines to execute. Main program will just have to run the initiation, then read sensor, then shutdown function and it will have its sensor values in memory ready to be analyzed and processed.

F. Flow charts

In figures B and C are of the command and data handling flow charts. Tracing the flow charts will show how the thermal sensor routine fits with in the big picture of the main satellite program.

Figure B is a flow chart of the command and data handling main program routine. High lighted is a finite state machine that processes and polls all of the satellite's sensors. This is where the thermal sensor routine will fit in.

Figure C is a flow chart of the sensor finite state machine main routine. Highlighted is the path the program will take while running through to the thermal sensor routines. Once the program hits the thermal sensor (AD7998 ADC) block it will then run the three functions stated in section D.

Figure D is a flow char of the gathering of the sensor values. Where the boxes are the main functions and the ovals are the tasks within the function.

DELIVERABLE

The finalized thermal system will consist of circuitry and software components. The circuitry will be placed on the telecom printed circuit board with wire leads to each thermister. Six thermisters will be externally located and 2 will be internally located on the walls of the CubeSat. The software component will be apart of the main program as shown in the flow chats of figures C and D.

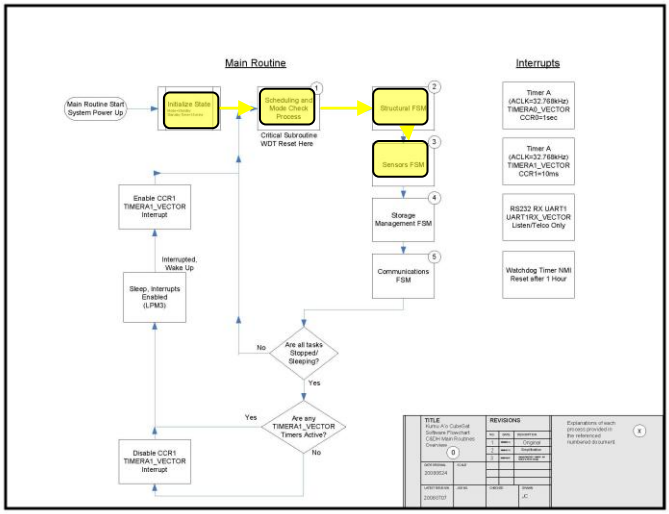

Figure B – CDH Main routine

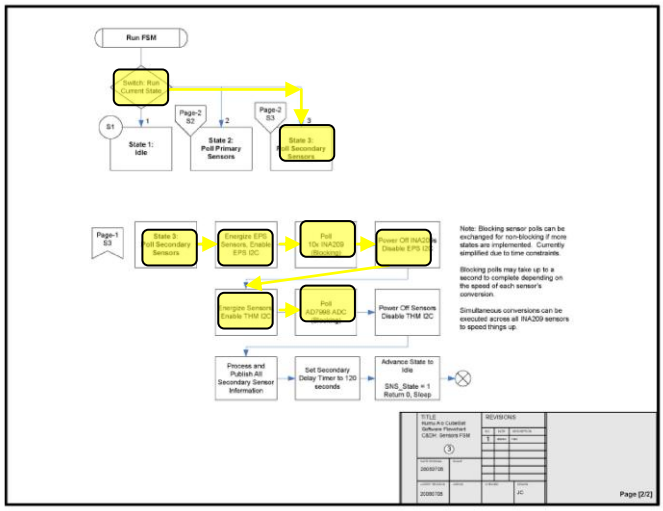

Figure C – Sensor FSM routine

Flow Chart of Thermal System Temperature gathering

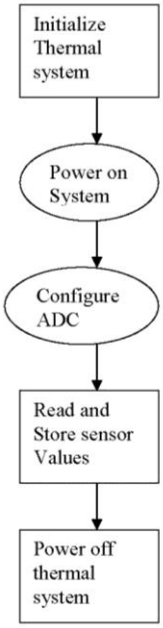

Figure D – Thermal Temperature gathering Flow chart

TEST PLAN

A. Hardware Testing

The first component to be tested will be the ADC. After a successful testing of the I2C communication we can now test the ADC. To test the ADC we will set up the circuit and program the micro controller to collect and display a set value in one of its ADC channels. This can be done with an external power supply. First we will test the limits of the ADC, meaning that we will test its max value and lowest value. This can be done by setting a channel of the ADC equal to the reference voltage of the ADC. There is a successful read if all bits displayed are high logic. If the result do not math the expected results then there maybe a problem with the ADC. We can verify this by also setting the channel to zero where we should get all low logic values. If all tests have passed, the ADC is verified to be in working condition.

The second component to test will be a thermister circuit. Since I2C and the ADC are validly working, we can now only worry about this circuitry. We will first start by setting up a circuit that will connect the processor, ADC, and a thermister together. The test will be to take an average temperature using an out side source then compare them to the temperature given by the ADC from the termister. If the temperature from the thermister is not similar, there is a circuit problem that will have to be debugged. If they are, we can verify it by heating or cooling the thermister to see if the temperature changes in its expected direction.

Once these individual components have been tested we can now move into the finalizing phase of the project.

B. Software Testing

To test the software we will start by testing the I2C communication. This test will be done with an LCD screen which can be written to through I2C. If this is successful, then I know that I2C is working. If it isn't there maybe code errors or hardware errors. An oscilloscope will be used to test for hardware failures. If there are no hardware failures, we should see square wave signals the oscilloscope for both the I2C lines. If there is a wave signal then we have a software problem. Debugging the code would be the next step. After we have successful communication, I2C is verified and now is proven to no be a problem of the system. Other than this the software should be the fairly easy to debug.

CONCLUSION

For the current status, for the thermal system, the research and design phase is completed. Since the design phase had just been completed, we haven't yet tested the circuit to find problems. Theoretically, this circuit should work; however, we may have issues with accuracy of the gathered data. The accuracy of our temperature depends on accuracy of our system. The next step is to prototyping, debugging and ultimately finalizing our system.

ACKNOWLEDGMENTS

I would like to thank the Hawai'i Space Grant Consortium for providing the opportunity for undergraduate research in sciences. I would also like to thank my mentors Lloyd French and Byron Wolfe who gave advices and supported me throughout the semesters.

REFERENCES

I²C. (2008, December 9). In Wikipedia, The Free Encyclopedia. Retrieved 08:49, December 19, 2008, from http://en.wikipedia.org/w/index.php?title=I%C2%B2C&oldid=256809889

Maxim-ic Website: Power Switch Available [Online]: http://www.maxim-ic.com/

Analog Devices Website: Analog to Digital Converter
Available [Online]: www.analog.com/en/analog-to-digital-converters/

KUMU A‘O CUBESAT: ELECTRICAL POWER SUBSYSTEM DESIGN

Jordan S. Torres
Department of Electrical Engineering
University of Hawai‘i at Mānoa
Honolulu, HI 96822

ABSTRACT

The objective of the electrical power subsystem (EPS) of the Kumu A‘o CubeSat will be to receive, store, and distribute the power required by the satellite. Solar energy will be received by solar cells that will be placed around the perimeter of the CubeSat. This energy will be converted and stored using a single lithium-ion battery. The battery will be monitored using a fuel gauge that the command and data handling (C&DH) will communicate with. From the battery, power will be distributed to the respected subsystems of the satellite through the use of DC-DC converters. All components of the EPS will be selected to be able to withstand the space environment. The fall 2007 semester was devoted to the design of the EPS while the spring 2008 semester was spent learning the PCB software and prototyping of the EPS. The fall 2008 Semester was spent prototyping the EPS as well as creating the EPS PCB board.

INTRODUCTION

The translation of “Kumu A‘o” is “source of learning”. The Kumu A‘o CubeSat will provide engineering students at the University of Hawai‘i of Mānoa with the opportunity to get hands on experience with a satellite project from “the cradle to the grave”. The Kumu A‘o CubeSat is a LEO (Lower Earth Orbit) mission, meaning the orbit of the satellite will reach the altitude of about 600 km. The Kumu A‘o Cubesat team is composed of electrical and mechanical engineers from the University of Hawai‘i at Mānoa. I am the EPS team lead with engineer Reid Yamura.

Prior to the fall 2007 semester, a requirements list was created by the previous CubeSat team. From the requirements list, the EPS established voltages and currents that will be required. With these parameters set, a tentative block diagram of the EPS was created. In October 2008, we were able to complete the preliminary design review (PDR) where each subsystem presented their requirements and possible designs for their subsystem. The first PDR that was given was incomplete and needed to be worked on. The EPS had several components that hadn’t been selected. By the second PDR, the EPS had made all component selections. With the second PDR, the EPS and the rest of the team would move on to the next stage of design.

The next step of the design process was the critical design review (CDR). At this design phase, every part of each subsystem should be finalized and ready for fabrication. The CDR was completed on March 2008. In the CDR, the finalized block diagram and the components of the EPS were proposed. In the CDR, the EPS introduced the expected power output factoring in rotation of the CubeSat and intensity from the sun while in space. During the time allocated for questions, key issues were brought up. One problem found was that one of our DC-DC converters didn’t provide enough current at the output. Another problem that was found was in the connections between the different components. Our presentation didn’t have a section that went over the specific connections between all the components.

DESIGN

At the end of the fall 2008 semester, the design of the EPS's block diagram was finalized. Many changes have been made to the components selected during the CDR. The finalized block diagram of the EPS can be found in Figure 1.

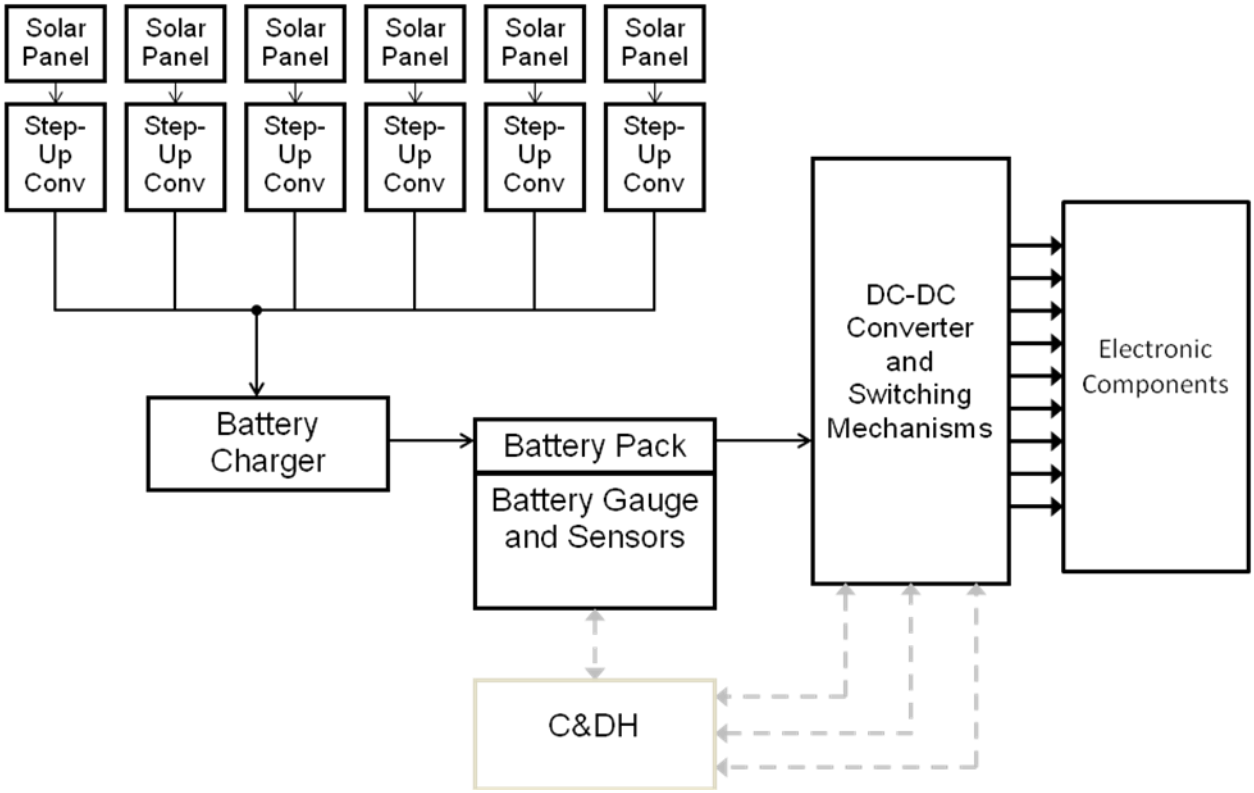

Figure 1: EPS Basic Block Diagram

Solar cells

Spectrolab's Ultra triple junction (UTJ) solar cells will be used for the flight model of the Kumu A'o CubeSat instead of the Improved Triple Junction (ITJ) solar cells previously selected. Each cell has an efficiency of 28.3%, with an output of 2.7 V and 456.4 mA when maximum power point is achieved. Each panel of the CubeSat will have two solar cells connected in series. Each panel of the CubeSat will then be connected in parallel, as shown in Figure 1. Connecting the panels in parallel will provide redundancy if one panel is not functional. Figure 2 shows a solar panel PCB populated with a set of test solar cells on board the Engineering Model (EM).

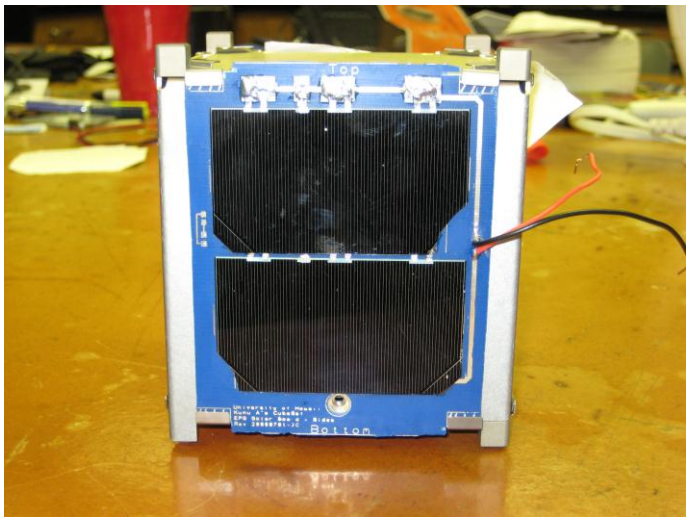

Figure 2: Populated Solar Panel on Engineering Model (EM)

The output voltage from each side of the Cubesat will be 4.46 V with a current of 450.8 mA when maximum power point is achieved. The EPS for the Kumu A‘o CubeSat will not have a maximum power point tracking system though. As a result, the solar cells will be operating at a power less than its full potential. Actual power output of the solar panel will be documented using a solar simulator. Each side of the satellite will also have a current sensor which will provide a way to determine the orientation of the satellite.

Battery charger

Since the Critical Design Review (CDR), the MAX1898 linear Li-ion battery charger has been replaced by the switch-mode LTC4001. This change was made for the higher efficiency obtained by the switch-mode charger. The prototyped circuit of the LTC4001 can be found in Figure 3.

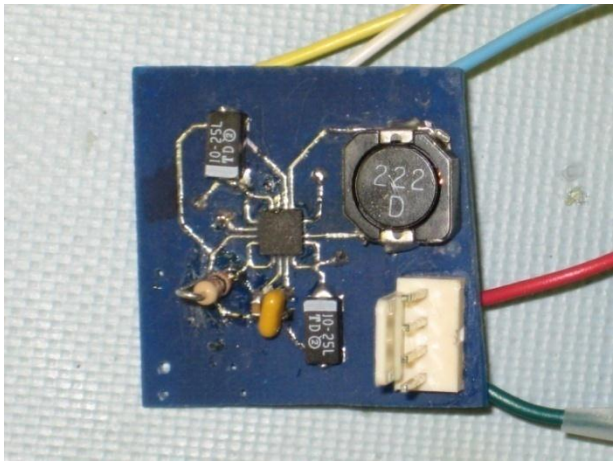

Figure 3: LTC4001 Switch-mode Li-ion Battery Charger

The battery charger was tested by using a variable power supply at the chip’s input and attaching a test battery at the output of the charger. The output of the charger was also monitored by a Digital Multi-Meter (DMM). The test battery used for this procedure is a Li-ion battery with a smaller capacity than the selected Saft battery. With the power supply set to 5 V,

the chip was found to be operational. The DMM showed the voltage of the battery increasing steadily. The LTC4001 charged the battery with the "constant current, constant voltage" characteristic that is required to charge the Li-ion chemistry.

Another change was made to the EPS in terms of design. The design used to complete the CDR stated that the EPS would not be able to charge and discharge the battery at the same time. This statement implies that the rest of the CubeSat will not be able to operate while the battery is being charged (during the sun times). Also meaning the charger would need to be turned off when the battery is being used to power the other subsystems. After reading the datasheet, it was found that the charger is capable of providing power to the other subsystems instead of only being used to charge the battery. The only drawback to this design consideration is that the load of the charger cannot exceed the output capabilities of the charger.

Battery

The battery selected for this mission is the Saft MP176065. The Saft MP176065 is a single lithium-ion battery and was chosen for its high capacity of 7 Ah and energy density of 26.25 Wh. The Saft battery has a mass of 146 g, which is within the allocated mass requirements set for the battery. The output voltage of the battery ranges between 2.5 V and 4.2 V, having a nominal voltage of 3.7 V. The procured battery which will be used for the Engineering Model of the CubeSat is shown in Figure 4.

Figure 4: Saft MP176065 Li-ion Battery

Fuel gauge

The IC that will be used to record the status of the battery is the BQ27200 fuel gauge. The fuel gauge will be used to read Li-ion batteries' temperatures, voltages, and currents. The IC is also capable of being programmed to monitor the battery's capacity. The prototyped circuit of the BQ27200 chip can be found in Figure 5.

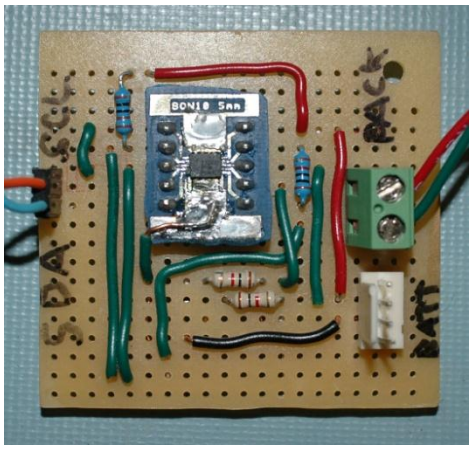

Figure 5: Prototyped BQ27200 Circuit

Once prototyped, the chip was interfaced with the MSP430 Micro-controller. The MSP430 was then interfaced with a computer where the user is able to "talk" to the BQ27200. The user is then able to identify registers already allocated on the chip

DC-DC Converters

The DC-DC converters were also changed during the fall 2008 semester. The TPS6300X converters will replace all DC-DC converters previously selected during the CDR. The TPS63001 and TPS63002 chips are able to output set 3.3 V and 5 V respectively. The converters were changed due to the high amount of space required for the MAX1771 chips, provided there were six circuits required for the design. Another reason for switching to the TPS63001 3.3 V DC-DC converter is for its buck/boost capabilities. The previous chip selected for the 3.3 V output was only a step-down converter, which wouldn't work if the voltage dropped below 3.3 V. The TPS family is also capable of converting the voltage more efficiently than the MAX1771 chips. A prototyped circuit of the TPS63002 PCB can be found in Figure 6.

Figure 6: Prototyped TPS63002 Circuit

The TPS63001 and TPS63002 circuit schematics are identical. Having prototyped the board, the chip was characterized by varying the input voltage with a power supply. The output of the chip was monitored by a DMM. The results of the 3.3 V and 5 V chips can be found in Figure 7 and Figure 8 respectively.

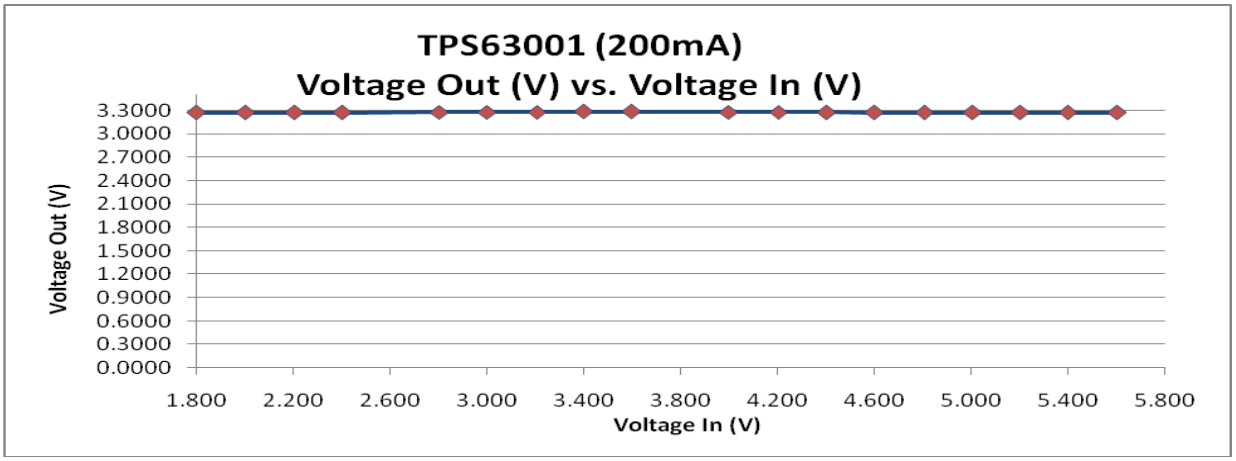

Figure 7: TPS63001 3.3 V Output Voltage vs. Input Voltage

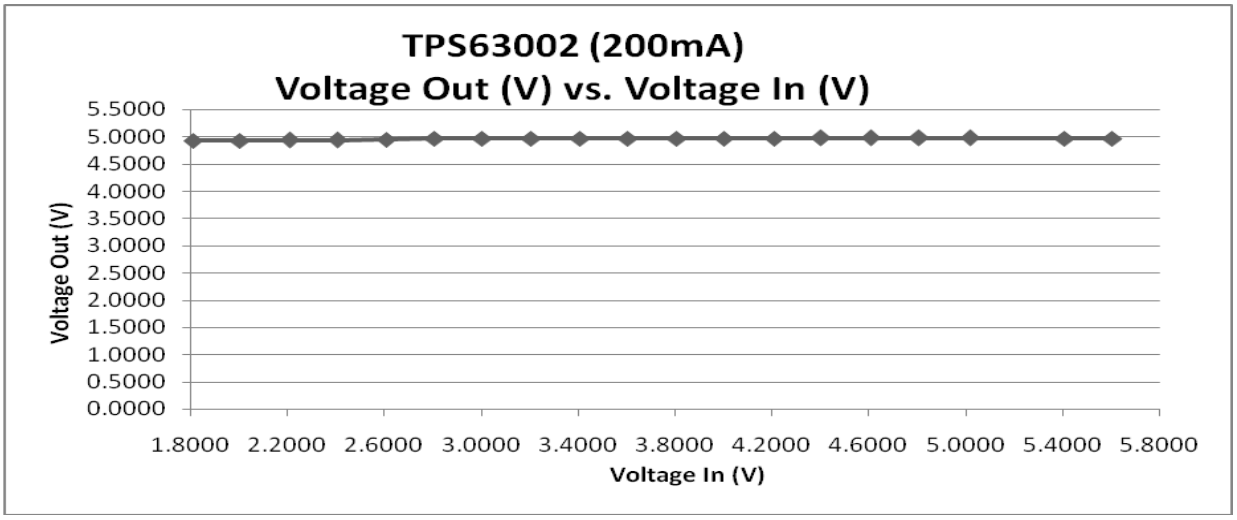

Figure 8: TPS63002 5 V Output Voltage vs. Input Voltage

From the characterizations, it is verified that the chips work properly throughout the varying voltages. It is also verified that the TPS63001 chip will be operational when the input voltage is dropped below 3.3 V.

Another addition to the changes made with the DC-DC converters is the absence of the 6 V DC-DC converter mentioned earlier in the CDR. The requirement for 6 V at 2 A was dismissed when an on-board DC-DC converter was discovered. This discovery was made when the Yaesu Transceiver was stripped for the FlatSat Model. A FlatSat model of the EPS is shown in Figure 8.

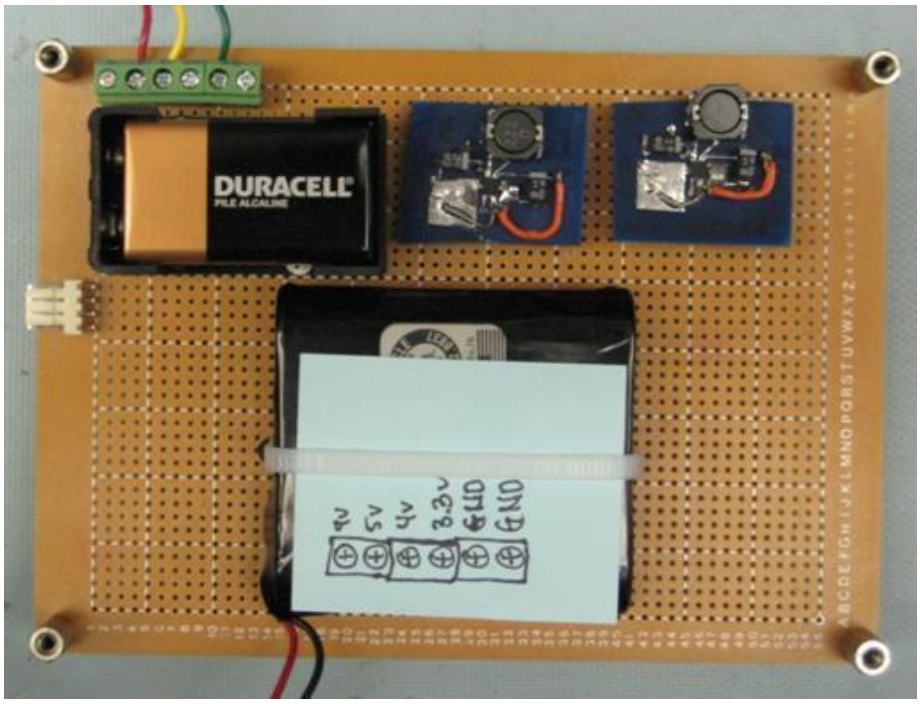

Figure 8: FlatSat EPS Board

The FlatSat EPS board consists of a 9 V primary battery, which will be used for the antenna deployment system, along with 3.3 V and 5 V TPS6300X chips and the secondary Saft battery. The FlatSat EPS model shown is missing the battery charger, fuel gauge, solar panels, and solar panel DC-DC converters. This model was able to power telecom and C&DH subsystems when transmitting and receiving data.

PCB Software

The first half of the spring 2008 semester was devoted to the learning of the PCB software. The software chosen for the PCB layout is Advanced Circuit's PCB Artist. Through the PCB software, the components of the EPS were placed on a PCB. The first step in using the software is to create the chip. Creation of specific chips was required because the library of PCB Artist was found to be limited to what chips were available. Once the chip was created, the creation of the circuit's schematic was done. The final step in the schematic design was placing the schematic on the PC104 template which was created by teammate Jeremy Chan. Once this was completed, the schematic was converted to PCB by software. The software provides an option to auto-place chips as well as auto-routing tracings between components. This stage of the design process gave problems because the software was not able to create all the connections required. Even with a four layer board, the software wasn't able to make all the connections. Placement of components, as well as routing tracings was done by hand. Indication of connections was made by software, through creating the schematic, to simplify routing of tracings. The finalized PCB layout for the EPS board is shown in Figure 9**.**

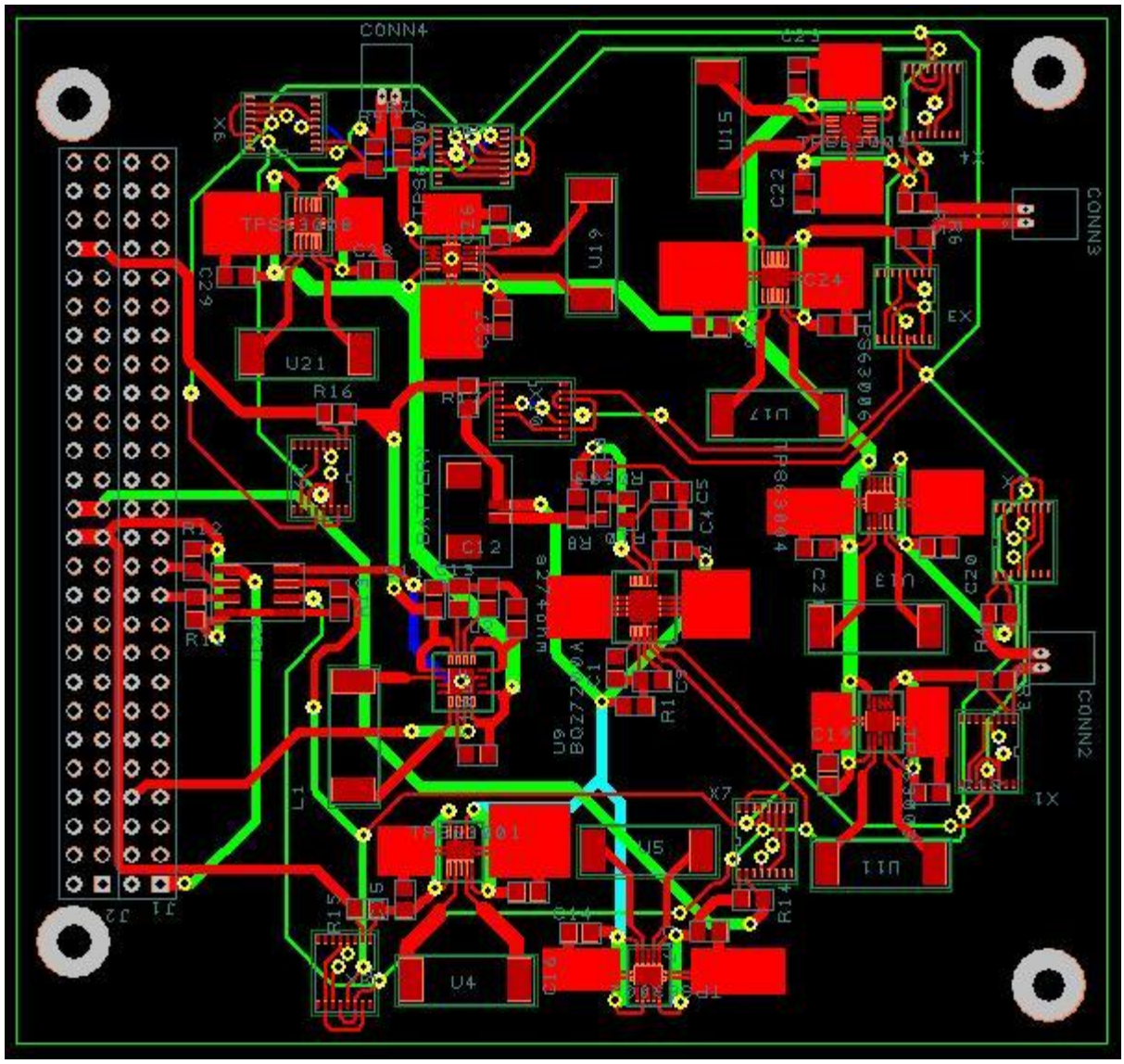

Figure 9: EPS PCB Layout

CONCLUSION

The fall 2008 semester, much progress was made in the design and fabrication of the EPS. A valuable lesson learned from this experience was that a chip's datasheet needs to be read through thoroughly to avoid problems later on in the design process. Prototyping and testing of individual circuits also proved to be more difficult to accomplish than expected. The circuit schematics were viewed to be simple in terms of design. When prototyping the chips however, roadblocks were ran into when trying to solder the QFN packages. By trial and error, the prototyping method of fabricating PCB's for the circuit was found to be the most effective. Through our experiences with PCB Artist, it was apparent that not everything can be done with the software.

ACKNOWLEDGEMENTS

I would like to thank the Hawai‘i Space Grant Consortium for granting me the irreplaceable experience to participate in a prestigious program. I would also like to thank all of the Kumu A‘o Cubesat team for being a cohesive unit. Also, thank you to mentors Lloyd French and Byron Wolfe who gave valued advice throughout the semesters.

REFERENCES

Maxim-ic Website: DC-DC Converters
Available [Online]: http://www.maxim-ic.com/index.cfm?CMP=KNC-8AO766069986

Saft Batteries Website: Li-ion Battery
Available [Online]: http://www.saftbatteries.com/

Spectrolab Website: Improved Triple Junction Solar Cells
Available [Online]: http://www.spectrolab.com/prd/space/cell-main.asp

Texas Instruments Website: Fuel Gauge
Available [Online]: http://www.ti.com/

KUMU A‘O CUBESAT: ELECTRICAL POWER SUBSYSTEM

Reid A. Yamura
Department of Electrical Engineering
University of Hawai‘i at Mānoa
Honolulu, HI 96822

ABSTRACT

The design and structure of the Electrical Power Subsystem (EPS) on the Kumu A‘o CubeSat from the University of Hawai‘i is described. The hardware selection and design of EPS is described in two fundamental blocks: Power Generation and Power Distribution. In the design of the Power Generation, a simple technique for optimizing the amount of power extracted from solar cells is described. The final design for EPS is also presented for the Kumu A‘o CubeSat.

INTRODUCTION

The mission of the Kumu A‘o CubeSat to develop, test, launch, and operate Hawai‘i’s first successfully launched CubeSat. The primary objective is to develop a fully functioning CubeSat bus to serve as a prototype for future UH CubeSat missions. The CubeSat project provides a way for the students to learn the various steps involved with a satellite design within a relatively short period compared to larger conventional satellite systems and allows opportunities to incorporate various experimental payloads for the scientific community. One of the team's main goals is to simplify the fabrication of the bus which will minimize the assembly time of the satellite.

The EPS objective is to generate, regulate, store, and distribute power to CubeSat’s bus and payload. The constant generation and distribution of energy will sustain the CubeSat for the duration of the mission. The basic structure of the EPS consists of solar cells that receive energy from the sun that is used to charge the onboard battery. The battery’s power is then distributed through various DC-DC converters that provide the necessary voltages and currents to the satellite bus and payload. The DC-DC converters are controlled by switching mechanisms and the battery is continuously monitored by a battery gauge. Both switching mechanisms and battery gauge are both controlled by a microprocessor to ensure proper power management. The basic block diagram of the EPS is shown in Figure 1.

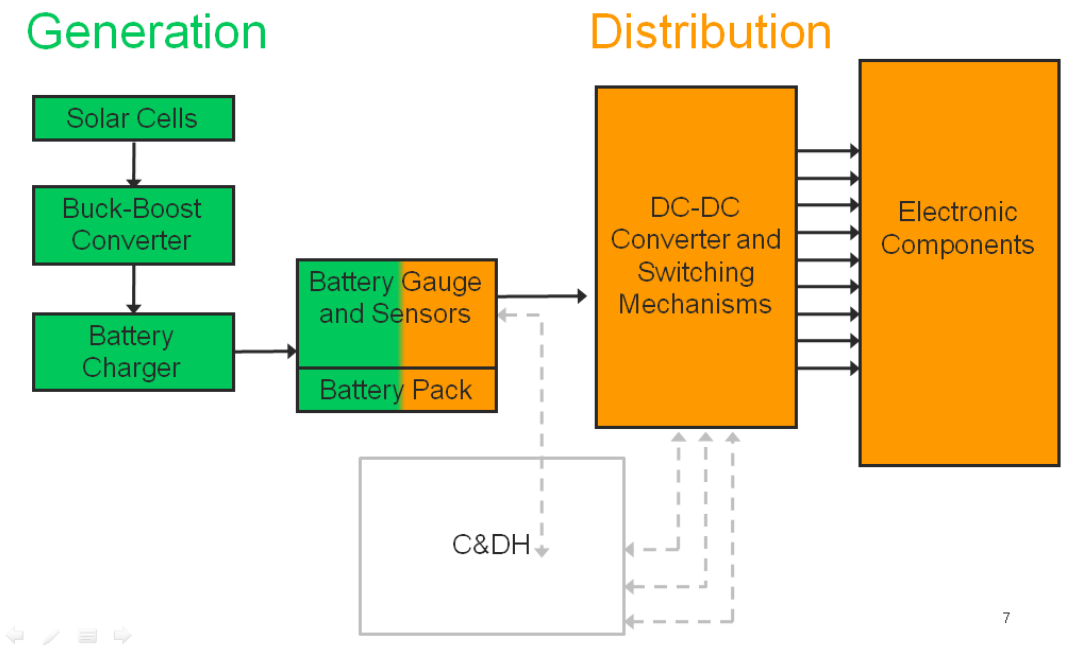

Figure 1: Basic EPS Block Diagram

POWER GENERATION

The objective of the power generation in EPS is to harvest enough energy from the solar cells during sun periods and store the power in the battery where it will be readily available for distribution during sun eclipses. Power generation will consist of six arrays of solar cells that will be regulated by DC-DC converters that will be used to charge the battery on the satellite. The basic power generation system on the satellite is shown on the left side in green in Figure 1.

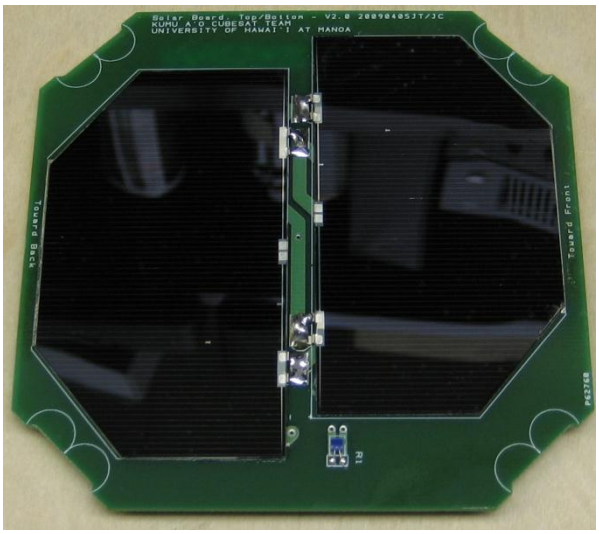

Figure 2: Side panel containing 2 UTJ solar cells connected in series

Spectrolab's 28.3% Ultra Triple Junction ($GeInP_2$/GaAs/Ge) solar cells were chosen due to their high efficiency. The solar cell arrays consist of two UTJ cells connected in series on a Printed Circuit Board (PCB) which produces 4.2V at 500mA which translates to 2.1W at AM0 conditions. Figure 2**Error! Reference source not found.** shows two of the UTJ solar cells soldered to a PCB for a side panel on the CubeSat. These arrays occupy five out of the six sides of the satellite. The sixth side of the CubeSat contains exterior connections such as a USB port, a remove before flight connection and 5V DC jack. To optimize the amount of power generation on the CubeSat, the unused surface area on the sixth side contains an array of seven pairs of Spectrolab's Triangular Advanced Solar

Cells (TASC) cells which have an efficiency of 27%. Each pair consists of two TASC cells connected in series to produce approximately 5V; each of the seven pairs is connected in parallel to increase the current output to approximately 196mA in AM1.5 conditions.

The input voltage for the Lithium-ion battery charger ranges from 4.0V to 5.5V; though the output voltage from the solar cells is 4.2V, it may not always be within that range. Texas Instrument's TPS63000 buck-boost DC-DC converters will step-up or step-down the input voltage of the charger to keep it within the accepted range. By conducting tests, the charger was found to be most efficient when 4.2V was the voltage input for the charger. Therefore, the buck-boost converter will regulate the input voltage to the charger at 4.2V to improve the efficiency of the system. Since the nominal output voltage of the solar cells and the most efficient input voltage of the charger is both 4.2V, the buck-boost converter is used as a pass-through voltage regulator. As a result, the converter will only buck or boost the voltage if the output voltage of the solar cells strays from 4.2V and the converter will be at its optimal efficiency greater than 90%. Each solar cell array output will have a dedicated step-up converter connected to it. The output of the converters will be connected in parallel to the input of the battery charger. Though this design uses more surface area on the PCB, it optimizes the maximum amount of power that can be extracted simultaneously from all the solar cells. Other cells that are not in direct sunlight are able to generate power from albedo energy and contribute to driving the load.

Linear Technology's LTC4001 buck switch-mode Lithium-ion charger was chosen for EPS for its adjustable charge rate capability and high efficiency. The Lithium-ion charger regulates the necessary voltage and current into the battery to properly charge the battery up to an end voltage of 4.2V. The charger can take an input voltage of 4.0 to 5.5V and the rate of charge is determined by the value of a resistor that is shunted to ground at one of the terminals. The LTC4001 buck switch-mode charger switches a power transistor between its saturation state and cutoff state. The saturation state of the transistor is the "completely on" state while the cutoff state is when the transistor is "completely off". The output voltage is taken from the average duty cycle created by this "switching." This operation proves to be more efficient when compared to a linear charger because there is little power dissipated in the "completely on" and "completely off" state.

To optimize the design and not be limited to one set charge rate, an adjustable resistor is connected from the feedback connection on the charger to ground. The resistor value can be adjusted by a MSP430 microcontroller that will adjust the charge rate according to the input voltage of the charger to maintain a steady 4.2V. Using a feedback scheme with a variable charge rate, the charger will not draw more power than the solar cells can provide. Another benefit is that the charger will draw the maximum power from the solar cells by regulating the charge current to insure that every single watt that the solar cell generates is stored in the battery.

Instead of using an adjustable feedback resistor, a Bipolar Junction Transistor (BJT) is used. The feedback port on the LTC4001 can be molded as a voltage source that regulates 1.2V across the feedback resistor to ground. The feedback resistor can be replaced with a current controlled current source which can be controlled directly from the MSP430. With the set output voltage of 1.2V and an adjustable current from the base to the emitter of the BJT that is defined by the amount of current injected into the base of the BJT, the BJT can now be used just like a variable resistor. The current injected into the base of the BJT is directly proportional to the charge rate, therefore, if more current is injected into the base, the charge rate increases and vice

versa. Using a BJT compared to a digital potentiometer saves precious space on the EPS PCB, responds faster and has much more resolution in altering the charge current of the LTC4001. The basic idea is shown in Figure 3, where the resistor R is used as a current limiting resistor into the base of the BJT.

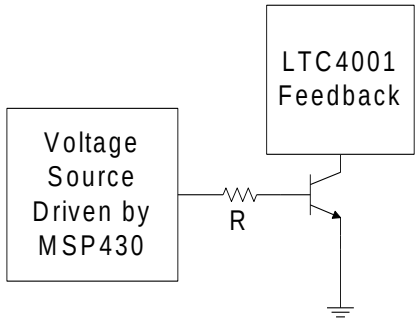

Figure 3: Basic configuration of using a BJT to adjust the charge rate of the LTC4001

Power Distribution

The second component to EPS is power distribution. The power distribution includes the fuel gauge and Lithium-ion battery to provide power the DC-DC converters. The Kumu A‘o CubeSat requires bus voltages of 3.3V, 3.7-4.2V, 5V, and 9V to distributed to the rest of the CubeSat via the PC104 bus. The 3.3V and 5V bus are generated through DC-DC converters that are connected to the Lithium-ion battery. The 3.7-4.2V bus is a direct line to the Lithium-ion battery as well as the 9V bus is a direct line to a typical Alkaline 9V battery. The DC-DC converters will be controlled by the Command and Handling Subsystem (C&DH), which is the brain of the satellite, through the use of the enable (EN) pin provided by each converter. By setting the pin high or low, C&DH will be able to turn the chip on or off while switching to different modes to save power consumption. The basic power distribution system on the satellite is shown on the right side in orange in Figure 1.

In any satellite, a battery is used to store the energy gathered from the solar cells. Of the many types of batteries that are commercially available on the market, a Lithium-ion battery was chosen for the satellite. The advantages of the Lithium-ion battery compared to Nickel-Metal Hydride (NiMH) batteries include: a high energy- to-mass ratio, low self-discharge rate, and no memory effect. A single cell battery was chosen to avoid complications with having to balance the charging of multiple cells. Saft’s MP176065 single cell Lithium-ion battery as shown in Figure 1Figure 4 was selected for its mass, capacity and energy density. The Saft MP176065 battery features a mass of 150 g, a capacity of 6.8 Ah, and an energy density of 26.5 Wh. When the MP176065 was compared to other batteries with similar capacities and energy densities, the other batteries did not meet the mass and size requirements.

Figure 4: Saft MP176065 Lithium-ion battery

To ensure the CubeSat will have the necessary amount of power required to carry-out its mission, C&DH will dictate which power mode the CubeSat will be in which will depend on the power capacity remaining in the Lithium-ion battery. In order for C&DH to make accurate decisions of what mode to be in, C&DH must be able to access vital information about the battery such as time till empty, average power output, average current output, the voltage of the battery, percent capacity remaining, and temperature. Battery fuel gauges are typically used to gather this type of information. The BQ27200 is a fuel gauge manufactured by Texas

Instruments that will be used to interface between the MSP430 and the Lithium-ion battery via I^2C to provide information to C&DH.

Texas Instrument's TPS63001 and TPS63002 buck-boost converters were selected to produce the 3.3V and 5V buses respectively. The converters were chosen for its high efficiency, its limited need for external components, and its small footprint on the PCB. Since both chips belong in the TPS63000 family of DC-DC converters, they share the same circuit configuration which simplifies the distribution design. The converters has a wide input voltage range of 1.8-5.5V and is able to output up to 1.8A of current, which is well within the requirements of the CubeSat. EPS can be summarized in Figure 5 which describes the both the power generation and distribution of the system. In addition to the fuel gauge which monitors the battery, there are a total of 10 INA209 power monitors that will report telemetry data to C&DH; one chip for each solar cell array (not shown) and four chips for the buses on the power distribution.

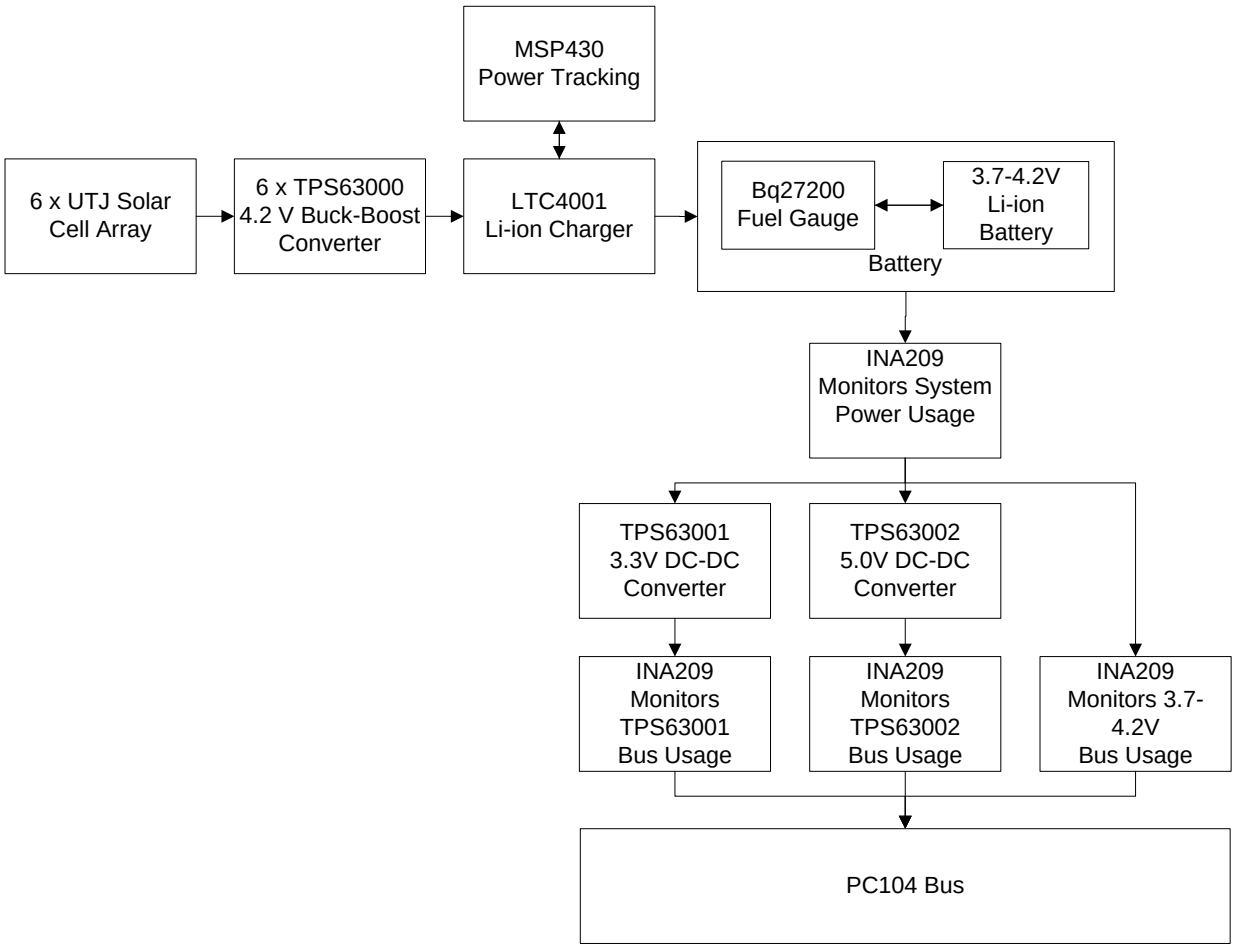

Figure 5: EPS power generation and distribution block diagram

CONCLUSION

After several design revisions and modifications to the EPS of the CubeSat, the fabrication of the Kumu Aʻo CubeSat is in its final stages of completion. Though the basic idea of an EPS system may seem simple in the design phase, there are many complications and

roadblocks that will occur during prototyping and fabrication. Much communication is needed between the various subsystems is needed in order to have a successful CubeSat that will function properly and meet each subsystem's requirements and demands. EPS has been a challenging but yet exciting task to accomplish on the CubeSat because everything was designed from the ground up and lots of thought and considerations was taken to ensure a successful system.

ACKNOWLEDGEMENTS

I would like to thank the Hawaii Space Grant Consortium for their continued support of providing undergraduate research opportunities to help students gain knowledge and experience. Thank you to the Native Hawaiian Science and Engineering Mentoring Program and the College of Engineering at the University of Hawaii for all the support on the project; to my mentors Lloyd French, Byron Wolfe, and Dr. Wayne Shiroma for their guidance, motivation, and technical support that they have provided throughout the project; the previous members of the Kumu A'o CubeSat team for allowing me to work on this projected; and finally to my family for supporting me.

REFERENCES

Linear Technology Corperation. "LTC4001 2A Synchronous Buck Li-ion Charger." 2006. Linear Technology. 10 June 2009 <http://cds.linear.com/docs/Datasheet/4001f.pdf>.

Saft Specialty Battery Group. "Rechargeable lithium-ion battery MP 176065." November 2005. Saft. 10 June 2009 <http://www.wamtechnik.com.pl/pdf/akumulatory/litowo-jonowe/mp_176065.pdf>.

Spectrolab Inc. "Triangular Advanced Solar Cells." 10 April 2002. Spectrolab. 10 June 2009 <http://www.spectrolab.com/DataSheets/PV/PV_NM_TASC_ITJ.pdf>.

Spectrolab Inc. "28.3% Ultral Triple Junction (UTJ) Solar Cells." 21 April 2008. Spectrolab. 09 June 2009 <http://www.spectrolab.com/DataSheets/TNJCell/utj3.pdf>.

Texas Instruments Incorporated. "High-Side Measurement, Bi-Directional Current/Power Monitor with I2C Interface." March 2009. Texas Instruments. 10 June 2009 <http://focus.ti.com/lit/ds/symlink/ina209.pdf>.

Texas Instruments Incorporated.. "Singel Cell Li-ion and Li-pol battery gas gauge IC for portable applications (bqJUNIOR)." March 2006. Texas Instruments. 10 June 2009 <http://focus.ti.com/lit/ds/symlink/bq27200.pdf>.

Texas Instrumets Incorporated. "TPS63000 High Efficent Single Inductor Buck-Boost Converter With 1.8-A Switches." 2009. Texas Instruments. 10 June 2009 <http://focus.ti.com/lit/ds/symlink/tps63000.pdf>.

DEMONSTRATING CAPABILITIES OF ISAAC (INSTRUMENT SHARED ARTIFACT FOR COMPUTING)

Chester N.V. Lim
Jet Propulsion Laboratory
Department of Electrical Engineering
University of Hawai‘i at Mānoa
Honolulu, HI 96822

ABSTRACT

ISAAC is a research and technology development project whose objective is to provide a FPGA-based computing and control platform that will control a variety of onboard instruments ranging from imagers, radar and radiometers. There are six sub-parts which makes up ISAAC (iBench, iCore, iPackage, iBus, iBoard, iTool) each performing separate tasks. The objectives for this summer are to assist the engineers who are working with the iCore and iPackage sub-parts. iCore is a sub-part that holds the library of RTL (Register-Transfer-Level) codes and is reconfigurable depending on the specific instrument. The task for iCore is to help with the verification, validation and resource usage estimations. iPackage includes a branch called iPanel and its purpose is a high level interface in which the user will be able to gather telemetry from the instruments. The task for iPanel is to create the GUI (Graphical User Interfaces) in Python that will display telemetry from the instruments and be able to have a command console for the user to send instructions to the instruments. Another task for iPackage is to put together a demo for the FPGA computer platform, which includes being able to gather telemetry from an I2C thermal sensor and UART motor.

INTRODUCTION

This paper will discuss about the work that as been done over the ten weeks span of this internship. The objectives for this internship was to assist Dr. Yutao He and his team in developing a highly capable, reusable, and modular FPGA-based computing and control platform for instrument digital electronics. The FPGA based technology called ISAAC will be used for signal processing, telemetry collection and motor control. The tasks for this internship are to assist Jason Zheng and Kayla Nguyen with the iCore sub-part and to assist William Zheng with the iPackage sub-part.

Two types of chips may be used for an implementation on an application and they are hard-wired chips and programmable chips. Hard-wired chips, like an ASIC (Application Specific Integrated Circuit), are designed for a specific application and are not ideal for modularity and not reconfigurable. Programmable chips like an FPGA (Field Programmable Gate Arrays) on the other hand allows more room for modularity and are reconfigurable.

The advantage of using an FPGA based technology is that it is possible to assemble the same FPGA devices to be used in different applications thus reducing the non-recurring engineering costs. In addition, unlike ASIC’s, if there is a mistake with the logic, FPGA’s have the ability to be reprogrammed. An FPGA device may also act as a redundant system for a random failure in a certain logic device. The redundant FPGA device may be reconfigured to take over the failed device.

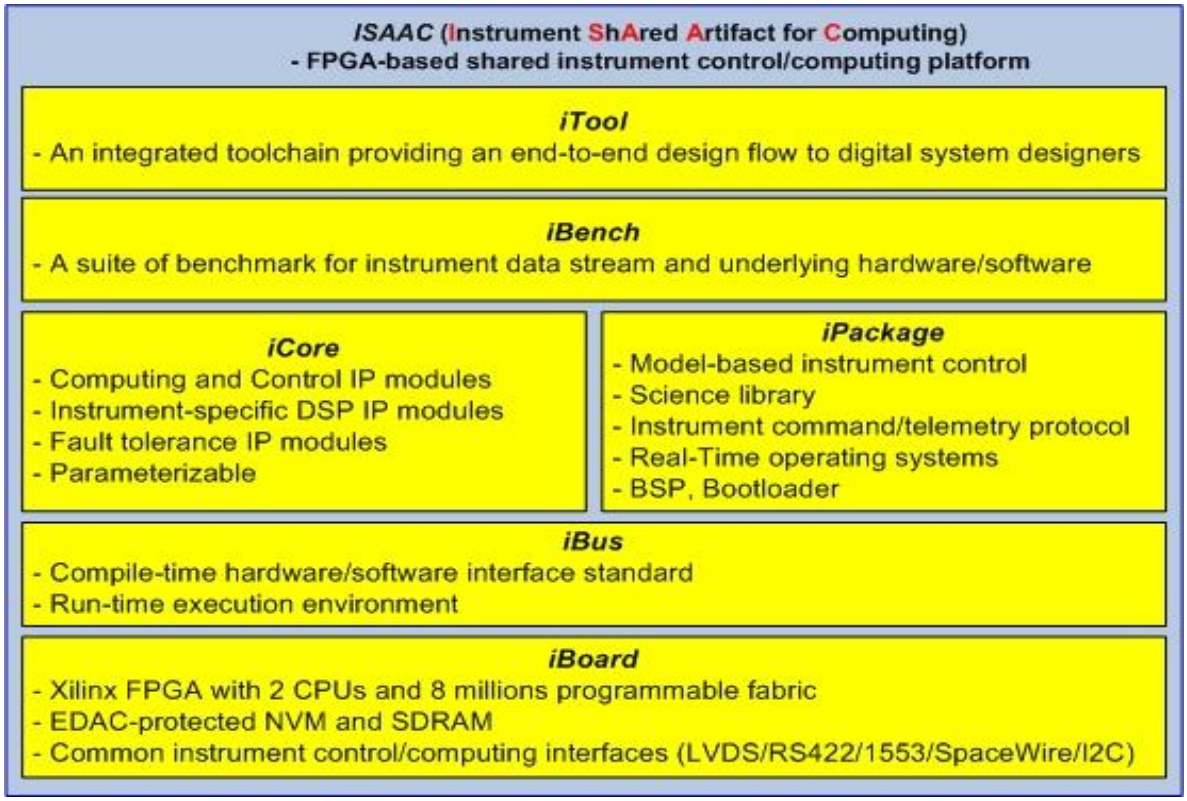

Figure 1: 6 sub-parts that make up ISAAC

	Isaac Newton (Radar)	**Isaac Asimov** (Imager)	**Isaac Stern** (Radiometer)
Mission Impact	**SMAP** Reduce downlink data rate	**MSPI** Data Reduction	**HAMSR** MBE-based Controller Instrument-S/C Interface
iBoard	ML410	ML410	ML410
iBus	CoreConnect	CoreConnect	CoreConnect
iCore	I/Q Demodulation & Decimation Filter	Bessel Function Fitting (Data Compression)	I2C Instrument Control & Timing
iPackage	BSP Linux, ICTP	BSP GSL, ICTP	BSP Linux, MBE, ICTP
iBench	Input: Memory Output: Matlab	Input: Hw generator Output: datafile	Input: Memory Output: iPanel/ICTP
iTool	ISE/EDK GNU SDE AccelDSP, TMRTool	ISE/EDK GNU SDE ImpulseC	ISE/EDK GNU SDE

Table 1: Implementation of ISAAC

ISAAC is an R&TD project whose objective is to provide a standard FPGA based computing and control platform for various types of instruments. There are six sub-parts that make up ISAAC. They are iTool, iBench, iCore, iPackage, iBus, and iBoard. Starting from the bottom of Figure 1, there is the iBoard, which is the hardware substrate that includes the Xilinx FPGA, a few standard hardware interfaces for external instruments and a few analog-to-digital converters for gathering telemetry. The iBus is a standard and unified interface that links the hardware to the software to provide easy adaptability and integration of modules during the system configuration and operation. Above the iBus is the iCore, which holds all the libraries of RTL codes which are like machine/hardware code. Depending on the user's application, they may choose to configure which libraries to include. The iPackage is much like the iCore except that iPanel hold libraries for the software such as instrument control software. The iBench is a compilation of data that may be used for benchmark, verification, validation, and calibration of the instrument. Finally, the iTool is a tool chain that provides smooth design flow from front end algorithm development to RTL implementation on FPGA device.

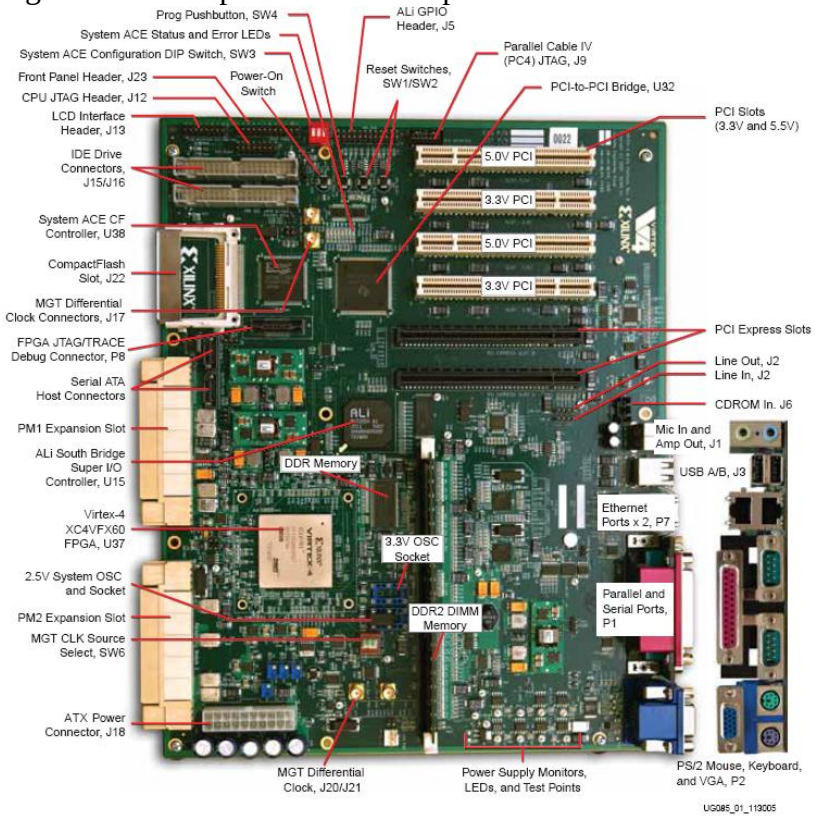

Figure 2: Prototype iBoard - Xilinx ML410
From: http://www.xilinx.com

ISAAC is currently developing control systems that will support instruments in the imagining, radar and radiometer field. The three projects demonstrating these capabilities are ISAAC Newton, which will demonstrate ISAAC's capabilities with radar instruments, ISAAC Asimov, which will demonstrate it's capabilities with imaging instruments and ISAAC Stern, which will demonstrate ISAAC's capabilities with radiometer instruments. Table 1 shows the different ISAAC projects and how they each utilize the six sub-parts that makes up ISAAC.

iCore Catalog

As mentioned earlier, iCore is storage for all the library of RTL codes. Figure 3 shows a breakdown of what RTL modules will be inside iCore. Currently iCore will support three types of instruments which include imaging, radar and radiometer instruments. The first task for iCore

was to construct a breakdown diagram that will help with getting a better understanding of how iCore is being implemented. The diagram will also speed the design process when building iCore because everything that needs to be in iCore has been thought out and sorted into its respective group.

iBoard Timing and Mapping for Digital Filtering Core

The task for the iCore sub-part was to verify how much resources the iBoard was using. This was done through a Linx machine that connected to the iBoard. The first thing that needed to be done was to check-out the program package that will be complied onto the iBoard. The ISAAC team uses Subversion (SVN) to manage its repository and uses SVN to check-out files. A check-out in SVN allows the user to copy the desired file into a specified directory for the user to modify. After check-out, the next step was to compile the code and run simulations to check if the RTL design is correct. Once the RTL design has been verified, the next step is to do the synthesis and Place-n-Route. In this step, the RTL code is complied and translated into a format that can be used to implement a Xilinx FPGA. After the RTL code has been complied, there is a 10 – 30 minute wait time for the Place-n-Route to finish. The Place-n-Route process is a process that takes the translated RTL code, reads the code, and configures the FPGA accordingly. After the Place-n-Route is finished, the next step is to verify the FPGA by checking its timing and mapping. There are two types of FPGA that the iBoard uses and they are Xilinx Virtex 2 and Xilinx Virtex4. For the verification, the numbers of multipliers, slices, flip-flops and look up tables (LUT), along with how fast the processor runs needs to be determined. Table 2 shows the end results of determining the timing and mapping of iBoard.

PARAMETER:	**Xilinx Virtex 2: speed grade 4**		**Xilinx Virtex 4: speed grade 10**	
Speed (Bandwidth)	91.4MHz		112.3MHz	
	Used / Total	**Percentage %**	**Used / Total**	**Percentage %**
Number of Multipliers	36 / 96	37%	36 / 128	28%
Number of Slices	10,498 / 14,336	73%	10,533 / 25,280	41%
Number of Flip Flops	15,753 / 28,672	54%	15,776 / 50,560	31%
Number of 4 input LUTs	11,910 / 28,672	41%	11,817 / 50,560	23%

Table 2: iBoard Verification

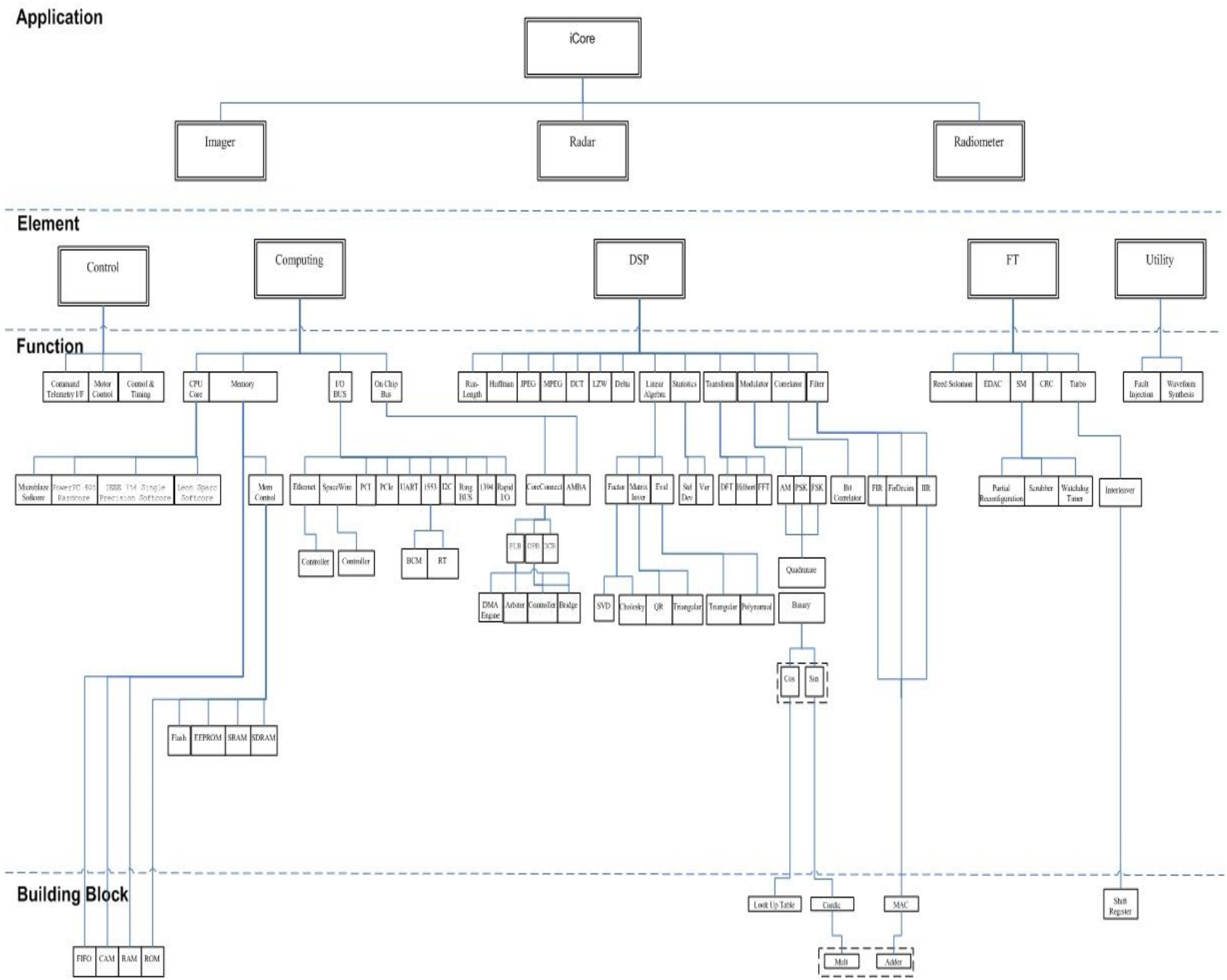

Figure 3: Breakdown of iCore

Motor Control

In order to keep the ISAAC project going, a demonstration was planned showing that it is possible to gather telemetry through iBoard. It was decided that telemetry would be gathered from a UART motor and an I^2C thermal sensor. Figure 4 shows a block diagram of the demonstration system.

The motor chosen for the demonstration is a Lin Engineering SilverPak 17CE motor. This motor is a bipolar stepper motor with integrated controller, driver, and encoder. To learn how the motor work, it was first connected to a UART RS485 to RS232 converter that was connected to the laptop. The user could choose to use the GUI software provided by the company or use HyperTerminal to send commands to the motor. Some of the problems that were encountered happened during setup. At first, the green LED that indicated that the motor was on didn't appear but it was later discovered that there was not enough current being supplied to the motor. Another problem that was encountered was that once the green LED indicator turned on, the motor would not spin. The problem was that the step size being inputted to the motor was too small; the motor needed an input of a step size larger than what was stated in the manual. The

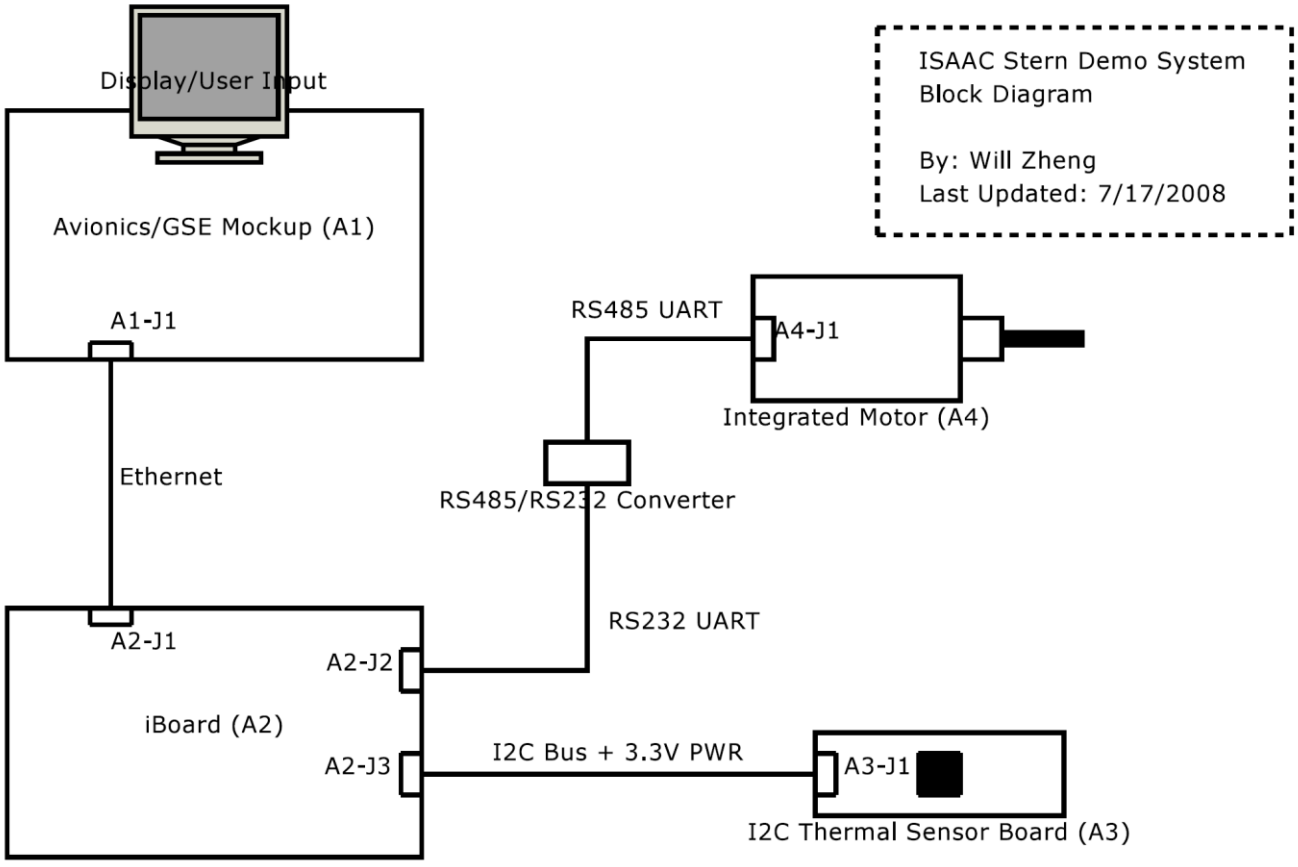

next step will be to implement the motor to the iBoard.

Figure 4: Demo System Block Diagram

Thermal Sensor

The thermal sensors for the demonstration are able to interface with the I^2C bus on the iBoard. The thermal sensor chosen was the MIC184 I^2C/SMBus thermal sensor. Before testing the thermal sensor with iBoard, it was tested on a PC laptop through an iPort/AI that connected to a RS232 connector. The iPort/AI is an I^2C host adapter that connects from the computer to an I^2C device. One of the major problems we had with the MIC184 was getting acknowledgement from the thermal sensor. According to the datasheet, the slave address is supposed to be 48h (in hexadecimal) however when calling that address in HyperTerminal, there is no response from the thermal sensor. It was discovered that for some reason, while using HyperTerminal, the user must left shift the address bit. Thus if the user wanted to talk to the slave whose address bit is 48h, the user has to convert 48h into binary, left shift and convert back to hexadecimal. The correct address bit to for the MIC184 while using HyperTerminal is 90h. After the address bit had been changed, the thermal sensor was able to acknowledge the master I^2C bus. However, the readings on the thermal sensors were not accurate. According to the company, the thermal sensors did not need any calibration and the sensor should be reading the ambient temperature.

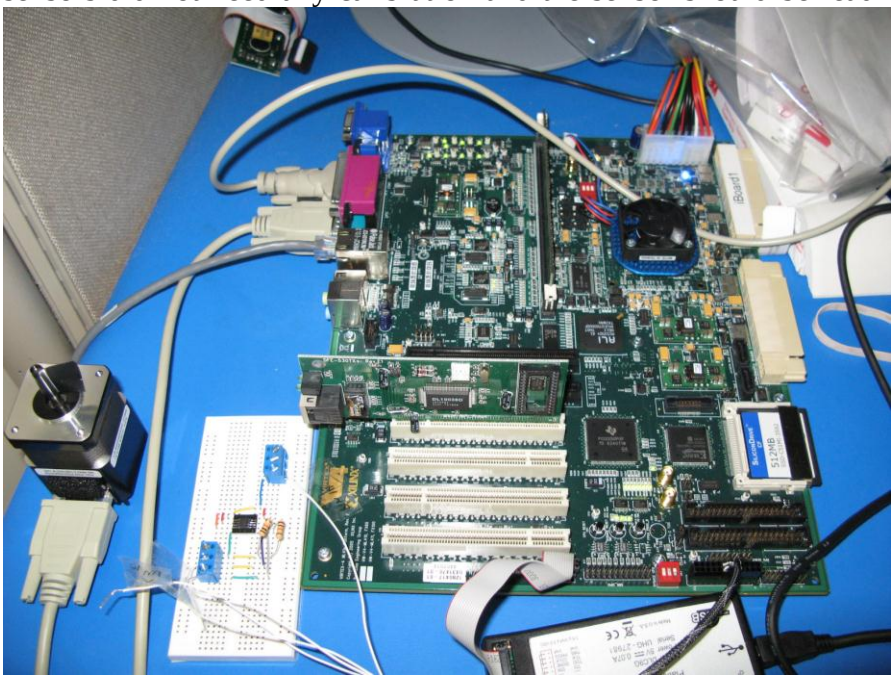

Figure 5: Actual Demo Setup

The MIC184 thermal sensor was found to be reading four degrees Celsius higher than ambient temperature after verification with a thermometer. Trying to read the temperature as closely as possible, another temperature sensor was ordered; LM75. Again, same as the MIC184, the address bit had to be shifted left in order to use HyperTerminal. The readings on the LM75 were also inaccurate however when the ambient temperature reached above a certain point, the LM75 was found to be accurate within $\pm 0.5^{\circ}C$. The LM75 was chosen to be the thermal sensor that will demonstrate the iBoard's ability to gather telemetry data.

Implementing motor and thermal sensor

Figure 5 shows the actual demo setup with the stepper motor and thermal sensors connected to the iBoard. Both the motor and the thermal sensor have been tested separately with a PC laptop and proven that they both work with the exception that the thermal sensor's reading was not accurate. The thermal sensor has been tested on the iBoard and proven to work however

the motor has not been tested yet with the iBoard. The problem now is that the connection with the motor and iBoard has not been established. Once a connection has been established, it will be possible to demonstrate the ability of iPackage. The demonstration consists of gathering telemetry from the thermal sensor. If the thermal sensor reads a temperature above a set threshold level, the iBoard will turn on the motor and start gathering telemetry from both the motor and the thermal sensor. The telemetry will then be sent to the host computer that will be displayed on the iPanel which will be discussed in the next section.

iPanel

Another part of iPackage is to provide the user with a graphical user interface (GUI) that will allow them to control the on board instruments remotely. In addition to being able to send commands to the instruments remotely, the user will also see telemetry data coming off the instruments. Figure 6 shows a flow diagram of how iPanel is intended to work for the demonstration. The program used to create the GUI was Python/Tkinter. In this demonstration, the telemetry coming from the LM75 thermal sensor along with some benchmark data and MBE (model based engineering) from the iBoard will be sent to the host computer. From the host computer, the data coming from the iBoard will be made into well-defined, standardized, data structure that will be passed along to the front-end display.

Figure 7 shows the envisioned design for iPanel's layout and Figure 8 shows the actual design of iPanel. iPanel allows the user to select an instrument to be controlled. When an instrument is selected, the user will be able to see the state of the instrument and resource usage. The user can select which telemetry they would like to track in a graph form and will also have the current telemetry displayed in a list form. The user can also control the instrument by sending commands in the command console in iPanel.

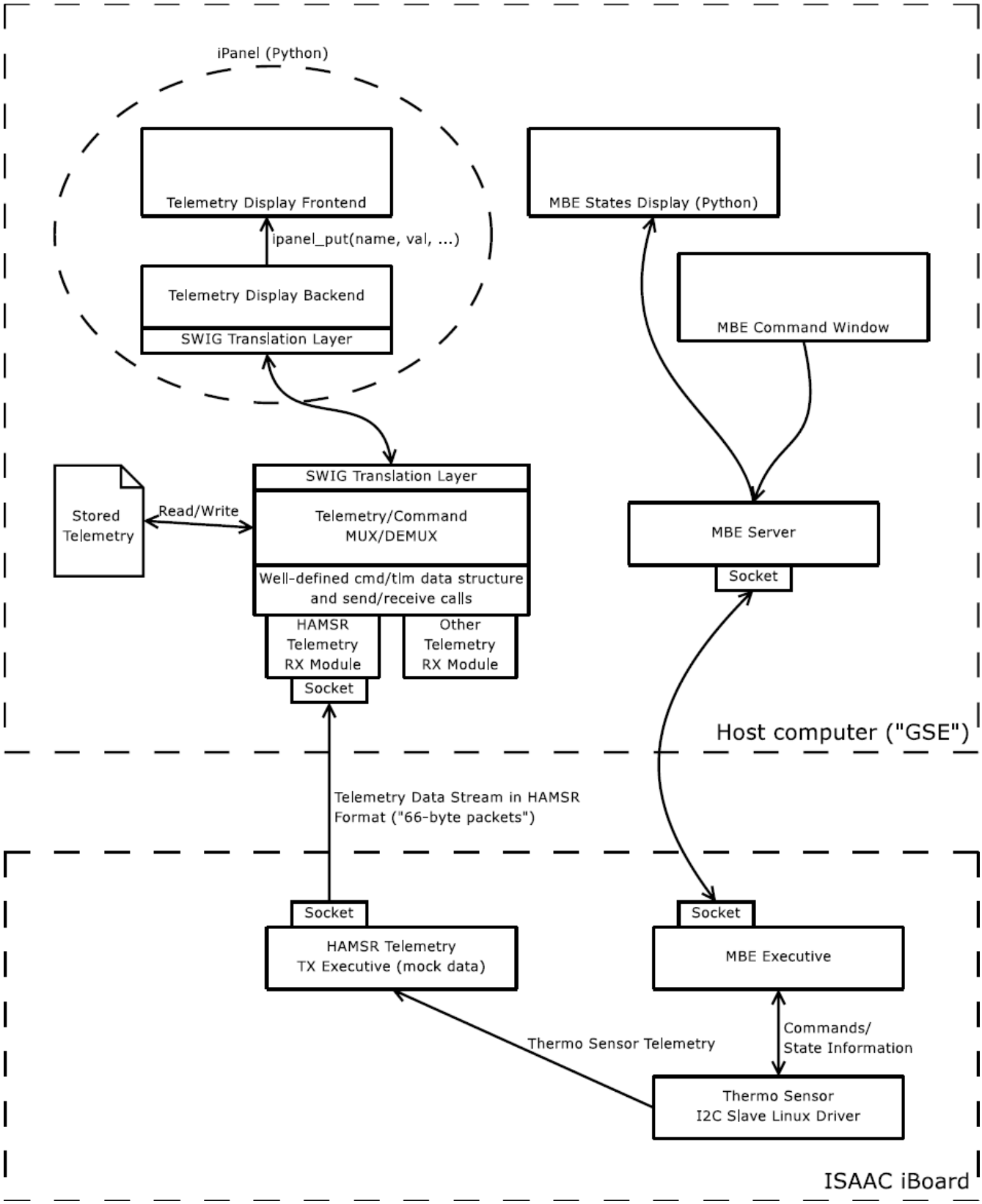

Figure 6: iPanel

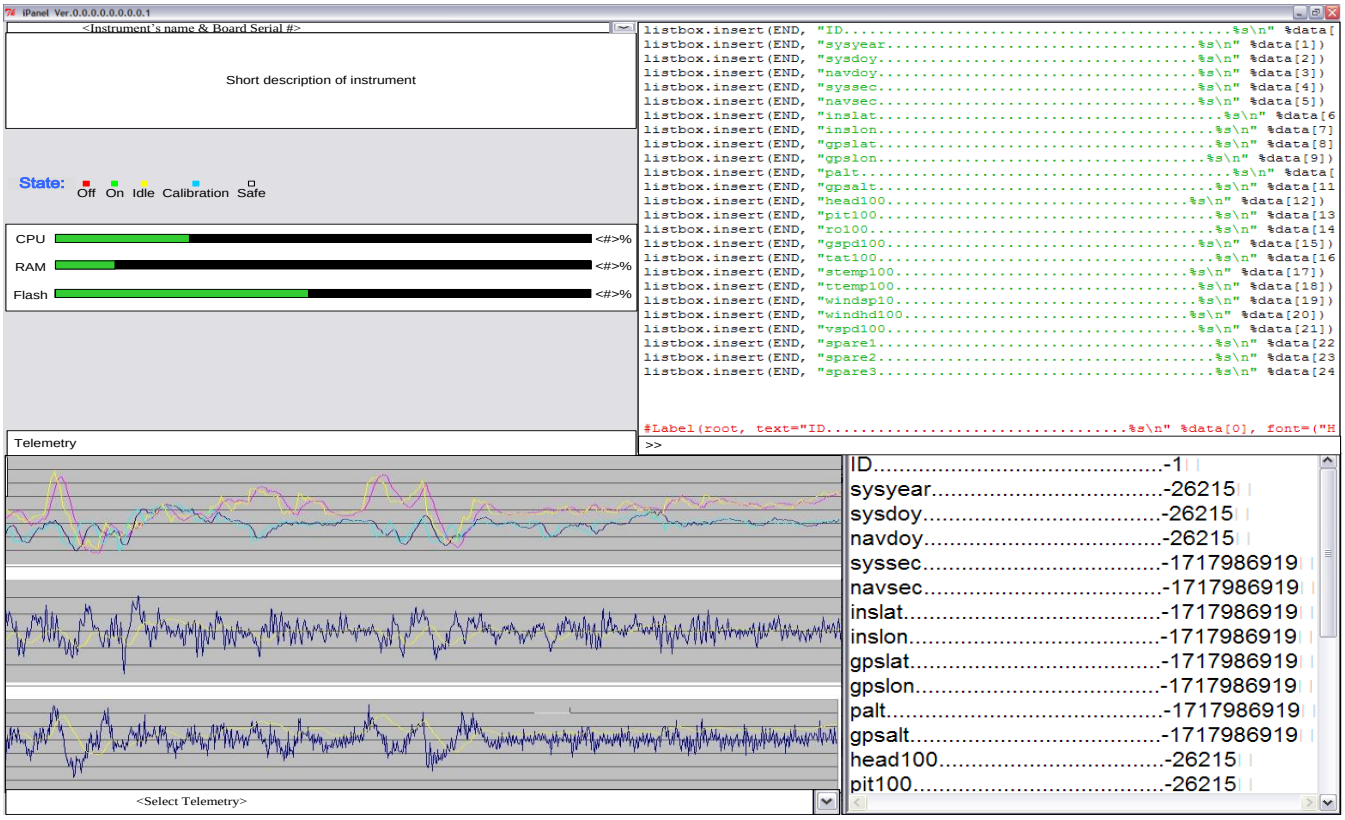

Figure 7: Envisioned design of iPanel

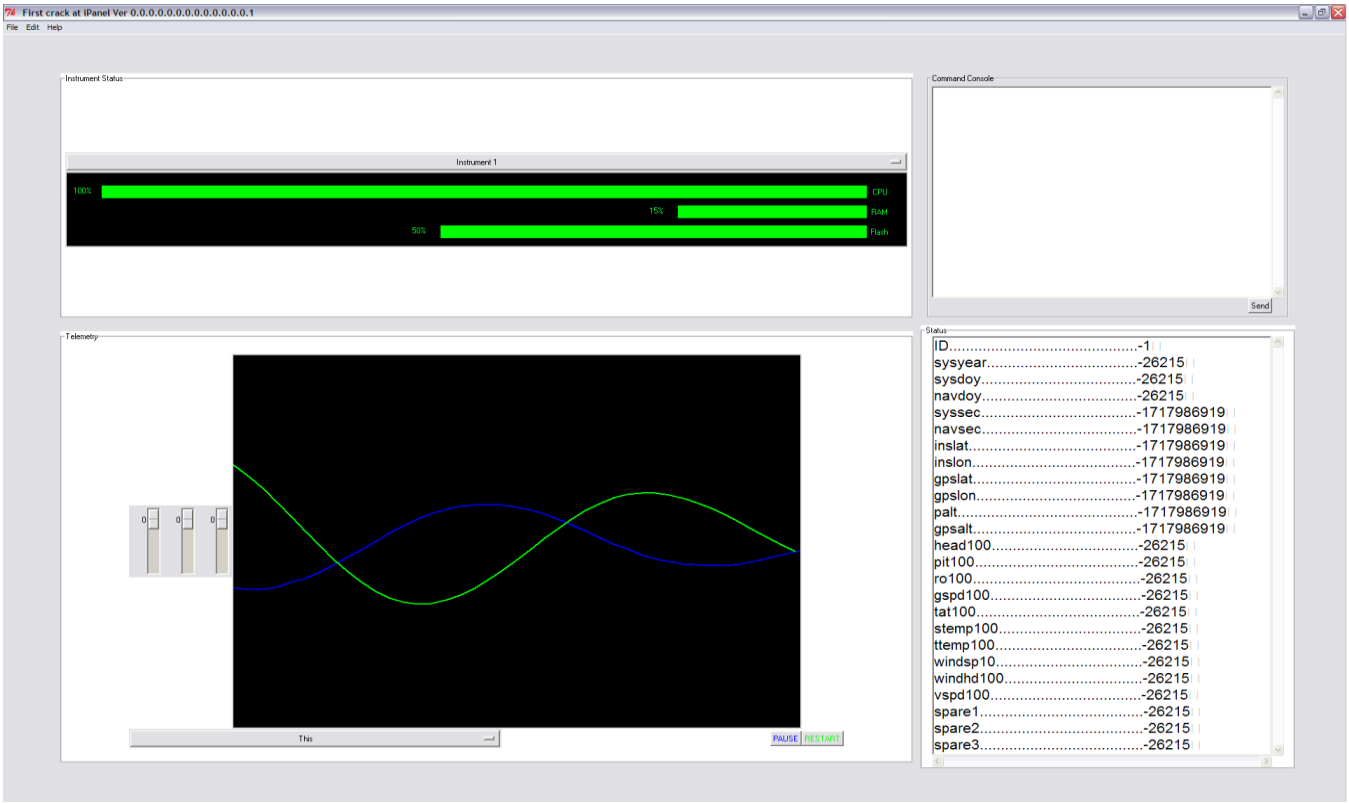

Figure 8: Actual design of iPanel

Contributions

1. Redesigned iCore catalog in Viso
2. Verified resource usage for the digital filtering core on iBoard
3. Ordered thermal sensors and stepper motors
4. Soldered and designed thermal circuit
5. Tested thermal sensors and stepper motors
6. Setup iBoard demo system
7. Designed iPanel GUI

CONCLUSION

This project required a large learning curve time period. Majoring in electrical engineering and concentrating in signal processing, embedded systems was a new thing that had to be learned. A lot of time went into learning the technical terms and acronyms in this field but not only understanding what they meant but how they work and why it was important. A new thing that had to be learned for this project was the programming language Python and TKinter. Learning how to use Linux didn't require much learning curve however; new techniques to enhance the Linux experience were learned. The next step for this project is to make a fully functional iPanel GUI display that is able to gather data in real time and send commands to the instruments. Also, although the thermal sensor and motors have been proven to work on the PC laptop and iBoard separately, they still need to be tested on iBoard together.

ACKNOWLEDGEMENTS

Dr. Yutao He was a great mentor. We had tag up meetings and quiet hours every week to make sure that if I had questions, I could ask. Also, even when he was busy, if I had a question, he would take some time to help me. Elizabeth Alfon and Debra Cuda were always there to help with JPL or office needs. They were very helpful in making things happen as quick as possible and always made sure everything that was needed was there. Will Zheng, Jason Zheng, and Kayla Nguyen helped with the project. They were like my mentors when I couldn't get a hold of Dr. He. Geoffrey Vaughan and William Jay were great officemates. If I had a question about JPL, they were more than happy to answer; they also helped me search for jobs at JPL and took me out to lunch every week. I would also like to thank Lindsey Holland, my co-intern, for helping me out in general.

REFERENCES

"FPGA vs. ASIC" [Online]. Available: http://www.xilinx.com/company/gettingstarted/fpgavsasic.htm

"FPGA Basics" July 25, 2008. [Online]. Available: http://www.andraka.com/whatisan.htm

Z. Junaid, "FPGA: The Chip That Flip-Flops" Oct. 1, 2004. [Online]. Available: http://209.85.173.104/search?q=cache:Fs2Kkub_FDwJ:www.cs.fredonia.edu/zubairi/training/fpga.ppt+why+FPGA&hl=en&ct=clnk&cd=1&gl=us

APPLYING ELECTRODYNAMIC DUST SHIELD TECHNOLOGY TO AN OPTICAL SURFACE ON A LUNAR ROVER

Jordan J. Olive
NASA AMES Robotics Academy
Computer Science Department
The University of Hawai‘i at Hilo
Hilo, HI 96720

ABSTRACT

Electrodynamic dust shield technology being researched in the Electrostatic and Surface Physics Laboratory at Kennedy Space Center is being adapted for use on an optical surface in a lunar environment . The tread driven design of the rover and placement of the camera between the treads warrants the need for an active dust deflection system. This paper will discuss preliminary dust deflection ideas, steps taken to create a working prototype, and the current status of the project.

INTRODUCTION

The Lunar Micro-Rover (LMR) project is currently underway at Ames Research Center. The purpose of this project is to create a relatively low cost universal lunar robotic platform to which various types of instrumentation could later be attached. The rover itself is approximately 35 cm long, 25 cm wide, and 15 cm tall. It has Teflon treads with Kevlar rope sewn on for grip. A camera is mounted in the chassis between the treads at the front of the rover with a glass window to look through. The camera will be used for both real time tele-operated driving as well as for taking high resolution images. A dust deflection system is needed to ensure that clear images can be continuously taken even while lunar regolith is stirred up and tossed around by the treads.

The surface of the moon can be described as a combination of fine dust and rocks. Most of the surface consists of a fine dust known as Lunar regolith, which has a bulk density of about 1.5 g/cm^3. According to The Lunar Sourcebook “roughly 10 to 20 percent of the [lunar] soil is finer than 20 μm, and a thin layer of dust adheres electrostatically to everything it contacts: spacesuits, tools, equipment, and lenses. In general, the particles are somewhat elongated and are angular to sub-angular.”

SUMMARY OF WORK

This semester’s work was dedicated to testing the electrodynamic dust shield based on three variables: voltage, frequency, and wave form. During the semester, I worked on creating a circuit that would allow me to alter these variables to find which would be most effective. After completing the circuit, I ran tests and collected data. After graphing the data, comparisons were made for effectiveness.

METHODS

The current power source I am using is the Ultra-Miniature High Voltage DC-DC power supply. For the clear circuit, I am using Indium tin oxide, currently at 8-12ohms per square foot. To measure and calculate the effectiveness of the dust repeller, I am using an electronic scale that measures out to the thousandths of a gram. The formula I am using to calculate the efficiency is:

CF: Clearing Factor

$$CF = \frac{m_i - m_f}{m_f} X100$$

Mi: Initial Weight of Dust

Mf: Weight of Dust after the use of the device.

Figure 1: clearing factor formula

DISCUSSION / DATA ANALYSIS

Each of the following graphs were run a total of ten times, and then the average was taken to figure out the mean efficiency using the Clearing factor formula.

VOLTAGE DATA

5Hz at **5,000volts** = average of 90.7% effectiveness (2.72 grams removed)

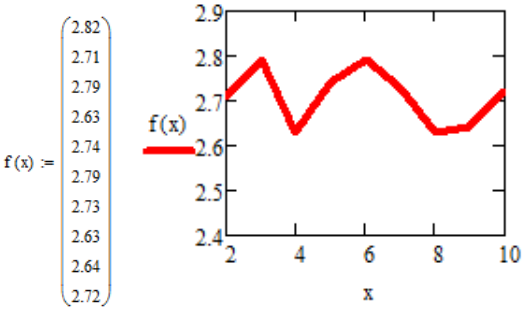

Figure 2: 5,000 volts graph

5Hz at **7,000volts** = Average of 61% effectiveness (2.01 grams removed)

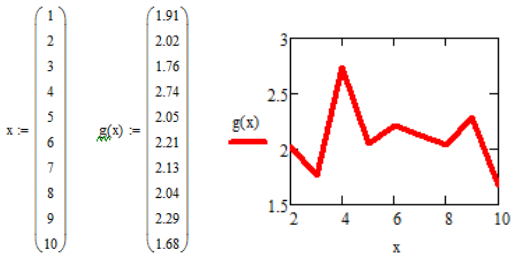

Figure 3: 7,000 volts graph

Frequency (Hz)	Voltage (v)	Effectiveness (grams removed)	Percent (%)
5	5,000	2.72	90.7%
5	6,000	2.01	61%
5	7,000	1.68	56%
5	8,000	0.03	1%

FREQUENCY DATA

7Hz at 5,000 volts = Average of 87% effectiveness (2.51 grams removed)

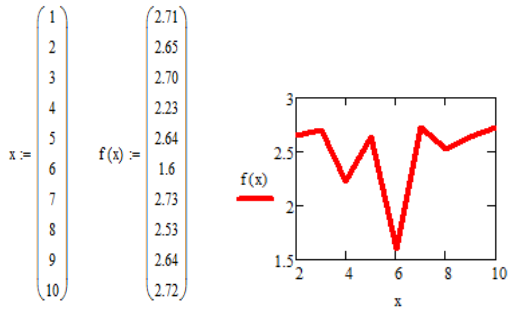

Figure 4: 7hz graph

15Hz at 5,000 volts = Average of 75.7% effectiveness (2.27 grams removed)

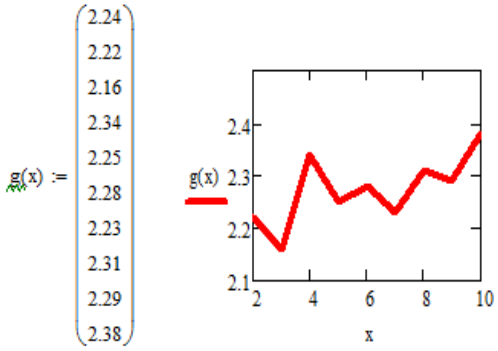

Figure 5: 15hz graph

60Hz at 5,000volts = Average of 87% effectiveness (2.51 grams removed)

$$f(x) := \begin{pmatrix} 2.03 \\ 1.97 \\ 2.12 \\ 2.01 \\ 1.99 \\ 2.07 \\ 2.13 \\ 2.07 \\ 2.34 \\ 2.12 \end{pmatrix}$$

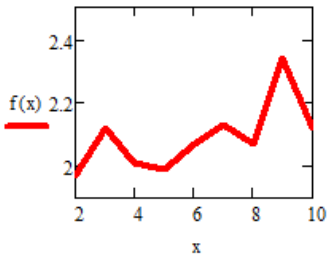

Figure 6: 60hz graph

Frequency (Hz)	Voltage (v)	Effectiveness (grams removed)	Percent (%)
5	5,000	2.72	90.7%
7	5,000	2.51	87%
15	5,000	2.27	75.7%
30	5,000	1.33	44.3%
60	5,000	2.068	66.8
120	5,000	0.89	29.7%

WAVEFORM DATA

Square wave at 5Hz at 5,000volts = average of 90.7% effectiveness (2.72 grams removed)

$$f(x) := \begin{pmatrix} 2.82 \\ 2.71 \\ 2.79 \\ 2.63 \\ 2.74 \\ 2.79 \\ 2.73 \\ 2.63 \\ 2.64 \\ 2.72 \end{pmatrix}$$

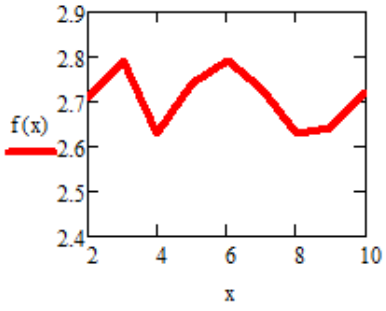

Figure 7: Squarewave graph

Sino wave at 5Hz at 5,000volts = average of 71.1% effectiveness (2.132 grams removed)

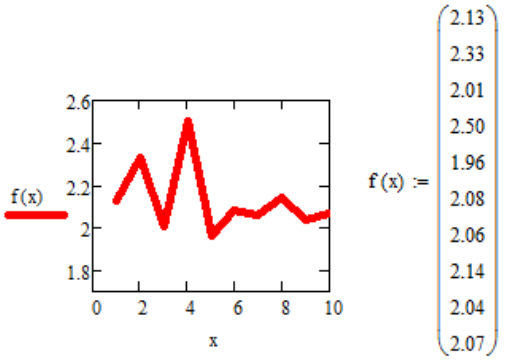

Figure 8: Sinowave graph

Triangle wave at 5Hz at 5,000volts = average of 90.7% effectiveness (2.132 grams removed)

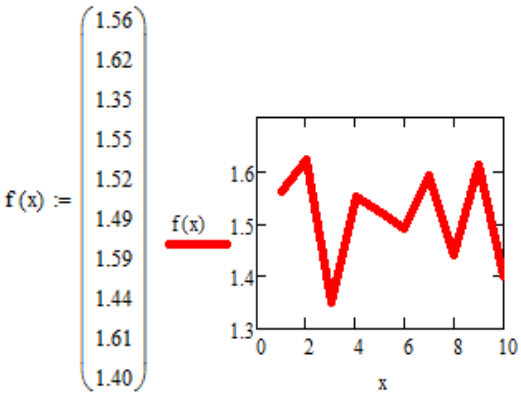

Figure 9: Trianglewave graph

Wave Form	Voltage (v)	Effectiveness (grams removed)	Percent (%)
Square	5,000	2.72	90.7%
Sino	5,000	2.132	71.1%
Triangle	5,000	1.513	50.4%

After looking over the data, it became evident that a frequency of 5 hertz at 5,000 volts with a wave form of a square is most effective.

FINAL CIRCUIT

The final circuit has the capabilities to vary Voltage, Frequency, Waveform and the radio control.

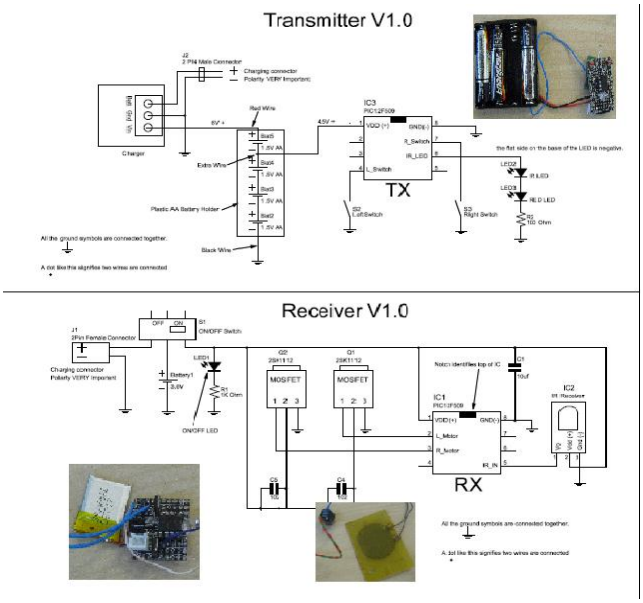

Figure 10: Picture of final circuit and pictures of the real circuit on vector boards.

CONCLUSION

In conclusion, I have successfully made a prototype that accomplishes the task at hand – to design a dust deflection shield which is light in weight, repels dust, draws low current, and is small enough to fit into the lunar micro rover. However, the size of the circuit and the power supply can still be improved.

With the testing I have completed this semester, I am confident in saying that the most efficient clearing factor is reached at 5 kilovolts, 5 Hertz, and a wave form of a square wave. This current design is going to be used in prototype 6 of the lunar micro rover.

However work still needs to be done in determining size both of the circuit and of the surface that is to be covered. This summer the robotics academy has given me the task of enlarging the area that the shield covers to encompass the entire robot, including the solar panels and the sensitive electronic probes that are going to be used to run di-electric testing on the moon.

The big question that needs to be answered is does the optimal voltage, frequency, and wave form of the current design stay constant as the surface area of the shield is expanded? To test these factors, I will need more time to create a new design for the electrodynamic circuit and to run the necessary tests to confirm system effectiveness.

ACKNOWLEDGEMENTS

Thanks goes out to my outstanding mentor Riley Ceria who guided me through my fellowship project this term. Also to the outstanding staff at the Hawai‘i Space Grant Consortium who made this awesome experience available. And more specifically to the following:

Riley Ceria – Mentor, Robotics Advisor for the College of Engineering, UH Mānoa

Marcia Rei Sistoso – Program Coordinator, Hawai‘i Space Grant Consortium

Edward Scott – Associate Director for Fellowships, Hawai‘i Space Grant Consortium

Sun Park – Advisor, University of Hawai‘i at Hilo

Art Kimura & Rene Kimura – Future Flight Director and Education Specialist, Hawai‘i Space Grant Consortium